Transport Phenomena in Cathode Catalyst Layer of PEM Fuel Cells

by

Prodip K. Das

A thesis
presented to the University of Waterloo
in fulfillment of the
thesis requirement for the degree of
Doctor of Philosophy
in
Mechanical Engineering

Waterloo, Ontario, Canada, 2010

I hereby declare that I am the sole author of this thesis. This is a true copy of the thesis, including any required final revisions, as accepted by my examiners.

I understand that my thesis may be made electronically available to the public.

Prodip K. Das

Abstract

Polymer electrolyte membrane (PEM) fuel cells have increasingly become promising green energy sources for automobile and stationary cogeneration applications but its success in commercialization depends on performance optimization and manufacturing cost. The activation losses, expensive platinum catalyst, and water flooding phenomenon are the key factors currently hindering commercialization of PEM fuel cells. These factors are associated with the cathode catalyst layer (CCL), which is about ten micrometers thick. Given the small scale of this layer, it is extremely difficult to study transport phenomena inside the catalyst layer experimentally, either intrusively or non-intrusively. Therefore, mathematical and numerical models become the only means to provide insight on the physical phenomena occurring inside the CCL and to optimize the CCL designs before building a prototype for engineering application.

In this thesis research, a comprehensive two-phase mathematical model for the CCL has been derived from the fundamental conservation equations using a volume-averaging method. The model also considers several water transport and physical processes that are involved in the CCL. The processes are: (a) electro-osmotic transport from the membrane to the CCL, (b) back-diffusion of water from the CCL to the membrane, (c) condensation and evaporation of water, and (d) removal of liquid water to the gas flow channel through the gas diffusion layer (GDL). A simple analytical model for the activation overpotential in the CCL has also been developed and an optimization study has been carried out using the analytical activation overpotential formulation. Further, the mathematical model has been simplified for the CCL and an analytical approach has been provided for the liquid water transport in the catalyst layer.

The volume-averaged mathematical model of the CCL is finally implemented numerically along with an investigation how the physical structure of a catalyst layer affects fuel cell performance. Since the numerical model requires various effective transport properties, a set of mathematical expressions has been developed for estimating the effective transport properties in the CCL and GDL of a PEM fuel cell. The two-dimensional (2D) numerical model has been compared with the analytical model to validate the numerical results. Subsequently, using this validated model, 2D numerical studies have been carried out to investigate the effect of various physical and wetting properties of CCL and GDL on the performance of a PEM fuel cell. It has been observed that the wetting properties of a CCL control the flooding behavior, and hydrophilic characteristics of the CCL play a significant role on the cell performance. To investigate the effect of concentration variation in the flow channel, a three-dimensional numerical simulation is also presented.

Acknowledgements

This work was supported by the National Research Council (NRC) and Natural Sciences and Engineering Research Council (NSERC) of Canada. I would also like to thank my supervisor, Dr. Xianguo Li, and Dr. Zhong-Sheng Liu for their guidance in the production of this thesis.

I want to extend my thanks to my colleagues at 20/20 Laboratory for Fuel Cells and Green Energy RD&D and NRC Institute for Fuel Cell Innovation for helping me to understand many concepts. Thanks to all of my friends from Bangladesh University of Engineering & Technology, University of Alberta, and Edmonton for their moral support over the last couple of years. A special thanks to A.K.M. Monjur Morshed (Mridul), Dulal Laha, Shafique Kamal, and Sukanta Pramanik for inspiring me over the last few years to finish this Ph.D. degree.

Lastly, but most importantly, I would like to thank my mom and siblings for their support throughout all my endeavors.

Dedication

This thesis is dedicated to Prof. Subir Bhattacharjee, who encouraged and inspired me to pursue a PhD and still has a strong influence in my personal life. It is also dedicated to Dr. Manas Shome and Prof. Abhijit Bhattacharyya, who brought me to the University of Alberta from a small town in Bangladesh.

Contents

List of Tables

List of Figures

List of Symbols

%N	weight percentage (%wt) of Nafion
%Pt	weight percentage (%wt) of platinum
A	interfacial mass-transfer rate ($\mathrm{kg\,m^{-3}\,s^{-1}\,Pa^{-1}}$)
A_s	catalyst surface area per unit mass of catalyst ($\mathrm{m^2\,g^{-1}}$)
A_v	reactive surface area per unit volume ($\mathrm{m^{-1}}$)
c	concentration ($\mathrm{mol\,m^{-3}}$)
C	integration constant
d_h	hydraulic diameter (m)
$\mathscr{D}$	binary diffusivity ($\mathrm{m^2\,s^{-1}}$)
D	diffusivity ($\mathrm{m^2\,s^{-1}}$)
E	cell voltage (V)
f	volume fraction; surface coverage
$\mathscr{F}$	Faraday's constant (96,487 $\mathrm{C\,mol^{-1}}$)
G	Gibbs free energy ($\mathrm{J\,mol^{-1}}$)
$H_{\mathrm{O_2}}$	Henrys constant ($\mathrm{Pa\,m^3\,mol^{-1}}$)
I	current (A)
J	current density ($\mathrm{A\,cm^{-2}}$)
$J_0^{\mathrm{O_2}}$	reference current density ($\mathrm{A\,cm^{-2}}$)
k_c	condensation rate constant ($\mathrm{s^{-1}}$)
k_{rg}	gas phase relative permeability
k_{rl}	liquid phase relative permeability
k_v	evaporation rate constant ($\mathrm{Pa^{-1}\,s^{-1}}$)
K	permeability ($\mathrm{m^2}$)
$\hat{M}$	molecular weight ($\mathrm{kg\,mol^{-1}}$)
m_{Pt}	Pt-loading per unit area ($\mathrm{mg\,cm^{-2}}$)
P	pressure (atm)
P_c	capillary pressure (atm)
P_{sat}	saturation pressure (atm)
$\mathscr{R}$	universal gas constant (8.314 $\mathrm{J\,mol^{-1}\,K^{-1}}$)

q	switching function
r	radius (m)
$\mathcal{R}_{c,\mathrm{red}}$	electrochemical reaction rate ($\mathrm{A\,cm^{-3}}$)
R	resistance to mass-transfer ($\mathrm{s\,m^{-1}}$)
R_H	relative humidity
s	saturation
S	entropy ($\mathrm{J\,K^{-1}}$)
Sh	Sherwood number
t	time (s)
T	temperature (K)
u, v, w	velocity ($\mathrm{m\,s^{-1}}$)
V	volume ($\mathrm{m^3}$)
x, y, z	coordinates
$\bar{x}$	dimensionless CCL thickness
$x_{\mathrm{H_2O}}$	water mole fraction
$x_{\mathrm{N_2}}$	nitrogen mole fraction
$x_{\mathrm{O_2}}$	oxygen mole fraction

Greek letters

α	drag coefficient
α_a	anodic transfer coefficient
α_c	cathodic transfer coefficient
γ	surface tension ($\mathrm{N\,m^{-1}}$)
γ^c	reaction order
Γ	source term
δ	thickness (μm)
ϵ	porosity
ϵ_p	percolation threshold
η	overpotential (V)
η_c	activation overpotential (V)
λ	geometry factor
$\omega_{\mathrm{H_2O}}$	water mass fraction

ω_{N_2}	nitrogen mass fraction
ω_{O_2}	oxygen mass fraction
ϕ	bulk property
Φ	potential (V)
θ_c	contact angle (°)
μ	viscosity (Pa s)
ν	kinematic viscosity ($m^2\,s^{-1}$)
ρ	density ($kg\,m^{-3}$)
σ	conductivity ($S\,cm^{-1}$)

Subscripts & Superscripts

0	operating or inlet condition
act	activation
b	boundary value; bulk value
c	cathode; capillary pressure
cell	cell characteristic
C	carbon
CL	catalyst layer
eff	effective value
g	gas phase
GDL	gas diffusion layer
H_2	hydrogen
H_2O	water
l	liquid phase; lower limit
m	Bruggeman exponent; membrane phase
N_2	nitrogen
oc	open circuit
ohm	ohmic
O_2	oxygen
q	saturation exponent
Pt	platinum
r	reversible

ref	reference value
rs	reaction sites
s	solid phase
u	upper limit
v	void space

Abbreviations

1D	one-dimensional
2D	two-dimensional
3D	three-dimensional
ACL	anode catalyst layer
BA	Bruggeman approximation
BP	bipolar plate
CCL	cathode catalyst layer
EMT	effective medium theory
GDL	gas diffusion layer
GFC	gas flow channel
HS	Hashin-Shtrikman
PEM	polymer electrolyte membrane
Pt/C	platinum supported on carbon

Chapter 1

Introduction

Global warming and greenhouse emissions are two critical issues currently addressed by the scientists all over the world. Some greenhouse gases, such as CO_2, occur naturally and are emitted to the atmosphere through natural processes and human activities. Among the human activities, automobiles, powered by internal combustion engines, are significant producers of harmful greenhouse emissions. For instance, in Canada, about 80% of the anthropogenic emissions of CO_2 during the past 20 years is due to burning fossil fuels and cement production [1]. The amount of greenhouse gas emissions come from the combustion of fossil fuels is about 90% in the United States [2]. Recent research also shows that the amount of CO_2 produces from a small car can be reduced by as much as 72% when powered by a fuel cell running on hydrogen reformed from natural gas instead of a gasoline internal combustion engine [3]. In addition, the world's fossil fuel reserve is limited; hence, alternative and green energy sources are required for better future of our next generation.

1.1 Motivation

Currently, two possibilities exist as alternative of fossil fuel that can meet the requirements of a zero-emission vehicle, batteries and fuel cells. Both batteries and fuel cells are electrochemical devices that convert the energy of a fuel/reactant directly into electricity through electrochemical reactions. In batteries, all the reactant contains within the battery, therefore, life of a battery is limited. Conversely, the reactants in a fuel cell are supplied from an external source, and thus a fuel cell can operate as long as fuel is supplied to it. Further, fuel cells are highly efficient compared to internal combustion engines. The efficiencies of fuel cells range from 40% to 60% due to direct conversion of chemical energy to electrical energy without the need to first produce mechanical energy, as in conventional power generation.

A variety of fuel cells is currently in different stages of development. The most common classification of fuel cells is by the type of electrolyte used in the cells. Based on the electrolyte used, fuel cell are classified as polymer electrolyte membrane fuel cell (PEMFC), solid oxide fuel cell (SOFC), alkaline fuel cell (AFC), direct methanol fuel cell (DMFC), phosphoric acid fuel cell (PAFC), and molten carbonate fuel cell (MCFC) [4]. Among them, the polymer electrolyte membrane (PEM) fuel cell is considered as most promising candidate for the next generation power source for portable, automobile, and stationary cogeneration applications due to its high power density, low operating temperature, quick start-up, and fast dynamic response. Further, its zero emission capabilities can reduce greenhouse gases as well as will mitigate the concerns about the global warming and climate change; and the PEM fuel cell is the focus of this thesis research.

1.2 Polymer Electrolyte Membrane Fuel Cells

The PEM fuel cell, also known as proton exchange membrane fuel cell, was first used in the 1960s in NASAs Gemini space flights as an auxiliary power source. A typical PEM fuel cell consists of two bipolar plates and the membrane electrode assembly (MEA), as illustrated in Fig. 1.1. The purpose of bipolar plate (BP) is to feed the reactant gases and to assemble individual cells into a cell stack. The MEA consists of a cathode and an anode gas diffusion layer (GDL) with a proton-conducting membrane as the electrolyte sandwiched in between GDLs, which is considered as heart of the fuel cells. The solid electrolyte layer made of a porous layer of hydrophobic polytetrafluoretyleen (PTFE), also known as Teflon. However, to make an electrolyte, hydrophilic sulphuric oxygen groups (HSO_3) are attached as a side chain. The function of MEA is to conduct protons efficiently while repelling the electrons, thus forcing the electrons to travel through an external circuit to produce electric energy. It also keeps the hydrogen fuel separate from the oxidant (air or oxygen), a feature essential to the efficient operation of a PEM fuel cell.

The electrodes are most often fabricated from porous carbon fiber layer whose internal surface has been impregnated with platinum (Pt) metal to act as a catalyst for the electrochemical reaction. The exact composition of catalyst layer also includes a complex matrix of electrolyte membrane, supported carbon particles, and void space. The thickness of the polymer electrolyte membrane layer ranges from 50 μm to 250 μm and the most popular polymer electrolyte membrane employed for PEM fuel cell is Nafion®, manufactured by DuPont™. The thickness of the electrodes are approximately 200 μm [5]. Each of these electrodes also consists of approximately 20 μm (or thinner) catalyst layer between the electrodes and membrane, known as anode catalyst layer (ACL) and cathode catalyst layer (CCL), respectively.

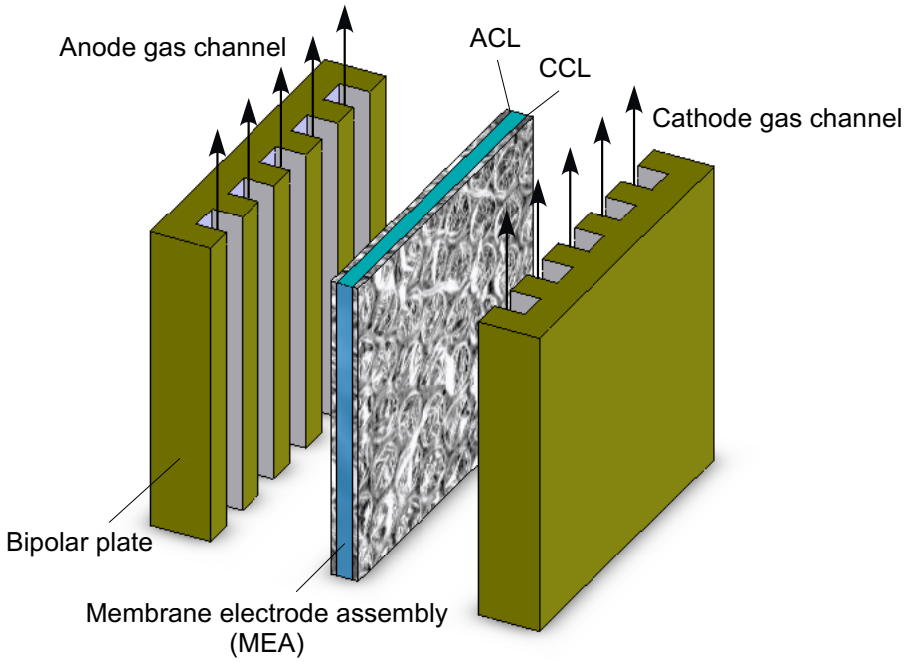

Figure 1.1: Schematic of PEM fuel cells components.

1.2.1 Operation Principle

Typically, humidified H_2 gas is supplied under pressure into the anode gas channel, which diffuses through the porous electrode until it reaches the ACL. In the presence of Pt-catalyst, hydrogen molecules are stripped of their electrons to produce protons through the following reaction:

$$H_2 \rightarrow 2H^+ + 2e^- \tag{1.1}$$

Protons (H^+) are transferred through the electrolyte membrane to the CCL and electrons are conducted through the anode to the current collector and travel through an external circuit to the cathode. Conversely, humidified O_2 gas or air is supplied to the cathode flow channel, where O_2 diffuses through the porous GDL until it reaches the CCL and is reduced on the platinum surface into two oxygen atoms. These combine with protons, driven through the electrolyte membrane, and with electrons traveling through the external circuit and arriving at the cathode. The reaction is

$$\frac{1}{2}O_2 + 2e^- + 2H^+ \rightarrow H_2O \tag{1.2}$$

In addition to water, heat is also produced in this reaction. The reaction occurs for only gas phase oxygen and liquid phase hydrogen ions (H^+) at the surface of the electrical

conductor (e^-). The overall electrochemical reaction occurring in the PEM fuel cell can be represented by the following reaction:

$$H_2 + \frac{1}{2}O_2 \rightarrow H_2O + \text{Heat} + \text{Electric Energy} \tag{1.3}$$

1.2.2 Performance

A PEM fuel cell operating at 25 ℃ and 1 atm, the potential difference across the cell would be about 1.22 V that is known as reversible cell potential. Due to the various losses, also known as polarizations or overpotentials, the actual cell voltage is always lower than the theoretical value. The losses are from three main sources, (i) activation overpotentials due to the kinetics of charge transfer reactions in anode and cathode catalyst layers, (ii) ohmic overpotentials due to the resistances of cell components, and (iii) concentration overpotentials due to the limited rate of mass transfer.

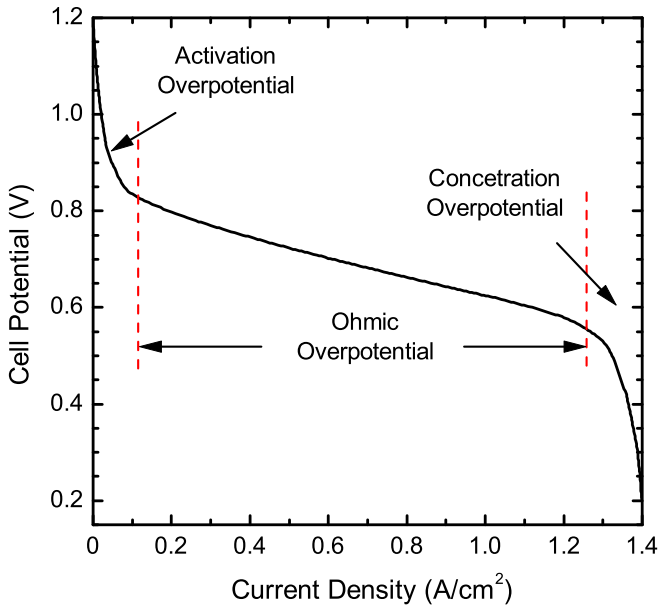

Figure 1.2: The polarization curve showing the activation, ohmic, and concentration overpotentials for a PEM fuel cell.

The losses are depicted in Fig. 1.2 for different values of current density in the polarization curve. The initial drop in the polarization curve is due to the O_2-reduction reaction at the CCL and the H_2-oxidation reaction at the ACL. The activation overpotential causes a steep voltage drop, which is significant at small current density. This includes losses in both the anode and cathode catalyst layers, known as anode activation overpotential and

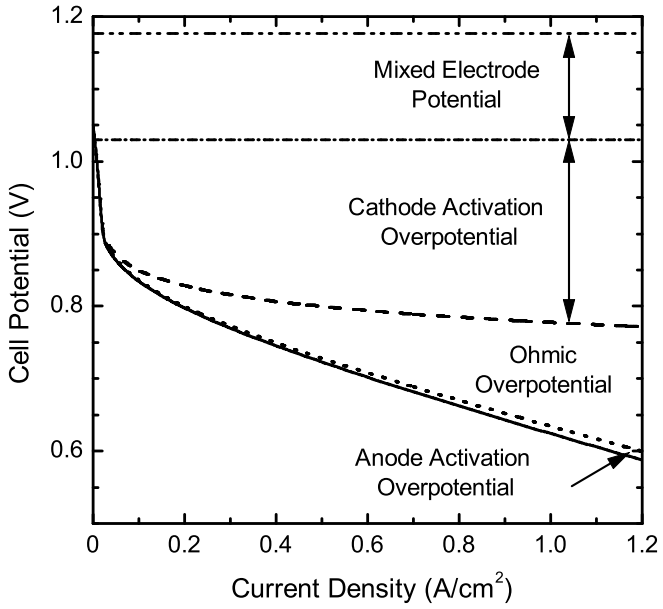

Figure 1.3: A typical breakdown of PEM fuel cells overpotentials, showing contribution of cathode activation overpotential, anode activation overpotential, ohmic overpotential, and mixed electrode potential.

cathode activation overpotential, respectively. As the current density increases, the ohmic losses become important in reducing the overall cell potential. The ohmic losses are linear at larger currents and it includes losses across the membrane, electrodes, and bipolar plates. At high current density, the mass-transport limitations (concentration overpotential) become an increasingly important factor in limiting the PEM fuel cell performance. These mass-transport losses mainly stem from the fact that the reactants cannot reach the reaction sites fast enough. This is mainly due to the inefficiency of mass-transport process through the GDL and CCL, and due to the liquid water flooding, where liquid water blocks the reactants from reaching the reaction sites.

Among the various losses, the highest irreversible losses in the cell voltage occur in the CCL, known as cathode activation overpotential, and then followed by the ohmic overpotential as shown in Fig. 1.3. While the losses in the ACL are negligible compared to these two losses [6, 7]. Further, there has been mixed potential at the electrodes, which is inherent in PEM fuel cell. It arises due to the unavoidable parasitic reactions that tend to lower the equilibrium electrode potential as well as due to the fuel crossover through the electrolyte membrane. To improve the performance, and to design the cost-effective fuel cell, one therefore needs to optimize the cathode activation overpotential along with the utilization of Pt-catalyst content in the CCL.

1.2.3 Technical Challenges

There are many technical barriers that need to be addressed before PEM fuel cell can be used commercially. Of the many issues, cost and durability are the major challenges nowadays. Further, thermal and water management are also barriers to the commercialization of fuel cells. In automotive applications, fuel cells face more stringent cost and durability requirements. In stationary power applications, raising the operating temperature of PEM fuel cell to increase fuel cell performance will also improve heat and power cogeneration and overall system efficiency. Despite high efficiencies, PEM fuel cells are not yet widespread in automotive applications just because of the cost of materials and current expenses associated with hydrogen fuel and its storage [2].

According to the United State Department of Energy (DOE), current costs for automotive internal combustion engines are about \$25/kW to \$35/kW, to be competitive in transportation applications, the cost of fuel cells system needs to be reduced to \$30/kW. Further, fuel cell power systems for the transportation applications will be required to be as durable and reliable as current automotive engines, i.e. 5,000 hour lifespan (150,000 miles equivalent) and be able to function over the full range of vehicle operating conditions (–40 ℃ to 40 ℃).

Table 1.1: Technical targets of 80-kW integrated transportation fuel cell power systems operating on direct hydrogen (*source*: U.S. Department of Energy)

Characteristic	**Units**	**2004 Status**	**2005**	**2010**	**2015**
Stack efficiency @ 25% of rated power	%	59	60	60	60
Stack efficiency @ rated power	%	50	50	50	50
Power density	W/L	450	500	650	650
Specific power	W/kg	420	500	650	650
Precious metal (Pt) loading[a]	g/kW	1.3	2.7	0.3	0.2
Cost	US \$/kW	120	125	45	30
Durability with cycling	hours	1,000	2,000	5,000	5,000
Transient response (time for 10% to 90% of rated power)	sec	1.5	2	1	1
Cold start-up time to 90% of rated power					
@ –20℃ ambient temperature	sec	120	60	30	30
@ +20℃ ambient temperature	sec	60	< 30	30	15
Survivability	℃	-20	-30	-30	-40

[a] US \$ 1627/oz

The DOE's technical targets for PEM fuel cell operating on direct hydrogen for transportation applications are listed in Table 1.1 that is based on 500,000 units/year. It is

observed that substantial amount of progresses have already been made in reducing PEM fuel cell cost and improving durability. By 2015, PEM fuel cell technologies will be in a state of competitive with current automotive technologies. It is clear that by 2010, we will be able to achieve required demand except cost and precious metal loading. DOE's current goal is to reduce the use of platinum in fuel cell catalyst layers by at least a factor of 10 or eliminate it altogether to decrease the cost of fuel cells to consumers. Most of these Pt-catalysts are used in the CCL to promote sluggish O_2-reduction reaction. Therefore, it is required to improve the predominance of the CCL. In addition, the highest reversible losses occur in the CCL; hence, the main focus is given to the CCL to reduce the activation polarization and Pt-loadings. From the better understating of transport processes, it would also be possible to address the thermal and water management barriers. It should also be noted that hydrogen production and its storage are also important for the commercialization of of PEM fuel cell. High-quality hydrogen can even prevent degradation of the fuel cell stack and enhance durability; this is, however, beyond the scope of this thesis research.

1.3 Research Objectives

There are several key processes occurring within the PEM fuel cell that have a major impact on the cell performance. The most important processes in different layers of PEM fuel cell include electrochemical reactions in the catalyst layers, proton migration in the PEM, and mass-transport within all regions of the PEM fuel cell. The processes occurring within each layer of the cell affect the performance of PEM fuel cell. Among the various processes and reactions, the most important ones are occurring inside the CCL that affect the cell performance the most. It is also a widely accepted fact that the CCL of a PEM fuel cell is the performance-limiting component due to slower kinetics of the O_2-reduction reaction and higher irreversible losses. Further, liquid water produced from the electrochemical reaction causes flooding, thereby reducing the cell performance. All of these events are responsible for high cost, which is impending commercialization of fuel cell, and low cell performances.

Typical dimensions of different layers in a PEM fuel cell are between few micrometers to millimeters, which make in-situ measurements in these layers extremely difficult. Since the CCL thickness is about ten micrometers or thinner, intrusive measurements for the transport processes inside the CCL are almost impossible. Conversely, the bipolar plates are made of solid materials and hence, the optical observation of the physical processes inside the CCL is not possible. Although several non-intrusive experimental studies have been reported in literature for the liquid water flooding in PEM fuel cell [8–10], these

measurements only provide qualitative results. Also the spatial resolutions of experimental techniques, such as NMR microscopy [8] and Neutron Radiography [9], are larger than the thickness of a catalyst layer. Hence, the measurement of liquid water flooding using NMR microscopy or Neutron Radiography can only provide qualitative results for the entire PEM fuel cell and it is not possible to quantify the amount of liquid water flooding inside the CCL. Due to these limitations of experimental measurements, mathematical and numerical models become the only means to study the transport phenomena inside the CCL; while without understanding the transport phenomena inside the CCL, it is impossible to optimize and design a better catalyst layer for PEM fuel cell.

In this thesis research, the main focus has been given to the CCL, particularly, to investigate transport phenomena inside the CCL taking into account the O_2-reduction reaction. More specifically, this study has the following major research objectives:

- To study the transport phenomena in the CCL of a PEM fuel cell.
- To gain an improved understanding of the transport phenomena, especially liquid water transport and distribution on the performance and optimization of CCL.
- To investigate the effect of CCL structure, composition, and wettability on the CCL performance and optimization.

In this chapter, a brief overview of the PEM fuel cell has been presented, followed by a description of the objectives of this thesis research. Chapter 2 presents a literature review of PEM fuel cell models that currently exist in the published literature. A general mathematical formulation of the transport processes for PEM fuel cells is derived in Chapter 3 and the simplified formulation for the CCL is provided in Chapter 4. In Chapter 5, a unique set of expressions is provided for the effective protonic conductivity, electronic conductivity, and oxygen diffusivity in both catalyst and gas diffusion layers along with several other key transport properties. Chapter 6 describes an analytical model for estimating the cathode activation overpotential and an analytical approach for the liquid water transport in the CCL. The numerical scheme is described in Chapter 7 with a grid independency test. The results are presented and discussed in Chapter 8. Finally, a summary of this research and a few suggestions for future research are provided in Chapter 9.

Chapter 2

Literature Review

2.1 Introduction

After the first use of PEM fuel cell developed by General Electric for use in the NASA Gemini space flights in the 1960s, it was almost dormant for over 20 years. The problem that deferred the PEM fuel cell from subsequent development was mainly due to its high cost and low power output. Recently, a "quantum jumps" has been observed in the PEM fuel cell research as it can be one of the most promising candidates for the next generation zero-emission power source for transportation applications [11, 12]. As a result, over the past two decades, many research studies have been conducted to improve the performance of PEM fuel cell and make it competitive with the automotive engines. For instance, Fig. 2.1 shows the number of articles published on fuel cells (in part (a) and PEM fuel cells (in part (b)) since 1991 as listed by the Engineering citation index Compendex® on Oct. 26, 2009, the majority of which are on mathematical modelings and numerical simulations. Mathematical and numerical models of PEM fuel cell have received signification attention since the use of these models is simple and efficient to predict the cell performance and the only means to study transport and electrochemical processes inside the various layers of PEM fuel cell.

In the mathematical models and numerical simulations, several modeling approaches have been observed in literature that can be classified as, one-dimensional (1D) and multi-dimensional models, steady-state and transient models, isothermal and non-isothermal models, single-phase and multi-phase models. Further, the modeling can be done as single component of a cell or as the stack model considering several fuel cells. Even the modeling can also be classified as empirical or mathematical models. In this chapter, previous work of PEM fuel cells modeling and performance optimization related to this thesis research

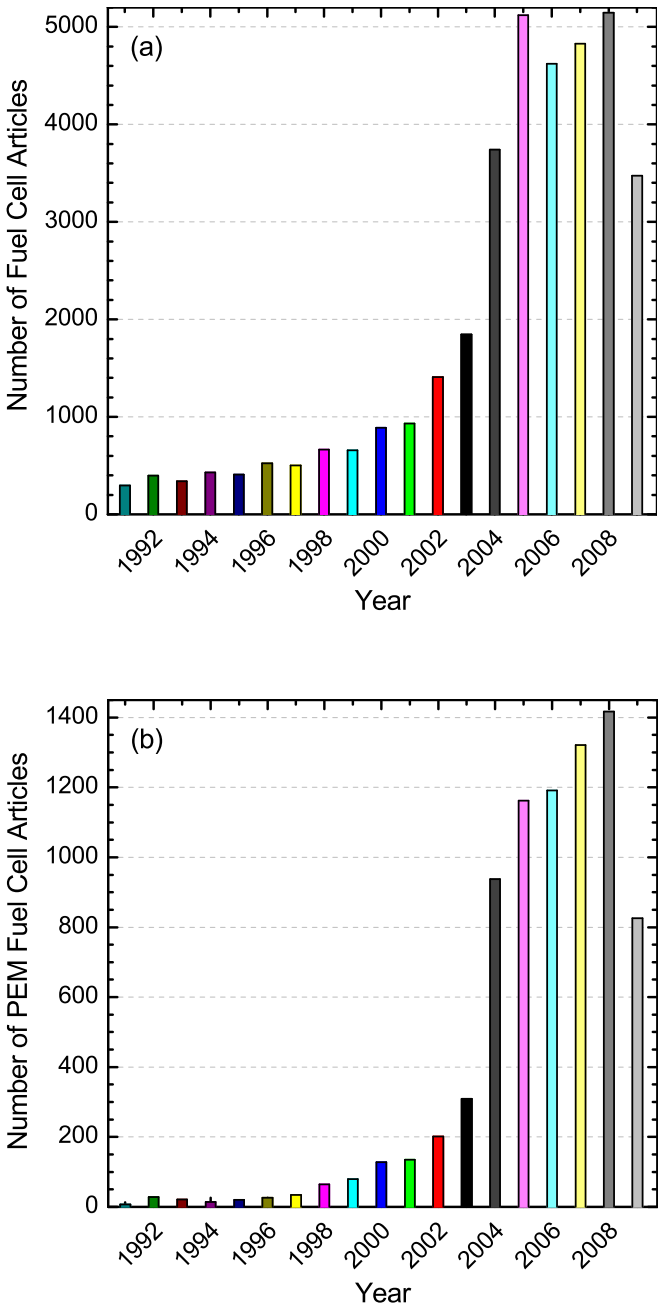

Figure 2.1: Number of articles related to fuel cells and PEM fuel cells listed on the Engineering citation index Compendex®.

have been discussed that is divided into empirical, analytical, and mathematical/numerical models.

2.2 Empirical Models

The approach of empirical models is dependent on the experimental results of PEM fuel cells, where the functional dependence of various cell parameters is developed by applying a curve-fitting scheme. The most general indicator of fuel cell performance is the polarization curve, hence, several attempts have been observed to provide to an empirical relation for the cell voltage and current in terms of cell parameters. However, to model the polarization curve empirically, electrode-kinetic parameters such as exchange current densities and transfer coefficients are required. Hence, Parthasarathy *et al.* [13] studied temperature dependence of the oxygen reduction kinetics. The empirical relation of exchange current densities and transfer coefficients were provided as a function of temperature.

Amphlett *et al.* [14, 15] developed a generalized steady-state electrochemical model of PEM fuel cell performance to model the polarization curve empirically using the following relationships:

$$E_{\text{cell}} = E_r + \eta_{\text{act}} + \eta_{\text{ohm}} \tag{2.1}$$

$$\eta_{\text{act}} = \xi_1 + \xi_2 T + \xi_3 T[\ln(c_{\text{O}_2})] + \xi_4 T[\ln(I)] \tag{2.2}$$

$$\eta_{\text{ohm}} = -I(\gamma_1 + \gamma_2 T + \gamma_3 I + \gamma_4 T I + \gamma_5 T^2 + \gamma_6 I^2) \tag{2.3}$$

where E_r is the reversible cell voltage, η_{act} is the activation overpotential, η_{ohm} is the ohmic overpotential, T is the cell temperature, c_{O_2} is the oxygen concentration, I is the cell current, and ξ, γ are the empirical constants, respectively. This empirical relation of the cell voltage is useful and one can avoid complicated numerical computation during the evaluation of activation and ohmic overpotentials. However, this relation is insufficient to capture the change in internal resistance in changing membrane content and fraction of water in the cathode catalyst layer since it is a function of temperature. Further, the relation is cell specific and valid only for isothermal case, and concentration overpotential is overlooked.

Kim *et al.* [16] developed an empirical relation that fits the entire polarization curve of a PEM fuel cell. The inclusion of an exponential term for the mass-transport overpotential (also referred to as concentration overpotential) with an adjustable parametric coefficient was found to accurately model the performance curves up to and including the mass-

transport limited region at high current densities. The cell voltage was calculated using the following relation:

$$E_{\text{cell}} = E_r - \eta_{\text{act}} - \eta_{\text{ohm}} - \eta_{\text{conc}} \quad (2.4)$$

$$= E_r - b \log \frac{J}{J_0} - RJ - m \exp(nJ) \quad (2.5)$$

Here last three terms in the right hand side represent the activation, ohmic, and concentration overpotentials, respectively, J is the cell current density, and b, J_0, R, m and n are empirical parameters. Later, Squadrito *et al.* [17] also provided an empirical expression between the cell potential and current density similar to Kim *et al.* [16]. The basic difference in their model is the mass-transport overpotential, which is fitted as logarithmic function instead of exponential function.

2.3 Analytical Models

The processes occurring within a PEM fuel cell include mass, momentum, species, and energy transports in the various layers of fuel cells. All these processes can be described, mathematically, by fundamental conservation laws. However, it is impossible to provide analytical solutions of these processes without simplifying the fundamental equations. Still to date, several attempts have been made to provide a simple relation for the prediction of voltage-current relationship. The pioneer work of analytical formulations of fuel cell models are reported by Standaert *et al.* [18, 19]. Several assumptions were made in order to develop an approximate analytical relation between the cell current and voltage for isothermal [18] and non-isothermal [19] cases. These relations are based on the linearized Nernst potential and valid only in high fuel utilization. Further, the theoretical framework for the analytical solution of activation overpotential in the CCL has been available for very low current densities or for large current densities too [20, 21]. Kulikovsky [22] also provided an analytical formulation for the voltage-current curve of a PEM fuel cell. This relation is valid only for the limiting case of small and large currents. None of these previous studies provide the exact analytical solution for the entire range of current density of the PEM fuel cell. Hence, it has been addressed in this thesis research.

2.4 Numerical Models

Empirical models are simple and efficient in predicting the performance of a typical PEM fuel cell [7], however, these models are unable to capture the transport processes in the

PEM fuel cell. To capture the details of the transport processes, it is required to develop a detailed mathematical model of PEM fuel cell and its numerical simulation. The mathematical and numerical models can be categorized in various groups as mentioned earlier. For simplicity, it has only been categorized into two groups, namely, single-phase models, and two-phase models, and will be discussed in the subsequent sections. Further, the cathode catalyst layer models are also reviewed in this section.

2.4.1 Single-phase Models

The most prominent mathematical modeling and numerical simulation of PEM fuel cell began in the early 90s. For instance, Bernardi and Verbrugge [23] developed the mathematical model for the oxygen electrode of PEM fuel cell. Later both the H_2-oxidation and the O_2-reduction reaction in the catalyst layers were modeled assuming a fully saturated membrane [24]. Both of these models were one-dimensional and assumed an isothermal fuel cell that operated at steady-state. The Nernst-Plank equation was employed to describe ionic transport and the Stefan-Maxwell equation for the gas transport. Further, the gas pressure in the flow channels was assumed constant, hence, only the conservation of species was applied to the gas in the gas flow channels. Due to the assumptions of fully hydrated membrane and constant water content in the membrane, the direction of water flow through the system was governed by the electro-osmotic forces. In addition, the pore water is charged with presence of H^+; hence, the transport of water in the membrane was along the membrane potential gradient.

The proton migration process in the PEM layer has been addressed by Verbrugge and Hill [25], along with water migration in the pores of a fully humidified PEM. Since the water is continuously producing from the electrochemical reactions, the amount of water content in the membrane will no longer be constant due to back-diffusion of water. Further, the protonic conductivity changes with the membrane water content, hence, Springer *et al.* [26, 27] developed a PEM fuel cell model in which the protonic conductivity was considered as a function of membrane hydration. These models are also one-dimensional (1D), however, partially humidified membrane was considered for the first time in their investigations. Nonetheless, these 1D models provide a fundamental framework for the numerical simulations.

In the above-mentioned models, the flow in the gas flow channels and electrode backing layers were solved separately. Thus, the interaction between the gas flow channels and the electrode backing layers was not modeled. Fuller and Newman [28] developed a quasi-two-dimensional mathematical model of transport in PEM fuel cell to address water

management, thermal management, and fuel utilization. The MEA was simplified by assuming ultra thin gas diffusion electrodes, while the liquid phase had been neglected. The water and heat management model of Nguyen and White [29] is also identical to the Fuller and Newman model [28], except the PEM layer was modeled using the variable hydration model of Springer *et al.* [26, 27], and the catalyst layer was considered to be an interface. In these models, the gas flow in the channel was considered as plug flow assuming no pressure drop across the channel. Also, the transport of species in the electrode backing and catalyst layers was by diffusion only. Further, the major heat source terms, the entropic and irreversible reaction heats, were not specified in their models. Later, Thirumalai and White [30] added the pressure variations in the gas flow channel in their fuel cell stacks model and Yi and Nguyen [31] extended the model of Nguyen and White [29] including the entropic and irreversible reaction heats along with the phase change heat.

Wohr *et al.* [32] developed a 1D model for heat and water transport in a PEM fuel cell stack. Both the entropic and irreversible reaction heats were accounted and the temperature profiles were computed in the through-membrane direction and predicted the maximum temperature as a function of the number of cells contained in a stack. Rowe and Li [33] also developed a 1D model in the through-membrane direction. Their model includes the entropic, irreversible, phase change heats, and Joule heating in the membrane and catalyst layers. Maggio *et al.* [34] performed a pseudo-three-dimensional simulations, neglecting the temperature gradient in the flow direction. Several two-dimensional (2D) and three-dimensional (3D) thermal models were also presented that accounted various heat generation mechanisms more rigorously [35–38].

Gurau *et al.* [39] developed a 2D single-phase model that included the gas flow channels, electrode backing layers, catalyst layers, and PEM layer. The mathematical model was unified in that the equations representing the conservation of mass, momentum, species, and energy in each layer had the same general form, and differed through the source terms. Um *et al.* [40] carried out a 2D simulation which coupled the electrochemical kinetics and transport processes. They used a single domain solution approach and neglect water uptake and release in the catalyst layer. These models later extended into three dimensions to study the complex gas flow and for better gas flow channel designs [41] and water transport in PEM fuel cells [42]. The simplest water transport model has been developed by Okada *et al.* [43] a linear transport equation. Water transport processes in the PEM layer was also modeled by several authors [44–47].

Most of the modeling studies assumed that the cell is operating in steady-state, except Um *et al.* [40, 42], whereas automobiles application requires the transient nature of the cell operation. In the transient modeling, van Bussel *et al.* [48] developed 2D dynamic model

of PEM fuel cell water management, based on the 1D model of Springer *et al.* [26, 27]. Conversely, Chen *et al.* [49] extend the theoretical model developed by Okada *et al.* [43] to an unsteady state model and investigated the transient behavior of water transport across the membrane as well as the influences of several physical parameters on the characteristic time to reach the steady state. Recently, Wu *et al.* [50] presented a single-phase non-isothermal transient model and investigated time response of transport processes.

2.4.2 Two-phase Models

A substantial number of single-phase PEM fuel cell models have already been reviewed in the previous section. These models are based on single-phase flow, and assume that the gas inside the fuel cell is a perfect gas. Although water transport had been considered in some cases, the water vapor and liquid water were considered two different species and assumed that there is no influence by condensation/evaporation on the gas mixture flow field. Results of these models suggest that in order to be applicable for both saturated and non-saturated gas conditions, water transport model should include two-phase transport, transport in a partially dry membrane and in a fully-flooded membrane. Water flooding is a well-known performance limiting factor for PEM fuel cell, and thus it is vital to understand the two-phase transport characteristics in the cathode side of fuel cell and their influences on the cell performance. Hence, more complex two-phase models have also been developed [51–76].

Traditionally, two-phase transport processes were modeled either with unsaturated flow theory (UFT) or using multi-phase mixture (M^2) formulation. In the UFT, a uniform gas-phase pressure is assumed across the entire porous layer, thereby ignoring the gas-phase flow counter to capillary-induced liquid motion. Here the liquid phase pressure is simply the negative of capillary pressure between gas and liquid phases. He *et al.* [52] developed a transport model based on unsaturated flow theory using an interdigated gas flow to investigate the effects of liquid water and its transport on the performance of the cathodes of PEM fuel cells. The transport of liquid water was considered through the completely wetted GDL, driven by the shear force of gas flow and capillary force, and the catalyst layer was considered as a boundary condition. Therefore, water production was considered to occur at the boundary of the CCL/GDL interface. In addition, it has been assumed that the capillary pressure has a constant slope across the GDL. Janssen [53] presented a two-phase water transport model, based on concentrated solution theory that appears to be quite rigorous. Berning and Djilali [56] presented a 3D model to describe the two-phase flow inside the GDL by the UFT that a uniform gas phase pressure is assumed within the GDL.

In contrast to the UFT, the model developed by Wang and Cheng [51] is based on multi-phase mixture (M^2) formulation and is pioneer in its kind. The assumption of constant gas pressure is released and it accounts for the gas flow counter to the capillary-driven liquid flow. Therefore, the liquid phase pressure is difference between the capillary and gas phase pressures. This M^2 model has been widely used recently to investigate the multi-phase and multi-component transport in cathode GDL [54, 55, 59, 63–66]. Further, Mazumder and Cole [58] developed a 3D non-isothermal, two-phase model that treated the transport in the catalyst layer as Knudsen diffusion. The water transport in the electrolyte was highly simplified in that water transport was through electro-osmotic drag only.

The model developed by Wang *et al.* [54] assumed that the GDL to be a hydrophilic material. The capillary pressure was described by the Leverett function for hydrophilic media. In the backing layer, a two-phase region co-exists with a single-phase region. The capillary action was discovered to be the dominant mechanism for water transport inside the two-phase zone of the hydrophilic structure. This model, like many in literature, assumes that the CCL is a thin interface [56, 77–79]. Hu *et al.* [61, 69] developed a 3D two-phase flow model to investigate a conventional and an interdigitated flow fields. The model results showed that the saturation of liquid water in the conventional flow field is less than that in the interdigitated flow field. Therefore, higher ohmic losses are encountered with the interdigitated flow field. However, the humidification of the reactant gases can be used in order to lower these ohmic losses and in turn enhance the performance of the cells with an interdigitated flow field. Most of these studies assumed the transport by capillary pressure only, and did not include mass-transport between the phases. Further, the catalyst layer structures and its effect have been overlooked.

2.4.3 Cathode Catalyst Layer Models

In the previous two sections, a review of PEM fuel cell models has been covered as single-phase and two-phase modeling approaches. This review will be incomplete without an intensive review of cathode catalyst layer (CCL) modeling, since one of the objectives of the proposed study is to optimize CCL structure and its performance. Although liquid water build-up in the cathode has a substantial influence on cell performance [59], most of the studies have only considered catalyst layer as an interface. Therefore, in this section focus has given to the CCL and performance optimization models that are available in literature.

In addition to cell polarization and water flooding, another factor that currently impeding commercialization of PEM fuel cell is the high materials and manufacturing cost. Substantial efforts are currently ongoing to reduce the overall fuel cell cost by maximizing

the individual cell performance while simultaneously minimizing the amount of catalyst and membrane material used per unit active area. Unless there is a tool for optimizing the amount of expensive materials used during the design of fuel cell, it is impossible to minimize the cost of manufacturing or optimize the cell performance. To improve the performance, and to design the cost-effective fuel cell, one therefore needs to optimize both the CCL activation overpotential and the utilization of Pt-catalyst and membrane contents in the catalyst layer.

Several studies have already been conducted considering these factors. For instance, an engineering model is used by Marr and Li [80] for performance study of the PEM fuel cell. A detailed mathematical formulation for the ohmic overpotential has also been provided, which can be used in future studies if the cell dimension and material properties are known. They also used the membrane model of Bernardi and Verbrugge [23, 24], but improved the gas flow channel and catalyst layer formulations. Instead of assuming that the pressure drop was zero, the pressure was allowed to vary in the gas flow channels through the assumption that the flow was equivalent to 1D pipe flow. Siegel *et al.* [81] developed catalyst layer model considering the catalyst layer void regions to be composed of gas and polymer electrolyte membrane. However, the catalyst layer void regions can be a combination of gas, liquid, and polymer electrolyte in the catalyst layers [82]. The formulation of Marr and Li [80] later used by Baschuk and Li [82] in their parametric study with variable degrees of water flooding in the cathode electrode. Although they incorporated the water flooding parameter, it is not possible to estimate the amount of flooding from this model. The amount of water flooding has been extrapolated by matching the model results with the experimental data of Kim *et al.* [16].

The CCL activation overpotential also shows a complex nature due to its dependency on the catalyst layer structure; for instance, whether it is agglomerate or macro-homogeneous, composition of the catalyst layer, types of the catalysts used, and how the reactants transport in the catalyst layer. The activation overpotential in the ACL is very small compared to the activation overpotential in the CCL. Therefore, the CCL activation overpotential has major influence on the fuel cell performance. Among the various structures of catalyst layers investigated so far, three different structures of cathode catalyst layer have been established in the past decade, namely, thin-film, macro-homogeneous, and agglomerate catalyst layers.

In the thin-film model, the catalyst particles are embedded on the thin-film of polymer membrane [83, 84], whereas in the macro-homogeneous model, the catalyst layer is considered as a homogeneous matrix of supported catalyst platinum, polymer electrolyte and void space [6, 20, 24, 27]. Conversely, in the agglomerate model, the catalyst layer

is considered as a uniform matrix of catalyst agglomerate, which is surrounded by the gas pores. Each of these catalyst agglomerates are assumed to be homogeneous mixture of catalysts, polymer electrolytes, and void spaces [85–90]. Although experimental studies [85, 91] showed that the agglomerate model might be a close approximation to model the catalyst layer, there are several other models that have also been developed, namely, cylindrical agglomerate, ordered catalyst layer, and non-uniform catalyst layer [62, 92, 93]. Hence, the CCL not only has complex structures but also influences cell performance in terms of the activation overpotential.

2.5 Summary

It is clear from the aforementioned literature review that the evolution of the fuel cell modeling is becoming more and more complex with the advancement of computing power. None of them actually provides any simpler formulation or simple model of entire cell polarization along with a complex model. Whereas polarization occurs in the operation of PEM fuel cell that influences both the performance and commercialization of PEM fuel cell. The formulation of ohmic overpotential is well established and does not require complicated mathematical formulation or numerical computation for fully-hydrated membranes [80, 82]. Hence, a need exists to develop simple analytical formulation for the CCL activation overpotential if possible.

The review of literature also shows that considerable information exists on the PEM fuel cell modeling, although information regarding detailed modeling of cathode catalyst layer is still elusive. It might be pertinent to assume catalyst layer as a boundary condition while solving the fuel cell stacks to reduce the computational load to investigate the overall stack performance. Investigation of the activation polarization and water transport processes without neglecting the cathode catalyst layer thickness is considerably more difficult. Further, the catalyst layer structures have significant effect on the cell performance, which in turn influence the transport processes [7, 94]. The overall consequence is that the transport processes in the CCL of a PEM fuel cell cannot be determined without considering a finite CCL. Therefore, the main focus in this thesis research is given to the CCL and its optimization.

Chapter 3

General Formulation

In a PEM fuel cell, several phases co-exist together including a liquid phase, a gas phase, and a solid phase. Further, the multi-phase mixture flows through narrow gas channels, porous gas diffusion layers, and porous catalyst layers. Therefore, the governing equations for PEM fuel cell are influenced by the physical structure of the cell and co-existing phases. The transport processes in the PEM fuel cell are governed by the standard physical laws of transport of mass, momentum, species, and energy in each phase at the microscopic level. However, solving a problem in the continuum level is much easier than the microscopic view of molecules and the continuum approach serves better for understanding the problem [95]. In addition, our experiences and observations are closely related to the continuum point of view than the molecular point of view. Hence, the local instant formulation of fundamental conservation equations need to be converted into a set of averaging conservation equations by proper averaging methods that can be applied as a continuum.

In this chapter, the physical structures of a PEM fuel cell is described along with the major assumptions and the procedure to incorporate the interfacial terms in the governing equations. Then the volume-averaged equations representing the conservation of mass, momentum, and species are derived from the fundamental microscopic conservation equations.

3.1 Physical Structure and Nature of Flows

A typical PEM fuel cell consists of two bipolar plates that include flow channels and membrane electrode assembly (MEA). Each of these layers have several co-existing phases as shown in Fig. 3.1. These phases are: solid, liquid, and gas. The bipolar plate (BP) has only solid phase, which is generally made of graphite or carbon-carbon composites [5]. The

purpose of BP is to conduct the current from the anode to the cathode of the cell. It also serves as a base plate for the gas flow channels, where the flow channels are grooved on the bipolar plates. As seen in Fig. 3.1, in the flow channel, both the liquid and gas phases are co-existing. Here liquid phase is water, as being composed of small droplets. Therefore, flow in the gas channel is mainly a dispersed flow where condensation or evaporation can take place as well as the collisions and coalescence of several droplets can happen [95]. However, recent study shows that the two-phase flow in a micron sized channel can be considered as stratified flow [96]. In the stratified flow, the structure and the dynamics of the interfaces greatly influence the rates of mass, momentum, and energy transfer between the phases. The gas diffusion layer (GDL) is made of either porous carbon paper or carbon cloth that allows diffusing the gas onto the catalyst and is also known as the "electrode backing layer". It also allows the liquid phase transported back to the gas flow channel. Therefore, a two-phase flow exists in the GDL. Since carbon is conductive, it also facilitates the transport of electrons. The catalyst layer consists of a mixture of platinum catalyst, polymer electrolyte, and void space. Hence, it is a porous medium that combines the structures of the electrode backing and polymer electrolyte layers. The multi-component reactant gases, liquid water, and polymer electrolyte are contained in the void spaces. Within the polymer electrolyte, the ion-containing liquid phase, reactant gas, and polymer backbone exist. The electrochemical reactions of hydrogen oxidation and oxygen reduction take place on the catalyst surfaces.

The polymer electrolyte layer is composed of Nafion® membrane that can also be considered as a combination of solid, liquid, and gas phases. In the presence of water, the Nafion® membrane is composed of various regions [97] as shown in Fig. 3.1. The inner region, electrolyte, contains water and hydrogen ions. The liquid water and hydrogen ions are contained within clusters that have a diameter of approximately 4 nm [98]. The surface of the polymer membrane is generally highly hydrophobic. However, to make an electrolyte, the polymer is "sulphonated" where a side chain is added, ending with sulphonic acid HSO_3. The HSO_3 group added is ionically bonded, and so the end of the chain which has SO_3^- ion. For this reason, the resulting structure is also called an "ionomer" and due to the presence of sulphonic acid group, the polymer electrolyte shows hydrophilic behavior. The second region is the rigid hydrophobic backbone of the polymer. In between the electrolyte and hydrophobic backbone, there is a gas permeable region, can be described as the amorphous part of the perfluorinated backbone. This hydrophobic region is permeable to gases; thus, transport of reactant gas occurs in this region.

Thus, a PEM fuel cell consists of several phases. The solid phases include the carbon in the BPs, GDLs, and catalyst layers, as well as the polymer matrix of the electrolyte. Pure liquid water is present in the gas flow channels, electrode backing, and catalyst layers,

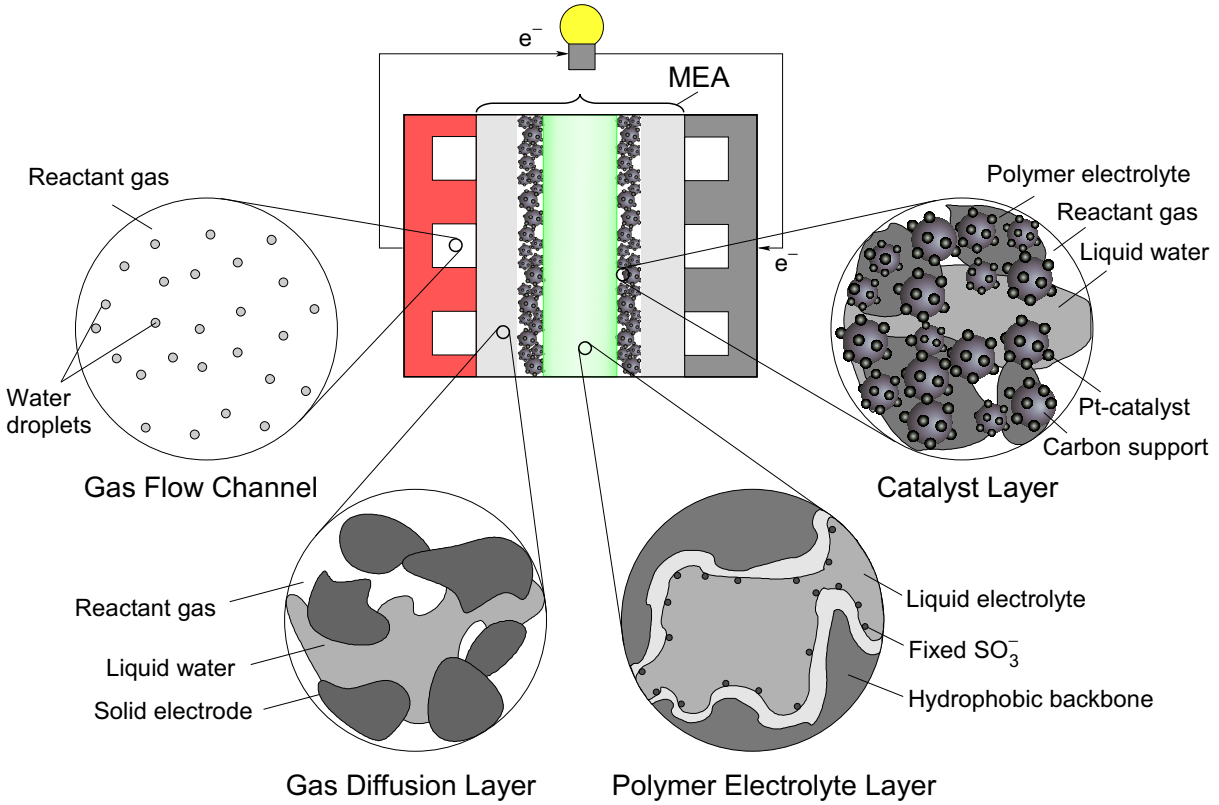

Figure 3.1: Schematic of a PEM fuel cell with the physical structures of various layers within the cell.

while a liquid mixture containing water and hydrogen ion is contained within the polymer electrolyte of the polymer electrolyte and catalyst layers. The multi-component reactant gases are present throughout the cell, except in the solid portions of BPs. The governing equations for each phase are derived using a volume-averaging method, which is examined in the next section.

3.2 Assumptions

The basic principle of volume-averaging procedure for multi-phase flow is to average the single-phase conservation equation over an elementary volume, where several phases co-exist. Thus, there is a connection between the single-phase and multi-phase governing equations through averaging processes. Birkhoff [99] first suggested the averaging of conservation equations, whereas Slattery [100] introduced the volume-averaging theorems of continuum mechanics to the flow through the porous media. The volume-averaging relations for the porous media are valid only when the characteristic length of the pores and phases are very small compared to the characteristic length of averaging volume as well

as characteristic length of the physical system. In this thesis, similar procedure has been used to derive the conservation equations for the PEM fuel cell. The major assumption in the general formulation developed in this section is the length scale that is considered. It is considered that the length scale of pores and phases are small enough that over the elementary volume phases are continuum. However, it is possible to model the conservation equations at the particle level where no averaging procedure is required [101]. The major difficulty for such model is each of the conservation equations need to be solved for individual molecules, which also need substantial amount of computational time and load. Thus, a continuum approach is used in this thesis, which is fast and can provide a clear overview of various transport processes in the macroscopic level for the PEM fuel cell. However, in order to accurately model the processes occurring within a PEM fuel cell, the interfacial source terms should include the effect of the micro-scale phenomena on the mean values considered in the model.

3.3 Multi-phase Volume-averaging Method

When two or more miscible fluids occupy the void space of a porous layer in the PEM fuel cell, they mix together because of diffusive and dispersive effects, leading ultimately to a multi-component mixture. However, within each phase, the transport of mass, momentum, species, and energy are governed by the fundamental microscopic conservation equations. The direct solution of these microscopic conservation equations is impractical, and such a solution may contain more information than is needed. In addition, such a solution will require rigorous numerical computation. Hence, it is always desirable to reduce numerical computational load. Further, we are mostly interested in describing the PEM fuel cell systems at the macroscopic scale. In order to accomplish this we need to develop the spatially smoothed transport equations. Hence, a volume-averaging procedure is invoked to derive the conservation equations for each phase that is capable of capturing the interactions between the phases.

Considering a "two-phase" fluid flow in the porous medium of PEM fuel cell, i.e. we actually have three phases: two fluids and the solid matrix. Here two fluids are considered as a liquid phase (which is labeled by the suffix l) and a gas phase (which is labeled by the suffix g). In the volume-averaging procedure presented below, the conserve quantities are integrated over a representative volume. The representative volume is illustrated in Fig. 3.2, where $\mathbf{n}_k$ is the unit normal to the interface of phases k and n and pointing outward from the k-phase. For the PEM fuel cell, the representative volume V_r can be occupied by the liquid, gas, and solid phases, whose interfaces may move with time. Hence,

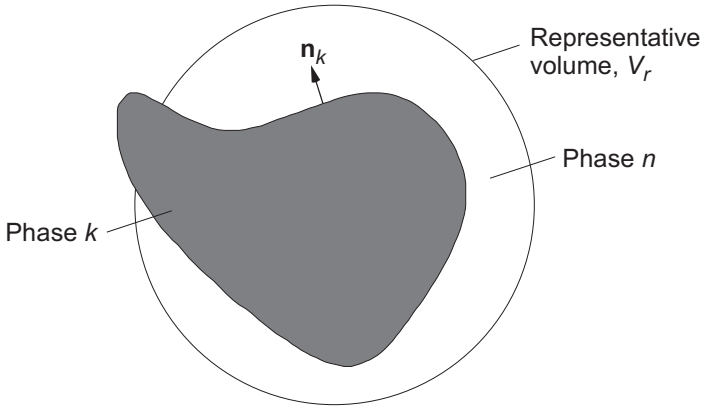

Figure 3.2: Representative volume for the volume-averaging method in a multi-phase system.

the representative volume is written as

$$V_r = V_l(t) + V_g(t) + V_s \tag{3.1}$$

where V_l, V_g, and V_s are the volumes of liquid, gas, and solid phases, respectively. Therefore, if the phase k in Fig. 3.2 is considered as the liquid phase then the phase n will represents both the solid and gas phases and so on.

For any quantity Ψ associated with the k-phase in a PEM fuel cell, the volume average of Ψ_k, which is also known as *superficial average*, is defined as

$$\langle \Psi_k \rangle = \frac{1}{V_r} \int_{V_r} \Psi_k dV \tag{3.2}$$

where k can be liquid, gas or solid phase, and Ψ_k is taken to be zero in other phases. Conversely, the intrinsic phase average of Ψ_k, which is also referred simply as *intrinsic average*, is defined as

$$\langle \Psi_k \rangle^k = \frac{1}{V_k} \int_{V_k} \Psi_k dV \tag{3.3}$$

In the above equation, the integration is carried out over the k-phase only, where V_k is the volume occupied by phase k in the representative volume V_r. Taking Ψ_k to be zero in other phases, the intrinsic phase average of Ψ_k can be re-written as

$$\langle \Psi_k \rangle^k = \frac{1}{V_k} \int_{V_r} \Psi_k dV \tag{3.4}$$

These two quantities, *superficial average* and *intrinsic average*, are related in a simple manner

$$\frac{\langle \Psi_k \rangle}{\langle \Psi_k \rangle^k} = \frac{V_k}{V_r} = \epsilon_k, \tag{3.5}$$

in which ϵ_k is the volume fraction of the k-phase within the representative volume. In a porous medium with the liquid, gas, and solid phases, the porosities (volume fractions) for each phase can be related to the porosity of the medium as

$$\epsilon_l + \epsilon_g = \epsilon \quad \text{and} \quad \epsilon_{\mathrm{s}} = 1 - \epsilon \tag{3.6}$$

where ϵ_l, ϵ_g, and ϵ_s are the volume fraction of liquid, gas, and solid phases, respectively, and ϵ is the porosity of the medium. It is worthwhile to note that many physical quantities, such as pressure, temperature, and density are measured in porous media, are intrinsic average (phase-averaged) quantities while the volume-averaged equations has to be in a function of volume-averaged quantities. Therefore, a careful attention is required to write the volume-averaged equations in terms of phase-averaged quantities.

One assumption is necessary in order to allow the volume-averaged equations to be a function of volume-averaged quantities. For the point values in phase k (Ψ_k and Ω_k), the deviations (from the respective average values, for the k-phase) are defined as [102, 103]

$$\tilde{\Psi}_k \equiv \Psi_k - \langle \Psi_k \rangle^k \quad \text{and} \quad \tilde{\Omega}_{\mathrm{k}} \equiv \Omega_{\mathrm{k}} - \langle \Omega_{\mathrm{k}} \rangle^{\mathrm{k}} \tag{3.7}$$

It is assumed that the intrinsic phase averages are constant in their averaging volumes, which lead to:

$$\langle \Psi_k \Omega_k \rangle^k = \langle \Psi_k \rangle^k \langle \Omega_k \rangle^k + \langle \tilde{\Psi}_k \tilde{\Omega}_k \rangle^k \tag{3.8}$$

and

$$\langle \Psi_k \Omega_k \rangle = \epsilon_k \langle \Psi_k \rangle^k \langle \Omega_k \rangle^k + \langle \tilde{\Psi}_k \tilde{\Omega}_k \rangle \tag{3.9}$$

where the dispersive term is expressed explicitly as

$$\langle \tilde{\Psi}_k \tilde{\Omega}_k \rangle = \frac{1}{V_r} \int_{V_k} \tilde{\Psi}_k \tilde{\Omega}_k dV \tag{3.10}$$

The above-expressions are only valid if the phase average and intrinsic average of a quantity are well-behaved such that

$$\left\langle \langle \Psi_k \rangle^k \right\rangle = \langle \langle \Psi_k \rangle^k \rangle^k = \langle \Psi_k \rangle^k \tag{3.11}$$

and

$$\langle \langle \Psi_k \rangle \rangle = \langle \langle \Psi_k \rangle \rangle^k = \langle \Psi_k \rangle \tag{3.12}$$

To derive the macroscopic volume-averaged transport equations from the microscopic transport equations, the following theorems will also be needed:

Average theorem [104]:

$$\langle \nabla \Psi_k \rangle = \nabla \langle \Psi_k \rangle + \frac{1}{V_r} \int_{A_k} \Psi_k \mathbf{n}_k dS \tag{3.13}$$

Modified average theorem [105]:

$$\langle \nabla \Psi_k \rangle = \epsilon_k \nabla \langle \Psi_k \rangle^k + \frac{1}{V_r} \int_{A_k} \tilde{\Psi}_k \mathbf{n}_k dS \tag{3.14}$$

Transport theorem [106]:

$$\left\langle \frac{\partial \Psi_k}{\partial t} \right\rangle = \frac{\partial}{\partial t} \langle \Psi_k \rangle - \frac{1}{V_r} \int_{A_k} \Psi_k \boldsymbol{w}_k \cdot \mathbf{n}_k dS \tag{3.15}$$

where A_k represents the interfaces between the k-phase and other phases, $\boldsymbol{w}_k$ is the velocity vector of the interfaces, $\mathbf{n}_k$ is the unit normal to the interface of phases and pointing outward from the k-phase, and S is the surface of the elementary volume. A comparison of the average theorem with the modified average theorem yields

$$\frac{1}{V_r} \int_{A_k} \langle \Psi_k \rangle^k \mathbf{n}_k dS = -\langle \Psi_k \rangle^k \nabla \epsilon_k \tag{3.16}$$

The theorems given by Eqs. (3.13)–(3.15) with expression given by Eqs. (3.2)–(3.9) serve as the basis of the derivation of macroscopic equations. In the following sections, the conservations equations are derived in the form of averaged quantities.

3.4 Conservation of Mass

For the PEM fuel cell, the conservation of mass applies only to the gas and liquid phases because the change of mass in the solid phase is zero. Hence, the microscopic conservation

of mass equation for the k-phase is [107]

$$\frac{\partial \rho_k}{\partial t} + \nabla \cdot (\rho_k \boldsymbol{u}_k) = 0 \tag{3.17}$$

which can be integrated oven the elementary volume to give:

$$\left\langle \frac{\partial \rho_k}{\partial t} \right\rangle + \langle \nabla \cdot (\rho_k \boldsymbol{u}_k) \rangle = 0 \tag{3.18}$$

where ρ_k and $\boldsymbol{u}_k$ are the density and velocity of the k-phase, respectively. Application of the transport theorem to the first term and the averaging theorem to the second term in Eq. (3.18), leads to

$$\frac{\partial}{\partial t} \langle \rho_k \rangle + \nabla \cdot \langle \rho_k \boldsymbol{u}_k \rangle + \sum_n \frac{1}{V_r} \int_{A_{kn}} \rho_k \left(\boldsymbol{u}_k - \boldsymbol{w}_{kn} \right) \cdot \mathbf{n}_k dS = 0 \tag{3.19}$$

where $\sum_n$ represents the summation over all adjacent n phases, subscript k represents liquid (l) phase or gas (g) phase, and subscript n can be liquid, gas, and solid (s) phases, where $k \neq n$. A_{kn} is the interfacial area of phases k and n which moves with velocity $\boldsymbol{w}_{kn}$ within the representative volume.

The integral term in Eq. (3.19) represents the mass-transfer due to change of phase between liquid, gas, and solid phases. In general, the mass-transfer between the liquid-gas interfaces is nonzero, but there is no mass-transfer across the liquid-solid and gas-solid interfaces. With the aid of Eq. (3.9), Eq. (3.19) is modified as

$$\frac{\partial}{\partial t} \left(\epsilon_k \langle \rho_k \rangle^k \right) + \nabla \cdot \left(\epsilon_k \langle \rho_k \rangle^k \langle \boldsymbol{u}_k \rangle^k + \langle \tilde{\rho}_k \tilde{\boldsymbol{u}}_k \rangle \right) + \sum_n \frac{1}{V_r} \int_{A_{kn}} \rho_k \left(\boldsymbol{u}_k - \boldsymbol{w}_{kn} \right) \cdot \mathbf{n}_k dS = 0 \tag{3.20}$$

The dispersive term, $\langle \tilde{\rho}_k \tilde{\boldsymbol{u}}_k \rangle$, is generally small and it can be neglected. Accordingly, Eq. (3.20) reduces to

$$\frac{\partial}{\partial t} \left(\epsilon_k \langle \rho_k \rangle^k \right) + \nabla \cdot \left(\epsilon_k \langle \rho_k \rangle^k \langle \boldsymbol{u}_k \rangle^k \right) + \sum_n \frac{1}{V_r} \int_{A_{kn}} \rho_k \left(\boldsymbol{u}_k - \boldsymbol{w}_{kn} \right) \cdot \mathbf{n}_k dS = 0 \tag{3.21}$$

where $n = l,\ g$, and $n \neq k$. If the volumetric liquid and gas saturations, s_l and s_g, are defined by the following relations:

$$s_l = \frac{V_l}{V_l + V_g} \quad \text{and} \quad s_g = \frac{V_g}{V_l + V_g} \tag{3.22}$$

so that,

$$s_l + s_g = 1, \quad \epsilon_l = \epsilon s_l, \quad \epsilon_g = \epsilon s_g, \quad \text{and} \quad \epsilon_{\mathrm{s}} = 1 - \epsilon \tag{3.23}$$

then Eq. (3.21) can be re-written in terms of *intrinsic average* velocity as

$$\frac{\partial}{\partial t}\left(\epsilon s_k \langle \rho_k \rangle^k\right) + \nabla \cdot \left(\epsilon s_k \langle \rho_k \rangle^k \langle \boldsymbol{u}_k \rangle^k\right) = \Gamma_{M,k} \tag{3.24}$$

or, in terms of *superficial average* velocity as

$$\frac{\partial}{\partial t}\left(\epsilon s_k \langle \rho_k \rangle^k\right) + \nabla \cdot \left(\langle \rho_k \rangle^k \langle \boldsymbol{u}_k \rangle\right) = \Gamma_{M,k} \tag{3.25}$$

The term denoted by $\Gamma_{M,k}$ in Eq. (3.25) represents the rate of production of phase k from the phase changes at the interface, i.e. the conservation of mass equation at the interfaces can be written as

$$\sum_k \Gamma_{M,k} = 0 \tag{3.26}$$

For a PEM fuel cell, the source term in Eq. (3.25) also includes production of species due to the reactions, i.e.

$$(\Gamma_{M,k})_{\mathrm{PEM}} = \Gamma_{M,k} + \Gamma_{M,k-\mathrm{react}} \tag{3.27}$$

where $\Gamma_{M,k-\mathrm{react}}$ is the production of mass in phase k due to the reactions.

3.5 Conservation of Momentum

The conservation of momentum also applies to the gas and liquid phases only, since the velocity of the solid phase is zero. Hence, the microscopic conservation of momentum equation for the k-phase is [107]

$$\frac{\partial}{\partial t}\left(\rho_k \boldsymbol{u}_k\right) + \nabla \cdot \left(\rho_k \boldsymbol{u}_k \boldsymbol{u}_k\right) + \nabla P_k - \nabla \cdot \boldsymbol{\tau}_k - \rho_k \boldsymbol{g} - \boldsymbol{b}_k = 0 \tag{3.28}$$

where P_k, $\boldsymbol{\tau}_k$, and $\boldsymbol{b}_k$ are the pressure, viscous stress tensor, and body force per unit mass of the phase k, respectively. The viscous stress is expressed as [107]

$$\boldsymbol{\tau}_k = \mu_k \left[\nabla \boldsymbol{u}_k + (\nabla \boldsymbol{u}_k)^{\dagger}\right] \tag{3.29}$$

where μ_k is the viscosity of phase k. The term $\nabla \boldsymbol{u}_k$ is a dyadic product and $(\nabla \boldsymbol{u}_k)^\dagger$ is the transpose of the velocity gradient tensor $\nabla \boldsymbol{u}_k$, where the velocity gradient tensor can be represented as

$$\nabla \boldsymbol{u}_k = \begin{pmatrix} \frac{\partial u_{k,1}}{\partial x_1} & \frac{\partial u_{k,2}}{\partial x_1} & \frac{\partial u_{k,3}}{\partial x_1} \\ \frac{\partial u_{k,1}}{\partial x_2} & \frac{\partial u_{k,2}}{\partial x_2} & \frac{\partial u_{k,3}}{\partial x_2} \\ \frac{\partial u_{k,1}}{\partial x_3} & \frac{\partial u_{k,2}}{\partial x_3} & \frac{\partial u_{k,3}}{\partial x_3} \end{pmatrix} \tag{3.30}$$

The body force, $\boldsymbol{b}_k$, in Eq. (3.28) only applies to the liquid phase in the polymer electrolyte membrane. Because of the immobile sulfonate ions, the liquid phase has a net positive charge. In the presence of an electric field, a force is exerted on the fluid and the body force becomes

$$\boldsymbol{b}_{l,e} = c_{l,e}^{H^+} \mathscr{F} \nabla \Phi_e \tag{3.31}$$

where $c_{l,e}^{H^+}$ is the concentration of hydrogen ions in the polymer electrolyte, $\mathscr{F}$ is the Faraday constant, and Φ_e is the potential in the polymer electrolyte.

Substituting Eqs. (3.29) and (3.31) into Eq. (3.28), and integrate the resulting equation over the representative volume to give

$$\left\langle \frac{\partial}{\partial t} \left(\rho_k \boldsymbol{u}_k \right) \right\rangle + \langle \nabla \cdot \left(\rho_k \boldsymbol{u}_k \boldsymbol{u}_k \right) \rangle + \langle \nabla P_k \rangle - \langle \nabla \cdot \boldsymbol{\tau}_k \rangle - \langle \rho_k \boldsymbol{g} \rangle - \langle \boldsymbol{b}_k \rangle = 0 \tag{3.32}$$

Applying the transport theorem to the first term and the averaging theorem to the second term yields

$$\begin{aligned} \left\langle \frac{\partial}{\partial t} \left(\rho_k \boldsymbol{u}_k \right) \right\rangle &= \frac{\partial}{\partial t} \langle \rho_k \boldsymbol{u}_k \rangle - \sum_n \frac{1}{V_r} \int_{A_{kn}} \rho_k \boldsymbol{u}_k \boldsymbol{w}_{kn} \cdot \mathbf{n}_k dS \\ &= \frac{\partial}{\partial t} \left(\epsilon_k \langle \rho_k \rangle^k \langle \boldsymbol{u}_k \rangle^k \right) + \frac{\partial}{\partial t} \langle \tilde{\rho}_k \tilde{\boldsymbol{u}}_k \rangle - \sum_n \frac{1}{V_r} \int_{A_{kn}} \rho_k \boldsymbol{u}_k \boldsymbol{w}_{kn} \cdot \mathbf{n}_k dS \end{aligned} \tag{3.33}$$

$$\begin{aligned} \langle \nabla \cdot \left(\rho_k \boldsymbol{u}_k \boldsymbol{u}_k \right) \rangle &= \nabla \cdot \langle \rho_k \boldsymbol{u}_k \boldsymbol{u}_k \rangle + \sum_n \frac{1}{V_r} \int_{A_{kn}} \rho_k \boldsymbol{u}_k \boldsymbol{u}_k \cdot \mathbf{n}_k dS \\ &= \nabla \cdot \left(\epsilon_k \langle \rho_k \rangle^k \langle \boldsymbol{u}_k \rangle^k \langle \boldsymbol{u}_k \rangle^k \right) + \nabla \cdot \left(\epsilon_k \langle \tilde{\rho}_k \tilde{\boldsymbol{u}}_k \rangle \langle \boldsymbol{u}_k \rangle^k \right) \\ &\quad + \nabla \cdot \langle (\tilde{\rho}_k \tilde{\boldsymbol{u}}_k) \tilde{\boldsymbol{u}}_k \rangle + \sum_n \frac{1}{V_r} \int_{A_{kn}} \rho_k \boldsymbol{u}_k \boldsymbol{u}_k \cdot \mathbf{n}_k dS \end{aligned} \tag{3.34}$$

Similarly for the third and fourth terms, applying the modified averaging theorem and the averaging theorem, respectively, we have

$$\langle \nabla P_k \rangle = \nabla \left(\epsilon_k \langle P_k \rangle^k \right) - \langle P_k \rangle^k \nabla \left(\epsilon_k \right) + \sum_n \frac{1}{V_r} \int_{A_{kn}} \tilde{P}_k \mathbf{n}_k dS \tag{3.35}$$

$$\langle \nabla \cdot \boldsymbol{\tau}_k \rangle = \nabla \cdot \left(\epsilon_k \langle \boldsymbol{\tau}_k \rangle^k \right) + \sum_n \frac{1}{V_r} \int_{A_{kn}} \boldsymbol{\tau}_k \cdot \mathbf{n}_k dS \tag{3.36}$$

in which the pressure deviation, $\tilde{P}_k$, and the phase-averaged forms of the viscous stress tensor, $\langle \boldsymbol{\tau}_k \rangle^k$, are given by

$$\tilde{P}_k = P_k - \langle P_k \rangle^k \tag{3.37}$$

$$\langle \boldsymbol{\tau}_k \rangle^k = \mu_k^{\text{eff}} \left[\nabla \langle \boldsymbol{u}_k \rangle^k + \left(\nabla \langle \boldsymbol{u}_k \rangle^k \right)^\dagger \right] \tag{3.38}$$

where the assumption of Eq. (3.8) was used to express the stress tensor in terms of phase-averaged quantities. The volume-averaged forms of the gravitational potential and body force are:

$$\langle \rho_k \boldsymbol{g} \rangle = \epsilon_k \langle \rho_k \rangle^k \boldsymbol{g} \tag{3.39}$$

$$\langle \boldsymbol{b}_{l,e} \rangle^k = \langle c_{l,e}^{H^+} \rangle^k \mathscr{F} \nabla \langle \Phi_e \rangle^k \tag{3.40}$$

Using Eqs. (3.33)–(3.40) in Eq. (3.32) and neglecting second and higher order dispersive terms, the conservation of momentum equation becomes

$$\begin{aligned} &\frac{\partial}{\partial t} \left(\epsilon_k \langle \rho_k \rangle^k \langle \boldsymbol{u}_k \rangle^k \right) + \nabla \cdot \left(\epsilon_k \langle \rho_k \rangle^k \langle \boldsymbol{u}_k \rangle^k \langle \boldsymbol{u}_k \rangle^k \right) + \nabla \left(\epsilon_k \langle P_k \rangle^k \right) \\ &\qquad - \langle P_k \rangle^k \nabla \epsilon_k - \nabla \cdot \left(\epsilon_k \langle \boldsymbol{\tau}_k \rangle^k \right) - \epsilon_k \langle \rho_k \rangle^k \boldsymbol{g} - \epsilon_k \langle \boldsymbol{b} \rangle^k = \Gamma_{F,k} \end{aligned} \tag{3.41}$$

in which $\Gamma_{F,k}$ represents the interfacial source term that is expressed as

$$\begin{aligned} \Gamma_{F,k} = &- \sum_n \frac{1}{V_r} \int_{A_{kn}} \rho_k \boldsymbol{u}_k \left(\boldsymbol{u}_k - \boldsymbol{w}_{kn} \right) \cdot \boldsymbol{n}_k \mathrm{d}S \\ &- \sum_n \frac{1}{V_r} \int_{A_{kn}} \tilde{P}_k \mathbf{n}_k dS - \sum_n \frac{1}{V_r} \int_{A_{kn}} \boldsymbol{\tau}_k \cdot \mathbf{n}_k dS \end{aligned} \tag{3.42}$$

where $\sum_n$ represents the summation over all adjacent n phases, A_{kn} is the interfacial

area of phases k and n, and $\boldsymbol{w}_{kn}$ is the velocity at the interface of k and n within the representative volume.

In order to solve the volume-averaged momentum equation, the interfacial source term must be expressed as a function of volume-averaged quantities. The expression for the interfacial source term depends on the actual phase distribution. Thus, the interfacial source term in the gas flow channels, where only the gas and liquid phases are present, is different from the interfacial source term for the other layers, where a solid phase is present. In general, there are two possible methods for dealing with two-phase liquid-gas flow. One method is to combine the gas and liquid conservation of momentum equations, eliminating the interfacial source terms. If homogeneous flow is assumed, then the gas and liquid velocities are equal and the conservation of momentum equation can be solved for the mixture velocity; this approach is referred to as the "mixture approach" [95] and can be used if one phase is dispersed in the other phase. The second approach, which is more widely applicable, is known as the "two-fluid approach", where the two conservation of momentum equations are solved separately. Here either the interfacial source term [108] or an expression for the velocity difference between the two phases [109] needs to be defined.

In the other layers of a PEM fuel cell, the gas and liquid phases are in contact with a solid phase, and the flow is characterized as porous media flow. If the gas diffusion layer is assumed to be isotropic, the interfacial source term can be expressed as a generalized Darcy term as [110–114]

$$\Gamma_{F,k} = -\frac{\mu_k}{K k_{rk}} \langle \boldsymbol{u}_k \rangle \tag{3.43}$$

where K denotes the intrinsic permeability, and k_{rk} is the relative permeability of phase k in the porous media, which is a dimensionless quantity.

The gravity induced mass flux of liquid water in the two-phase zone in a PEM fuel cell is less than 0.1% of that caused by capillary action. This is because the Bond number is only about 0.04 for GDL, implying negligible gravitational effect compared to the surface tension effect in the two-phase zone [115]. Hence, neglecting the gravitational effect, and using the definition of liquid saturation, the conservation of momentum equation is finally written as

$$\begin{aligned}\frac{\partial}{\partial t}\left(\epsilon s_k \langle \rho_k \rangle^k \langle \boldsymbol{u}_k \rangle^k\right) + \nabla \cdot \left(\epsilon s_k \langle \rho_k \rangle^k \langle \boldsymbol{u}_k \rangle^k \langle \boldsymbol{u}_k \rangle^k\right) + \nabla\left(\epsilon s_k \langle P_k \rangle^k\right) \\ - \langle P_k \rangle^k \nabla\left(\epsilon s_k\right) - \nabla \cdot \left(\epsilon s_k \langle \boldsymbol{\tau}_k \rangle^k\right) - \epsilon s_k \langle \boldsymbol{b} \rangle^k = \Gamma_{F,k}\end{aligned} \tag{3.44}$$

Both the conservation of mass and momentum equations can be solved by solving each

phase separately or by considering a pseudo-fluid mixture. The first method requires appropriate interfacial source term, where the second method does not need source term as they are canceled each other. The pseudo-fluid mixture method, however, requires the proper definition of mixture proprieties. Therefore, appropriate measure requires before choosing the solving procedure.

3.6 Conservation of Species

The species conservation equation is defined as [107]

$$\frac{\partial}{\partial t}\left(\rho_k \omega_k^\alpha\right) + \nabla \cdot \left(\rho_k \omega_k^\alpha \boldsymbol{u}_k + \boldsymbol{\mathcal{J}}_k^\alpha\right) = 0 \tag{3.45}$$

where the index, α, refers to different species, including oxygen, nitrogen, and water vapor, ω_k^α is the mass fraction of species α within phase k, and $\boldsymbol{\mathcal{J}}_k^\alpha$ is the molecular mass flux of species α in phase k, respectively. The expression for the mass flux $\boldsymbol{\mathcal{J}}_k^\alpha$ in a multi-component system will consist of three contributions associated with the mechanical driving forces and an additional contribution associated with the thermal driving force, hence

$$\boldsymbol{\mathcal{J}}_k^\alpha = \boldsymbol{\mathcal{J}}_k^{\alpha(x)} + \boldsymbol{\mathcal{J}}_k^{\alpha(P)} + \boldsymbol{\mathcal{J}}_k^{\alpha(g)} + \boldsymbol{\mathcal{J}}_k^{\alpha(T)} \tag{3.46}$$

where $\boldsymbol{\mathcal{J}}_k^{\alpha(x)}$ is the ordinary (concentration) diffusion, $\boldsymbol{\mathcal{J}}_k^{\alpha(P)}$ is the pressure diffusion, $\boldsymbol{\mathcal{J}}_k^{\alpha(g)}$ is the forced diffusion, and the term, $\boldsymbol{\mathcal{J}}_k^{\alpha(T)}$, represents the contribution of thermal diffusion.

Neglecting the pressure diffusion and temperature diffusion, the mass flux due to the molecular diffusion can be written as [107]

$$-c_k^\alpha \nabla \ln a_k^\alpha - \frac{z_\alpha c_k^\alpha \mathscr{F}}{\mathscr{R} T_k} \nabla \Phi_k = \sum_{\beta \neq \alpha} \frac{\hat{M}_k}{\hat{M}_\alpha \hat{M}_\beta \mathscr{D}_{\alpha-\beta,k}} \left(\omega_k^\beta \boldsymbol{\mathcal{J}}_k^\alpha - \omega_k^\alpha \boldsymbol{\mathcal{J}}_k^\beta\right) \tag{3.47}$$

where $\mathscr{F}$ is the Faraday's constant (96,487 C/mol) and $\mathscr{R}$ is the Universal gas constant (8.314 J/mol·K). The term z_α represents the charge of species α, and Φ_k denotes the potential of phase k. The molar concentration is c_k^α and the molecular weights of the phase and species are denoted by $\hat{M}_k$ and $\hat{M}_\alpha$, respectively. The activity, a_k^α, is given by

$$a_k^\alpha = \gamma_k^\alpha x_k^\alpha \tag{3.48}$$

where γ_k^α is the activity coefficient and x_k^α is the mole fraction of species α in phase k,

respectively. The definition of activity given in Eq. (3.48) is valid for both charged and uncharged species. For an ideal gas or a dilute solution, the activity coefficient is unity.

Similar to the conservation of mass and momentum equations, the conservation of species equation can also be integrated over the representative volume to give

$$\left\langle \frac{\partial}{\partial t}\left(\rho_k \omega_k^\alpha\right) \right\rangle + \left\langle \nabla \cdot \left(\rho_k \omega_k^\alpha \boldsymbol{u}_k + \boldsymbol{\mathcal{J}}_k^\alpha\right) \right\rangle = 0 \tag{3.49}$$

Applying the volume-averaging procedure and after simplification, Eq. (3.49) becomes

$$\frac{\partial}{\partial t}\left(\epsilon_k \langle \rho_k \rangle^k \langle \omega_k^\alpha \rangle^k\right) + \nabla \cdot \left(\epsilon_k \langle \rho_k \rangle^k \langle \omega_k^\alpha \rangle^k \langle \boldsymbol{u}_k \rangle^k + \epsilon_k \langle \boldsymbol{\mathcal{J}}_k^\alpha \rangle^k\right) = \Gamma_{S,k}^\alpha \tag{3.50}$$

where $\Gamma_{S,k}^\alpha$ represents gain or loss of species α from adjacent phases as

$$\Gamma_{S,k}^\alpha = -\sum_n \frac{1}{V_r} \int_{A_{kn}} \rho_k \omega_k^\alpha \left(\boldsymbol{u}_k - \boldsymbol{w}_{kn}\right) \cdot \mathbf{n}_k dS \tag{3.51}$$

It should be noted that the source term in Eq. (3.25) is equal to the sum of the species interfacial source terms, hence

$$\Gamma_{M,k} = \sum_\alpha \Gamma_{S,k}^\alpha, \tag{3.52}$$

In addition, several species can be produced and consumed due to the chemical reaction in a PEM fuel cell, therefore, the interfacial source terms for the conservation of species equation need to be modified as

$$\left(\Gamma_{S,k}^\alpha\right)_{\text{PEM}} = \sum_{n \neq k} \Gamma_{S,k-n}^\alpha + \Gamma_{S,k-\text{react}}^\alpha \tag{3.53}$$

where $\Gamma_{S,k-n}^\alpha$ represents the transfer of species α from phase n to phase k and $\Gamma_{S,k-\text{react}}^\alpha$ is the production of species α due to the reactions. Therefore, the second source term in Eq. (3.27) can be written as

$$\Gamma_{M,k-\text{react}} = \sum_\alpha \Gamma_{S,k-\text{react}}^\alpha \tag{3.54}$$

Assuming no interaction between the solid-liquid phase and solid-gas phase, the first

term in the right hand side of Eq. (3.53) can be expressed as [52]

$$\Gamma^{\mathrm{H_2O}}_{S,g-l} = -\Gamma^{\mathrm{H_2O}}_{S,l-g} = A\left(P_{\mathrm{sat}} - \langle x_g^{\mathrm{H_2O}}\rangle^k \langle P_g\rangle^k\right) \tag{3.55}$$

in which P_{sat} is the saturation pressure of water and A is a constant. The second term in Eq. (3.53) that represents the mass-transfer due to the heterogeneous electrochemical reactions is expressed as

$$\Gamma^{\alpha}_{S,k-\mathrm{react}} = \hat{M}_{\alpha} A_v \dot{\mathscr{P}}^{\alpha} \tag{3.56}$$

where $\dot{\mathscr{P}}^{\alpha}$ is the molar production or consumption of species α and A_v is the reactive surface area per unit volume in the catalyst layer. The expression for $\dot{\mathscr{P}}^{\alpha}$ depends on the reaction kinetics, which will be discussed in next chapter.

3.7 Summary

The governing volume-averaged equations for multi-phase transport processes in the porous medium derived in this chapter for various phases can be summarized as follows:

Conservation of mass:

$$\frac{\partial}{\partial t}\left(\epsilon_k \langle\rho_k\rangle^k\right) + \nabla\cdot\left(\epsilon_k \langle\rho_k\rangle^k \langle\boldsymbol{u}_k\rangle^k\right) = \Gamma_{M,k} \tag{3.57}$$

Conservation of momentum:

$$\begin{aligned}\frac{\partial}{\partial t}\left(\epsilon_k \langle\rho_k\rangle^k \langle\boldsymbol{u}_k\rangle^k\right) + \nabla\cdot\left(\epsilon_k \langle\rho_k\rangle^k \langle\boldsymbol{u}_k\rangle^k \langle\boldsymbol{u}_k\rangle^k\right) + \nabla\left(\epsilon_k \langle P_k\rangle^k\right) \\ - \langle P_k\rangle^k \nabla\left(\epsilon_k\right) - \nabla\cdot\left(\epsilon_k \langle\boldsymbol{\tau}_k\rangle^k\right) - \epsilon_k \langle\boldsymbol{b}\rangle^k = \Gamma_{F,k}\end{aligned} \tag{3.58}$$

Conservation of species:

$$\frac{\partial}{\partial t}\left(\epsilon_k \langle\rho_k\rangle^k \langle\omega_k^{\alpha}\rangle^k\right) + \nabla\cdot\left(\epsilon_k \langle\rho_k\rangle^k \langle\omega_k^{\alpha}\rangle^k \langle\boldsymbol{u}_k\rangle^k + \epsilon_k \langle\boldsymbol{\mathcal{J}}_k^{\alpha}\rangle^k\right) = \Gamma^{\alpha}_{S,k} \tag{3.59}$$

The formulated volume-averaged equations apply to each layer and phase in a PEM fuel cell. However, it should be considered that in the solid phase, velocity is zero. Hence, the conservation of mass and momentum equations are not valid for the solid phase. Further, in the conservation of momentum equation, the interfacial source term, $\Gamma_{F,k}$, depends on the adjacent phases. If a solid phase is present, the momentum interfacial source term

becomes the Darcy term. The interfacial source term in the conservation of mass equation has two contributions. One contribution represents the interfacial mass transport of water between the gas and liquid phases, which is applicable for each layer within a PEM fuel cell. Conversely, contribution on the interfacial source term due to the electrochemical reaction only exists in the catalyst layers. Similarly, the interfacial source term in the conservation of species equation also has two contributions. One is the interfacial mass-transport of water between the gas and liquid phases and the other is the production or consumption of mass due to the electrochemical reactions. Hence, the governing equations derived in this chapter represent a general description of the processes occurring within a PEM fuel cell. The inclusion of all these processes, however, may not be necessary in order to model the performance of a PEM fuel cell successfully. The interfacial source term in each equation can be simplified or neglected depending upon the specific requirement. For instance, in the numerical modeling, it is required to simplify each of these source terms to model a PEM fuel cell successfully. In the next chapter, each of these conservation equations will be simplified and each of the source terms will be specified that can be applied in the numerical modeling of PEM fuel cell catalyst layer.

Chapter 4

Simplified Formulation for PEM Fuel Cell Cathode

The basic conservation laws presented in Chapter 3 represent a general formulation for modeling a PEM fuel cell. However, the solution of these conservation equations for the entire fuel cell is beyond the scope of this thesis research. In this thesis, the focus has only been given to the cathode side of fuel cell. Therefore, several simplifications and assumptions are made before applying the general governing equations. Although the general governing equations of Chapter 3 apply to each phase in the PEM fuel cell, the specific details of the governing equations, such as the interfacial source terms, can be unique to each phase. Thus, these governing equations for each phase are presented in this chapter along with specific source terms for the cathode side of a PEM fuel cell.

4.1 Physical Problem and Assumptions

A typical PEM fuel cell is considered that consists of a cathode and an anode electrode with a proton conducting membrane as the electrolyte sandwiched in between as shown in Fig. 4.1. Here, humidified H_2 gas is supplied under pressure into the anode gas flow channel, which diffuses through the porous gas diffusion layer until it reaches the anode catalyst layer, and forms protons (H^+) and electrons via electro-oxidation reaction at the catalyst surface. The protons are transferred through the membrane to the cathode catalyst layer, and the electrons are transported via the external circuit to the cathode. Conversely, humidified air is supplied to the cathode gas flow channel, where O_2 gas (a component of air) diffuses through the porous electrode until it reaches the cathode catalyst layer and forms water reacting with protons and electrons. The overall electrochemical reaction

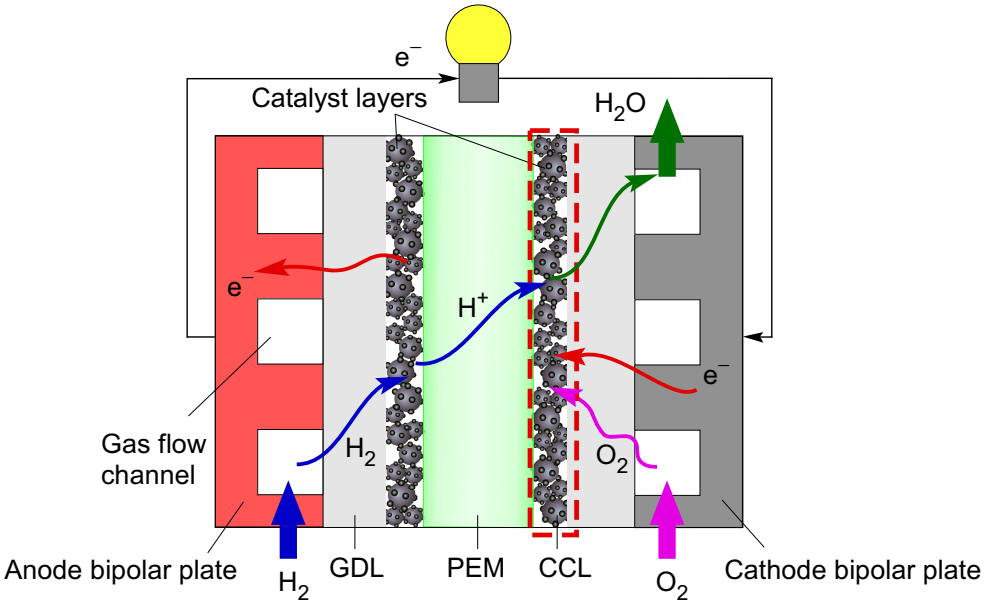

Figure 4.1: A schematic of PEM fuel cell with key transport processes, indicated by the arrows, and the area of interest, indicated by the dashed rectangle.

occurring in a PEM fuel cell can be represented by the following reaction:

$$2H_2 + O_2 \rightarrow 2H_2O + \text{Heat} + \text{Electric Energy} \tag{4.1}$$

In this thesis research, the focus is given to the transport processes in the cathode side of a PEM fuel cell that includes cathode catalyst layer, gas diffusion layer, and cathode gas flow channel, will be simply referred as CCL, GDL, and GFC, respectively. The schematic of a PEM fuel cell along with the area of interest (dashed rectangle) is demonstrated in Fig. 4.1. Hence, in the subsequent sections, the governing equations and the pertinent source terms are provided that are applicable for the cathode side of a PEM fuel cell.

The general governing equations are influenced by the physical structure of a PEM fuel cell, which consists of several co-existing phases. The conservation equations govern the transport of mass, momentum, and species in each phase. Since several phases co-exist, interfacial interactions between the phases also occur. Here the interfacial interactions between the solid phases and other phases have been neglected, hence, only liquid and gas phases are considered. The set of equations used in this model are manipulated to solve for each phase individually. The 3D two-phase model consists of nonlinear, coupled partial differential equations representing the conservation of mass, momentum, species, and charges. The major assumptions invoked in the model formulation are summarized as follows [40, 41]:

- Membrane is impermeable to gas species.
- Flow in the gas channel is laminar due to small Reynolds numbers.
- Negligible capillary effects in gas flow channel.
- Liquid water in gas flow channel travels as droplet of negligible volume with bulk gas phase velocity.
- Negligible liquid water saturation at the GDL/GFC interface.
- Gas mixture is an ideal fluid.
- Gravity effect is negligible due to small Bond numbers.
- Production of water in the catalyst layer is liquid form only.
- Gas diffusion and catalyst layers are isotropic and homogeneous.
- Contact resistance between any two layers in the fuel cell is negligible.
- Isothermal operating condition.

4.2 Gas Transport

The gas phase transport processes in the PEM fuel cell is described by the conservation of mass, momentum, and species as

$$\frac{\partial}{\partial t}\left(\epsilon_g \langle \rho_g \rangle^g\right) + \nabla \cdot \left(\epsilon_g \langle \rho_g \rangle^g \langle \boldsymbol{u}_g \rangle^g\right) = \Gamma_{M,g} \tag{4.2}$$

$$\begin{aligned}\frac{\partial}{\partial t}\left(\epsilon_g \langle \rho_g \rangle^g \langle \boldsymbol{u}_g \rangle^g\right) + \nabla \cdot \left(\epsilon_g \langle \rho_g \rangle^g \langle \boldsymbol{u}_g \rangle^g \langle \boldsymbol{u}_g \rangle^g\right) + \nabla\left(\epsilon_g \langle P_g \rangle^g\right) \\ - \langle P_g \rangle^g \nabla\left(\epsilon_g\right) - \nabla \cdot \left(\epsilon_g \langle \boldsymbol{\tau}_g \rangle^g\right) = \Gamma_{F,g}\end{aligned} \tag{4.3}$$

$$\frac{\partial}{\partial t}\left(\epsilon_g \langle \rho_g \rangle^g \langle \omega_g^\alpha \rangle^g\right) + \nabla \cdot \left(\epsilon_g \langle \rho_g \rangle^g \langle \omega_g^\alpha \rangle^g \langle \boldsymbol{u}_g \rangle^g + \epsilon_g \langle \boldsymbol{\mathcal{J}}_g^\alpha \rangle^g\right) = \Gamma_{S,g}^\alpha \tag{4.4}$$

In order to obtain a solution for the conservation equations (Eq. (4.2) to Eq. (4.4)), it is required to provide a close form of each source term. Although the major focus has given to the CCL, it is also required to solve the conservation equations in the GFC and GDL in order to study the transport processes inside the fuel cell catalyst layer. In the following subsections, source terms required for the conservation equations in the GFC, GDL, and CCL of a PEM fuel cell are described explicitly.

4.2.1 Mass Transport in Gas Phase

In the gas phase mass-transport, the interfacial mass-transfer has been considered negligible in the gas flow channel in lieu of simplifying the conservation equation. In the GDL, the interfacial source term is taken account as the mass-transfer between the liquid and gas phases due to the phase change. While in the CCL, it is assumed that the production of water is in liquid form. This assumption is reasonable, as the operating pressure is considered higher than 1 atm and the operating temperature is considered below 100 ℃. Further, the phase-change at the liquid-gas interfaces has also been considered. Therefore, the source terms for the conservation of mass equation in the GFC, GDL, and CCL are summarized as

$$\Gamma_{M,g} = \begin{cases} 0 & \in \text{GFC} \\ A\left(P_{\text{sat}} - x_g^{\text{H}_2\text{O}}\langle P_g\rangle^g\right) & \in \text{GDL} \\ \hat{M}_{\text{O}_2} A_v \dot{\mathscr{P}}^{\text{O}_2} + A\left(P_{\text{sat}} - x_g^{\text{H}_2\text{O}}\langle P_g\rangle^g\right) & \in \text{CCL} \end{cases} \tag{4.5}$$

where A is a constant that represents the interfacial mass-transfer rate of water between the gas and liquid phases.

The interfacial mass-transfer rate is defined as [52, 116]

$$A = k_c \frac{\epsilon s_g x_g^{\text{H}_2\text{O}} \hat{M}_{\text{H}_2\text{O}}}{\mathscr{R}T} q + k_v \epsilon s_l \langle \rho_l \rangle^l (1-q) \tag{4.6}$$

where the first term in the right-hand side represents the condensation rate and the second term represents the evaporation rate. Equation (4.6) is basically assuming that the interfacial mass-transfer rate is proportional to the amount of reactant in the porous media and the driving force, the difference between water partial pressure and its saturation pressure. Here ϵ represents the porosity of the medium, s_l is the liquid saturation, P_g is the total pressure of the gas phase, $\hat{M}_{\text{H}_2\text{O}}$ is the molecular weight of water, and $\mathscr{R}$ and T are the gas constant and operating temperature, respectively. The terms, k_c and k_v, are the rate constants for condensation and vaporization, and the values are 100 s^{-1} and 9.869×10^{-6} $\text{Pa}^{-1}\text{s}^{-1}$, respectively [116].

In Eq. (4.5), $x_g^{\text{H}_2\text{O}}$ is the mole fraction of water vapor in the gas phase and P_{sat} represents the saturation pressure of water at operating temperature. The saturation pressure in atmosphere is estimated using the following correlation [26, 27]:

$$\log_{10} P_{\text{sat}} = -2.1794 + 0.02953T - 9.1837 \times 10^{-5} T^2 + 1.4454 \times 10^{-7} T^3 \tag{4.7}$$

where P_{sat} is in units of atm and T is in units of ℃. The term q in Eq. (4.6) is a switching function that was selected such that it is one when the water partial pressure is greater than the water saturation pressure and zero otherwise. Hence,

$$q = \begin{cases} 0 & \text{when } \dfrac{x_g^{\text{H}_2\text{O}} \langle P_g \rangle^g}{P_{\text{sat}}} \leq 1 \\ 1 & \text{when } \dfrac{x_g^{\text{H}_2\text{O}} \langle P_g \rangle^g}{P_{\text{sat}}} > 1 \end{cases} \tag{4.8}$$

In the numerical modeling, the above relations are expressed as single expression as

$$q = 0.5 \left[1 + \frac{\left| P_{\text{sat}} - x_g^{\text{H}_2\text{O}} \langle P_g \rangle^g \right|}{P_{\text{sat}} - x_g^{\text{H}_2\text{O}} \langle P_g \rangle^g} \right] \tag{4.9}$$

The terms, A_v and $\dot{\mathscr{P}}^{\text{O}_2}$, in Eq. (4.5) represent the catalyst reactive surface area per unit volume and the molar consumption of O_2, respectively. The expression for $\dot{\mathscr{P}}^{\text{O}_2}$ will be described later in this chapter. While the specific reaction surface area per unit volume (A_v) can be estimated from the catalyst mass loading per unit area of cathode (m_{Pt}), catalyst surface area per unit mass of catalyst (A_s), and catalyst layer thickness (δ_{CL}) as follows [6]:

$$A_v = \frac{A_s m_{\text{Pt}}}{\delta_{\text{CL}}} \tag{4.10}$$

4.2.2 Momentum Transport in Gas Phase

Similar to the conservation of mass equation, the conservation of momentum equation for the gas phase does not have the source term in the gas flow channel. In the GDL and CCL, the gas and liquid phases are in contact with a solid phase; and under such condition, the flow can be characterized as porous media flow. For a isotropic GDL, the interfacial source term can be expressed as a generalized Darcy term as [110–114]

$$\Gamma_{F,g} = -\frac{\epsilon_g \mu_g}{K k_{rg}} \langle \boldsymbol{u}_g \rangle^g \tag{4.11}$$

where K is the permeability, ϵ_g represents the effective porosity, and κ_{rg} denotes the relative permeability of the gas phase in the porous medium. Therefore, the source terms for conservation of momentum equation in the GFC, GDL, and CCL are summarized as

$$\Gamma_{F,g} = \begin{cases} 0 & \in \text{GFC} \\ -\frac{\epsilon_g \mu_g}{K k_{rg}} \langle \boldsymbol{u}_g \rangle^g & \in \text{GDL} \\ -\frac{\epsilon_g \mu_g}{K k_{rg}} \langle \boldsymbol{u}_g \rangle^g & \in \text{CCL} \end{cases} \tag{4.12}$$

The term μ_g in Eq. (4.12) represents the viscosity of the gas mixture. For the PEM fuel cell cathode, the gas mixture consists of water vapor, oxygen, and nitrogen. Therefore, the viscosity of the gas mixture can be defined as [117]

$$\mu_g = x_g^{\mathrm{H_2O}} \mu_{\mathrm{H_2O}} + x_g^{\mathrm{O_2}} \mu_{\mathrm{O_2}} + x_g^{\mathrm{N_2}} \mu_{\mathrm{N_2}} \tag{4.13}$$

where $x_g^{\mathrm{H_2O}}$, $x_g^{\mathrm{O_2}}$, and $x_g^{\mathrm{N_2}}$ are the mole fractions, and $\mu_{\mathrm{H_2O}}$, $\mu_{\mathrm{O_2}}$, and $\mu_{\mathrm{N_2}}$ are the viscosities of water vapor, oxygen, and nitrogen, respectively. The gas viscosities are estimated from the following correlations [118–121]:

$$\mu_\alpha = \begin{cases} 0.1470 \times 10^{-6}\ T^{0.862} & \text{for } \mathrm{O_2} \\ 0.2369 \times 10^{-6}\ T^{0.756} & \text{for } \mathrm{N_2} \\ 0.0185 \times 10^{-6}\ T^{1.101} & \text{for } \mathrm{H_2O} \end{cases} \tag{4.14}$$

where μ_α is in $\mathrm{N{\cdot}s/m^2}$, and T is in Kelvin.

The effective porosity of the catalyst layer depends on the composition of the catalyst layer, i.e. the Pt-loading and ionomer loading determine the effective porosity. For a dry catalyst layer, the porosity can be calculated from the following relation:

$$\epsilon_g = 1 - f_m + f_s \tag{4.15}$$

where f_m represents the ionomer fraction (or Nafion fraction) and f_s is the fraction of solid Pt/C in the catalyst layer. The volume fraction of ionomer membrane in the catalyst layer can be related through the Nafion content $\%N$ (defined as the weight percentage of Nafion in the sum of Nafion and solid particles) by [122]

$$f_m = \frac{\%N}{(1 - \%N)\,\rho_m} \frac{m_{\mathrm{Pt}}}{\%\mathrm{Pt} \cdot \delta_{\mathrm{CL}}} \tag{4.16}$$

in which ρ_m is the density of Nafion, %Pt is the mass percentage of platinum in the combined total mass of the solid particles of platinum and carbon, m_{Pt} is the Pt-loading, and δ_{CL} is the catalyst layer thickness. If the catalyst layer surface area (A_{CL}) and carbon

weight (W_C) are known, %Pt can be calculated from the following relation [122]:

$$\%\mathrm{Pt} = \frac{m_{\mathrm{Pt}} A_{\mathrm{CL}}}{m_{\mathrm{Pt}} A_{\mathrm{CL}} + W_{\mathrm{C}}} \tag{4.17}$$

The volume fraction of solid Pt/C in the catalyst layer is related to %Pt, catalyst layer thickness, and the platinum and carbon black densities (ρ_{Pt} and ρ_{C}) as [7]

$$f_s = \left(\frac{1}{\rho_{\mathrm{Pt}}} + \frac{1 - \%\mathrm{Pt}}{\%\mathrm{Pt} \cdot \rho_{\mathrm{C}}} \right) \frac{m_{\mathrm{Pt}}}{\delta_{\mathrm{CL}}} \tag{4.18}$$

4.2.3 Species Transport in Gas Phase

The gas phase in the PEM fuel cell is considered as an ideal three-component gas mixture, consisting water vapor, oxygen, and nitrogen. Therefore, the conservation of species equation for each component needs to be considered separately. For the water vapor transport, Eq. (4.4) is re-written as

$$\frac{\partial}{\partial t} \left(\epsilon_g \langle \rho_g \rangle^g \langle \omega_g^{\mathrm{H_2O}} \rangle^g \right) + \nabla \cdot \left(\epsilon_g \langle \rho_g \rangle^g \langle \omega_g^{\mathrm{H_2O}} \rangle^g \langle \boldsymbol{u}_g \rangle^g + \epsilon_g \langle \boldsymbol{\mathcal{J}}_g^{\mathrm{H_2O}} \rangle^g \right) = \Gamma_{S,g}^{\mathrm{H_2O}} \tag{4.19}$$

where $\omega_g^{\mathrm{H_2O}}$ is the mass fraction and $\boldsymbol{\mathcal{J}}_g^{\mathrm{H_2O}}$ is the molecular mass flux of water vapor in the gas phase. For the oxygen transport, Eq. (4.4) is re-written as

$$\frac{\partial}{\partial t} \left(\epsilon_g \langle \rho_g \rangle^g \langle \omega_g^{\mathrm{O_2}} \rangle^g \right) + \nabla \cdot \left(\epsilon_g \langle \rho_g \rangle^g \langle \omega_g^{\mathrm{O_2}} \rangle^g \langle \boldsymbol{u}_g \rangle^g + \epsilon_g \langle \boldsymbol{\mathcal{J}}_g^{\mathrm{O_2}} \rangle^g \right) = \Gamma_{S,g}^{\mathrm{O_2}} \tag{4.20}$$

where $\omega_g^{\mathrm{O_2}}$ is the mass fraction and $\boldsymbol{\mathcal{J}}_g^{\mathrm{O_2}}$ is the molecular mass flux of oxygen in the gas phase, whereas the mass fraction of nitrogen in the gas phase is calculated from the following relation:

$$\omega_g^{\mathrm{N_2}} = 1 - \omega_g^{\mathrm{H_2O}} - \omega_g^{\mathrm{O_2}} \tag{4.21}$$

The gas phase density in Eq. (4.19) can be calculated assuming that the gas mixture obeys the ideal gas law. Hence, the gas density is

$$\langle \rho_g \rangle^g = \frac{\langle P_g \rangle^g \hat{M}_g}{\mathscr{R} \langle T_g \rangle^g} \tag{4.22}$$

where $\hat{M}_g$ the molecular weight of the gas mixture in the PEM fuel cell is calculated from

the molecular weight of water vapor, oxygen, and nitrogen as

$$\hat{M}_g = \left[\frac{\omega_g^{\mathrm{H_2O}}}{\hat{M}_{\mathrm{H_2O}}} + \frac{\omega_g^{\mathrm{O_2}}}{\hat{M}_{\mathrm{O_2}}} + \frac{\omega_g^{\mathrm{N_2}}}{\hat{M}_{\mathrm{N_2}}} \right]^{-1} \tag{4.23}$$

The source term for Eq. (4.19) is found as

$$\Gamma_{S,g}^{\mathrm{H_2O}} = \begin{cases} 0 & \in \mathrm{GFC} \\ A\left(P_{\mathrm{sat}} - x_g^{\mathrm{H_2O}} \langle P_g \rangle^g\right) & \in \mathrm{GDL} \\ A\left(P_{\mathrm{sat}} - x_g^{\mathrm{H_2O}} \langle P_g \rangle^g\right) & \in \mathrm{CCL} \end{cases} \tag{4.24}$$

and for Eq. (4.20) as

$$\Gamma_{S,g}^{\mathrm{O_2}} = \begin{cases} 0 & \in \mathrm{GFC} \\ 0 & \in \mathrm{GDL} \\ \hat{M}_{\mathrm{O_2}} A_v \dot{\mathscr{P}}^{\mathrm{O_2}} & \in \mathrm{CCL} \end{cases} \tag{4.25}$$

Clearly, Eqs. (4.24) and (4.25) satisfy the following relation:

$$\Gamma_{M,g} = \sum_{\alpha} \Gamma_{S,g}^{\alpha} \tag{4.26}$$

The gas phase generalized Stefan-Maxwell transport equation is simplified by assuming that the solid phase does not interfere with the diffusion of the gas species. Hence, the generalized Stefan-Maxwell equation for the gas phase becomes [123]

$$-\langle c_g \rangle^g \nabla \langle x_g^{\alpha} \rangle^g = \sum_{\beta \neq \alpha} \frac{\hat{M}_g}{\hat{M}_{\alpha} \hat{M}_{\beta} \mathscr{D}_{\alpha-\beta,g}^{\mathrm{eff}}} \left(\langle \omega_g^{\beta} \rangle^g \langle \boldsymbol{\mathcal{J}}_g^{\alpha} \rangle^g - \langle \omega_g^{\alpha} \rangle^g \langle \boldsymbol{\mathcal{J}}_g^{\beta} \rangle^g \right) \tag{4.27}$$

It is clear that the above-mentioned Stefan-Maxwell equation provides the transport equation 'the wrong way around' that is expression of species concentration in terms of fluxes. For the conservation of species equation (Eq. (4.4)), we need species fluxes in terms of concentrations. There are two possible methods that can re-solve this issue, either invert Eq. (4.27) directly or using a Fickian approximation to the Stefan-Maxwell transport equation. In the following section, a direct inversion expression is given and then a Fickian approximation of the Stefan-Maxwell transport equation is also provided. Both methods can be used in solving the species transport equations for the PEM fuel cell, where former provides better accuracy with higher computational load and later is an approximation that needs less computational load.

In the first step of inversion, Eq. (4.27) is re-written as

$$-\langle c_g\rangle^g \nabla \langle x_g^\alpha\rangle^g = \frac{\langle \boldsymbol{\mathcal{J}}_g^\alpha\rangle^g}{\hat{M}_\alpha} \sum_{\beta\neq\alpha} \frac{\langle x_g^\beta\rangle^g}{\mathscr{D}^{\text{eff}}_{\alpha-\beta,g}} - \frac{\langle \omega_g^\alpha\rangle^g}{\hat{M}_\alpha} \sum_{\beta\neq\alpha} \frac{\hat{M}_g \langle \boldsymbol{\mathcal{J}}_g^\beta\rangle^g}{\hat{M}_\beta \mathscr{D}^{\text{eff}}_{\alpha-\beta,g}} \tag{4.28}$$

where the molar fraction and mass fraction for the species α are defined as

$$\langle x_g^\alpha\rangle^g = \frac{\langle c_g^\alpha\rangle^g}{\langle c_g\rangle^g}, \qquad \langle \omega_g^\alpha\rangle^g = \frac{\langle \rho_g^\alpha\rangle^g}{\langle \rho_g\rangle^g} \tag{4.29}$$

and the molar fraction of each species is related to its mass fraction by

$$\langle x_g^\alpha\rangle^g = \frac{\langle \omega_g^\alpha\rangle^g \hat{M}_g}{\hat{M}_\alpha}, \text{ where } \sum_\alpha x_g^\alpha = 1 \tag{4.30}$$

The molecular weight of the gas mixture can be calculated by

$$\hat{M}_g = \sum_\alpha x_g^\alpha \hat{M}_\alpha = \left[\sum_\alpha \frac{\omega_g^\alpha}{\hat{M}_\alpha}\right]^{-1} \tag{4.31}$$

Hence, Eq. (4.28) gives the diffusional flux of species α as

$$\begin{aligned}
\langle \boldsymbol{\mathcal{J}}_g^\alpha\rangle^g &= \hat{M}_\alpha \sum_{\beta\neq\alpha} \frac{\mathscr{D}^{\text{eff}}_{\alpha-\beta,g}}{\langle x_g^\beta\rangle^g} \left[-\langle c_g\rangle^g \nabla\langle x_g^\alpha\rangle^g + \frac{\langle \omega_g^\alpha\rangle^g}{\hat{M}_\alpha} \sum_{\beta\neq\alpha} \frac{\hat{M}_g \langle \boldsymbol{\mathcal{J}}_g^\beta\rangle^g}{\hat{M}_\beta \mathscr{D}^{\text{eff}}_{\alpha-\beta,g}}\right] \\
&= \hat{M}_\alpha \sum_{\beta\neq\alpha} \frac{\mathscr{D}^{\text{eff}}_{\alpha-\beta,g}}{\langle x_g^\beta\rangle^g} \left[-\langle c_g\rangle^g \left(\frac{\hat{M}_g}{\hat{M}_\alpha}\nabla\langle \omega_g^\alpha\rangle^g + \langle \omega_g^\alpha\rangle^g \frac{\nabla \hat{M}_g}{\hat{M}_\alpha}\right) + \frac{\langle \omega_g^\alpha\rangle^g}{\hat{M}_\alpha} \sum_{\beta\neq\alpha} \frac{\hat{M}_g \langle \boldsymbol{\mathcal{J}}_g^\beta\rangle^g}{\hat{M}_\beta \mathscr{D}^{\text{eff}}_{\alpha-\beta,g}}\right] \\
&= \sum_{\beta\neq\alpha} \frac{\mathscr{D}^{\text{eff}}_{\alpha-\beta,g}}{\langle x_g^\beta\rangle^g} \left[-\langle \rho_g\rangle^g \nabla\langle \omega_g^\alpha\rangle^g - \langle c_g\rangle^g \langle \omega_g^\alpha\rangle^g \nabla \hat{M}_g + \langle \omega_g^\alpha\rangle^g \sum_{\beta\neq\alpha} \frac{\hat{M}_g \langle \boldsymbol{\mathcal{J}}_g^\beta\rangle^g}{\hat{M}_\beta \mathscr{D}^{\text{eff}}_{\alpha-\beta,g}}\right]
\end{aligned} \tag{4.32}$$

Finally, Eq. (4.32) is simplified and the diffusional flux of species α expressed as a function of mass fraction as [124]

$$\langle \boldsymbol{\mathcal{J}}_g^\alpha\rangle^g = -\langle \rho_g\rangle^g D^{\text{eff}}_{\alpha-g} \nabla\langle \omega_g^\alpha\rangle^g + \frac{\langle \omega_g^\alpha\rangle^g D^{\text{eff}}_{\alpha-g}}{\left(1-\langle x_g^\alpha\rangle^g\right)} \sum_{\beta\neq\alpha} \left[\frac{\langle \rho_g\rangle^g \hat{M}_g}{\hat{M}_\beta}\nabla\langle \omega_g^\beta\rangle^g + \frac{\hat{M}_g \langle \boldsymbol{\mathcal{J}}_g^\beta\rangle^g}{\hat{M}_\beta \mathscr{D}^{\text{eff}}_{\alpha-\beta,g}}\right] \tag{4.33}$$

where $D^{\text{eff}}_{\alpha-g}$ is the overall effective diffusion coefficient of species α in the gas phase that

is expressed as

$$\frac{1-\langle x_g^{\alpha}\rangle^g}{D_{\alpha-g}^{\text{eff}}} = \sum_{\beta\neq\alpha}\frac{\langle x_g^{\beta}\rangle^g}{\mathscr{D}_{\alpha-\beta,g}^{\text{eff}}} \tag{4.34}$$

Clearly, Eq. (4.33) does not provide the diffusional flux of species α in terms of concentration of species. It is also a function of diffusional flux of species β, hence, an alternative approach has also been considered. In the alternative approach, the Fickian approximations is used to the Stefan-Maxwell transport equation that is given as [107]

$$\langle \boldsymbol{\mathcal{J}}_g^{\alpha}\rangle^g = -\langle\rho_g\rangle^g\langle\omega_g^{\alpha}\rangle^g\sum_{j=1}^{N-1}\mathbf{D}_{\alpha j}\nabla\langle x_g^{j}\rangle^g, \quad j\neq\alpha \tag{4.35}$$

where N is the number of component in the multi-component mixture and $\mathbf{D}_{\alpha j}$ is the Maxwell-Stefan diffusivities. The matrix $\mathbf{D}_{\alpha j}$ of Ficks diffusion coefficient is a square matrix of dimension $(N-1)\times(N-1)$ that is strongly dependent on the composition of the mixture. For a ternary mixture, the component are given by the following expressions [125, 126]:

$$\mathbf{D}_{11} = \frac{\frac{(\omega_2+\omega_3)^2}{x_1\mathscr{D}_{23}} + \frac{\omega_2^2}{x_2\mathscr{D}_{13}} + \frac{\omega_3^2}{x_3\mathscr{D}_{12}}}{D'} \tag{4.36}$$

$$\mathbf{D}_{22} = \frac{\frac{\omega_1^2}{x_1\mathscr{D}_{23}} + \frac{(\omega_1+\omega_3)^2}{x_2\mathscr{D}_{13}} + \frac{\omega_3^2}{x_3\mathscr{D}_{12}}}{D'} \tag{4.37}$$

$$\mathbf{D}_{12} = \mathbf{D}_{21} = \frac{\frac{\omega_1(\omega_2+\omega_3)}{x_1\mathscr{D}_{23}} + \frac{\omega_2(\omega_1+\omega_3)}{x_2\mathscr{D}_{13}} - \frac{\omega_3^2}{x_3\mathscr{D}_{12}}}{D'} \tag{4.38}$$

where

$$D' = \frac{x_1\mathscr{D}_{23} + x_2\mathscr{D}_{13} + x_3\mathscr{D}_{12}}{\mathscr{D}_{12}\mathscr{D}_{13}\mathscr{D}_{23}} \tag{4.39}$$

In Eqs. (4.36)−(4.38), indices in the right hand side represent the three components of the gas phase mixture. For example, if water vapor is represented by 1, oxygen as 2 and nitrogen as 3, then $\mathscr{D}_{12}$ represents the binary diffusion coefficient of water vapor in oxygen and so forth. Note that it is the $\mathscr{D}_{ij}$ rather than D_{ij} and that the $\mathscr{D}_{ij}$ are virtually independent of composition. It is worthwhile to note that the bulk diffusion coefficient in

the GFC can be calculated according to [127]:

$$\frac{1-x_g^{\mathrm{O_2}}}{D_{\mathrm{O_2,bulk}}}=\frac{x_g^{\mathrm{N_2}}}{\mathscr{D}_{\mathrm{O_2-N_2}}}+\frac{x_g^{\mathrm{H_2O}}}{\mathscr{D}_{\mathrm{O_2-H_2O}}} \tag{4.40}$$

where $x_g^{\mathrm{O_2}}$, $x_g^{\mathrm{N_2}}$, and $x_g^{\mathrm{H_2O}}$ are the mole fractions of oxygen, nitrogen, and water vapor in the flow channel, respectively.

4.3 Liquid Transport

In the PEM fuel cell, the liquid phase consists of liquid water only. Therefore, for the liquid water transport, the conservation of mass, momentum, and species equations can be derived using Eqs. (3.57)–(3.59) as follows:

$$\frac{\partial}{\partial t}\left(\epsilon_l\langle\rho_l\rangle^l\right)+\nabla\cdot\left(\epsilon_l\langle\rho_l\rangle^l\langle\boldsymbol{u}_l\rangle^l\right)=\Gamma_{M,l} \tag{4.41}$$

$$\begin{aligned}\frac{\partial}{\partial t}\left(\epsilon_l\langle\rho_l\rangle^l\langle\boldsymbol{u}_l\rangle^l\right)+\nabla\cdot\left(\epsilon_l\langle\rho_l\rangle^l\langle\boldsymbol{u}_l\rangle^l\langle\boldsymbol{u}_l\rangle^l\right)+\nabla\left(\epsilon_l\langle P_l\rangle^l\right)&\\ -\langle P_l\rangle^l\nabla\left(\epsilon_l\right)-\nabla\cdot\left(\epsilon_l\langle\boldsymbol{\tau}_l\rangle^l\right)=\Gamma_{F,l}&\end{aligned} \tag{4.42}$$

$$\frac{\partial}{\partial t}\left(\epsilon_l\langle\rho_l\rangle^l\langle\omega_l^\alpha\rangle^l\right)+\nabla\cdot\left(\epsilon_l\langle\rho_l\rangle^l\langle\omega_l^\alpha\rangle^l\langle\boldsymbol{u}_l\rangle^l+\epsilon_l\langle\boldsymbol{\mathcal{J}}_l^\alpha\rangle^l\right)=\Gamma_{S,l}^\alpha \tag{4.43}$$

Similar to the gas phase conservation equations, the liquid phase conservation equations also require the close form of each source term. In the following subsections, the source terms for the liquid phase conservation equations are described.

4.3.1 Mass Transport in Liquid Phase

The interfacial mass-transfer has been neglected in the flow channel, and only considered inside the GDL and CCL. Further, the capillary effects are neglected within the gas channel and the liquid is assumed to travel as droplets of negligible volume with a velocity that is equal to the bulk gas velocity. It has also been assumed that the production of water in the CCL from the electrochemical reaction is in liquid form. Hence, the source terms for the liquid phase in the GFC, GDL, and CCL are written for the conservation of mass equation as

$$\Gamma_{M,l} = \begin{cases} 0 & \in \text{GFC} \\ -A\left(P_{\text{sat}} - x_g^{\text{H}_2\text{O}}\langle P_g\rangle^g\right) & \in \text{GDL} \\ \hat{M}_{\text{H}_2\text{O}} A_v \dot{\mathscr{P}}^{\text{H}_2\text{O}} - A\left(P_{\text{sat}} - x_g^{\text{H}_2\text{O}}\langle P_g\rangle^g\right) & \in \text{CCL} \end{cases} \tag{4.44}$$

4.3.2 Momentum Transport in Liquid Phase

The source terms for the liquid phase momentum equation are

$$\Gamma_{F,l} = \begin{cases} 0 & \in \text{GFC} \\ -\frac{\epsilon_l \mu_l}{K k_{rl}}\langle \boldsymbol{u}_l\rangle^l & \in \text{GDL} \\ -\frac{\epsilon_l \mu_l}{K k_{rl}}\langle \boldsymbol{u}_l\rangle^l & \in \text{CCL} \end{cases} \tag{4.45}$$

where κ_{rl} is the relative permeability of liquid phase in the GDL and CCL. The definition of the relative permeability and the corresponding empirical correlation for relative permeability are provided in Chapter 5.

Due to very small Reynolds and capillary numbers in the GDL and CCL, the convective and viscous terms in Eq. (4.42) can be neglected. Hence, Eq. (4.42) is simplified for the steady-state case as the Darcy equation as

$$\nabla\left(\epsilon_l\langle P_l\rangle^l\right) - \langle P_l\rangle^l \nabla\epsilon_l = \Gamma_{F,l} \tag{4.46}$$

For the CCL and GDL, the above equation can be written as

$$\epsilon_l \nabla\langle P_l\rangle^l = -\frac{\epsilon_l \mu_l}{K k_{rl}}\langle \boldsymbol{u}_l\rangle^l \tag{4.47}$$

The liquid phase pressure can be written by the gas phase pressure and capillary pressure, hence Eq. (4.47) yields

$$-\nabla\langle P_c\rangle + \nabla\langle P_g\rangle^g = -\frac{\mu_l}{K k_{rl}}\langle \boldsymbol{u}_l\rangle^l \tag{4.48}$$

where P_c is the capillary pressure that is defined later in Chapter 5. Taking the divergence of above equation and using the Darcy's law for the gas phase pressure, Eq. (4.48) becomes

$$\nabla \cdot \left(\frac{K k_{rl} \langle \rho_l \rangle}{\mu_l} \nabla \langle P_c \rangle + \frac{k_{rl} \mu_g \langle \rho_l \rangle}{k_{rg} \mu_l} \langle \boldsymbol{u}_g \rangle^g \right) = \nabla \cdot \left(\langle \rho_l \rangle \langle \boldsymbol{u}_l \rangle^l \right) \tag{4.49}$$

and in terms of liquid saturation, s_l, as

$$\nabla \cdot \left(\frac{K k_{rl}}{\mu_l} \langle \rho_l \rangle \frac{dP_c}{ds_l} \nabla s_l + \frac{k_{rl} \mu_g}{k_{rg} \mu_l} \langle \rho_l \rangle \langle \boldsymbol{u}_g \rangle^g \right) = \Gamma_{M,l} \tag{4.50}$$

Finally, the governing equation for the liquid water transport in the PEM fuel cell is written as

$$\nabla \cdot (D_c \nabla s_l) = \Gamma_{S,l} \tag{4.51}$$

where D_c is the capillary diffusivity for the liquid water that can be represented by the following expression:

$$D_c = \frac{K k_{rl}}{\mu_l} \langle \rho_l \rangle \frac{dP_c}{ds_l} = \epsilon_l \frac{K k_{rl}}{\mu_l} \langle \rho_l \rangle^l \frac{dP_c}{ds_l} \tag{4.52}$$

Clearly, the above equation is completely different than the widely used liquid water transport equation in literature and commercial software Fluent® user guide. The liquid volume fraction term in the right hand side is widely omitted, which seems incorrect based on the volume-average method describe in this thesis.

The source terms for the liquid water equation (Eq. (4.51)) in the GDL and CCL of a PEM fuel cell are written as

$$\Gamma_{S,l} = \begin{cases} -A \left(P_{\text{sat}} - x_g^{\text{H}_2\text{O}} \langle P_g \rangle^g \right) - \nabla \cdot \left(\dfrac{k_{rl} \mu_g}{k_{rg} \mu_l} \langle \rho_l \rangle \langle \boldsymbol{u}_g \rangle^g \right) & \in \text{GDL} \\ \hat{M}_{\text{H}_2\text{O}} A_v \dot{\mathscr{P}}^{\text{H}_2\text{O}} - A \left(P_{\text{sat}} - x_g^{\text{H}_2\text{O}} \langle P_g \rangle^g \right) - \nabla \cdot \left(\dfrac{k_{rl} \mu_g}{k_{rg} \mu_l} \langle \rho_l \rangle \langle \boldsymbol{u}_g \rangle^g \right) & \in \text{CCL} \end{cases} \tag{4.53}$$

The last term in the above equation represents the amount of liquid water transport hindered by the gas flow from the flow channel to the CCL. Most of the previous studies neglected that term by assuming a uniform gas pressure in the GDL [56, 113, 128]. This assumption seems unrealistic as gradient of gaseous pressure necessary for gas transport unless we are attempting for an analytical solution. Hence, the amount of liquid water hindered by gas flow is explicitly considered in the numerical simulation of this thesis research.

4.4 Electron and Proton Transports

In the previous sections, the conservation of mass, momentum, and species equations are derived for the gas and liquid phases in a PEM fuel cell, except the conservation of species equation for the solid phase. The solid phase of a PEM fuel cell consists of solid electrode and polymer membrane phase. Therefore, the species that are needed to be considered for the solid phases are: electron for the solid carbon phase and proton for the polymer electrolyte membrane. For the electron transport, the governing equation is derived from the conservation of species equation. Since the solid phase does not have convective velocity, therefore, the conservation of electron equation in terms of electronic molar flux can be written as

$$\nabla \cdot \left(\epsilon_s \langle \boldsymbol{N}_s^{e^-} \rangle^s \right) = \Gamma_{S,s}^{e^-} \tag{4.54}$$

where $\boldsymbol{N}_s^{e^-}$ is the molar flux of electrons in the solid phase that that can be expressed in terms of current density through the Faraday's law [129]:

$$\boldsymbol{N}_s^{e^-} = \frac{\boldsymbol{J}_s}{z_- \mathscr{F}} \tag{4.55}$$

where $\boldsymbol{J}_s$ is the solid phase current density and z is the charge number. The following relation expresses the current density in terms of corresponding phase potential:

$$\boldsymbol{J}_s = -\sigma_s^{\text{eff}} \nabla \langle \Phi_s \rangle^s \tag{4.56}$$

where σ_s^{eff} is the effective electronic conductivity and Φ_s is the solid phase potential, respectively. Hence, using Eqs. (4.55) and (4.56) in Eq. (4.54) yields to

$$\nabla \cdot \left(\epsilon_s \sigma_s^{\text{eff}} \nabla \langle \Phi_s \rangle^s \right) = \mathscr{F} \Gamma_{S,s}^{e^-} \tag{4.57}$$

where $\Gamma_{S,s}^{e^-}$ is the generation or consumption of electron in the solid phase that is given by in term of production of electron, $\dot{\mathscr{P}}^{e^-}$, as

$$\Gamma_{S,s}^{e^-} = A_v \dot{\mathscr{P}}^{e^-} \tag{4.58}$$

Similar to the conservation of electron equation, the conservation of proton equation can be written as

$$\nabla \cdot \left(\epsilon_m \langle \boldsymbol{N}_m^{p^+} \rangle^m \right) = \Gamma_{S,m}^{p^+} \tag{4.59}$$

where $\boldsymbol{N}_m^{p^+}$ is the molar flux of proton in the polymer electrolyte phase that is expressed in terms of current density through the Faraday's law [129]:

$$\boldsymbol{N}_m^{p^+} = \frac{\boldsymbol{J}_m}{z_+ \mathscr{F}} \tag{4.60}$$

where $\boldsymbol{J}_m$ is the membrane phase current density, which is expressed in terms of corresponding phase potential:

$$\boldsymbol{J}_m = -\sigma_m^{\text{eff}} \nabla \langle \Phi_m \rangle^m \tag{4.61}$$

where σ_m^{eff} is the effective protonic conductivity and Φ_m is the potential of membrane phase, respectively. Hence, Eq. (4.59) simplifies to

$$\nabla \cdot \left(\epsilon_m \sigma_m^{\text{eff}} \nabla \langle \Phi_m \rangle^m \right) = -\mathscr{F} \Gamma_{S,m}^{p^+} \tag{4.62}$$

where $\Gamma_{S,m}^{p^+}$ is the generation or consumption of proton (H^+) in the polymer electrolyte phase, which is given by the production of proton, $\dot{\mathscr{P}}^{H^+}$, as

$$\Gamma_{S,m}^{p^+} = A_v \dot{\mathscr{P}}^{H^+} \tag{4.63}$$

4.5 Chemical Reaction in Catalyst Layer

The major reaction occurring in the cathode catalyst layer is the oxygen reduction that can be represented by the following reaction:

$$O_2 + 4H^+ + 4e^- \rightleftharpoons 2H_2O \tag{4.64}$$

The rate of reaction for the above-mentioned chemical reaction can be represented more precisely by Volmer/Erdey-Gruz kinetics as [130]

$$\mathcal{R}_{c,\text{red}} = \frac{J_0^{O_2}}{4\mathscr{F}} \left\{ \left[\frac{c_{l,e}^{H_2O}}{\bar{c}_{l,e}^{H_2O}} \right]^2 \exp\left(\frac{\eta_c}{B_c^{O_2}} \right) - \left[\frac{c_{g,e}^{O_2}}{\bar{c}_{g,e}^{O_2}} \right] \left[\frac{c_{l,e}^{H^+}}{\bar{c}_{l,e}^{H^+}} \right]^4 \exp\left(-\frac{\eta_c}{B_c^{O_2}} \right) \right\} \tag{4.65}$$

where $J_0^{O_2}$ is the reference exchange current density for oxygen reduction and c_k^α is the concentration of species α.

An overbar on the concentration term denotes the reference concentrations. The reference concentrations for the gas phase species are the concentrations of the pure species at a reference pressure of 1 atm and the cell temperature. The reference current density

($J_0^{O_2}$) at the reference concentration of $\bar{c}_{g,e}^{O_2}$ can be calculated using the experimental data of Parthasarathy *et al.* [13], and the reference oxygen concentration, $\bar{c}_{g,e}^{O_2}$, is generally taken as 1.2 mol/m^3 [6, 13]. The experimental data of the reference exchange current density in A/cm^2 for oxygen reduction in Nafion were correlated with the cell temperature in Kelvins by the following correlation [6]:

$$\log_{10}\left(J_0^{O_2}\right) = 3.507 - \frac{4001}{T} \tag{4.66}$$

The Tafel slope is denoted by $B_c^{O_2}$ and is given by:

$$B_c^{O_2} = \frac{\mathscr{R}T}{\mathscr{F}} \tag{4.67}$$

where $\mathscr{F}$ is the Faraday's constant and $\mathscr{R}$ is the universal gas constant. The definition of Tafel slope in Eq. (4.67) does not match the general expression for Tafel slope in Eq. (4.65). However, Eq. (4.67) results in a Tafel slope of 68 mV/decade at a temperature of 70 ℃, which agrees with the experimental value of 70 mV/decade from [13]. The discrepancy between the actual and theoretical Tafel slope is because the oxygen reduction reaction is not a single step reaction; the general expression for Tafel slope is valid only for a single step reaction. Further, Eq. (4.65) still needs the experimental values of $c_{l,e}^{H^+}$ and $c_{l,e}^{H_2O}$ that are still unknown. Alternatively, the rate of reaction for the Eq. (4.64) can be represented by the Butler-Volmer equation as [4]

$$\mathcal{R}_{c,\text{red}} = \frac{J_0^{O_2}}{4\mathscr{F}}\left[\frac{c_{g,e}^{O_2}}{\bar{c}_{g,e}^{O_2}}\right]^{\gamma_c}\left\{\exp\left(\frac{\alpha_a n\eta_c}{B_c^{O_2}}\right) - \exp\left(-\frac{\alpha_c n\eta_c}{B_c^{O_2}}\right)\right\} \tag{4.68}$$

where γ_c is the overall reaction order, α_a and α_c are the apparent transfer coefficients for the anodic and cathodic reactions, respectively. The term n represents the number of electrons transferred in the electrochemical reaction, and η_c represents the activation overpotential, which is the driving force for the electrochemical reactions.

The production and consumption of species in the catalyst layer are related to the reaction rate. In the cathode catalyst layer, the productions of different species are given by:

$$\dot{\mathscr{P}}^{O_2} = -\mathcal{R}_{c,\text{red}} \tag{4.69}$$

$$\dot{\mathscr{P}}^{H_2O} = 2\mathcal{R}_{c,\text{red}} \tag{4.70}$$

$$\dot{\mathscr{P}}^{H^+} = -4\mathcal{R}_{c,\text{red}} \tag{4.71}$$

$$\dot{\mathscr{P}}^{e^-} = -4\mathcal{R}_{c,\text{red}} \tag{4.72}$$

where $\mathcal{R}_{c,\text{red}}$ is the rate of electrochemical reaction, as given by Eq. (4.68).

4.6 Summary

The simplified governing equations for the gas, liquid, and solid phases in a PEM fuel cell are given explicitly in this chapter. The liquid and gas phase conservation equations consist of the conservation of mass, momentum, and species equations. Since the electrochemical reaction occurs in the catalyst layer of PEM fuel cell, the conservation of charge equation is also considered that includes the conservation of electron and conservation of proton equations. Therefore, in the simplified formulation, total 8 equations have been given in this chapter, which contains 4 conservation equations for the gas phase including 2 species conservation equations, 2 conservation equations for liquid phase, and 2 conservation of charge equations. Conversely, the number of primary variables that are required to be solved is 9. The primary variables are: velocity, pressure, partial densities of oxygen, water vapor and nitrogen in the gas phase; velocity and pressure in the liquid phase; potential in the solid phase; and potential in the electrolyte membrane. The partial density of nitrogen is calculated considering the total mass fraction in the gas phase is unity.

Chapter 5

Effective Transport Properties

The transport of species and charges in the porous layers of PEM fuel cell are modeled using the generalized Stefan-Maxwell equation and Ohms law. Expressions for the effective properties in these equations are needed for the closure of formulation. Further, an accurate estimation of the effective properties in PEM fuel cell, e.g. effective conductivities and diffusivities in the catalyst layers (CLs) and gas diffusion layers (GDLs), is crucial for accurately predicting the fuel cell performance and optimizing design parameters in the numerical modeling/simulation. Hence, a set of mathematical expression is derived for the effective transport properties in PEM fuel cell. The model and results presented in this chapter are based on the published articles.[1,2]

5.1 Overview of Empirical Correlations

In the PEM fuel cell literature, the Bruggeman approximation has been widely used for the effective conductivities and diffusivities. In several instances both the Wiener bounds and Bruggeman approximation were used together for estimating the effective properties [7, 33, 82, 94, 122, 131]. The average of Wiener bounds has also been recommended for the effective thermal conductivity [132]. Previous studies, however, have not used or attempted to implement the HS bounds. It was further observed that the results reported in literature lack information on several physical and electrochemical parameters. In some cases, it has been found that replicating published results is very difficult because of the missing information or parameter values [7, 82]. Further, the effective properties of composite systems depend on the internal microstructure; and no such straightforward

[1]P.K. Das, X. Li, and Z.S. Liu. *Proc. of 4th International Green Energy Conference*, pp. 164–174, Beijing, China, October 2008.

[2]P.K. Das, X. Li, and Z.S. Liu. *Applied Energy*, 87:2785–2796, 2010.

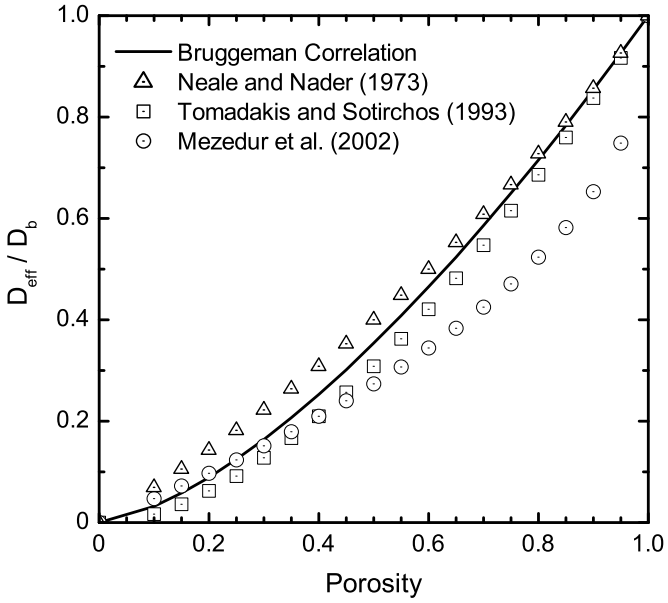

Figure 5.1: Comparison of the effective diffusivities using the expressions available in literature with the Bruggeman correlation.

method exists to consider the effect of microstructure. Even formulations for the effective properties discussed earlier did not agree with each other. As shown in Fig. 5.1, while comparing several correlations with the Bruggeman correlation, all the correlations are underestimating the effective diffusivity compared to the Bruggeman correlation [133–135]. Clearly, each of these correlations has different estimate and it is not reasonable to argue which correlation is a better fit for the numerical modeling of PEM fuel cell. The differences observed in this comparison (Fig. 5.1) could be that these correlations are empirically fitted to certain experimental results and none of these experiments used similar geometrical and physical parameter values.

The effective transport property formulations were mainly developed for different porous media, for example, fibrous porous media [134], spherical shell porous media [133], sand [136], rock [137], shaly sandstone [138], etc. None of them is specifically developed for the CLs and GDLs of PEM fuel cell. Further, the GDLs are made of hydrophilic carbon cloth and hydrophobic PTFE (Teflon). Hence, the wettability and composition of these materials in GDLs not only change the effective transport properties but also influence the water flooding that can further change the effective properties. Therefore, it is crucial to provide a better mathematical expression for the effective properties of a PEM fuel cell that has fundamental mathematical proof rather than empirical verification, which would be more useful in the numerical modeling of PEM fuel cells. Numerical approaches,

like finite volume, finite element, and lattice Boltzmann methods [139, 140], can also be used in estimating the effective properties for the PEM fuel cell. These methods, however, require complicated numerical modeling, sophisticated programming knowledge, and time-consuming calculation. Hence, a simple correlation for the effective properties has been developed that can be easily implemented in PEM fuel cell modeling/simulation. In the following sections, the formulations of the effective properties are described along with the procedure to estimate the binary diffusion coefficients.

5.2 Formulation

Using the effective bulk modulus formulation developed by Hashin [141], Hashin and Shtrikman [142] showed an exact expression for the effective conductivity of a coated sphere assemblage. A schematic representation of both the Hashin coated sphere and coated sphere assemblage are shown in two parts of Fig. 5.2. Here, the coated sphere in a coated sphere assemblage represents a two-phase spherical particle, where phase 1 can be coated by phase 2 (or vice versa) that is shown in Fig. 5.2a. Each coated sphere in the coated sphere assemblage, shown in Fig. 5.2b, was considered as a scaled version of the original prototype coated sphere. Practically, it might be impossible to build a macro-homogenous layer using an infinite number of coated spheres. However, considering a composite system with large number of coated spheres that can fill more than 90% of the total volume or higher, it can be shown that the effective property of the composite system will obey the following relation [143]:

$$\phi_1 + \frac{3f_2\phi_1\left(\phi_2 - \phi_1\right)}{3\phi_1 + f_1\left(\phi_2 - \phi_1\right)} \geqslant \phi_{\text{eff}} \geqslant \phi_2 + \frac{3f_1\phi_2\left(\phi_1 - \phi_2\right)}{3\phi_2 + f_2\left(\phi_1 - \phi_2\right)} \tag{5.1}$$

where ϕ_{eff} represents the effective property of the coated sphere assemblage shown in Fig. 5.2b, ϕ_1 and ϕ_2 are the bulk properties, and f_1 and f_2 are the volume fractions of phases 1 and 2 in the coated sphere, respectively. It was also assumed that phases have been labeled, such that $\phi_1 > \phi_2$. Using Eq. (5.1), the effective transport property expressions are derived for the CLs and GDLs that are given in the following paragraphs.

The microstructure of a PEM fuel cell catalyst layer consists of a matrix of catalyst particles, electrolyte membrane (also known as ionomer), and void space. Ideally, the platinum (Pt) particles supported on a large carbon particle surrounded by ionomer form a catalyst agglomerate, or several carbon particles combine together that is surrounded by ionomer form a large agglomerate. Such a catalyst is also known as platinum supported on carbon or simply referred as Pt/C particle. Figure 5.3 shows a schematic representation of the idealized structure of catalyst agglomerate with single carbon particle in part (a)

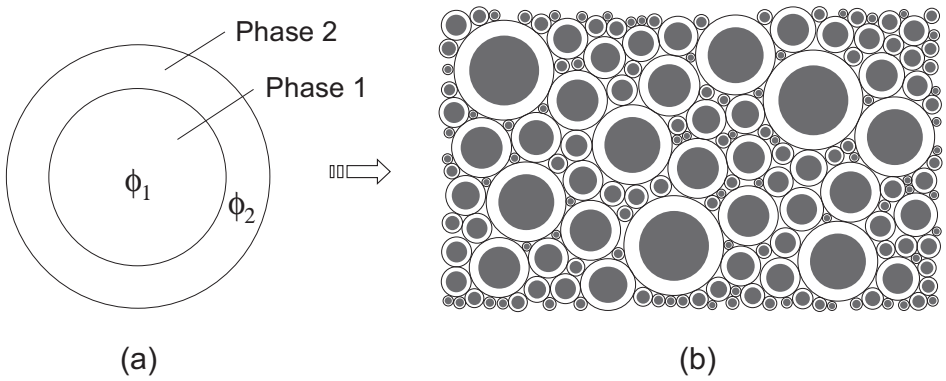

Figure 5.2: Schematic representation of: (a) the Hashin coated sphere, and (b) cross section of the Hashin coated sphere assemblage. Each coated sphere in part (b) is a scaled version of the coated sphere shown in part (a).

and idealized structure of a large catalyst agglomerate formed by multiple carbon particles in part (b). Part (c) of Fig. 5.3 illustrates an idealized microstructure of catalyst layer made of such small and large agglomerates with negligible void region, and a simplified structure of catalyst agglomerate is shown in part (d). Here, each of these agglomerates is a scaled version of the original single-carbon agglomerate (Fig. 5.3a) or multi-carbon agglomerate (Fig. 5.3b). Generally, the size of the Pt-particles is much smaller than the carbon particles; hence, both the platinum and carbon particles can be considered as one solid phase. Therefore, the catalyst agglomerate can be simplified as a two-phase coated sphere that has a solid core (phase 1) coated with ionomer membrane (phase 2) as shown in Fig. 5.3d, which is identical to the Hashin coated sphere shown in Fig. 5.2a. The volume fraction occupied by phase 1 in the coated sphere is represented by

$$f_1 = \frac{r_1^3}{r_2^3} = 1 - f_2 \tag{5.2}$$

where f_2 is the volume fraction of phase 2, and r_1 and r_2 are the radii of the inner core (phase 1) and the outer coating (phase 2), respectively.

The outer radius of the simplified agglomerate shown in Fig. 5.3d is identical to the radius of the original agglomerate (Fig. 5.3a), whereas the inner radius needs to be calculated from the volume occupied by the platinum particles and carbon particles that is defined as

$$r_1^3 = n_{\mathrm{C}} r_{\mathrm{C}}^3 + n_{\mathrm{Pt}} r_{\mathrm{Pt}}^3 \tag{5.3}$$

where r_{C} and r_{Pt} are the radii of carbon and platinum particles, and n_{C} and n_{Pt} are the numbers of carbon and platinum particles in a catalyst agglomerate, respectively. Using

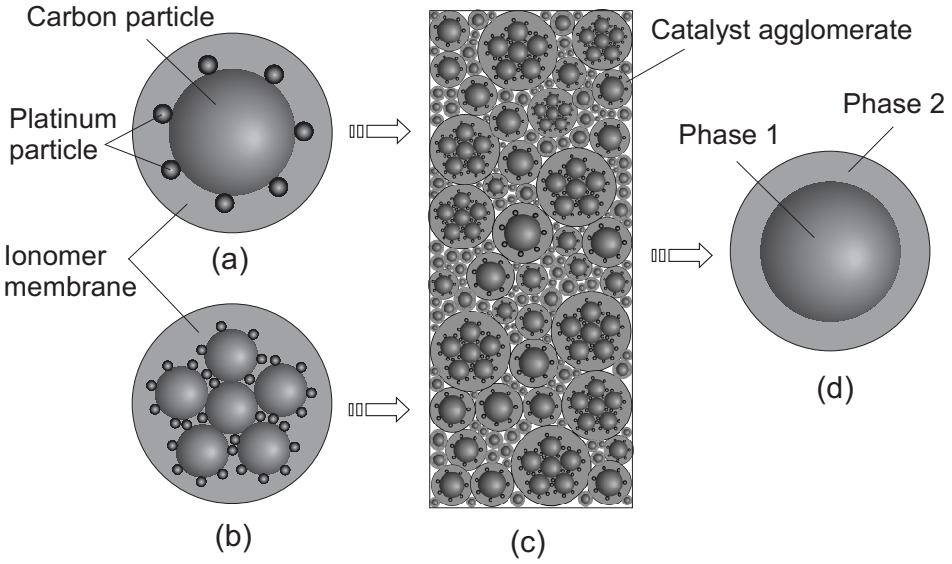

Figure 5.3: Schematic representation of: (a) the idealized structure of a small catalyst agglomerate with platinum catalyst particles and single carbon particle, (b) idealized structure of a large catalyst agglomerate formed by multiple carbon particles, (c) idealized microstructure of catalyst layer made of small and large agglomerates with negligible void region, and (d) simplified structure of a catalyst agglomerate.

the simplified catalyst agglomerate shown in Fig. 5.3d, it is possible to re-build a macro-homogenous layer with negligible void space fraction that would be identical to the catalyst layer shown in Fig. 5.3c. For instance, if the fraction of void space in the CL is 0.1, then 90% of the total CL volume needs to be filled with ionomer coated Pt/C spheres. Practically, this can be attainable. Further, it has been observed that the ionomer membrane forms a layer on the surface of Pt/C agglomerate when the paste method is used for the fabrication of catalyst layer [144], which is almost identical to the coated sphere assemblage shown in Fig. 5.3c. Hence, the catalyst layer made of such simplified agglomerates can be compared with the Hashin's two-phase coated sphere assemblage [143], where the Pt/C particle can be treated as phase 1 and the ionomer membrane as phase 2. Therefore, the effective conductivity of the catalyst layer can be estimated from the upper bound of HS formula:

$$\left(\sigma_{12}^{\text{eff}}\right)_u = \sigma_1 + \frac{3f_2\sigma_1\left(\sigma_2 - \sigma_1\right)}{3\sigma_1 + f_1\left(\sigma_2 - \sigma_1\right)} \tag{5.4}$$

and the lower bound formula:

$$\left(\sigma_{12}^{\text{eff}}\right)_l = \sigma_2 + \frac{3f_1\sigma_2\left(\sigma_1 - \sigma_2\right)}{3\sigma_2 + f_2\left(\sigma_1 - \sigma_2\right)} \tag{5.5}$$

where $\sigma_1 > \sigma_2$, and σ_1 and σ_2 are the conductivities of inner core (i.e. Pt/C for the PEM

fuel cell catalyst layer) and outer coating (i.e. ionomer membrane), respectively. The term f represents the volume fraction for different phases as denoted by subscripts.

5.2.1 Effective Protonic Conductivity

For proton transport in the catalyst layer shown in Fig. 5.3c, the inner core of the coated sphere does not transport protons. Protons can only be transported through the membrane phase or the outer coating of the coated sphere, i.e. $\sigma_1 < \sigma_2$. Hence, the HS bounds need to be modified for $\sigma_1 < \sigma_2$ as

$$\sigma_2 + \frac{3f_1\sigma_2\left(\sigma_1 - \sigma_2\right)}{3\sigma_2 + f_2\left(\sigma_1 - \sigma_2\right)} \geqslant \sigma_{12}^{\text{eff}} \geqslant \sigma_1 + \frac{3f_2\sigma_1\left(\sigma_2 - \sigma_1\right)}{3\sigma_1 + f_1\left(\sigma_2 - \sigma_1\right)} \tag{5.6}$$

After re-arranging, Eq. (5.6) yields

$$\sigma_2 + \frac{3\left(1 - f_2\right)\sigma_2}{f_2 - \frac{3\sigma_2}{\sigma_2 - \sigma_1}} \geqslant \sigma_{12}^{\text{eff}} \geqslant \sigma_1 + \frac{3\left(1 - f_1\right)\sigma_1}{f_1 - \frac{3\sigma_1}{\sigma_1 - \sigma_2}} \tag{5.7}$$

where σ_{12}^{eff} is the effective protonic conductivity of the composite system of phases 1 and 2. Since the inner core is inactive for proton transport, i.e. $\sigma_1 = 0$.

For the outer phase, we have $\sigma_2 = \sigma_m$, where σ_m is the bulk protonic conductivity of membrane phase. Hence, the effective conductivity for membrane phase (or the effective protonic conductivity) can be written as

$$\sigma_m - \frac{3f_s\sigma_m}{3 - f_m} \geqslant \sigma_m^{\text{eff}} \geqslant 0 \tag{5.8}$$

where σ_m^{eff} is the effective conductivity of membrane phase, and f_s and f_m are the volume fractions of solid Pt/C and ionomer membrane in the catalyst layer, respectively. Practically, the effective protonic conductivity cannot be zero; in such case, there will be no proton transport from the anode side to the cathode side of a PEM fuel cell. For an operating fuel cell that seems impossible too. The lowest possible protonic conductivity has always to be higher than zero; therefore, the lower bound in Eq. (5.8) cannot exist so that Eq. (5.8) becomes

$$\sigma_m - \frac{3f_s\sigma_m}{3 - f_m} \geqslant \sigma_m^{\text{eff}} > 0 \tag{5.9}$$

Eq. (5.9) also implies that the highest possible effective protonic conductivity would be

$$\sigma_{m,\max}^{\text{eff}} = \sigma_m - \frac{3\,(1-f_m)\,\sigma_m}{3-f_m} \equiv \sigma_m^{\text{eff}} \tag{5.10}$$

The lower limit of Eq. (5.9) can be extracted from Eq. (5.10) when $f_m \to 0$. Further, Eq. (5.10) is valid for a composite layer composed of solid Pt/C and ionomer membrane with negligible fraction of void space, i.e. for $(f_s + f_m) \to 1$. In such situation, the diffusion of reactant gases in the catalyst layer of a PEM fuel cell will be almost "completely" hindered due to the significantly smaller diffusion coefficient of the reactant in the membrane. Therefore, it would be worthwhile to consider a certain fraction of void space over the ionomer membrane phase, which can be considered as doubly coated sphere as shown in Fig. 5.4. Practically, the void spaces are randomly distributed over the entire catalyst layer. To simplify the problem, the void space is assumed uniform over the catalyst agglomerate as shown in Fig. 5.4, where the outer radius of doubly coated sphere can be estimated for the same equivalent volume

$$\sum \left(\frac{4}{3}\Pi {r_3}^3 - \frac{4}{3}\Pi {r_2}^3 \right) = f_3 V \tag{5.11}$$

where r_3 is the outer radius of doubly coated sphere and r_2 is the outer radius of phase 2. The term f_3 represents the volume fraction of phase 3 that is equivalent to the total volume fraction of void space in the catalyst layer and V is the total volume of the catalyst layer. In a doubly coated sphere assemblage, proton conductivity through the void space would be smaller (or even no proton transport) than the effective proton conductivity of solid Pt/C and ionomer membrane coated sphere, i.e. $\sigma_{12}^{\text{eff}} > \sigma_3$.

The expression for the doubly coated sphere assemblage can also be derived from the above-mentioned simplified coated sphere formulation. Using the similar approach, it can be shown for a doubly coated sphere assemblage ($\sigma_{12}^{\text{eff}} > \sigma_3$) as

$$\sigma_{12}^{\text{eff}} + \frac{3\,(1-f_{12})\,\sigma_{12}^{\text{eff}}}{f_{12} - \dfrac{3\sigma_{12}^{\text{eff}}}{\sigma_{12}^{\text{eff}} - \sigma_2}} \geqslant \sigma_{123}^{\text{eff}} \geqslant \sigma_3 + \frac{3\,(1-f_3)\,\sigma_3}{f_3 - \dfrac{3\sigma_3}{\sigma_3 - \sigma_{12}^{\text{eff}}}} \tag{5.12}$$

where $\sigma_{123}^{\text{eff}}$ is the effective conductivity of a three-phase composite system made of doubly coated spheres as shown in Fig. 5.4. For the CL of a PEM fuel cell, Eq. (5.12) finally yields

$$\sigma_{m,\text{CL}}^{\text{eff}} = \sigma_m^{\text{eff}} + \frac{3\,(1-f_s-f_m)\,\sigma_m^{\text{eff}}}{(f_s+f_m) - \dfrac{3\sigma_m^{\text{eff}}}{\sigma_m^{\text{eff}} - \sigma_v}} \tag{5.13}$$

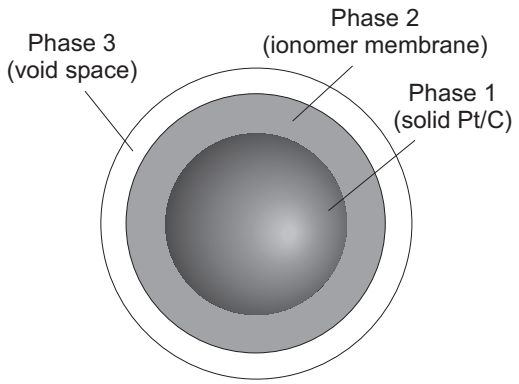

Figure 5.4: Schematic representation of a doubly coated sphere.

where σ_v is the protonic conductivity of void space, and σ_m^{eff} is the effective protonic conductivity when only solid Pt/C and ionomer membrane phases are considered (given in Eq. (5.10)).

For an un-flooded CL, the void spaces are filled with the reactant gases only; hence, the protonic conductivity of void space is zero. Conversely, for a flooded case, liquid water in the pore can act as a liquid electrolyte and participate in proton transportation. However, such transportation will be negligible compared to the proton transport through the ionomer membrane. In addition, liquid water needs free acidic group to be an electrolyte. Assuming the ionomer membrane was fully saturated before being assembled in the membrane electrode assembly of a PEM fuel cell, then there will be no such free acidic group for the liquid water to be an electrolyte. Therefore, it is justifiable to neglect the protonic conductivity of void spaces even under the flooding situation. Hence, Eq. (5.13) simplifies to

$$\sigma_{m,\text{CL}}^{\text{eff}} = \sigma_m - \frac{3\left(1-f_m\right)\sigma_m}{3-f_m} - \frac{3f_v\left(\sigma_m - \dfrac{3\left(1-f_m\right)\sigma_m}{3-f_m}\right)}{2+f_v} \tag{5.14}$$

where f_v is the volume fraction of void space in the catalyst layer, which is simply the catalyst layer porosity. For the practical scenarios, the protonic conductivity will be even lower, i.e.

$$\sigma_{m,\text{CL}}^{\text{eff}} = \sigma_m - \frac{3\lambda_m\left(1-f_m\right)\sigma_m}{3-f_m} - \frac{3\lambda_m f_v\left(\sigma_m - \dfrac{3\left(1-f_m\right)\sigma_m}{3-f_m}\right)}{2+f_v} \tag{5.15}$$

where λ_m is a multiplying factor which will be relying on the geometrical structure of membrane phase in a catalyst layer, for instance, membrane connectivity in the catalyst

layer or shape of the agglomerate. The bounds for λ_m can be written as

$$\frac{3 - f_m}{3(1 - f_m)} > \lambda_m \geqslant 1 \quad \text{for } f_m \neq 0 \text{ or } 1 \tag{5.16}$$

5.2.2 Effective Electronic Conductivity

For electron transport in the catalyst layer shown in Fig. 5.3c, both the membrane phase and the void space act as electric insulators, and only the solid Pt/C phase transports electron. Therefore, the membrane and void space together can be considered as phase 2. Although the Pt/C particles are considered coated with non-electron conducting phase as shown is Fig. 5.3d, it is assumed that the Pt/C particles are actually in contact with some small contact area while assembled in the catalyst layer that would not affect the estimate of proton conductivity and mass diffusivity. Further, it is assumed that the contact area is sufficient without impairing electron conductivity since the Pt/C particle has very high electronic conductivity compared to the protonic conductivity. Hence, for the electronic conductivity, we have $\sigma_1 = \sigma_s$ and $\sigma_2 = 0$, and the effective conductivity for the solid phase (or the effective electronic conductivity) can be written as

$$\sigma_s - \frac{3\,(1 - f_s)\,\sigma_s}{3 - f_s} \geqslant \sigma_s^{\text{eff}} \geqslant 0 \tag{5.17}$$

where σ_s^{eff} and σ_s are the effective and bulk electronic conductivities in the solid phase of CL, respectively, and f_s is the volume fraction of Pt/C. Similar to the analogy provided for the protonic conductivity, it can be claimed that the effective electronic conductivity cannot be zero. It has to be higher than zero to maintain a properly operating PEM fuel cell. Hence, the effective electronic conductivity should obey the following relation:

$$\sigma_s - \frac{3\,(1 - f_s)\,\sigma_s}{3 - f_s} \geqslant \sigma_s^{\text{eff}} > 0 \tag{5.18}$$

The above expression also implies that the highest possible value for the effective electronic conductivity would be

$$\sigma_{s,\max}^{\text{eff}} = \sigma_s - \frac{3\,(1 - f_s)\,\sigma_s}{3 - f_s} \equiv \sigma_s^{\text{eff}} \tag{5.19}$$

The bulk electronic conductivity is significantly higher than the bulk protonic conductivity in PEM fuel cells; hence, it can easily be presumed that the effective electronic conductivity will be close to its highest value. This statement may not be valid for every composite

system; however, this approximation is justifiable for a PEM fuel cell, where the electronic conductivity has much less influence on the cell performance compared to the protonic conductivity. To be more precise, the above equation can be re-written as

$$\sigma_s^{\text{eff}} = \sigma_s - \lambda_s \frac{3\,(1-f_s)\,\sigma_s}{3-f_s} \tag{5.20}$$

where λ_s is the solid phase geometry factor and the bound is found as

$$\frac{3-f_s}{3(1-f_s)} > \lambda_s \geqslant 1 \quad \text{for } f_s \neq 0 \text{ or } 1 \tag{5.21}$$

It is worthwhile to note that the GDL of a PEM fuel cell is composed of solid carbon phase and void space, which is a combination of two phases. Therefore, Eq. (5.20) is valid for both CLs and GDLs of a PEM fuel cell.

5.2.3 Effective Diffusivity

For the catalyst layer effective diffusivity, it is required to consider a coated sphere assemblage where both the liquid and gas phases co-exist in the void space. In the PEM fuel cell, the formation of liquid water inside the cathode catalyst layer is still unknown. It can be film-wise or drop-wise or may be a combination of both. A good approximation would be to consider a uniform mixture of gas and liquid phases in the void space. Such approximation, however, will require complicated mathematical approach to derive an expression for the effective diffusivity. Therefore, a random liquid water film over the ionomer membrane surface has been considered as shown in Fig. 5.5 as phase 3, and this sphere can be referred as a triply coated sphere when phase 2 is completely covered by phase 3. In the following paragraphs, a general formulation is first derived by considering a triply coated sphere, where the solid core (phase 1) is first considered coated by phase 2 and the coated sphere is considered subsequently covered by phase 3, and then simplified for the case when phase 2 is partially covered by phase 3 or liquid water.

As described earlier for a coated sphere assemblage that has two phases (phases 1 and 2 as shown in Fig. 5.3d), the lower bound of an effective property is

$$\phi_{12}^{\text{eff}} = \phi_2 + \frac{3\,(1-f_2)\,\phi_2}{f_2 - \dfrac{3\phi_2}{\phi_2 - \phi_1}} \tag{5.22}$$

Therefore, the effective diffusivity for a coated sphere assemblage that has two phases can be written as

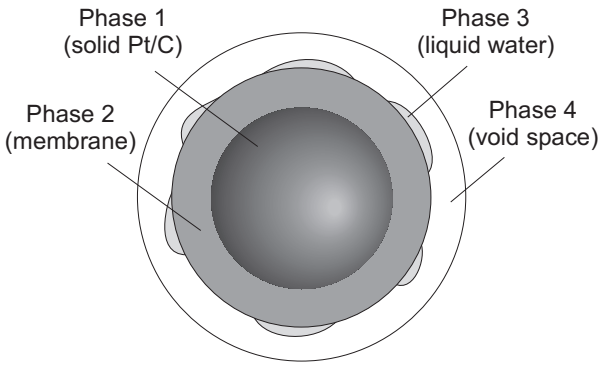

Figure 5.5: Schematic representation of a coated sphere with liquid water film (referred as phase 3) in the void space.

$$D_{12}^{\text{eff}} = D_2 + \frac{3\left(1-f_2\right)D_2}{f_2 - \dfrac{3D_2}{D_2 - D_1}} \quad \text{for } D_2 > D_1 \tag{5.23}$$

where D_1 and D_2 are the bulk diffusivities of phases 1 and 2, respectively, and D_{12}^{eff} is the effective diffusivity of the entire composite system. Since phase 1 for the PEM fuel cell catalyst layer is made of Pt/C particles that do not allow gas to diffuse, the lower bound must be considered for estimating the effective diffusivity.

Using the similar approach mentioned above, it can be considered that sphere made of phases 1 and 2 that is coated with phase 3, i.e. the doubly coated sphere assemblage, has the effective diffusivity of

$$D_{123}^{\text{eff}} = D_3 + \frac{3\left(1-f_3\right)D_3}{f_3 - \dfrac{3D_3}{D_3 - D_{12}^{\text{eff}}}} \tag{5.24}$$

where D_{123}^{eff} is the effective diffusivity of a three-phase composite system and D_3 is the bulk diffusivity in phase 3. The terms f_1, f_2, f_3 are the volume fractions of different phases in the coated sphere shown in Fig. 5.4. Since the solid phase does not allow reactant gas to diffuse through it, the diffusivity of the solid medium is taken to be zero. Hence, the effective diffusivity in a CL made of doubly coated spheres can be simplified as

$$D_{123}^{\text{eff}} = D_3 + \frac{3\left(1-f_3\right)D_3}{f_3 - \dfrac{3D_3}{D_3 - D_2 - \dfrac{3\left(1-f_2\right)D_2}{f_2 - 3\left(1-f_3\right)}}} \tag{5.25}$$

Referring to the PEM fuel cell catalyst layer structure shown in Fig. 5.3b, it is easily recognizable that phase 1 represents the solid Pt/C particles, phase 2 represents the ionomer membrane layer over the Pt/C particles, and phase 3 is the void space over the entire catalyst agglomerate. Since a part of void space in the catalyst layer can also be occupied with liquid water that is produced from the electrochemical reaction, phase 3 shown in Fig. 5.4 is divided into two phases, phases 3 and 4, to make the doubly coated sphere to a triply coated sphere. For a triply coated sphere assemblage system, the formulation of doubly coated sphere assemblage can further be extended by considering a continuous film of phase 3 over phase 2; hence, the effective diffusivity for such a four-phase coated sphere system becomes

$$D_{1234}^{\text{eff}} = D_4 + \frac{3\left(1-f_4\right)D_4}{f_4 - \dfrac{3D_4}{D_4 - D_{123}^{\text{eff}}}} \tag{5.26}$$

where D_{123}^{eff} represents the effective diffusivity when the phase 2 is completely covered by phase 3. In the PEM fuel cell catalyst layer, however, phase 2 is partially covered by phase 3 as shown in Fig. 5.5. Here, a random liquid water film has been considered to specify the geometry explicitly instead of a random distribution for both the liquid water and void spaces. Hence, Eq. (5.26) is modified for a coated sphere system that is partially covered by phase 3 as

$$D_{1234}^{\text{eff}} = D_4 + \frac{3\left(1-f_4\right)D_4}{f_4 - \dfrac{3D_4}{D_4 - \left(D_{123}^{\text{eff}}\right)_{\text{CL}}}} \tag{5.27}$$

where $\left(D_{123}^{\text{eff}}\right)_{\text{CL}}$ is defined as a function of the liquid water surface coverage, f_θ, as [145, 146]

$$\left(D_{123}^{\text{eff}}\right)_{\text{CL}} = f_\theta D_{123}^{\text{eff}} + (1-f_\theta) D_{12}^{\text{eff}} \tag{5.28}$$

Simplifying Eq. (5.27), the effective diffusivity for a PEM fuel cell catalyst layer is found as

$$D_{\text{CL}}^{\text{eff}} = D_g - \frac{3\left(1-f_g\right)D_g}{\dfrac{3D_g}{D_g - f_\theta D_A - (1-f_\theta)D_B} - f_g} \tag{5.29}$$

where

$$D_A = D_l - \frac{3\left(1-f_l\right)D_l}{\dfrac{3D_l}{D_l - D_m - \dfrac{3\left(1-f_m\right)D_m}{f_m - 3\left(1-f_l\right)}} - f_l} \tag{5.30}$$

$$D_B = D_m - \frac{3\,(1 - f_m)\,D_m}{3 - f_m} \tag{5.31}$$

The terms, D_g, D_l, D_m, are the diffusivities in gas phase, liquid water, and ionomer membrane, respectively, and f_g, f_l, f_m are the volume fractions of gas phase, liquid water, and ionomer membrane, respectively. Since the Knudsen effect is dominant in the catalyst layers, the bulk diffusion coefficient must be modified so that the Knudsen effect is counted while using the proposed diffusivity formula in the PEM fuel cell catalyst layers.

Conversely, the GDL is composed of solid carbon and void space only. The void space can also be partially filled with liquid water. In such case, the effective diffusivity for the partially flooded GDL of a PEM fuel cell can be calculated from the relations of flooded-GDL and dry-GDL using the relation given in Eq. (5.28). The expression for the effective diffusivity in a flooded-GDL can be written as

$$D^{\text{eff}}_{\text{flooded}-\text{GDL}} = D_g - \frac{3\,(1 - f_g)\,D_g}{\dfrac{3D_g}{D_g - D_l - \dfrac{3\,(1 - f_l)\,D_l}{f_l - 3\,(1 - f_g)}} - f_g} \tag{5.32}$$

where f_g and f_l are the volume fractions of gas phase and liquid water in the GDL, respectively; whereas for a dry electrode, it can be written as

$$D^{\text{eff}}_{\text{dry}-\text{GDL}} = D_g - \frac{3\,(1 - f_g)\,D_g}{3 - f_g} \tag{5.33}$$

It should be noted that neither the void space is uniformly distributed nor the solid phase is perfectly spherical in the GDL. Therefore, the second term in Eqs. (5.29), (5.32) and (5.33) needs to be multiplied by a geometrical factor (λ_g). The simplest bounds for λ_g can be obtained from Eq. (5.33), which can be written as

$$\frac{3 - f_g}{3(1 - f_g)} > \lambda_g \geqslant 1 \quad \text{for } f_g \neq 0 \text{ or } 1 \tag{5.34}$$

5.3 Comparisons of Effective Properties

To estimate the effective diffusivities using the proposed formulations, the binary diffusion coefficients between the different species need to be calculated first. Hence, the mathematical expressions for the binary diffusivities are described first. Then a set of estimates based on the above-mentioned formulations is provided and compared with the Bruggeman

approximation and Weiner model for the effective transport properties in the catalyst and gas diffusion layers of a PEM fuel cell.

5.3.1 Binary Diffusivity

The binary diffusion coefficient of oxygen and nitrogen (cm^2/s) is calculated using Chapman-Enskog formula because this expression provides better accuracy for low density non-polar binary mixture [127]

$$\mathscr{D}_{O_2-N_2} = 0.00188 \frac{T^{3/2}\left(\frac{1}{\hat{M}_{O_2}} + \frac{1}{\hat{M}_{N_2}}\right)^{1/2}}{P\lambda^2_{O_2-N_2}\Omega_{D,O_2-N_2}} \tag{5.35}$$

where $\hat{M}_{O_2}$ and $\hat{M}_{N_2}$ are the molecular weights of oxygen and nitrogen, respectively. The term, Ω_{D,O_2-N_2}, is a dimensionless function of the temperature and of the intermolecular potential field of one molecule of O_2 and one molecule of N_2, $\lambda_{O_2-N_2}$ is the Lennard-Jones parameter, and temperature, T, is in Kelvin. The binary diffusion coefficient of oxygen and water vapor in cm^2/s is calculated from the critical pressure and temperature of oxygen ($T^{cr}_{O_2}$ and $P^{cr}_{O_2}$) and water vapor ($T^{cr}_{H_2O}$ and $P^{cr}_{H_2O}$) using the Slattery-Bird equation [107]

$$P\mathscr{D}_{O_2-H_2O} = 0.000364\left(\frac{T}{\sqrt{T^{cr}_{O_2}T^{cr}_{H_2O}}}\right)^{2.334}\left(P^{cr}_{O_2}P^{cr}_{H_2O}\right)^{1/3}\left(T^{cr}_{O_2}T^{cr}_{H_2O}\right)^{5/12}\left(\frac{1}{\hat{M}_{O_2}} + \frac{1}{\hat{M}_{H_2O}}\right)^{1/2} \tag{5.36}$$

where the temperatures are in Kelvin and the pressures are in atm.

It is also noted that the binary diffusion coefficient in cm^2/s for oxygen in the liquid water ($H_2O_{(l)}$) can be obtained using Wilke-Chang correlation, as this correlation is for diffusivities of dilute, binary mixtures of non-electrolytes in liquids [127]

$$\mathscr{D}_{O_2-H_2O_{(l)}} = \frac{7.4\times10^{-8}\left(\Phi_{H_2O}\hat{M}_{H_2O}\right)^{1/2}T}{\mu_{H_2O_{(l)}}(V_{O_2})^{0.6}} \tag{5.37}$$

where $\mu_{H_2O_{(l)}}$ is the dynamic viscosity of liquid water in cP (1 cP = 10^{-3} Pa·s), Φ_{H_2O} is the 'association' parameter of H_2O, V_{O_2} is the molar volume of the oxygen in $cm^3/g{\cdot}mol$ at its normal boiling point. The value of Φ_{H_2O} for water was originally reported as 2.6, later it was found using the empirical best fit as 2.26. Therefore, in the present investigation, 2.26 is used instead of 2.6. Since the dynamic viscosity of H_2O is a function of temperature, a polynomial fitting of $\mu_{H_2O_{(l)}}$, as a function of T, is used. A plot of water viscosity data in

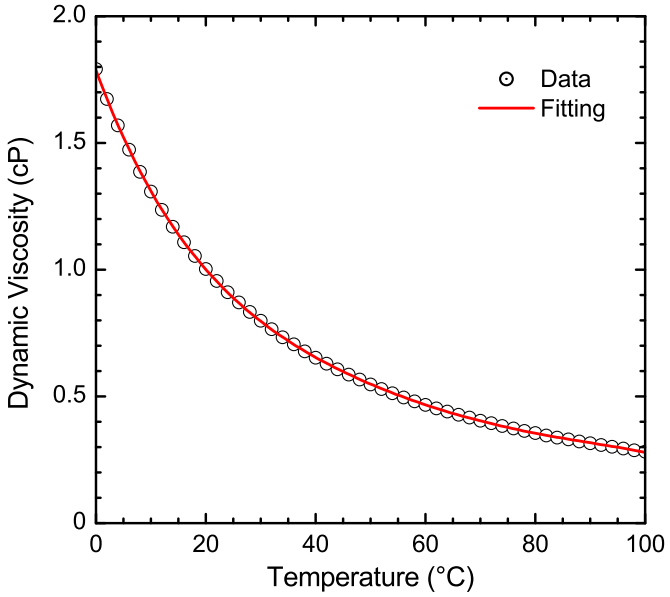

Figure 5.6: Polynomial fitting of water viscosity as a function of temperature. The symbols represent data points and the line depicts best-fitted correlation as given in Eq. (5.38).

cP as a function of temperature in ℃ is shown in Fig. 5.6, while the polynomial function is found with a coefficient of determination of 0.99998 as

$$\mu_{\mathrm{H_2O}_{(l)}} = 1.786 - 0.059T + 1.265\times10^{-3}T^2 - 1.709\times10^{-5}T^3 + 1.258\times10^{-7}T^4 - 3.783\times10^{-10}T^5 \tag{5.38}$$

The diffusion coefficient (cm^2/s) for oxygen in Nafion membrane is calculated from the following relation [6]:

$$\mathscr{D}_{\mathrm{O_2}-m} = -1.0664\times10^{-5} + 9.0215\times10^{-6}\exp\left(\frac{T-273.15}{106.65}\right) \tag{5.39}$$

where the temperature, T, is in Kelvin. Values for parameters used in the above equations are listed in Table 5.1 with appropriate units.

5.3.2 Effective Protonic Conductivity in Catalyst Layer

Figure 5.7 shows the comparison of the effective protonic conductivities in the CL of a PEM fuel cell as a function of catalyst layer porosity that are calculated using the formulation developed in this thesis and the Bruggeman approximation. Two different combinations of solid Pt/C particles and ionomer membrane volume fractions in the solid phase of CL, namely, 70% of Pt/C and 30% of ionomer membrane, and 60% of Pt/C

Table 5.1: Parameter used in the calculations of diffusion coefficients at 3 atm and 80 ℃

Parameter	Value
Ω_{D,O_2-N_2}	0.8827
$\lambda_{O_2-N_2}$	3.6325
$T^{cr}_{O_2}$ (K)	154.4
$P^{cr}_{O_2}$ (atm)	49.7
$T^{cr}_{H_2O}$ (K)	647.15
$P^{cr}_{H_2O}$ (atm)	217.7
μ_{H_2O} (cP)	0.355
V_{O_2} (cm^3/g·mol)	25.6

and 40% of ionomer membrane, were considered as indicated in the legend as f_s/f_m ratio. Here, both the lines represent the Bruggeman correlation results, while the symbols depict corresponding results obtained using the expression developed in this study. The effective protonic conductivity of Bruggeman approximation is estimated using the following correlation, referred in Fig. 5.7 as Bruggeman correlation

$$\sigma_m^{\text{eff}} = \sigma_m \left(f_m(1-\epsilon)\right)^{1.5} \tag{5.40}$$

All other parameters used in the calculation are taken from Refs. [7, 122] that are listed in Table 5.2. As observed at low porosities ($\epsilon < 0.2$), the present formulation overestimates the effective conductivity compared to what has been estimated using the BA. Whereas for moderate porosities (e.g. $0.2 < \epsilon < 0.4$), the present results show a better agreement, particularly for the case when the fraction of membrane in the CL is higher. For higher porosities (e.g., $\epsilon > 0.5$), an underestimation has been observed for both cases, while the case of lower fraction of membrane provides less discrepancy with the Bruggeman correlation. Hence, this variation can be attributed to the multi-phase effect, which is more prominent in the present formulation than the Bruggeman correlation. For instance, the present model results merging toward the Bruggeman's results when $\epsilon \to 1.0$ and the lower membrane fraction case is merging faster implies that the membrane phase has less effect at higher porosity. Clearly for a range of porosity ($0.2 < \epsilon < 0.6$) that is applicable for PEM fuel cells, the present formulation would be more useful than widely used Bruggeman approximation as the present formulation is directly derived considering the agglomerate

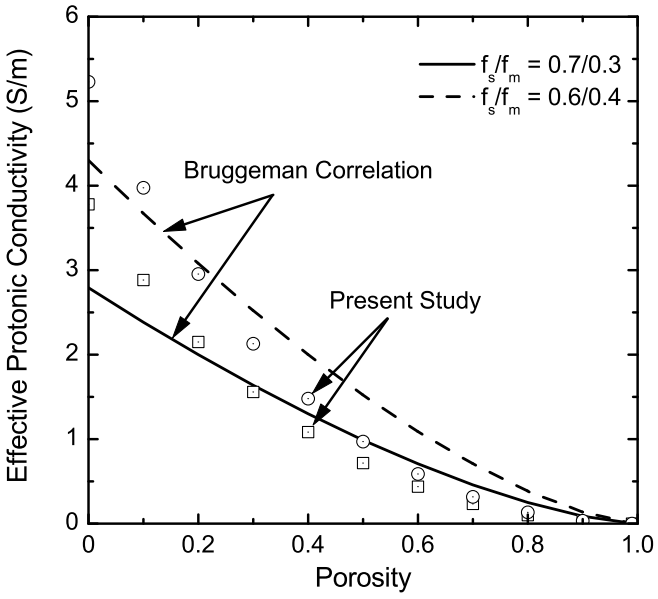

Figure 5.7: Comparison of the effective protonic conductivity in the catalyst layer of a PEM fuel cell with the Bruggeman correlation. Lines represent the Bruggeman correlation results, while the symbols depict the present model results for two combinations of Pt/C and membrane volume fractions.

Table 5.2: Parameter values used in the model calculation of effective properties

Parameter	Value
T (K)	323
D_g (cm^2/s)	2.585×10^{-1}
D_l (cm^2/s)	3.98×10^{-5}
D_m (cm^2/s)	3.73×10^{-6}
f_l	0.1
f_s/f_m	0.7/0.3 and 0.6/0.4
f_θ	0.5
λ_m	1.0
λ_s	1.0
σ_m (S/cm)	0.17
σ_s (S/cm)	7.27×10^{2}

geometry. Furthermore, this comparison shows that the proposed formulation is capable of predicting the effective protonic conductivity that can be estimated using the Bruggeman correlation, while the Bruggeman correlation is an empirical correlation and the present expression is derived from the fundamental mathematical formulation.

5.3.3 Effective Electronic Conductivity

Figure 5.8 depicts a comparison of the effective electronic conductivity in the catalyst layer of a PEM fuel cell with the BA results as a function of catalyst layer porosity. Similar to the effective protonic conductivity, two different combinations of ionomer membrane and solid Pt/C fractions in the catalyst layer were considered as indicated in the legend. Here also an overestimation of the effective electronic conductivity has been observed compared to the Bruggeman's result over the entire range of porosity. No matter what percentages of solid Pt/C and ionomer membrane are present in a catalyst layer, the present formulation provides slightly higher effective electronic conductivity for the catalyst layer of PEM fuel cell. This might be acceptable, as the membrane conductivity is performance-limiting factor for the PEM fuel cell and the electronic conductivity has very little influence on the performance of a cell. Further, the results presented in Fig. 5.8 for the case when $\lambda_s = 1$, hence the maximum limit for the effective electronic conductivities. However, practically the effective electronic conductivities will be lower than the values shown in Fig. 5.8 due to irregular solid phase geometry and ionomer layer over the Pt/C phase.

Conversely, the effective electronic conductivity in the GDL of a PEM fuel cell shows an excellent agreement with the Bruggeman correlation results as shown in Fig. 5.9. Clearly, the multi-phase effect is insignificant in a dry-GDL as it has only solid carbon phase. Therefore, both the present formulation and the Bruggeman correlation show identical behavior. However, for higher porosity values ($\epsilon > 0.4$), the present model over-predicts slightly. Here, the overestimation is considerably less than what is observed for the catalyst layer's effective conductivities. This is reasonable as the CL is composed of solid Pt/C particles, ionomer membrane, and void space, while the GDL only consists of solid carbon and void space. For a similar porosity, the GDL consists of more solid carbon phase than the CL, which results in higher electronic conductivity. Therefore, it can be claimed that the effective electronic conductivity formulation derived in this thesis research would be more accurate while we have higher fraction of solid phase in a composite system. Conversely, the effective protonic conductivity formulation will provide more accurate results while the CL consists of higher fraction of ionomer membrane.

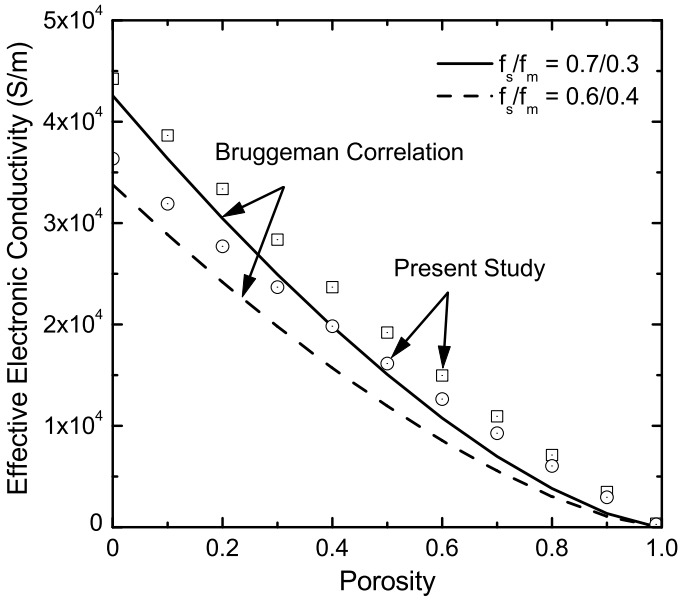

Figure 5.8: Comparison of the catalyst layer effective electronic conductivity with the Bruggeman correlation. The lines represent the Bruggeman correlation results, while the symbols depict the present model results.

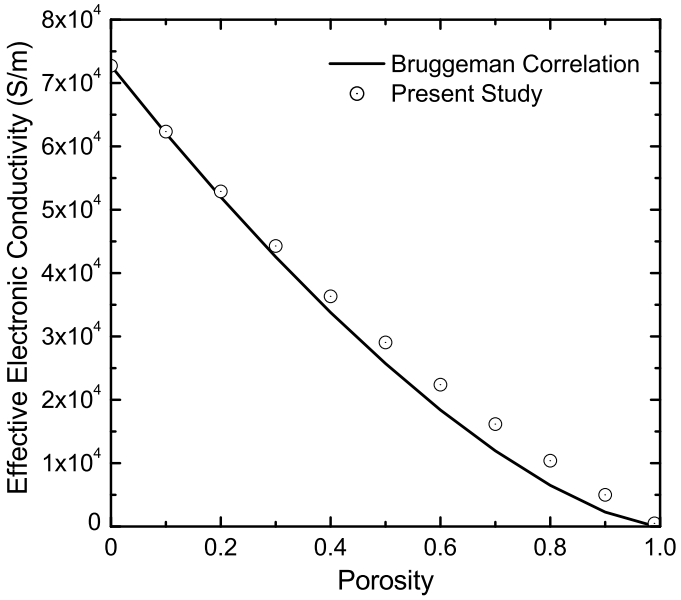

Figure 5.9: Comparison of the proposed effective electronic conductivity in the gas diffusion layer of a PEM fuel cell with the Bruggeman correlation.

5.3.4 Effective Diffusivity in Catalyst Layer

For the effective diffusivity in the catalyst layer of a PEM fuel cell, several empirical models are available. The most popular and widely used for the individual effective diffusivity is once again Bruggeman's approximation. Here, the individual effective diffusivity represents the diffusion coefficient of a reactant gas in a phase of a multi-phase composite system, for example, effective oxygen diffusivity in ionomer membrane phase of PEM fuel cell catalyst layer. Conversely, the overall effective diffusivity represents the total diffusivity of a reactant gas in a composite layer of PEM fuel cell, for example, effective oxygen diffusivity in the CL or GDL of a PEM fuel cell. If a layer consists of more than one phase then the overall effective diffusivity has contributions from the individual effective diffusivities within that layer. Therefore, the Bruggeman approximation of the individual effective diffusivity needs to be further modified based on the volume fractions of various phases present in a composite (multi-phase) layer using other approaches. Several approaches have been used in literature based on the Wiener's series and parallel models for the composite system. For instance, it can be either a series model [6, 82, 147, 148] or a parallel model [33, 147, 148] or a mixed model [122, 147, 148]. In the following paragraphs, a comprehensive comparison for the effective diffusivity of present model predictions with the above-mentioned models has been provided.

Figure 5.10 represents a comparison between the effective oxygen diffusivities in the catalyst layer of a PEM fuel cell that are calculated using the present effective diffusivity expression and a series model [6, 82, 147, 148]. The solid phase of the catalyst layer is considered as made of 70% of Pt/C and 30% ionomer membrane. All other parameters are listed in Table 5.2. Here, the line represents the result obtained from the series model, while the symbols show the result estimated using the expression derived in this study. Surprisingly, a complete miss-match has been observed with the series model that is almost several orders of magnitude. This disagreement probably arises due to the assumption usually made in the mathematical formulation of series model that various phases in a composite system were lumped in a layer one after another. For instance, in the cathode catalyst layer of a PEM fuel cell, layers of Pt/C, ionomer membrane, liquid water, and gas phase are lumped in a layer so that each layer of a phase is covered continuously by another phase. Therefore, neither the Pt/C layer nor the ionomer membrane layer has direct contact with the gas diffusion layer, while the present model does not have such continuous film of liquid water. Since both layers are separated from void spaces by the liquid water film in a series model, the reactant gas needs to be dissolved in liquid water to come contact with Pt/C and ionomer membrane. The solubility of oxygen in liquid water is very low, which gives diffusivity of oxygen in liquid water several orders of magnitude lower than that of the void space. Hence, the series model formulation predicts

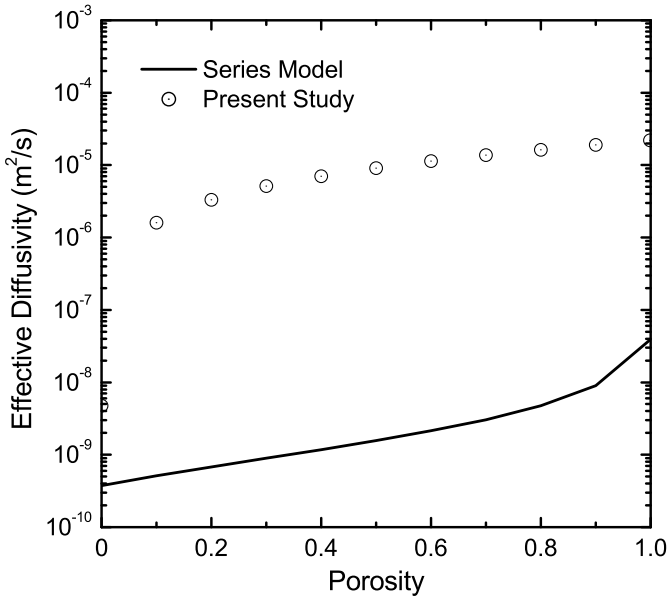

Figure 5.10: Comparison of the proposed effective oxygen diffusivity in the catalyst layer of a PEM fuel cell with the series model for 70% of Pt/C and 30% of ionomer membrane in the catalyst layer.

the effective oxygen diffusivity in the order of oxygen diffusivity in liquid water that is about 3 to 4 orders lower than the oxygen diffusivity in gas phase inside the void space. Nonetheless, this disagreement can easily be attributed to the Weiner series model used in Refs. [6, 82, 147, 148] and 100% surface coverage for the liquid water used in Ref. [82]. Conversely, the surface coverage of the liquid water has been considered less than unity in the proposed formulation. Therefore, the gas phase has direct contact with the membrane phase that allows faster reactant diffusion than the Weiner series model.

Although several orders of magnitude differences have been observed between the present model predictions and the results of a series model, an excellent agreement has been found with a parallel model formulation [33, 147, 148] as shown in Fig. 5.11. Here, a comparison between the effective oxygen diffusivities in the catalyst layer of a PEM fuel cell is shown that are estimated using the expression developed in this study and from a parallel model for 70% of Pt/C and 30% ionomer membrane in the solid phase of a catalyst layer. In this figure, the line represents the parallel model result, while the symbols depict the prediction of proposed model. For high porosity values ($\epsilon > 0.7$), the present results show very good agreement, although for intermediate porosity values (e.g. $0.2 < \epsilon < 0.7$) some differences between the predictions have been observed. It should also be noted that in the parallel model, the effective diffusivity is calculated by applying Wiener's parallel model followed by the Bruggeman approximation [33]; while in the series

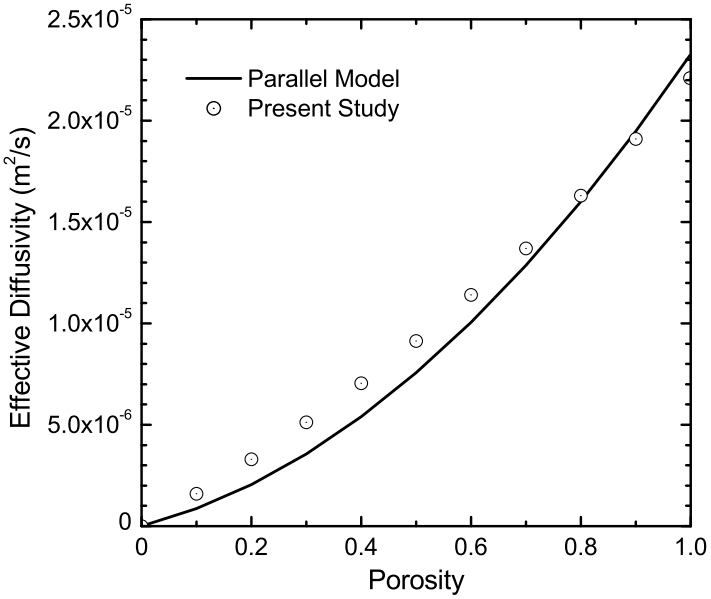

Figure 5.11: Comparison of the proposed effective oxygen diffusivity in the catalyst layer of a PEM fuel cell with the estimates based on a parallel model for the composition of 70% of Pt/C and 30% of ionomer membrane.

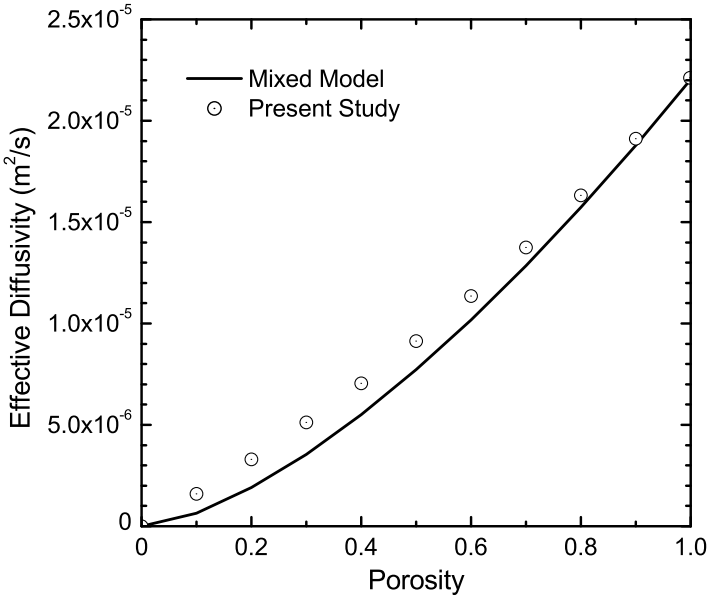

Figure 5.12: Comparison of the effective oxygen diffusivity in the catalyst layer of a PEM fuel cell with the mixed model prediction for the composition of 70% of Pt/C and 30% of ionomer membrane.

model, the effective diffusivity is calculated using the Bruggeman approximation followed by Wiener's series model [82]. Hence, it seems that the Wiener parallel model is better than the Wiener series model for the effective diffusivities in PEM fuel cell. Like the effective conductivity formulation, comparison in Fig. 5.11 nonetheless shows the predictive abilities of the proposed effective diffusivity formulation.

A comparison between the effective oxygen diffusivities that are calculated using the proposed formulation and a mixed model [122, 147, 148] is shown in Fig. 5.12. Like the comparison with the parallel model, the present model results also show a good agreement with the mixed model results, particularly for higher porosity values. At low porosities, however, a slight overestimation has been observed. Nonetheless, this comparison once again provides a clear idea of how well the present formulation can predict the effective properties. It should also be noted that the mixed model formulation is a combination of both the Bruggeman approximation and Wiener's mixed model that is based on the empirical correlation, whereas the present model is entirely a mathematical formulation.

5.4 Relative Permeability

The phase relative permeability is defined as the ratio of the intrinsic permeability for the phase at a given saturation to the total intrinsic permeability of a porous medium. Physically, the relative permeability of a phase describes the extent to which one phase is hindered by others in pore spaces, and hence it can be formulated as a function of liquid saturation. The simplest approach is to consider the relative permeability as a linear function of saturation [56] and the most used model is the cubical function of saturation [54, 114].

Several other relative permeability models are available in literature, which are summarized in Table 5.3 in terms of wetting phase saturation [149, 150]. Since the cubic relation is most widely used for the PEM fuel cell GDLs and CCLs, the following empirical correlation is used for the gas phase relative permeability [114]

$$k_{rg} = {s_g}^3 = (1 - s_l)^3 \tag{5.41}$$

where s_l is the liquid saturation, defined as the ratio between the volume of liquid water to the pore volume. Similarly, the liquid phase relative permeability in the porous electrode and catalyst layer is estimated using the following empirical correlation [114]

$$k_{rl} = {s_l}^3 \tag{5.42}$$

Table 5.3: Summary of the relative permeability models

Models	Relative permeability (non-wetting phase)	Relative permeability (wetting phase)
Corey model	$(1-s_l)^2(1-s_l^2)$	s_l^4
Brooks-Corey model	$(1-s_l^2)(1-s_l^{2+\lambda/\lambda})$	$s_l^{2+3\lambda/\lambda}$
van Genuchten model	$(1-s_l)^{1/3}(1-s_l^{1/m})^{2m}$	$s_l^{0.5}(1-(1-s_l^{1/m})^m)^2$

λ represents the pore size distribution and m is a fitting parameter.

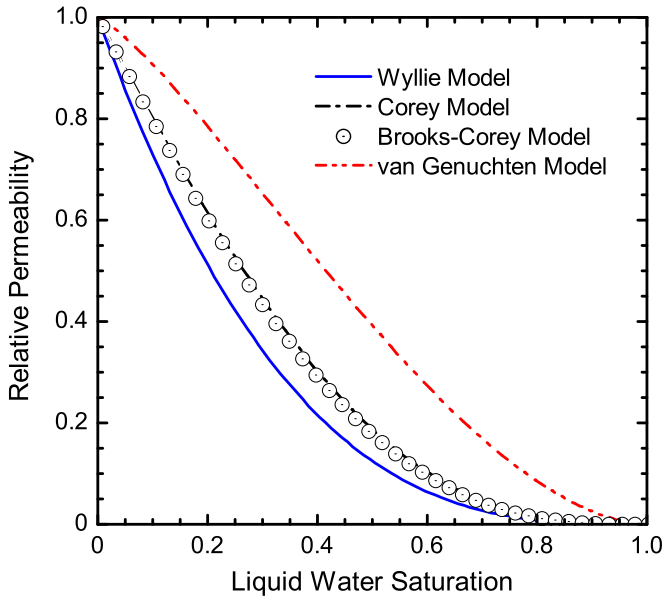

Figure 5.13: Comparison of the relative permeability models.

The cubical model (also known as Wyllie model) has often been criticized [151, 152], while we did not find any significant difference between the cubical model and the Corey and Brooks-Corey models. A plot of these models along with the van Genuchten model is shown in Fig. 5.13, which is showing the gas phase relative permeability with the liquid water saturation. The cubical and Corey models are independent of materials and are only the function of liquid saturation. While the Brooks-Corey and van Genuchten models are material dependent. Here E-Tek Cloth-A has been considered with the pore size distribution of 1.59 and the fitting parameter for the van Genuchten model is taken as

0.7262 [151]. Clearly the Corey model and the Brooks-Corey model are identical, though one is material dependent and other is not. If we compare the Corey and Brooks-Corey models with the cubical model, we can easily neglect the variation observed in Fig. 5.13. Conversely, if we criticize the cubical model, we have to criticize the Corey and Brooks-Corey model as well. As seen from Fig. 5.13, there is a significant difference between both the Corey models with the van Genuchten model and it is still not clear which model would be a good fit for the PEM fuel cell. Hence, the use of cubical model in this study is reasonable.

5.5 Capillary Pressure

The relative permeabilities are also function of capillary pressure, while the capillary pressure is the difference between non-wetting and wetting phase pressures [52, 55, 63, 117, 152]. Hence, it can be written as

$$P_c = P_{nw} - P_w = \begin{cases} P_g - P_l & \text{if } \theta_{c,w} < 90^\circ \Rightarrow \text{Hydrophilic} \\ P_l - P_g & \text{if } \theta_{c,nw} > 90^\circ \Rightarrow \text{Hydrophobic} \end{cases} \tag{5.43}$$

where P_{nw} and P_w are the non-wetting and wetting phase pressures, respectively, and $\theta_{c,w}$ and $\theta_{c,nw}$ are the wetting and non-wetting phase contact angles (in a 0 to 180° scale), respectively. To use the above-mentioned definition of capillary pressure, the contact angle has to be chosen carefully.

The capillary pressure is always a function of wetting phase contact angle, while the typical definition of hydrophilic and hydrophobic surfaces is based on both wetting and non-wetting phase contact angles. In literature, it has been observed that the capillary pressure is defined according to Eq. (5.43) and using the both wetting and non-wetting phase contact angles [74, 152, 153], which will yield an erroneous result. It is, however, possible to avoid such confusion by defining the capillary pressure that is irrespective to the wetting and non-wetting phases. Hence, the capillary pressure is defined as [52, 55, 63, 117, 154]

$$P_c = P_g - P_l \tag{5.44}$$

Eq. (5.44) is valid for both the hydrophilic and hydrophobic surfaces when the liquid phase contact angle is used for the capillary pressure instead of wetting phase contact angle. Hence, the capillary pressure as a function of liquid phase contact angle is defined

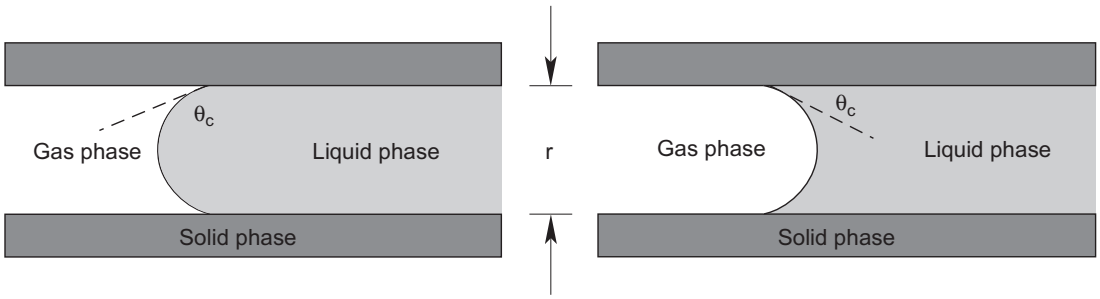

(a) Hydrophobic Pore (b) Hydrophilic Pore

Figure 5.14: Cylindrical pore having (a) hydrophobic and (b) hydrophilic characteristics.

as [155]

$$P_c = \frac{2\gamma \cos\theta_c}{r} \tag{5.45}$$

This equation is based on the assumption that the gravitational and viscous forces in the GDL and CCL of a PEM fuel cell are relatively small compared to capillary forces. Here γ is the surface tension between the gas phase and liquid phase, θ_c is the contact angle of liquid phase, and r is the pore radius. The contact angle, θ_c, is defined as the angle between the liquid-gas interface and the solid surface measured at the triple point where all three phases intersect. If the pore material is hydrophilic, the contact angle is less than 90° and P_c is positive; hydrophobic materials have a negative P_c and the contact angle greater than 90°, as illustrated in Fig. 5.14.

For the two-phase flow in a porous medium, the capillary pressure can be modeled by the following empirical correlation [156]:

$$P_c = \gamma \cos\theta_c \left(\frac{\epsilon}{K}\right)^{0.5} F(s_l) \tag{5.46}$$

The term $F(s_l)$ is the Leverett function that represents the dimensionless capillary pressure as a function of the liquid saturation, and the term $(\epsilon/K)^{0.5}$ is characteristic of the pore length scale. For the hydrophilic and hydrophobic mediums, the Leverett functions are given as

$$F(s_l) = \begin{cases} 1.417(1-s_l) - 2.120(1-s_l)^2 + 1.263(1-s_l)^3 & \text{if } \theta_c < 90^\circ \\ 1.417 s_l - 2.120 {s_l}^2 + 1.263 {s_l}^3 & \text{if } \theta_c > 90^\circ \end{cases} \tag{5.47}$$

The Leverett function was proposed by Udell [157] for packed beds that only considers

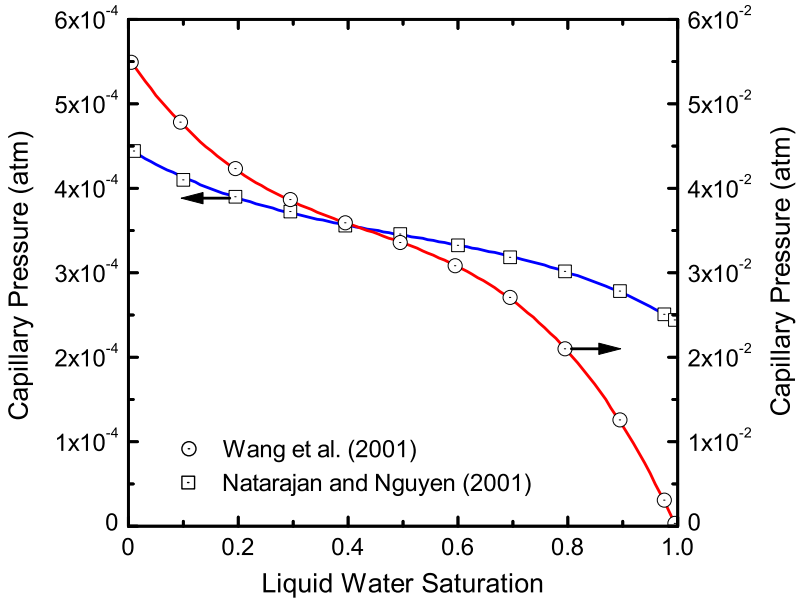

Figure 5.15: Variation of capillary pressure with liquid (water) saturation used by Natarajan and Nguyen [59] and Wang *et al.* [54]. The symbols represent the data taken from literature and the lines are indicating estimated best-fitted correlation as given in Eq. (5.48).

the influence of porosity and permeability of a porous medium, while ignoring the effect of detailed pore morphology. This approach has often been criticized [151, 152] since the applicability of Leverett function to the GDL and CCL of a PEM fuel cell requires experimental verification, which is still absent in the literature. It still holds certain merits for PEM fuel cell [158]. Several other empirical constitutive equations are also found in the literature that relate the liquid saturation, s_l, to the capillary pressure, P_c [59, 113, 159, 160]. Among these empirical equations, Natarajan and Nguyen [59] provided the expression based on fitting the model to experimental fuel cell data, while the Leverett's correlation in Wang *et al.* [54] was based on experimental data on porous media like soil. The profile of the capillary pressure as a function saturation in the GDL of a PEM fuel cell used by Natarajan and Nguyen [59] and Wang *et al.* [54] are shown in Fig. 5.15. Here, the symbols are the experimental data, while the lines represent the best-fitted correlation. The correlations between the capillary pressure in atm and the liquid water saturation are found as

$$P_c = \begin{cases} (-3.623{s_l}^3 + 5.428{s_l}^2 - 3.849s_l + 4.465) \times 10^{-4} & \text{for Natarajan and Nguyen [59]} \\ -0.126{s_l}^3 + 0.165{s_l}^2 - 0.095s_l + 0.055 & \text{for Wang } et\ al. \text{ [54]} \end{cases} \tag{5.48}$$

Clearly, these correlations are completely different than the Leverett function. In addition,

these correlations do not agree each other. Since the Leverett function has been widely used for the PEM fuel cell, this thesis adopts the Leverett function to be consistent with the majority of the PEM fuel cell literatures.

5.6 Summary

In this chapter, a unique set of expressions for the effective protonic conductivity, electronic conductivity, and oxygen diffusivity in both the catalyst and gas diffusion layers of a PEM fuel cell, which has similar mathematical formulation, has been derived. The mathematical expressions for the effective transport properties in a PEM fuel cell are compared with results available in literature. Also the relative permeability and capillary pressure are described and the widely used correlations are provided. These correlations are also compared with various empirical correlations that are available in fuel cell literatures.

In summary, the mathematical expressions for the effective transport properties are quite capable of predicting reasonably accurate and comparable results. Further, for the effective electronic conductivity, the higher the volume fraction of Pt/C in a catalyst layer, the better the model's prediction has been found. Similar statement can be given for the effective protonic conductivity; a higher membrane fraction will provide better model predictions. Conversely, if the catalyst layer has high porosity with less water saturation, the proposed model is found to be in better agreement with the models that used both the Bruggeman and Weiner type of correlations together for the effective diffusivity. While the Bruggeman correlation is purely an empirical correlation and is valid for single-phase porous medium, the proposed formulation has its physical and mathematical origins and is valid for multi-phase porous medium. Furthermore, the complexities involved in using the Bruggeman approximation and Weiner models together can be avoided by employing the effective diffusivity formulation developed in this thesis [161]. Hence, the present expressions are recommended for the numerical modeling of PEM fuel cells. Although these expressions are derived focusing on the PEM fuel cell, the present formulations for the effective transport properties are equally applicable for other hydrogen fuel cells, porous media flow, and multi-phase composite systems.

Chapter 6

Analytical Model

This chapter describes analytical approaches to performance optimization and liquid water transport in the catalyst layer. The analytical model of performance optimization is developed using an exact solution of activation overpotential, while the liquid water transport model is developed using the conservation equations for the liquid phase in the cathode catalyst layer of a PEM fuel cell. It worthwhile to note that the models presented in this chapter are based on the published articles.[1,2,3]

6.1 Analytical Approach to Performance Optimization

To optimize the PEM fuel cell performance, it is required to estimate the reversible cell voltage and various losses. Among the various losses, ohmic overpotential and activation overpotential are the most significant in the typical operating range of a PEM fuel cell. The formulation of ohmic overpotential is well established and does not require complicated mathematical formulation or numerical computation for fully hydrated membranes [80, 82]. It is mostly dependent on the ohmic resistance of the cell material with the exception of the membrane resistance, where the amount of water content might change the effective ohmic resistance in some instances. Nonetheless, using these ohmic overpotential formulations, one can optimize the ohmic overpotential; a part of the total polarization of PEM fuel cell except the activation overpotential. The activation overpotential formulation, a significant part of the cell voltage losses, is still elusive. Therefore, a simple model for studying cathode

[1]P.K. Das, X. Li, and Z.S. Liu. *Journal of Electroanalytical Chemistry*, 604:72–90, 2007.

[2]P.K. Das, X. Li, and Z.S. Liu, *Proc. of ASME 2009 Seventh International Fuel Cell Science, Engineering and Technology Conference*, Paper ID 85189, Newport Beach, California, June 2009.

[3]P.K. Das, X. Li, and Z.S. Liu, *International Journal of Hydrogen Energy*, 35:2403–2416, 2010.

activation losses in PEM fuel cell and its optimization has been proposed. This model has been developed using a combination of analytical solution and empirical formula, which includes:

- An analytical expression for the activation overpotential and its comparison with the various data available in literature that covers empirical results, experimental data, and numerical predictions.
- The composition and performance optimization modeling of the catalyst layer of PEM fuel cell, where Pt-loading, catalyst layer composition, and thickness have been optimized.

In the first part, a simple and efficient analytical solution for estimating cathode activation overpotential in the PEM fuel cells is derived that can be used as a benchmark solution to validate numerical models. In the second part, all design parameters have incorporated in the model for focusing on the optimization of CCL including Nafion content (%wt of Nafion), platinum content (%wt of platinum), platinum loading (mg/cm^2), void fraction, and catalyst layer thickness. The importance of this analytical model is that it can be used to model the performance of fuel cell system as well as it will be a useful tool for optimizing the structures of membrane electrode assembly, catalyst layer parameters, and operating parameters. Investigation has also been conducted for the optimum conditions for Nafion content, Pt-loading as well as effect of the operating conditions on the performance of PEM fuel cell. In the following sections, the analytical model to estimate the activation overpotential and how the ohmic overpotential and reversible cell potential are estimated have been described; while the performance optimization results are reported in Chapter 8.

6.2 Estimation of Activation Overpotential

In the analytical formulation of activation overpotential, the cathode catalyst layer is assumed as a macro-homogeneous mixture of Nafion membrane, supported catalyst and void space. The volume fractions of these components can be varied as can the effective surface area of catalyst that can be characterized by different loadings and catalyst types. Since only the catalyst layer is needed to be considered, the governing equations stated in Chapter 3 are simplified for single-phase gaseous reactants. It should be noted that the anode activation overpotential is negligible compared to the cathode activation overpotential [6, 24, 33]. Hence, the cathode activation overpotential will be referred as the activation overpotential neglecting the anodic overpotential and the details of the activation overpotential derivation are provided in the following sections.

6.2.1 Governing Equations

Assuming the fuel cell is operating in steady-state condition and the membrane is fully humidified, the conservation equations for the reactants, electron, and proton in the CCL are simplified as follows:

$$\nabla \cdot \left(D_i^{\text{eff}} \nabla c_i\right) = -\left[\frac{s_i}{n\mathscr{F}}\right] 4A_v \mathscr{F} \mathcal{R}_{c,\text{red}} \tag{6.1}$$

$$\nabla \cdot \left(\sigma_s^{\text{eff}} \nabla \Phi_s\right) = -4A_v \mathscr{F} \mathcal{R}_{c,\text{red}} \tag{6.2}$$

$$\nabla \cdot \left(\sigma_m^{\text{eff}} \nabla \Phi_m\right) = 4A_v \mathscr{F} \mathcal{R}_{c,\text{red}} \tag{6.3}$$

where the subscript i in represents the reactant species and the superscript "eff" represents the effective transport coefficients. Here s_i is a constant equals 2 for H_2, and -1 for O_2, respectively, n (=4) is the number of electrons transferred in the cathodic reaction (Eq. (1.2)), and c denotes the concentration of gas species. The terms Φ_s and Φ_m are the electrical potential in the solid electrode and the membrane electrolyte, respectively, σ_s^{eff} and σ_m^{eff} are the effective conductivities of the solid catalyst and the membrane, respectively, and $\mathcal{R}_{c,\text{red}}$ is the rate of electrochemical reaction that is given by the Butler-Volmer equation in Eq. (4.68).

6.2.2 One-dimensional Formulation

The schematic of a macro-homogeneous CCL is shown in Fig. 6.1 along with the spatial coordinate x with the positive direction pointing from the membrane/CCL interface toward the GDL. Since the thickness of the cathode catalyst layer is almost 4 to 5 order of magnitude smaller than the cell height, therefore Eqs. (6.1)–(6.3) can be simplified as a first approximation in one dimension for constant $D_{\text{O}_2}^{\text{eff}}$, σ_s^{eff}, and σ_m^{eff} as

$$\frac{d^2 c_{\text{O}_2}}{dx^2} = \frac{A_v \mathcal{R}_{c,\text{red}}}{D_{\text{O}_2}^{\text{eff}}} \tag{6.4}$$

$$\frac{d^2 \Phi_s}{dx^2} = -\frac{4A_v \mathscr{F} \mathcal{R}_{c,\text{red}}}{\sigma_s^{\text{eff}}} \tag{6.5}$$

$$\frac{d^2 \Phi_m}{dx^2} = \frac{4A_v \mathscr{F} \mathcal{R}_{c,\text{red}}}{\sigma_m^{\text{eff}}} \tag{6.6}$$

For simplicity the effective properties are calculated using the Bruggemann correction from the bulk values according to the following correlations [6, 82, 122]:

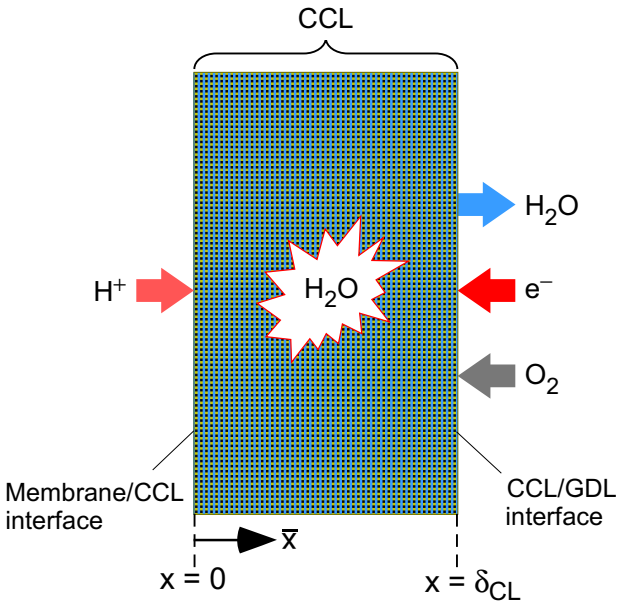

Figure 6.1: Sketch of a cathode catalyst layer (CCL) along with the spatial coordinate x. The arrows are indicating the directions of species transports.

$$D_i^{\text{eff}} = D_i \epsilon^{1.5} \tag{6.7}$$

$$\sigma_s^{\text{eff}} = \sigma_s f_s^{1.5} \tag{6.8}$$

$$\sigma_m^{\text{eff}} = \sigma_m \left(\epsilon f_m\right)^{1.5} \tag{6.9}$$

Here ϵ is the void fraction, f_m denotes the membrane volume fraction in the catalyst layer void region, and D_i, σ_s and σ_m are the bulk diffusivity, bulk electronic conductivity, and bulk membrane conductivity, respectively. The catalyst layer void fraction is calculated from the known values of catalyst loading (f_{Pt}), the catalyst layer thickness (δ_{CL}) and the densities of platinum and carbon black (ρ_{Pt} and ρ_{C}) using Eq. (4.18). However, it is always recommended to use the effective property expressions provided in Chapter 5.

Defining the potential drop across the CCL as $\eta_c = \Phi_m - \Phi_s$ and combining Eq. (6.2) and Eq. (6.3), it can be written as

$$\frac{d^2\eta_c}{dx^2} = \frac{d^2\Phi_m}{dx^2} - \frac{d^2\Phi_s}{dx^2} \tag{6.10}$$

also combining Eqs. (6.5) and (6.6) yields

$$\sigma_s^{\text{eff}} \frac{d^2\Phi_m}{dx^2} = -\sigma_m^{\text{eff}} \frac{d^2\Phi_m}{dx^2} \tag{6.11}$$

Table 6.1: Catalyst surface areas as a function of the fraction of Pt-catalyst [162]

Catalyst type	%Pt	$A_s(\mathrm{m}^2/\mathrm{g})$
	10	140
	20	112
Pt on	30	88
Carbon black	40	72
	60	32
	80	11
Pt black	100	28

Typically, the electrical conductivity in the conducting solid (σ_s^{eff}) is several orders of magnitude larger than the conductivity of the membrane phase (σ_m^{eff}). Therefore, it can be immediately recognized from the above equation that the second order derivative of the potential in the solid phase will be very small compared to the second order derivative of the membrane phase potential. Hence, using Eq. (4.68) in Eq. (6.10) yields

$$\frac{d^2\eta_c}{dx^2} = \frac{A_v J_0^{\mathrm{O}_2}}{\sigma_m^{\text{eff}}} \left[\frac{c_{\mathrm{O}_2}}{c_{\mathrm{O}_2,\text{ref}}}\right]^{\gamma_c} \left\{\exp\left(-\frac{\alpha_a n \mathscr{F} \eta_c}{\mathscr{R} T}\right) - \exp\left(\frac{\alpha_c n \mathscr{F} \eta_c}{\mathscr{R} T}\right)\right\} \tag{6.12}$$

where c_{O_2} represents the oxygen concentration in the cathode catalyst layer. The reference current density ($J_0^{\mathrm{O}_2}$) is calculated using the experimental data of Parthasarathy *et al.* [13] (given in Eq. (4.66)) and the reference oxygen concentration, $c_{\mathrm{O}_2,\text{ref}}$ corresponding to $J_0^{\mathrm{O}_2}$ is taken as 1.2 mol/m^3 [13, 82]. The specific reaction surface (A_v) is estimated from the catalyst mass loading per unit area of cathode (m_{Pt}), catalyst surface area per unit mass of the catalyst (A_s), and catalyst layer thickness (δ_{CL}) using Eq. (4.10). The catalyst surface area per unit mass of the catalyst is also a function of the fraction of the Pt-catalyst on the carbon support (%Pt) and the typical values of the catalyst surface area as a function of the amount of Pt-loading are listed in Table 6.1.

6.2.3 Exact Solution of Activation Overpotential

Neglecting the concentration overpotential, assuming the oxygen concentration in the CCL is uniform and $\alpha_a = \alpha_c$, Eq. (6.12) can be simplified as

$$\frac{d^2\eta_c}{dx^2} = -\kappa' \sinh\left(\frac{\alpha_c n \mathscr{F} \eta_c}{\mathscr{R}T}\right) \tag{6.13}$$

where κ' is a constant. Further, considering the following scaled variables, scaled CCL thickness ($\bar{x}$) and scaled activation overpotential ($\bar{\eta}_c$)

$$\bar{x} = \frac{x}{\delta_{\text{CL}}}; \quad \bar{\eta}_c = \frac{\alpha_c n \mathscr{F} \eta_c}{\mathscr{R}T} \tag{6.14}$$

Eq. (6.13) is written in scaled form as

$$\frac{d^2\bar{\eta}_c}{d\bar{x}^2} = -\kappa \sinh(\bar{\eta}_c) \tag{6.15}$$

where the dimensionless parameter κ is defined by the following relation:

$$\kappa = \frac{A_v J_0^{\text{O}_2}}{\sigma_m^{\text{eff}}} \left[\frac{c_{\text{O}_2}}{c_{\text{O}_2,\text{ref}}}\right]^{\gamma_c} \frac{2\alpha_c n \mathscr{F} \delta_{\text{CL}}^2}{\mathscr{R}T} \tag{6.16}$$

The scaled form of the governing equation for the activation overpotential, Eq. (6.15), is a second order nonlinear equation, which can be solved analytically for appropriate boundary conditions. The steps of the analytical solution along with the boundary conditions are given below. The exact solution of Eq. (6.15) is obtained by multiplying both side by $\frac{d\bar{\eta}_c}{d\bar{x}}$ and integrating twice as follows:

$$\frac{d}{d\bar{x}}\left[\left(\frac{d\bar{\eta}_c}{d\bar{x}}\right)^2\right] = -2\kappa \sinh(\bar{\eta}_c)\frac{d\bar{\eta}_c}{d\bar{x}} \tag{6.17}$$

$$\frac{d\bar{\eta}_c}{d\bar{x}} = \pm\sqrt{2\kappa \cosh(\bar{\eta}_c) + C_1} \tag{6.18}$$

It is noticed that the gradient of the membrane potential on the CCL/GDL interface is zero. In addition, if the membrane potential at $x = \delta_{\text{CL}}$ is considered as the reference potential then the following boundary conditions are available.

$$\frac{d\bar{\eta}_c}{d\bar{x}} = 0 \quad \text{at} \quad x = \delta_{\text{CL}} \tag{6.19}$$

$$\bar{\eta}_c = 0 \quad \text{at} \quad x = \delta_{\text{CL}} \tag{6.20}$$

Applying these boundary conditions in Eq. (6.18), the integration constant C_1 is found as -2κ. Also $\frac{d\bar{\eta}_c}{d\bar{x}}$ has to be negative to satisfy second boundary condition, hence

$$\frac{d\bar{\eta}_c}{d\bar{x}} = -\sqrt{2\kappa\left[\cosh(\bar{\eta}_c) - 1\right]} \tag{6.21}$$

To obtain the relation between the current density and the activation overpotential, the second boundary condition is required that is specified as

$$\sigma_m^{\text{eff}} \frac{d\Phi_m}{dx} = J \quad \text{at} \quad x = 0 \tag{6.22}$$

where J is the total current density drawn from the cell. Using Eq. (6.22) in Eq. (6.21), the exact relation between the current density and the activation overpotential in the CCL is found as

$$J = \frac{\mathscr{R}T\sigma_m^{\text{eff}}}{\alpha_c n \mathscr{F} \delta_{\text{CL}}} \sqrt{2\kappa\left[\cosh\left(\frac{\alpha_c n \mathscr{F} \eta_c}{\mathscr{R}T}\right) - 1\right]} \tag{6.23}$$

and hence, the activation overpotential in the CCL of a PEM fuel cell can be expressed by the following expression [7, 163]:

$$\eta_c = \frac{\mathscr{R}T}{\alpha_c n \mathscr{F}} \cosh^{-1}\left[1 + \frac{J^2}{4\sigma_m^{\text{eff}}\left(\frac{\mathscr{R}T}{\alpha_c n \mathscr{F}}\right) A_v J_0^{\text{O}_2}\left(\frac{c_{\text{O}_2,\text{rs}}}{c_{\text{O}_2,\text{ref}}}\right)}\right] \tag{6.24}$$

where $c_{\text{O}_2,\text{rs}}$ represents the oxygen concentration at the reaction site. It is worthwhile to note that the activation overpotential expression represents only the cathodic overpotential, and is obtained by assuming no variation of oxygen concentration in the CCL of a PEM fuel cell and for equal transfer coefficients in the Butler-Volmer equation. Since all the parameters are known for a specific fuel cell except oxygen concentration in the catalyst layer, it can easily be estimated by knowing the oxygen concentration. In the following sections, an approximate formulation to calculate the oxygen concentration and how the ohmic overpotential and reversible cell potential are estimated have been described.

6.3 Oxygen Concentration

For fully hydrated membrane in the cathode catalyst layer, the concentration of proton at the reaction sites is fixed and constant, and its specific value depends on the type of the membrane used. Conversely, the concentration of oxygen depends on the rate of electrochemical reaction or current density, as well as diffusion through the electrode and liquid water. Also concentration within the catalyst layer varies with the distance from the

CCL/GDL interface. For small current densities, the concentration variation is very small. At intermediate and high current densities, concentration of oxygen decays sharply within a small region in the catalyst layer near the CCL/GDL interface [6]. Since the region of the catalyst layer where electrochemical reactions occurs, is very small; it can be assumed that the oxygen concentration is almost uniform in that small region and independent of the length scale x in the CCL. Unlike Marr and Li [6], it is considered that oxygen concentration at $x = 0$ is known but depends on the current density. This will eventually provide a better approximation of oxygen concentration than the estimates of Marr and Li [6]. In the following subsections, the details of oxygen concentration calculations in the CCL and on the catalyst surface are provided.

6.3.1 Oxygen Concentration in Flooded GDL

During the transport process, oxygen in the flow channels first convects to the surface of the GDL, and then diffuses through the GDL to the catalyst layer surface as shown in Fig. 6.2. Considering a uniform oxygen concentration in the cathode gas flow channel (c_{ch}), the average concentration at the GDL/GFC interface (c_{es}) can be defined as a function of current density by [82]

$$c_{\text{es}} = c_{\text{ch}} - \frac{d_h W L}{4\text{Sh}\mathscr{F} D_{\text{O}_2,\text{bulk}} A_c} J \tag{6.25}$$

Here d_h is the hydraulic diameter of the flow channel, W is the width of the cell, L is the length of the cell, $D_{\text{O}_2,\text{bulk}}$ represents the diffusion coefficient of oxygen in the gas mixture of the flow channel, and A_c is the area of the flow channels exposed to the electrode. In the above equation, the Sherwood number is denoted by Sh, and due to the laminar flow in the flow channels, is equal to 2.3. The bulk diffusion coefficient is calculated according to [127]

$$D_{\text{O}_2,\text{bulk}} = \frac{1 - x_g^{\text{O}_2}}{\dfrac{x_g^{\text{N}_2}}{\mathscr{D}_{\text{O}_2-\text{N}_2}} + \dfrac{x_g^{\text{H}_2\text{O}}}{\mathscr{D}_{\text{O}_2-\text{H}_2\text{O}}}} \tag{6.26}$$

where $x_g^{\text{O}_2}$, $x_g^{\text{N}_2}$, and $x_g^{\text{H}_2\text{O}}$ are the mole fractions of oxygen, nitrogen, and water vapor in the gas flow channel, respectively. The binary diffusion coefficient of oxygen and nitrogen, $\mathscr{D}_{\text{O}_2-\text{N}_2}$, is calculated using Chapman-Enskog formula given in Eq. (5.35) and the binary diffusion coefficient of oxygen and water vapor, $\mathscr{D}_{\text{O}_2-\text{H}_2\text{O}}$, is calculated using Slattery-Bird equation given in Eq. (5.36).

Once the concentration on the GDL surface is known, the oxygen concentration on the

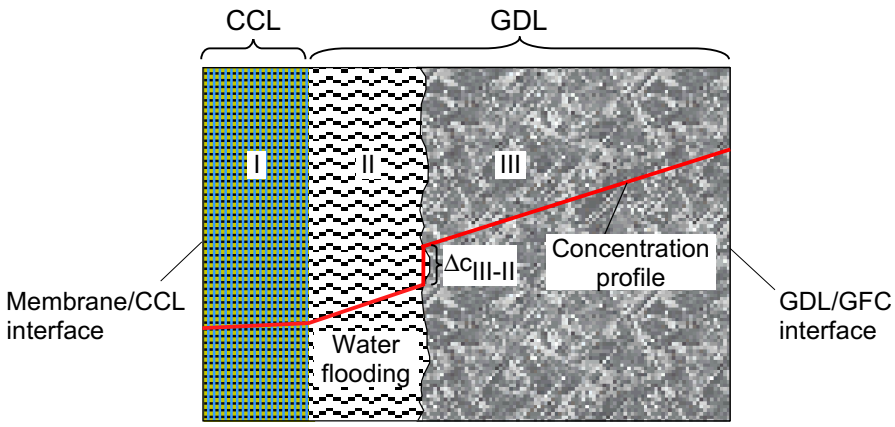

Figure 6.2: Schematic profile of oxygen concentration in the CCL and partially flooded GDL.

other side of the GDL (at the interface with liquid water in Fig. 6.2) is estimated using the Fick's law of diffusion

$$c_{III-II} = c_{\text{es}} - N''_{\text{O}_2} R_{III} \tag{6.27}$$

where R_{III} is the resistance to mass-transfer caused by the oxygen diffusion through the GDL and N''_{O_2} is the molar flux of oxygen that is defined as

$$N''_{\text{O}_2} = \frac{J}{4\mathscr{F}} \tag{6.28}$$

At the interface of liquid water and GDL, oxygen concentration is further reduced due to the limitation of transport processes in the liquid medium. Since the oxygen is weakly soluble in liquid water under the typical fuel cell operating environment, the amount of concentration drop at the liquid-gas interface can be related by using the perfect gas law and Henry's law as

$$\Delta c_{III-II} = c_{III-II} \left(1 - \frac{\mathscr{R}T}{H_{\text{O}_2}}\right) \tag{6.29}$$

where H_{O_2} is Henry's constant for oxygen gas dissolution in liquid water, which is determined from the following empirical correlation [24]:

$$H_{\text{O}_2} = 0.1013 \exp\left(14.1 - \frac{666}{T}\right) \tag{6.30}$$

where the temperature T is in Kelvins, and H_{O_2} is in the unit of Pa·m^3/mol.

Although the thickness of water flooding layer is non-uniform in real case, in the present investigation the liquid water thickness in the GDL is considered uniform, consistent with the present 1D analysis. Hence, the decay of oxygen concentration in the liquid water layer is approximated using the Fick's law formulation as

$$c_{II-I} = (c_{III-II} - \Delta c_{III-II}) - N''_{\mathrm{O_2}} R_{II} \tag{6.31}$$

where R_{II} is the resistance to mass-transfer caused by the oxygen dissolving into the liquid water. Considering f_w is the fraction of void region in the GDL that is flooded by liquid water, both the resistances (R_{II} and R_{III}) are expressed by the volume fraction divided by the corresponding diffusion coefficient

$$R_{II} = \frac{f_w \delta_{\mathrm{GDL}}}{\mathscr{D}^{\mathrm{eff}}_{\mathrm{O_2-H_2O}_{(l)}}} \tag{6.32}$$

$$R_{III} = \frac{(1 - f_w)\delta_{\mathrm{GDL}}}{D^{\mathrm{eff}}_{\mathrm{O_2,GDL}}} \tag{6.33}$$

where δ_{GDL} is the GDL thickness. The terms, $\mathscr{D}^{\mathrm{eff}}_{\mathrm{O_2-H_2O}_{(l)}}$ and $D^{\mathrm{eff}}_{\mathrm{O_2,GDL}}$, are the effective diffusion coefficients of oxygen through the liquid water zone and the gas zone in the GDL as shown in Fig. 6.2, respectively.

The binary diffusion coefficient of oxygen in liquid water can be obtained using Wilke-Chang relation given in Eq. (5.37). Combining Eqs. (6.27)–(6.29) and (6.31) yields

$$c_{II-I} = c_{\mathrm{es}} \frac{\mathscr{R}T}{H_{\mathrm{O_2}}} - \frac{J}{4\mathscr{F}} \left(R_{II} + R_{III} \frac{\mathscr{R}T}{H_{\mathrm{O_2}}} \right) \tag{6.34}$$

It should be noted here that the concentration given by Eq. (6.34) is valid only when $f_w > 0$. The concentration further drops down before reaching the catalyst particles, i.e. at the surface of the catalyst particles; the actual oxygen concentration is slightly lower than the above-mentioned concentration. Since the actual composition of the catalyst layer is more complex and not available in the literature, one may neglect the composition effect and assume the constant concentration profile in the CCL using Eq. (6.34).

In the present investigation, an uniform concentration profile is considered in the catalyst layer, which is equal to the concentration at the CCL/GDL interface, i.e. $c_{\mathrm{O_2,CL}} = c_{II-I}$. However, to study the effect of the Nafion content in the catalyst layer and water flooding, it is required to consider the oxygen concentration on the catalyst particle's surface. Considering the catalyst particles are surrounded by Nafion membrane and liquid water layer, the oxygen concentration on the surface of the catalyst particle is approxi-

mated by applying the Fick's law

$$c_{\mathrm{O_2,rs}} = c_{II-I} - \frac{J}{4\mathscr{F}}\left(R_{w,\mathrm{CL}} + R_{m,\mathrm{CL}}\right) \tag{6.35}$$

where $R_{w,\mathrm{CL}}$ and $R_{m,\mathrm{CL}}$ represent the resistance to mass-transfer in the liquid water and the resistance to mass-transfer in the Nafion content of the CCL, respectively. If the GDL is assumed partially flooded, then the catalyst layer would be fully flooded, and the resistances can be determined as

$$R_{w,\mathrm{CL}} = \frac{f_{\mathrm{H_2O}_{(l)}}\delta_{\mathrm{CL}}}{\mathscr{D}^{\mathrm{eff}}_{\mathrm{O_2-H_2O}_{(l)},\mathrm{CL}}} \tag{6.36}$$

$$R_{m,\mathrm{CL}} = \frac{f_m\delta_{\mathrm{CL}}}{\mathscr{D}^{\mathrm{eff}}_{\mathrm{O_2}-m,\mathrm{CL}}} \tag{6.37}$$

where $f_{\mathrm{H_2O}_{(l)}}$ and f_m are the volume fraction of liquid water and membrane in the void region of the catalyst layer, respectively. The effective diffusion coefficients of oxygen through the liquid water and the Nafion in the catalyst layer are denoted by $\mathscr{D}^{\mathrm{eff}}_{\mathrm{O_2-H_2O}_{(l)},\mathrm{CL}}$ and $\mathscr{D}^{\mathrm{eff}}_{\mathrm{O_2}-m,\mathrm{CL}}$, respectively. These effective values can be estimated using the formulation derived in Chapter 5, while the diffusion coefficient for oxygen in Nafion membrane ($\mathscr{D}_{\mathrm{O_2}-m}$) can be calculated using the empirical relation given in Eq. (5.39) [6].

6.3.2 Oxygen Concentration in Dry GDL

Formulation given in the above-section is valid only when the GDL is flooded as shown in Fig. 6.2. For dry GDL ($f_w = 0$), zone II does not exist in Fig. 6.2. Then the oxygen concentration at the CCL/GDL interface is calculated directly using the Fick's law as

$$c_{III-I} = c_{\mathrm{es}} - \frac{J}{4\mathscr{F}}R_{III} \tag{6.38}$$

where R_{III} is the resistance to mass-transfer by the oxygen diffusion through the dry GDL. If an un-flooded GDL is considered, which means catalyst particles are no longer completely surrounded by the Nafion and liquid water. In this circumstance, there will be some void space over the catalyst particle that is filled with gas mixture. Therefore, oxygen has to penetrate three layers, namely, Nafion membrane, liquid water, and gas mixture layer. In reality, it can be more than three layers as mentioned; it can be any combinations of the Nafion, liquid water, and gases. However, for simplification it has been considered that catalyst particles are surrounded by three distinct layers of Nafion, liquid water, and gas. Hence, the following resistance for the mass-transfer associated with the gas mixture in the partially flooded catalyst layer is formulated along with Eqs. (6.36)–(6.37) for the

liquid water and the Nafion membrane:

$$R_{g,\mathrm{CL}} = \frac{\left(1 - f_m - f_{\mathrm{H_2O}_{(l)}}\right)\delta_{\mathrm{CL}}}{D^{\mathrm{eff}}_{\mathrm{O_2,CL}}} \tag{6.39}$$

where $D^{\mathrm{eff}}_{\mathrm{O_2,CL}}$ is the effective diffusion coefficient of oxygen through the gas phase. Similar to the formulations of Eqs. (6.34)–(6.35), the expression for the oxygen concentration on the reaction sites for the partially flooded catalyst layer is written as

$$c_{\mathrm{O_2,rs}} = c_{II-I}\frac{\mathscr{R}T}{H_{\mathrm{O_2}}} - \frac{J}{4\mathscr{F}}\left(R_{g,\mathrm{CL}}\frac{\mathscr{R}T}{H_{\mathrm{O_2}}} + R_{w,\mathrm{CL}} + R_{m,\mathrm{CL}}\right) \tag{6.40}$$

6.4 Cell Potential

To investigate the fuel cell performance using the proposed activation overpotential formulation, the electric output of a PEM fuel cell is defined by neglecting the concentration overpotential as

$$E_{\mathrm{cell}} = E_{\mathrm{oc}} - \eta_c - \eta_{\mathrm{ohm}} \tag{6.41}$$

where E_{oc} is the open circuit voltage at zero current, η_c is the activation overpotential, and η_{ohm} is the ohmic overpotential. Although the concentration overpotential is neglected in the above equation, the effect of mass-transfer limitation on the cell potential is incorporated through the estimation oxygen concentration at the reaction sites as described in the previous sections.

As observed in Fig. 1.3, the activation overpotential in the anode catalyst layer is negligible compared to the overpotential in the cathode catalyst layer. Therefore, activation overpotential is considered as potential losses in the cathode catalyst layer only. In an ideal fuel cell, the cell voltage is independent of the current drawn, and the open circuit potential would remain equal to the reversible cell potential (E_r). Practically, the ideal cell potential is not possible to attain at the zero current due to another problem for PEM fuel cells, fuel crossover through the membrane, which results in a mixed potential at the cathode and thereby lowers the cell performance [164]. Hence, the following expression is considered for the open circuit potential.

$$E_{\mathrm{oc}} = E_r - E_{\mathrm{mixed}} \tag{6.42}$$

where E_{mixed} is the mixed potential at the electrodes. This amount of potential drops is

mainly due to unavoidable parasitic reactions that tend to lower the equilibrium electrode potential. For instance, it might be due to the crossover of fuel through the electrolyte from anode to cathode or vice versa, slow oxygen-reduction kinetics, Pt-oxide formation and/or impurity oxidation, or some other unknown factors.

6.4.1 Reversible Cell Potential

The reversible cell voltage (E_r) is the cell potential obtained at the thermodynamic equilibrium. For the reaction of the PEM fuel cells shown in Eq. (1.3), the reversible cell potential can be found from a modified version of the Nernst equation as [4, 23, 82]

$$E_r = \frac{\Delta G}{2\mathscr{F}} + \frac{\Delta S}{2\mathscr{F}}\left(T - T_{\text{ref}}\right) - \frac{\mathscr{R}T}{2\mathscr{F}}\ln\left(\frac{x_g^{\text{H}_2\text{O}}}{x_g^{\text{H}_2} {x_g^{\text{O}_2}}^{0.5}}\right) + \frac{\Delta N \mathscr{R}T}{2\mathscr{F}}\ln\left(\frac{P_{\text{ref}}}{P}\right) \tag{6.43}$$

where ΔG is the change in Gibbs free energy and ΔS is the change in entropy. The variable T denotes the cell operating temperature, with T_{ref} denoting a reference temperature (298 K). Similarly, P denotes the operating pressure and P_{ref} denoting reference pressure (1 atm). The term ΔN is the changes in the number of mole in the gas product side and the gas reactant side of Eq. (1.3). Using the standard-state Gibbs free energy change and entropy change, and considering the product water is in the vapor state, Eq. (6.43) can now be written as

$$E_r = 1.185 - 2.302\times10^{-4}\left(T - T_{\text{ref}}\right) - 4.308\times10^{-5}T\ln\left(\frac{x_g^{\text{H}_2\text{O}}}{x_g^{\text{H}_2} {x_g^{\text{O}_2}}^{0.5}}\right) - 2.154\times10^{-5}T\ln\left(\frac{P_{\text{ref}}}{P}\right) \tag{6.44}$$

6.4.2 Ohmic Overpotential

The ohmic overpotential is the total overpotential resulting from the resistance to proton transfer through the membrane and the resistance to electron transfer in the collector plates and the electrodes. Therefore, the total drop in potential due to the ohmic resistance can be defined via an Ohm's law relation as

$$\eta_{\text{ohm}} = \eta_{\text{ohm},p} + \eta_{\text{ohm},e} + \eta_{\text{ohm},m} = R''_{\text{total}}J \tag{6.45}$$

where R''_{total} is the equivalent of total internal resistance, J is the cell current density, $\eta_{\text{ohm},p}$, $\eta_{\text{ohm},e}$, and $\eta_{\text{ohm},m}$ are the potential drop due to the ohmic resistance of flow channel

plate, the electrodes, and membrane layer, respectively. Mathematical formulation for each of these resistances has already been developed [82]. However, careful attention is required to calculate these resistances, since these expressions are dependent on the cell geometry, material properties, and reactant concentration. One can also approximate the total internal resistance from the following empirical relation for typical PEM fuel cell, which is a function of cell temperature in Kelvin and current [14, 15]:

$$R_{\text{total}} = 0.01605 - 3.5 \times 10^{-5} T + 8.0 \times 10^{-5} I \tag{6.46}$$

In addition, experimental values of ohmic resistance for PEM fuel cells operating between 50 ℃ to 70 ℃ and 1 atm to 5 atm pressure are available in Ref. [16].

6.5 Analytical Approach to Liquid Water Transport

There are numerous theoretical and numerical studies related to liquid water transport available in literature [23, 26, 28, 53, 65, 116, 151, 152, 165–168], however, all of them are for the liquid water transport in the membrane or the GDL of a PEM fuel cell. These studies also addressed the water flooding in the GDL and gas flow channel, and none of the previous studies specifically addressed the liquid water transport in the CCL of a PEM fuel cell. Further, these studies were based on the assumption that most of the liquid water produced at the CCL/GDL interface or the catalyst layer is very thin. While the highest reaction rate occurs at the membrane/CCL interface [94] and the CCL thickness needs to be higher than 10 μm to obtain optimum performance from a PEM fuel cell [7]. Therefore, the approximation of a thin CCL or considering the CCL as an interface seems to be insufficient to explore the overall liquid water transport in a PEM fuel cell. Substantial amount of experimental studies have also been conducted for the flooding in PEM fuel cells to understand the fundamental water transport processes [9, 169–175]. Furthermore, Pasaogullari and Wang [63] developed an analytical model of liquid water transport in the GDL of a PEM fuel cell. Although water flooding in the CCL likely occurs prior to that in the flow channel and GDL because of water is produced in the CCL from the electrochemical reaction and is expelled from the CCL to the flow channel through the GDL, the studies related to the CCL flooding are still elusive. Here, a 1D analytical model of liquid water transport is derived from the fundamental transport equations to investigate the water transport in the CCL.

To investigate the liquid water transport in the CCL analytically, a macro-homogeneous catalyst layer is considered as shown in Fig. 6.1. In the CCL, the transport of liquid water is governed by the microscopic conservation of mass and momentum equations of liquid

water phase. To apply the microscopic conservation equations macroscopically within the catalyst layer, the volume-averaged microscopic conservation equations described in Section 4.3 are considered. In the following subsections, the proposed model and the required boundary conditions are described.

6.5.1 One-dimensional Liquid Water Transport

Assuming the liquid water transport inside the CCL is mainly driven by the liquid pressure gradient according to the Darcy's law, the conservation of momentum equation for the liquid phase is simplified by neglecting the convective and viscous terms (due to very small Reynolds and capillary numbers) for the steady-state case as

$$\epsilon_l \nabla \langle P_l \rangle^l = -\frac{\epsilon_l \mu_l}{K k_{rl}} \langle \boldsymbol{u}_l \rangle^l \tag{6.47}$$

Using the definition of capillary pressure, Eq. (6.47) yields

$$-\nabla P_c + \nabla \langle P_g \rangle^g = -\frac{\mu_l}{K k_{rl}} \langle \boldsymbol{u}_l \rangle^l \tag{6.48}$$

The gas phase pressure can be considered constant throughout the CCL and GDL of a PEM fuel cell, and is equal to the gas phase pressure in the cathode flow channel [63]. Assuming a constant gas phase pressure and solving Eq. (6.48) for $\langle \boldsymbol{u}_l \rangle^l$ and substituting into Eq. (4.41) yields

$$\nabla \cdot \left(\frac{K k_{rl}}{\mu_l} \langle \rho_l \rangle \frac{dP_c}{ds_l} \nabla s_l \right) = \Gamma_{M,l} \tag{6.49}$$

Considering the one-dimensional transport of liquid water in the through-plane direction of catalyst layer, Eq. (6.49) reduces to an ordinary differential equation that can be solved analytically with appropriate approximation and boundary conditions. Assuming the reactant gas is fully humidified, the evaporation part from Eq. (4.6) can be neglected and hence, the right hand part of Eq. (6.49) reduces to

$$\Gamma_{M,l} = \hat{M}_{\mathrm{H_2O}} A_v \dot{\mathscr{P}}^{\mathrm{H_2O}} + k_c \frac{\epsilon x_g^{\mathrm{H_2O}} \hat{M}_{\mathrm{H_2O}}}{\mathscr{R} T} \left(x_g^{\mathrm{H_2O}} \langle P_g \rangle^g - P_{\mathrm{sat}} \right) \tag{6.50}$$

The molar production of liquid water, $\dot{\mathscr{P}}^{\mathrm{H_2O}}$, is the function of reaction rate and hence, oxygen concentration and activation overpotential. In Sections 6.2 and 6.3, the formulations for the activation overpotential and oxygen concentration are already described.

After integrating Eq. (6.49) with respect to x yields

$$\frac{Kk_{rl}}{\mu_l}\left\langle \rho_l \right\rangle \frac{dP_c}{ds_l}\nabla s_l = x\Gamma_{M,l} + C_1 \tag{6.51}$$

where C_1 is the integration constant.

The boundary condition for Eq. (6.51) at the membrane/CCL interface can be written as

$$\left[\frac{Kk_{rl}}{\mu_l}\left\langle \rho_l \right\rangle \frac{dP_c}{ds_l}\nabla s_l\right]\Bigg|_{x=0} = 2\alpha\left(\frac{J}{2\mathscr{F}}\hat{M}_{\mathrm{H_2O}}\right) \tag{6.52}$$

where α is the net drag coefficient, J is the current density, $\mathscr{F}$ is the Faraday's constant, and $\hat{M}_{\mathrm{H_2O}}$ is the molar mass of water. The net drag coefficient includes both electro-osmotic drag and back-diffusion between the membrane and CCL. Hence, the right-hand side term in Eq. (6.52) describes the overall liquid water transport through the membrane to the CCL [176, 177]. The coefficient, α, is positive when water transport by the electro-osmotic drag is higher than the back-diffusion from the CCL to the membrane, and will be negative when water transport by the electro-osmotic process is lower than the back-diffusion process. If water transport by the electro-osmotic drag is equal to the back-diffusion, then one can assume that the net transport of water across the membrane is zero. Using the boundary condition given in Eq. (6.52), the first integration constant is found as

$$C_1 = 2\alpha\left(\frac{J}{2\mathscr{F}}\hat{M}_{\mathrm{H_2O}}\right) \tag{6.53}$$

The volume-averaged liquid water density, $\langle \rho_l \rangle$, can be written in terms of phase-averaged density as

$$\left\langle \rho_l \right\rangle = \epsilon s_l \langle \rho_l \rangle^l = \epsilon s_l \rho_l \tag{6.54}$$

Hence, using the Leverett function, Eq. (6.51) simplifies in terms of liquid saturation for a hydrophilic CCL ($\theta_c < 90^\circ$) as

$$s_l^4(-0.966 + 3.338s_l - 3.789{s_l}^2)\frac{ds_l}{dx} = xR_w + R_d \tag{6.55}$$

and for a hydrophobic CCL ($\theta_c > 90^\circ$) as

$$s_l^4(1.417 - 4.240s_l + 3.789{s_l}^2)\frac{ds_l}{dx} = xR_w + R_d \tag{6.56}$$

The terms, R_w and R_d, are represented by the following expressions:

$$R_w = \frac{\nu_l}{\epsilon\left(\epsilon K\right)^{0.5}\gamma\cos\theta_c}\left[2\hat{M}_{\mathrm{H_2O}}A_v\mathcal{R}_{c,\mathrm{red}} + k_c\frac{\epsilon x_g^{\mathrm{H_2O}}\hat{M}_{\mathrm{H_2O}}}{\mathscr{R}T}\left(x_g^{\mathrm{H_2O}}\langle P_g\rangle^g - P_{\mathrm{sat}}\right)\right] \tag{6.57}$$

$$R_d = \frac{\nu_l}{\epsilon\left(\epsilon K\right)^{0.5}\gamma\cos\theta_c}\left[\frac{\alpha\hat{M}_{\mathrm{H_2O}}J}{\mathscr{F}}\right] \tag{6.58}$$

where ν_l is the kinematic viscosity of liquid water.

After integrating Eqs. (6.55) and (6.56), the liquid water saturation expressions have been obtained for a hydrophilic CCL as

$$-0.541s_l^7 + 0.556s_l^6 - 0.193s_l^5 = 0.5x^2R_w + xR_d + C_{21} \tag{6.59}$$

and for a hydrophobic CCL as

$$0.541s_l^7 - 0.707s_l^6 + 0.283s_l^5 = 0.5x^2R_w + xR_d + C_{22} \tag{6.60}$$

where C_{21} and C_{22} are the second integration constants that are governed by the second boundary condition, which is the liquid saturation at the CCL/GDL interface of a PEM fuel cell.

Once the liquid saturation at the CCL/GDL interface is known, C_{21} and C_{22} can easily be calculated. In addition, the terms, R_w and R_d, in the liquid saturation expressions are the functions of reaction rate and current density, respectively. Hence, it is possible to relate liquid saturation with the cathode activation overpotential that will eventually allow us to study the effect of liquid saturation on the PEM fuel cell performance. In the following subsections, the boundary condition at the CCL/GDL interface is derived from the formulation proposed by Pasaogullari and Wang [63].

6.5.2 Boundary Condition

The boundary condition at the membrane/CCL interface is already given in Eq. (6.52), while the boundary condition for Eqs. (6.59) and (6.60) at the CCL/GDL interface can be defined as

$$s_l\big|_{x=\delta_{\mathrm{CL}}} = s_b \tag{6.61}$$

where s_b is a known liquid saturation at the CCL/GDL interface. To estimate s_b, we employed the analytical formulation developed by Pasaogullari and Wang [63] for the liquid water transport in the GDL of a PEM fuel cell. Using the formulation of Pasaogullari and Wang [63], the following expressions are derived:

$$s_b^4(0.354 - 0.848s_b + 0.613s_b^2) = -\frac{J}{2\mathscr{F}}\hat{M}_{\mathrm{H_2O}}\frac{\nu_l\delta_{\mathrm{GDL}}}{(\epsilon K)^{0.5}\,\gamma\cos\theta_c} \quad \text{for } \theta_c > 90^\circ \tag{6.62}$$

$$s_b^4(-0.241 + 0.668s_b - 0.613s_b^2) = -\frac{J}{2\mathscr{F}}\hat{M}_{\mathrm{H_2O}}\frac{\nu_l\delta_{\mathrm{GDL}}}{(\epsilon K)^{0.5}\,\gamma\cos\theta_c} \quad \text{for } \theta_c < 90^\circ \tag{6.63}$$

where δ_{GDL} is the GDL thickness.

It should be noted here, for simplicity, Pasaogullari and Wang [63] assumed that no liquid saturation is present in the gas flow channel. However, it is possible to consider a liquid saturation in the flow channel; in such case, the formulation of Pasaogullari and Wang [63] needs to be re-derived to obtain the boundary value of liquid saturation (s_b). It has also been assumed in Ref. [63] that the net transport of water across the membrane is zero. Since the objective of this study is to use the formulation given in Ref. [63] to obtain the boundary condition at the CCL/GDL interface, no changes have been made to the above-mentioned assumptions.

The variations of liquid saturation at the CCL/GDL interface (s_b) with the current density for GDLs having contact angles of 80° and 100° are shown in Fig. 6.3. These results are plotted using the expressions given in Eqs. (6.62)–(6.63). The results show that the liquid saturation at the CCL/GDL interface for a current density of 1.4 A/cm^2 would be about 11% higher for a GDL having contact angle of 80° compared to a GDL having contact angle of 100°. Hence, the liquid water removal rate will be higher for a hydrophobic GDL than a hydrophilic GDL. Therefore, only hydrophobic GDL is considered while investigating the liquid water transport in the CCLs of PEM fuel cells.

6.5.3 Dimensionless Liquid Water Profile

Using the boundary condition at the CCL/GDL interface given in the previous section, the expressions for liquid water transport in the CCL become:

$$-0.541(s_l^7 - s_b^7) + 0.556(s_l^6 - s_b^6) - 0.193(s_l^5 - s_b^5) = (\bar{x}^2 - 1)\bar{R}_w + (\bar{x} - 1)\bar{R}_d \tag{6.64}$$

$$0.541(s_l^7 - s_b^7) - 0.707(s_l^6 - s_b^6) + 0.283(s_l^5 - s_b^5) = (\bar{x}^2 - 1)\bar{R}_w + (\bar{x} - 1)\bar{R}_d \tag{6.65}$$

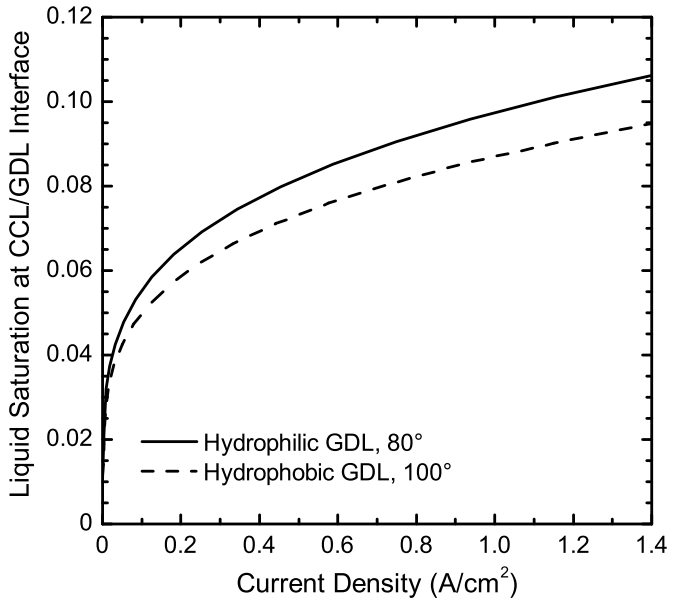

Figure 6.3: Liquid saturation at the CCL/GDL interface of a PEM fuel cell as a function of current density for GDLs having contact angles of 80° and 100° as indicated in the legend.

where Eq. (6.64) is for the hydrophilic CCL and Eq. (6.65) is for the hydrophobic CCL. Here s_b is the liquid saturation at the CCL/GDL interface that can be obtained from Eqs. (6.62) and (6.63) for hydrophobic and hydrophilic CCLs, respectively, $\bar{x}$ is the dimensionless distance along the catalyst layer thickness, $\bar{R}_w$ is the dimensionless water production in the CCL from the electrochemical reaction and condensation, and $\bar{R}_d$ is the dimensionless net water transport from the membrane to the CCL by the electro-osmotic drag and back-diffusion. The dimensionless distance along the CCL thickness is defined as

$$\bar{x} = \frac{x}{\delta_{\mathrm{CL}}} \tag{6.66}$$

where δ_{CL} is the CCL thickness.

The dimensionless water production inside the CCL from the electrochemical reaction and condensation is defined by the following expression:

$$\bar{R}_w = \frac{0.5\mu_l\delta_{\mathrm{CL}}^2}{\epsilon\left(\epsilon K\right)^{0.5}\gamma\cos\theta_c}\left[\frac{2\hat{M}_{\mathrm{H_2O}}A_v\mathcal{R}_{c,\mathrm{red}}}{\rho_l} + k_c\frac{\epsilon x_g^{\mathrm{H_2O}}\hat{M}_{\mathrm{H_2O}}}{\rho_l\mathscr{R}T}\left(x_g^{\mathrm{H_2O}}\langle P_g\rangle^g - P_{\mathrm{sat}}\right)\right]$$

$$= \mathrm{CDT}\left[(\mathrm{EPT})^{-1} + (\mathrm{PCT})^{-1}\right] = \Pi_1 + \Pi_2 \tag{6.67}$$

where Π_1 and Π_2 are the dimensionless numbers that are named as the "*dimensionless time of first kind*" and "*dimensionless time of second kind*", respectively. The dimensionless time of first kind represents the ratio between the capillary diffusion time (CDT) to the electrochemical production time (EPT). The dimensionless time of second kind represents the ratio between the capillary diffusion time to the phase change time (PCT) at steady-state. Conversely, the term $\bar{R}_d$ is defined as

$$\bar{R}_d = \frac{0.5\mu_l\delta_{\mathrm{CL}}^2}{\epsilon\left(\epsilon K\right)^{0.5}\gamma\cos\theta_c}\left[\frac{2\alpha J\hat{M}_{\mathrm{H_2O}}}{\rho_l\delta_{\mathrm{CL}}\mathscr{F}}\right] = \Pi_3 \tag{6.68}$$

where Π_3 is the "*dimensionless time of third kind*", which represents the ratio between the capillary diffusion time to the time required for liquid water transport by the net electro-osmotic drag and back-diffusion processes across the CCL. These dimensionless time constants will provide insight about how much liquid water would be accumulated in the CCL and transported from the CCL to the gas flow channel through the GDL. Since the capillary diffusion is the major mode of water transport from the CCL to the GDL, the higher the time constants are, the higher the liquid water accumulation. Hence, the water saturation will also be higher in the CCL for higher time constant values.

6.6 Summary

In this chapter, the analytical models for estimating the activation overpotential and the liquid water distribution in the CCL of a PEM fuel cell are described. These analytical expressions are simple and easy to implement. The analytical expression of the activation overpotential has been compared with the various data available in literature that covers empirical results, experimental data, and numerical predictions and an optimization study has also been carried out [7, 163]. The results of these comparisons and optimization study are provided in Chapter 8. Similarly, the analytical solutions of liquid water profile have been used to investigate the effect of catalyst layer wettability and liquid water flooding on the fuel cell performance [178, 179], and the corresponding results are also available in Chapter 8.

Chapter 7

Numerical Implementation

This chapter describes the numerical procedure to solve the governing equations presented in Chapter 4, along with the required boundary conditions (BCs). The mesh generation procedure and mesh independency test are also described.

7.1 Computational Domains and Boundary Conditions

A schematic of PEM fuel cell is shown in Fig. 7.1 with the computational domain used in investigating transport phenomena in the CCL that is marked by a dashed rectangle. The bottom parts of Fig. 7.1 depict the two-dimensional (2D) and three-dimensional (3D) computational domains. Although the main focus is given to the catalyst layer, it is also required to include GDL, BP, and GFC in the numerical simulation. For the 2D simulation, the flow channel can be omitted by provided the species concentration at the GDL/GFC interface as a boundary condition.

At the channel inlet, the Dirichlet boundary conditions are adopted for the gas mixture average velocity and the species concentrations. The gas mixture velocity is specified by

$$u_g = \xi_c \frac{J_0^{\mathrm{O_2}}}{4\mathscr{F}} A \frac{\mathscr{R} T_0}{P_0} \frac{1}{x_{g,\mathrm{in}}^{\mathrm{O_2}}} \frac{1}{A_c} \quad \text{for } \partial\Omega \in \text{GFC inlet} \tag{7.1}$$

and the species concentrations are specified as

$$c_{\mathrm{O_2}} = \frac{0.21(P_0 - R_H P_{\mathrm{sat}})}{\mathscr{R} T_0} \quad \text{for } \partial\Omega \in \text{GFC inlet} \tag{7.2}$$

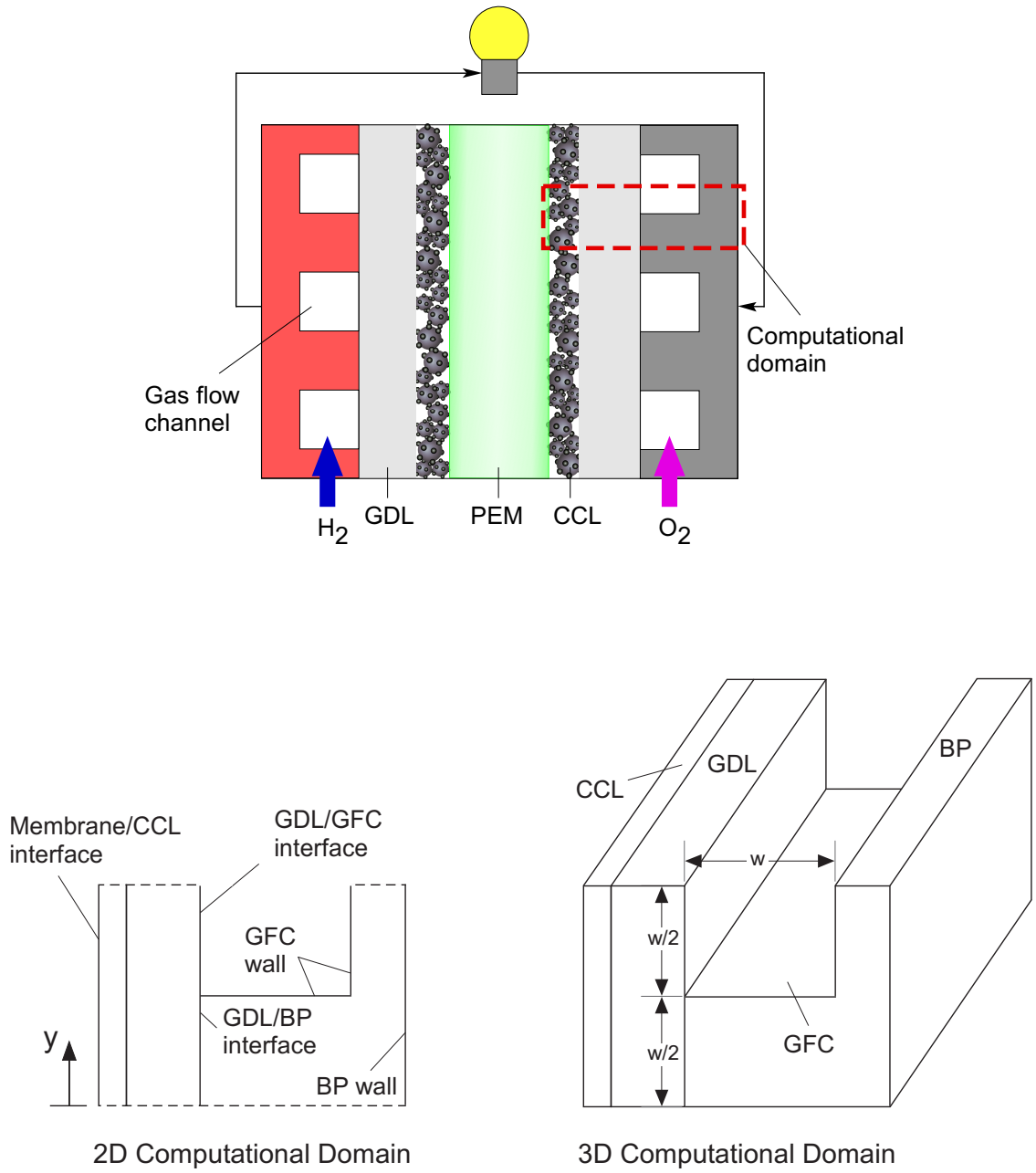

Figure 7.1: A schematic PEM fuel cell with computational domain indicated by dashed rectangle and the two-dimensional (bottom-left) and three-dimensional (bottom-right) computational domains used in the numerical simulations. The dashed line in the 2D computational domain represents the line of symmetry.

$$c_{\mathrm{H_2O}} = \frac{R_H P_{\mathrm{sat}}}{\mathscr{R} T_0} \quad \text{for } \partial\Omega \in \text{GFC inlet} \tag{7.3}$$

where ξ_c is the stoichiometric ratio, $\partial\Omega$ represents the boundary of the computational domain, R_H is the inlet relative humidity, P_0 is the operating pressure, and T_0 is the operating temperature. The coefficient 0.21 in Eq. (7.2) represents the molar fraction of oxygen in air. For the 2D simulation, the above BCs are applied to the GDL/GFC interface to simulate the transport processes for the inlet conditions.

At the channel outlets, the fully developed conditions are applied to the velocity and species concentration fields. Thus, the fluxes of all variables do not vary in the normal direction and the gas pressure is specified. At the channel wall, no-slip boundary condition is applied. Since the Darcy equation is considered for the CCL and GDL and the Navier-Stokes equation is used for the GFC. The boundary conditions are needed for both equations at the GDL/GFC interface. Here we employed variable coupling to solve these equations. In the coupling process, one equation is solved using the initial guess and then the numerical results is used as boundary condition for the other equation and vice versa. Hence, the boundary values are defined as

$$u_{g,\mathrm{NS}} = u_{g,\mathrm{Darcy}} \quad \text{for } \partial\Omega \in \text{GDL/GFC interface} \tag{7.4}$$

$$v_{g,\mathrm{NS}} = v_{g,\mathrm{Darcy}} \quad \text{for } \partial\Omega \in \text{GDL/GFC interface} \tag{7.5}$$

$$w_{g,\mathrm{NS}} = w_{g,\mathrm{Darcy}} \quad \text{for } \partial\Omega \in \text{GDL/GFC interface} \tag{7.6}$$

$$P_{g,\mathrm{Darcy}} = P_{g,\mathrm{NS}} \quad \text{for } \partial\Omega \in \text{GDL/GFC interface} \tag{7.7}$$

where u, v, w are the three components of the velocity vector and P is the pressure. The subscript Darcy represents the solution of Darcy equation and NS represents the values from the Navier-Stokes solver. Since the Navier-Stokes equation is not considered in the 2D simulation, the following BC is applied to the Darcy equation:

$$P_{g,\mathrm{Darcy}} = P_0 \quad \text{for } \partial\Omega \in \text{GDL/GFC interface} \tag{7.8}$$

The von Neumann boundary condition is applied to the membrane phase potential for all boundaries of the computational domain. Hence, the boundary conditions for the membrane phase potential are:

$$-\sigma_m^{\mathrm{eff}} \nabla \Phi_m = J_m \quad \text{for } \partial\Omega \in \text{membrane/CCL interface} \tag{7.9}$$

$$\nabla \Phi_m = 0 \text{ for } \partial\Omega \notin \text{membrane/CCL interface} \tag{7.10}$$

where Φ_m is the membrane phase potential and J_m is the membrane phase current density.

The von Neumann boundary condition is also applied to the solid phase potential for all boundaries of the computational domain except the wall of the bipolar plate (BP). The boundary conditions for the solid phase potential are:

$$\Phi_s = V_{\text{cell}} \quad \text{for } \partial\Omega \in \text{BP wall} \tag{7.11}$$

$$\nabla\Phi_s = 0 \quad \text{for } \partial\Omega \notin \text{BP wall} \tag{7.12}$$

$$-\sigma_s^{\text{eff}}\nabla\Phi_s = J_s \quad \text{for } \partial\Omega \in \text{CCL/GDL interface} \tag{7.13}$$

where Φ_s is the solid phase potential and J_s is the solid phase current density, which is the cell current density. The BC given in Eq. (7.13) is not required when the CCL, GDL, and BP are considered as a single-domain. This BC, however, is required when the governing equations are only solved in the CCL.

The boundary condition for the liquid water equation at the membrane/CCL interface is quite complex that is given in Eq. (6.52). Applying such boundary condition in the numerical simulation is not straight forward as the coefficient term in the LHS of Eq. (6.52) is also a function of liquid water saturation. Hence, a simplified BC is applied at the membrane/CCL interface that can be written as

$$\nabla s_l = \frac{\alpha J_{\text{cell}}\hat{M}_{\text{H}_2\text{O}}}{\mathscr{F}} \quad \text{for } \partial\Omega \in \text{membrane/CCL interface} \tag{7.14}$$

where α is a drag coefficient that represents the net liquid water transport between the membrane and catalyst layer, and J_{cell} is the cell current density.

In the 2D numerical simulation, the drag coefficient is considered to be zero, which represents water transport by the electro-osmotic drag is equal to the back-diffusion. Conversely, the liquid saturation at the GDL/GFC interface is defined as

$$s_l = s_{l,\text{GFC}} \quad \text{for } \partial\Omega \in \text{GDL/GFC interface} \tag{7.15}$$

where $s_{l,\text{GFC}}$ is the liquid saturation in the gas flow channel that is considered to be zero for the 2D simulation and a small value (usually in the order 10^{-3} or lower) for the 3D simulation.

In the rest of the boundaries, the following boundary condition is applied

$$\mathbf{n}.\nabla\Theta = 0 \tag{7.16}$$

where Θ can be any parameter. This statement actually provides the symmetry conditions on the boundaries, implying that the gradients of a parameter normal to the boundaries are zero.

7.2 Numerical Procedure

The governing equations containing mass, momentum, species, and charges are solved using COMSOL Multiphysics®, utilizing a finite element method to solve the system of coupled partial differential equations. Several versions of COMSOL used in this study including v3.2 and v3.4. The main advantage of COMSOL is that it can be run either as a programmable toolbox for development of finite element solutions on MATLAB® (The MathWorks, Inc., USA), or as a simple graphical user interface (GUI) based integrated environment for solution of partial differential equations using the finite element technique. In order to solve the governing equations, the following modules are used:

- The Stefan-Maxwell diffusion and convection module is used to solve the conservation of species (oxygen, nitrogen, and water vapor) equations.
- The Darcy equation module is used to solve the conservation of mass and momentum equations in the porous GDL and CCL.
- The AC/DC module is employed for the solid and electrolyte potentials.
- The PDE coefficient module is used for the liquid water equation.
- The compressible Navier-Stokes module is used to solve the conservation of mass and momentum equations in the gas flow channel for the 3D simulation.

In this thesis research, the employed approach for obtaining the polarization is the galvanostatic-method, which is setting the cell current density and calculating the activation polarization. Since all the governing equations are coupled with each other through the source terms, they ought to be solved simultaneously with the iterative method. Thus, the numerical procedure for 2D simulation is described as follows. At first, the initialization of the dependent variables is assumed. The initial concentrations (or mass fractions) take the inlet values for the gas channel and a small value in the electrode, such as 10^{-3}. The potentials are initialized as equal to the cell voltage for whole computational domain (including the electrode and catalyst layer). The liquid saturation in the GDL and CCL are also initialized to a small value, such as 10^{-2}. After initialization, both the solid-phase potential and membrane-phase potential equations are solved together. Once the potential

profiles are obtained, the conservation of species equations are solved for the entire domain and then the Darcy equation using the previous solution as initial values. Finally, the liquid water equation is solved and the entire solution procedure is repeated until the desire convergence is achieved. The solution is considered to be converged when the relative error of each dependent variable between two consecutive iterations is less than 10^{-6}. Once the converged solutions are obtained, the activation overpotential is calculated by plotting the membrane and solid phase potentials at the membrane/CCL interface.

For 2D simulation, the UMFPACK solver is chosen to solve the governing partial differential equations (PDEs) as it is faster. However, the UMFPACK solver requires higher computer memory compared to other solvers available in COMSOL Multiphysics®. Hence, the SPOOLES solver is also used in some cases, particularly for the refined meshes, as it saves half the memory [180]. For 3D simulation, the stationary nonlinear solver is used, and the general form of solution is chosen with the GMRES iterative solver and the geometric multigrid or SSOR techniques are used as pre-conditioners. Further, the governing equations are coupled together with the reaction rate term, hence, in the solution methodology an initial solution first obtained in a lower mesh and then the governing equations are solved individually at the higher level of mesh. The solutions are considered as converged solution when the preset tolerance value goes below 10^{-6} for each case. Detail description of the solvers, the pre-conditioners, and the error estimation used in this study can be found in the COMSOL Multiphysics® user's guide [180].

It is worthwhile to mention that the effective diffusivity in a two-phase system is dependent on the amount of liquid saturation. Therefore, the effective diffusivities are no more constant within the CCL and GDL of a PEM fuel cell. In reality, the amount of liquid saturation in the CCL and GDL varies significantly along the thickness of these layers. Hence, we employed the variable effective property approach. In this approach, the effective properties are first estimated based on the initial value of the liquid saturation using the formulation provided in Chapter 5. Once we obtain a solution of the liquid water equation based on the initial guess, the effective properties have been defined as a function of liquid water saturation for the subsequent iterations. Thus, the initial effective diffusivity is defined as

$$D_i^{\text{eff}} = D^{\text{eff}}\left(s_{l,i}\right) \tag{7.17}$$

where i represents the reactant species.

7.3 Mesh Generations

The 2D computational domain is initially discretized into a triangular mesh and Lagrangian elements of second order (quadratic elements) are used. It should also be noted that the numerical convergence becomes faster when quadratic elements are used in lieu of linear elements. However, elements of order greater than two may increase the computational load or cause instabilities in the solution. The use of quadratic elements implies that a triangular element has six nodes on its boundary (three at the vertices, and three at the midpoints of each side). Conversely, the 3D computational domain is discretized into a tetrahedral mesh with Lagrangian elements of second order. A hexahedral mesh is also used in the 3D simulation to compare the results of different meshes. Both of these meshes are shown in Fig. 7.2. It is worthwhile to note that the use of hexahedral mesh requires fairly regular-shaped geometries, while the tetrahedral mesh can be used for irregular-shaped geometries.

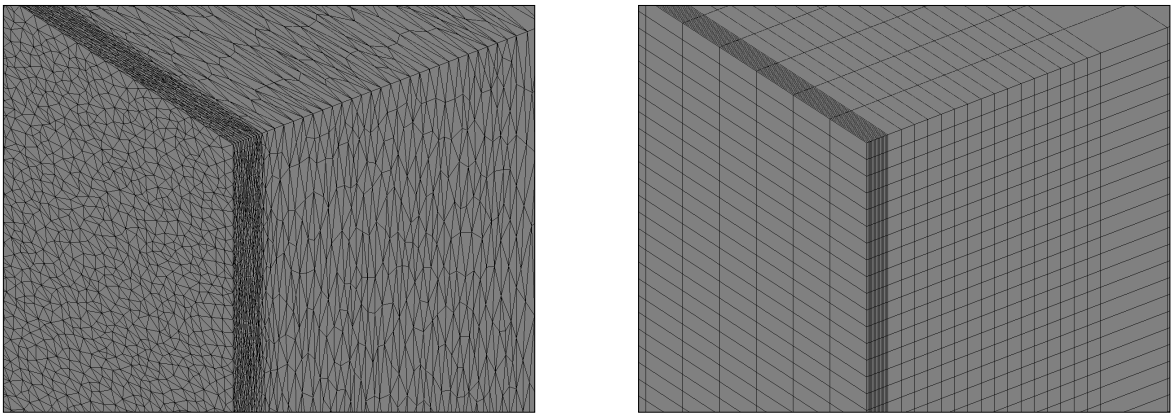

(a) Tetrahedral Mesh (b) Hexahedral Mesh

Figure 7.2: Demonstration of different meshes used in the 3D numerical simulations.

7.4 Convergence Criteria

The nonlinear iterations in COMSOL Multiphysics® terminate when a pre-defined convergence criterion is satisfied. If the current approximation to the true solution vector is U and the estimated error in this vector is E, then the software stops the iterations when the relative tolerance exceeds the relative error computed as the weighted Euclidean

norm [180]

$$\text{err} = \left(\frac{1}{N} \sum_{i=1}^{N} \left(\frac{|E_i|}{W_i} \right)^2 \right)^{1/2} \tag{7.18}$$

Here N is the number of degrees of freedom (DOF) and $W_i = \max(|U_i|, S_i)$, where S_i is a scale factor that the solver determines on the basis of the type of scaling option. For an automatic option, S_i is the average of $|U_j|$ for all DOFs j having the same name as DOF i times a factor equal to 10^{-5} for highly nonlinear problem or 0.1 otherwise. In this study, a relative tolerance of 10^{-6} is used as convergence criteria.

7.5 Grid Independent Solution

In order to ensure that the numerical results are grid independent, the governing variables are estimated in different grid sizes. Figure 7.3 shows the variation of oxygen mass fraction and liquid water saturation along the dimensionless distance from the membrane/CCL interface along the CCL and GDL thicknesses to the GDL/GFC interface for three different grids. Here the line represents the result of a coarser grid and the symbols are for the fine grids as indicated in the legend, namely, grid 1 (45409 triangular elements), grid 2 (60046 triangular elements), and grid 3 (104837 triangular elements). These results are plotted across the CCL and GDL thickness under the flow channel at a distance of $w/4$ from the top line of symmetry (see Fig. 7.1). Although a higher grid shows better results for the oxygen concentration in the CCL (comparing grid 1 with grid 3), the variation is merely visible in the GDL. Conversely, all the grids show almost identical liquid saturation results. Even liquid saturations at the CCL do not show any significant deviation with grid sizes. Hence, the results are presented for a grid size of 60000 triangular elements or higher for the 2D simulation. Similar test has been carried out for the 3D simulation to ensure a grid independent solution.

7.6 Summary

In this chapter, a detailed description of numerical implementation techniques developed in this thesis research for the PEM fuel cell have been presented along with pertaining boundary conditions. Further, a grid independency test results is provided to ensure that the results presented in this thesis are independent of the grid resolution.

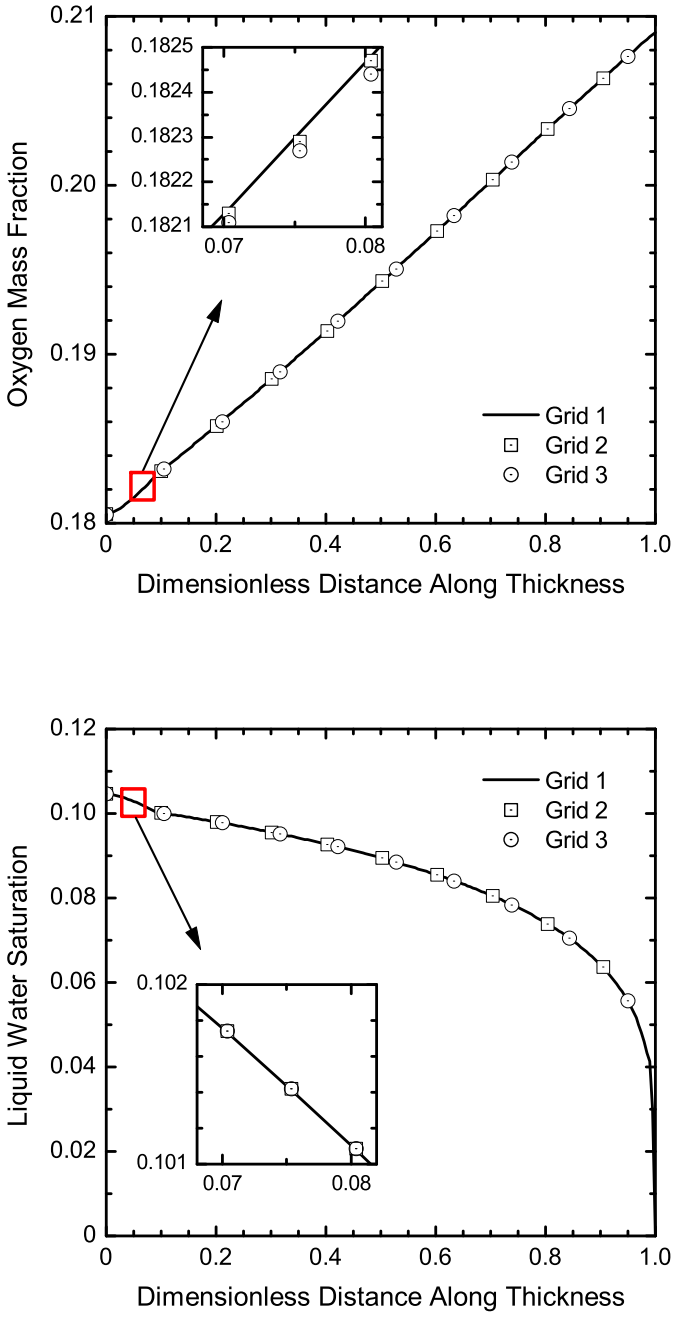

Figure 7.3: Oxygen mass fraction and liquid saturation profiles along the dimensionless thickness of CCL and GDL for different grids at $y = 3w/4$.

Chapter 8

Results and Discussion

In the previous chapters, the mathematical model of transport processes in the catalyst layer of a PEM fuel cell are described along with a 1D solution of liquid water transport and activation overpotential. The results based on these models are presented in this chapter that is divided into two segments. First the analytical model results and then the numerical model results are presented and discussed.

The performance and optimization of a PEM fuel cell is investigated using the analytical expression of activation overpotential presented in Chapter 6. The analytical expression of activation overpotential is also compared with the various data available in literature that covers empirical results, experimental data, and numerical predictions. Then design parameters have been incorporated in the model for focusing on the catalyst layer optimization including Nafion content (%weight (%wt) of Nafion), platinum content (%wt of platinum), platinum loading (mg/cm^2), void fraction, and catalyst layer thickness. An investigation has also been conducted for the effect of operating conditions on the cell performance. The liquid water transport in the CCL of PEM fuel cell is investigated using the 1D analytical model presented in Chapter 6. The effect of CCL wettability on liquid water transport and the effect of excessive liquid water (which is also known as "flooding") on reactant transport and cell performance have also been investigated. In addition, the liquid water saturation in the catalyst layer is analyzed using a dimensionless time contact analysis that is described in Section 6.5.3.

The numerical results include both the 2D and 3D model results of transport processes along with the result of a study of catalyst layer structure on the performance of fuel cell. Using the 2D numerical model, a parametric study has been performed to investigate how the catalyst layer structure and its surface wettability influence the liquid water transport. Conversely, in the 3D model, the main focus was given to the implementation

the volume-average mathematical model for future research. In addition, the effects of CCL surface wettability results are presented for the 3D case along with the effect of condensation/evaporation process on the overall liquid water production in a PEM fuel cell.

8.1 Activation Overpotential Model Comparison

In this section, a comparison between the present activation overpotential model predictions with the results available in the literature is provided [14, 16, 33, 181]. Although the analytical solution of activation overpotential provided in Chapter 6 is mathematically "exact", the comparison will provide an idea how accurate is the assumption made during the derivation process. Following this, the effect of operating conditions on the cell performance and results of an optimization study using the analytical activation overpotential formulation are provided. First a wide range of comparison has been covered that includes comparison with the empirical correlations [16], comparison with the experimental data [14, 181], and comparison with the numerical predictions [33] that are provided in the following subsections.

8.1.1 Comparison with Empirical Correlations

In the first set of comparison, the empirical correlation provided by Kim *et al.* [16] is used to generate empirical results. Two different sets of reactant gases were considered in their correlations. In the first set, air is used as the cathode gas and hydrogen as the fuel and in the second set, oxygen is used as the cathode gas and hydrogen as the fuel. In the empirical correlations, the experimental results were curve-fitted with an empirical equation for a PEM fuel cell with distinct terms of open circuit potential, activation overpotential, and ohmic overpotential. This empirical correlation eventually allowed us to incorporate their experimental estimates of ohmic resistance to obtain the total cell polarization. In addition, Kim *et al.* [16] provided another empirical relation that included mass-transport overpotential as an exponential function of the current density. The mass-transport overpotential is significant at higher current densities, particularly at close to the limiting current density. For comparison purpose, mass-transport term is also incorporated with one set of present model data. Finally, the cell voltage is calculated using the following relation, with the activation overpotential derived in Section 6.2:

$$E_{\text{cell}} = E_r - \frac{\mathscr{R}T}{\alpha_c n \mathscr{F}} \cosh^{-1}\left[\frac{1}{2\kappa}\left(\frac{\alpha_c n \mathscr{F} J \delta_{\text{CL}}}{\mathscr{R}T\sigma_m^{\text{eff}}}\right)^2 + 1\right] - R''_{\text{total}} J - a\exp(bJ) - E_{\text{mixed}} \tag{8.1}$$

Table 8.1: Parameters used to model the data from Kim *et al.* [16]

Parameter	Value
Cell width, W (cm)	7.07
Cell length, L (cm)	7.07
Electrode (GDL) thickness, δ_{GDL} (μm)	250
Catalyst layer thickness for O_2 as the cathode gas, δ_{CL} (μm)	12.3
Catalyst layer thickness for Air as the cathode gas δ_{CL} (μm)	0.26
Void fraction of the cathode electrode, ϵ_{GDL}	0.4
Membrane fraction in the catalyst layer for O_2 as the cathode gas, f_m	0.4
Membrane fraction in the catalyst layer for Air as the cathode gas, f_m	0.1
Catalyst loading per unit area, m_{Pt} (mg/cm^2)	0.3
Percentage of platinum on the carbon support for O_2, %Pt (%)	20
Percentage of platinum on the carbon support for Air, %Pt (%)	100
Mixed electrode potential for 1 atm of pressure, E_{mixed} (V)	0.17
Mixed electrode potential for 5 atm of pressure, E_{mixed} (V)	0.16

where a and b are the mass-transport coefficients [16].

Figure 8.1 depicts a comparison of the total polarization with the empirical results of Kim *et al.* [16] for air as the cathode gas in part (a), and oxygen as the cathode gas in part (b). Here, both lines represent the results of the present investigation for cell operating at 1 atm of pressure and 70 ℃; and symbols represent the corresponding empirical results. For both cases (with mass-transport overpotential and without mass-transport overpotential), the total cell potential is calculated using the identical parameters as provided in the literature with appropriate water flooding parameters [82]. The ohmic overpotential and the mass-transport overpotential are obtained directly using the equivalent internal ohmic resistance (R''_{total}) and the mass-transport coefficients (a and b in Eq. (8.1)). These values are available in Ref. [16] and the cell design parameters used in the model calculation are listed in Table 8.1. The comparison with the empirical results for cell operating condition of 5 atm of pressure and 70 ℃ is illustrated in Fig. 8.2. All parameters are the same as in Fig. 8.1 except the water flooding parameter, which is taken from Baschuk and Li [82] for the 5 atm and 70 ℃.

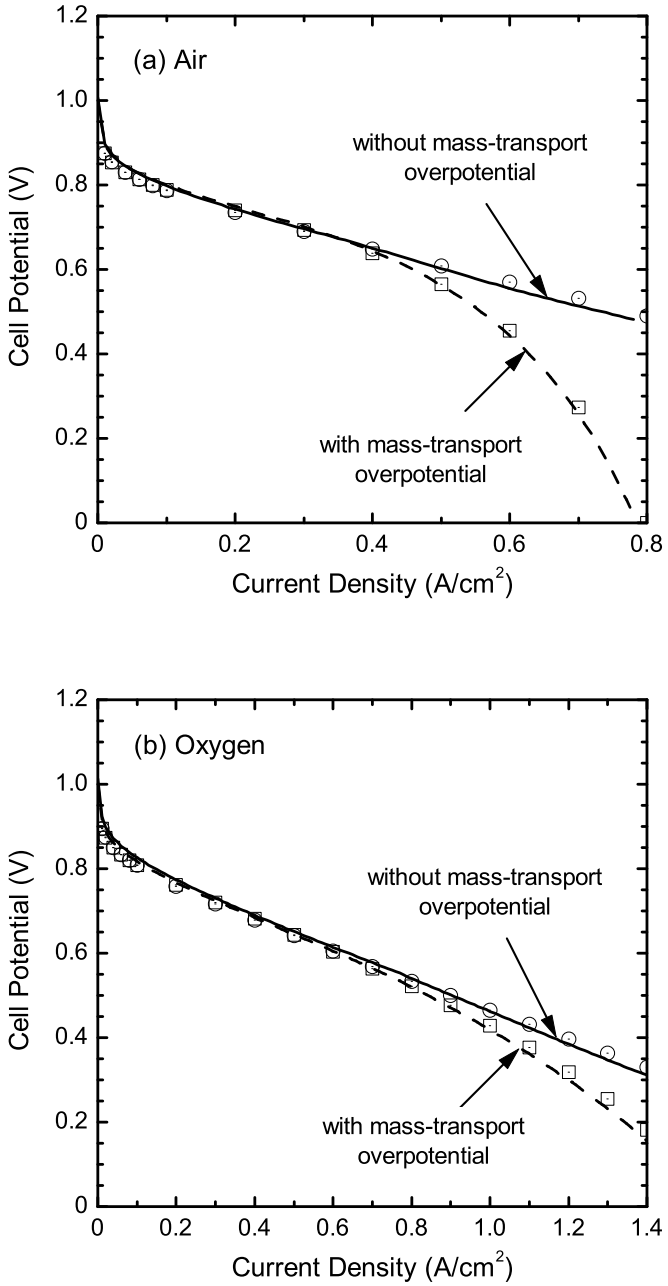

Figure 8.1: Comparison of the present analytical estimates of the cell polarization operating at 1 atm and 70 ℃ with the empirical data of Kim *et al.* [16] for (a) air as the cathode gas and hydrogen as the anode gas, and (b) oxygen as the cathode gas and hydrogen as the anode gas. The lines represent the analytical results of the present investigation whereas the symbols represent the empirical results for without mass-transport overpotential and with mass-transport overpotential as indicated in the figure.

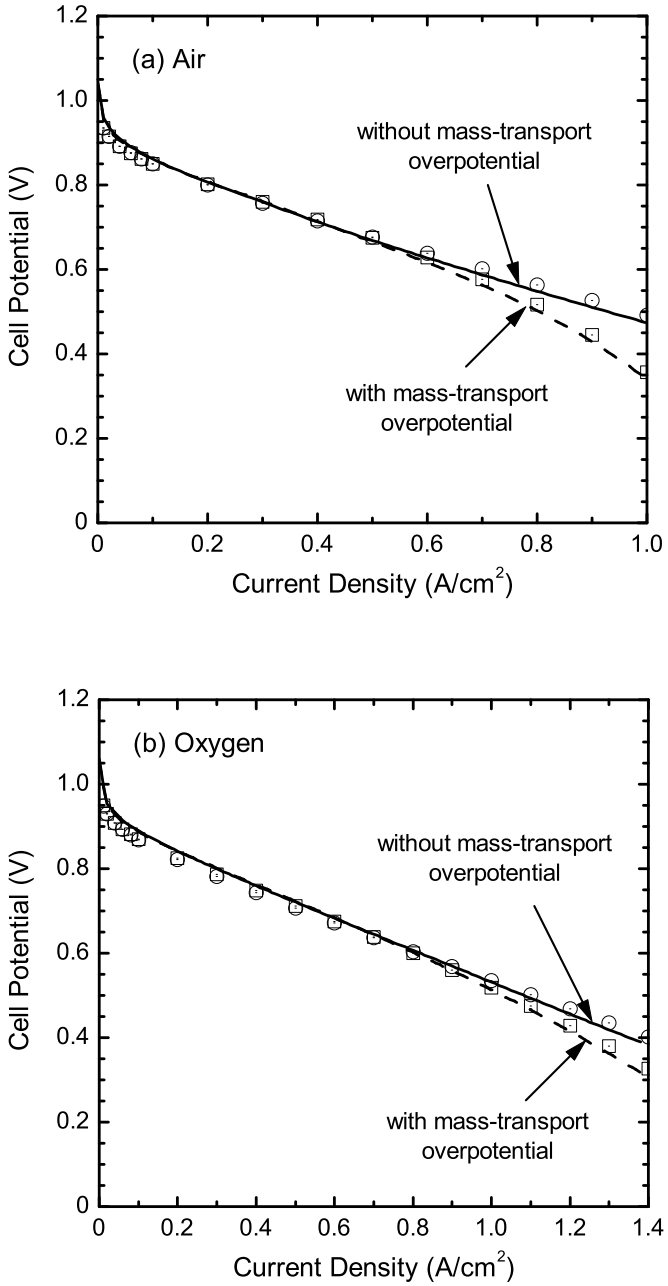

Figure 8.2: Comparison of the present analytical estimates of the cell polarization operating at 5 atm and 70 ℃ with the empirical data of Kim *et al.* [16] for (a) air as the cathode gas and hydrogen as the anode gas, and (b) oxygen as the cathode gas and hydrogen as the anode gas. The lines represent the analytical results of the present investigation whereas the symbols represent the empirical results for without mass-transport overpotential and with mass-transport overpotential as indicated in the figure.

The model results presented in Figs. 8.1 and 8.2 show that there is an excellent agreement between the empirical data and the estimates of the analytical model when water flooding of the cathode electrode is incorporated, particularly at intermediate current densities. In all the cases, the cell potential is slightly overestimated by the analytical model at lower current densities when $J < 0.1$ A/cm^2. Whereas the cell potential is slightly underestimated at higher current densities ($J > 0.6$ A/cm^2 for air and $J > 1.0$ A/cm^2 for oxygen). This is probably due to the assumption made for the analytical formulation. Here a constant oxygen concentration is assumed in the catalyst layer, which is giving lower activation overpotential in the CCL. Also the mixed electrode potential in the analytical model is estimated by matching the ohmic resistances at the intermediate current density. It has been found that the mixed electrode potential is approximately 0.17 V for 1 atm pressure and 70 ℃, and 0.16 V for 5 atm pressure and 70 ℃. The main reasons why an excellent agreement has been observed between the empirical data and analytical estimates are smaller cell dimension, high reactant flow rate, and activation overpotential (exists at low current density only). For a smaller cell with high reactant flow rate and at low current density, the variation of oxygen concentration inside the CCL is small (or negligible) that lies within the assumptions used in the analytical formulation.

It should also be noted that the water flooding data is not available for low current densities, and zero flooding has been assumed for those cases. This is also a reason for the slight overestimation of the cell potential at low current densities. Conversely, Kim *et al.* [16] reported various open circuit voltages, which imply various mixed electrode potentials involved in their experiments. Here, only the cathodic activation overpotential has been considered along with the ohmic overpotential and iterative estimates of mixed electrode potential. The anodic overpotential has been neglected, which might be another reason for this slight overestimation. Further, at higher current densities, the estimated oxygen concentration is lower than the real fuel cell's concentration as only 1D linear decay of oxygen profile has been considered. Oxygen concentration might not decay that rapidly in the test fuel cell due to the 3D distribution of the liquid water in the GDL. Hence, a high activation overpotential value has been estimated at a large current density and lower cell potential. Nonetheless, these comparisons reveal the robustness of the present analytical formulation.

8.1.2 Comparison with Experimental Data

In the second set of comparison, the present model predictions are compared with the experimentally determined cell performance data. Figures 8.3 and 8.4 show the comparison between the model predictions and the experimental results of Ballard's BAM® Composite

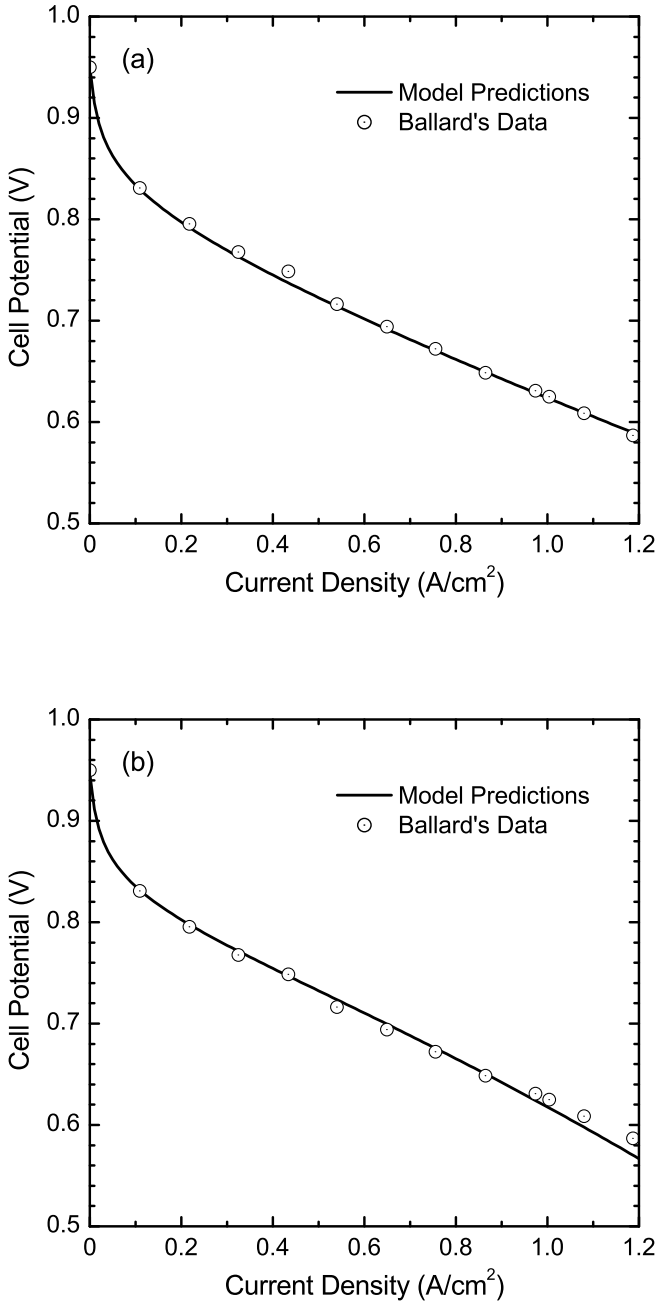

Figure 8.3: Comparison between the present analytical predictions and the experimental results of Ballard's BAM® Composite cell operating at 3.02 bar and 80 ℃ for air as the cathode gas and hydrogen as the anode gas [181] for two types of ohmic resistances (a) constant ohmic resistance, and (b) variable ohmic resistance calculated using Eq. (6.46) taken from Ref. [14, 15], originally developed for Mark® IV fuel cells.

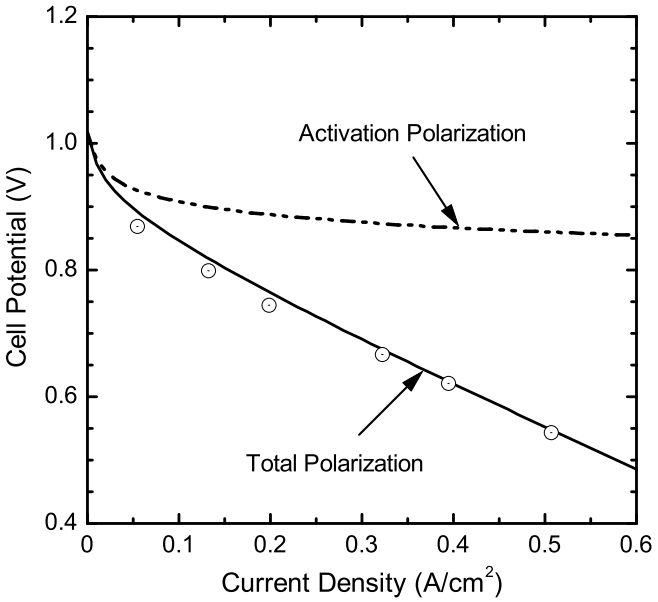

Figure 8.4: Comparison between the present analytical predictions with the experimental results of Ballard Mark® IV fuel cell system operating at 70 ℃ using 30 psig H_2 and 30 psig O_2 [14].

fuel cell [181] and Ballard Mark® IV fuel cell [14], respectively. The Ballard BAM® Composite cell data were from a cell being operated at 3.02 bara pressure, 80 ℃ and using air as the oxidant. The Ballard Mark® IV fuel cell system data were taken from a cell operating at 30 psig pressure, 70 ℃ and using oxygen as the oxidant. The cell design parameters used for fitting these experimental data are listed in Table 8.2. For the Ballard BAM® Composite cell data, two techniques in ohmic overpotential calculation have been considered. In Fig. 8.3a, the ohmic resistance is estimated directly from the slope of the experimental polarization curve; whereas in Fig. 8.3b, the total internal ohmic resistance is obtained using Eq. (6.46) taken from Ref. [14, 15], originally developed for the Mark® IV fuel cells. Both sets of the model predictions and the experimental results show good agreement like the empirical results shown in the previous section. The empirical formulation for internal ohmic resistance provides a slight underestimation of the cell potential for higher current densities (Fig. 8.3b). This underestimation could easily be explained by comparing the ohmic resistance variations with current density, as ohmic resistances are higher for higher current densities in Fig. 8.3b compared to the ohmic resistance in Fig. 8.3a. The ohmic resistance in Fig. 8.4 is considered as constant and calculated directly from the experimental data. For illustration purpose, the activation polarization curve is also included in Fig. 8.4. It has been seen that the present model also agrees with Mark® IV fuel cell data, like the comparison with Ballard BAM® Composite cell.

Table 8.2: Cell design parameter used to model Ballard BAM® Composite cell and Ballard Mark® IV cell data

Parameter	Value	
	BAM®	Mark® IV
Electrode (GDL) thickness, δ_{GDL} (μm)	200	200
Catalyst layer thickness, δ_{CL} (μm)	10	10
Electrode void fraction, ϵ_{GDL}	0.4	0.4
Membrane fraction in catalyst layer, f_m	0.65	0.4
Catalyst loading per unit area, m_{Pt} (mg/cm^2)	0.332	0.3
Platinum percentage on the carbon support, %Pt (%)	40	20
Mixed electrode potential, E_{mixed} (V)	0.243	0.189

8.1.3 Comparison with Numerical Results

Figure 8.5 demonstrates the present model predictions and the 1D numerical results of Rowe and Li [33] for a PEM fuel cell running with 3 atm and 80 ℃ air as the cathode gas and hydrogen as the anode gas as the third set of comparison. Using the parameter values listed in Table 8.2, the predicted polarizations based on the analytical formulation are compared with the numerical data for 20%wt of Pt/C catalyst loading. The solid line depicts the total polarization curve for constant ohmic overpotential, and the dashed line represents the total polarization with variable ohmic overpotential (using Eq. (6.46)), whereas the dashed-dot-dot line shows the corresponding activation polarization curve. Here symbols are showing the numerical predictions of Rowe and Li [33]. It is seen from this comparison that the proposed analytical model is also capable of producing the identical results of numerical model developed earlier in literature. Both the constant ohmic overpotential case and the variable ohmic overpotential results agree well with the numerical result up to $J \leqslant 0.6$ A/cm^2. Once again, variable ohmic overpotential model underestimates the cell potential for large current densities like Fig. 8.3b. Unlike Fig. 8.4, here more common trend has been noticed in the cell polarization that the activation overpotential is larger than the ohmic overpotential.

The results provided in the previous subsections elucidate a considerable insight about the proposed analytical model and its robustness. It should also be noted that no adjustment to the reactive surface area, A_v, or the reference exchange current density, $J_0^{\text{O}_2}$,

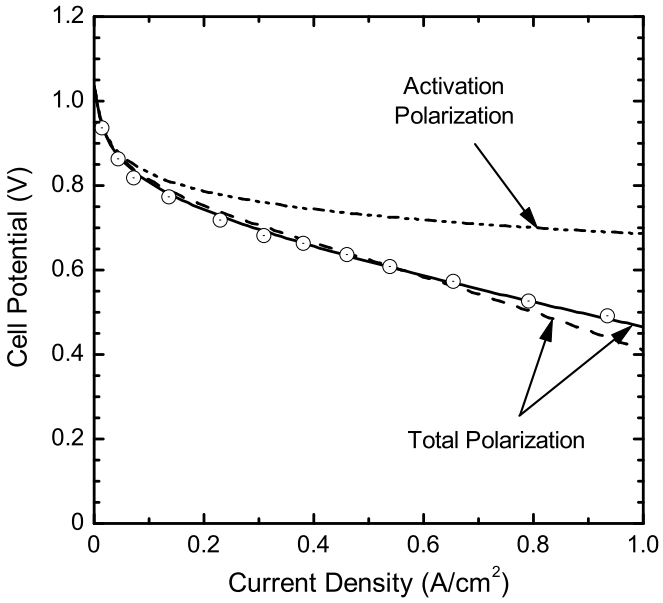

Figure 8.5: Polarization curve estimated by the present analytical model with the 1D numerical model of Rowe and Li [33] for a PEM fuel cell operating at 3 atm and 80 ℃ with air as the cathode gas. Solid line represents the analytical polarization curve for constant ohmic overpotential, the dashed line is for variable ohmic overpotential (using Eq. (6.46)), and symbols represent the numerical results of Rowe and Li [33]; whereas dashed-dot-dot line shows the corresponding activation polarization curve.

is required to achieve the level of agreement shown in Figs. 8.1–8.5 as all the parameter values are taken directly from the literature. However, the results shown in Section 8.1.2 for the comparison with the experimental results, the reactive surface area, A_v, and the exchange current density, $J_0^{\mathrm{O_2}}$, have been assumed similar to the value used in Fig. 8.1 as no such data were reported by Amphlett *et al.* [14]. In addition, fraction of Pt-loading in the catalyst layer has also been assumed in modeling the experimental results due to missing information in the literature.

The model predictions have also been tested by changing the fraction of Pt-loading, and that does not show any significant effect on the total cell polarization. For instance, for the Ballard BAM® composite fuel cell changing the %Pt between 30% to 50% provides almost identical results as shown in Fig. 8.3. The only parameter that has been adjusted during these comparisons is the mixed electrode potential (E_{mixed}). Even for Ballard BAM® composite fuel cell, it has been observed that without using Eq. (6.42) one can generate identical results of Ballard's experimental results by taking $E_{\mathrm{oc}} = E_{\mathrm{cell}}$ for $J \to 0$ from their experimental curve. Also noted here, the adjustment on the mixed electrode potential does not change the behavior of the polarization curve as E_{mixed} is independent of

Table 8.3: Parameters used to model the data of Rowe and Li [33]

Parameter	Value
Electrode (GDL) thickness, δ_{GDL} (μm)	200
Catalyst layer thickness, δ_{CL} (μm)	7
Electrode void fraction, ϵ_{GDL}	0.4
Membrane fraction in the cathode catalyst layer, f_m	0.45
Catalyst layer flooding (%)	99
Platinum percentage on the carbon support, %Pt (%)	20
Specific reaction surface area, A_v (cm^2/cm^3)	1×10^5
Reference current density, $J_0^{\text{O}_2}$ (A/cm^2)	9.5×10^{-8}
Membrane conductivity, σ_m (S/cm)	0.15
Mixed electrode potential for 1 atm of pressure, E_{mixed} (V)	0.158

cell parameters as well as independent of current density. Hence, the analytical formulation can be used in the performance and optimization study with proper ohmic overpotential formulation avoiding complicated numerical computations or expensive experiments to predict the polarization of PEM fuel cell. Moreover, this method is not only as simple as shown in Eq. (6.24) but also as accurate as experimental predictions.

8.2 Cell Performance and Optimization

A comprehensive comparison of the present analytical model predictions with the various data available in literature has already been provided in the previous section. In this section, a performance and optimization analysis will be carried out based on the analytical formulation developed in this thesis. In the following section, the results are given using the analytical expression given in Eq. (6.24) and the ohmic overpotential is calculated using the ohmic resistance given by Eq. (6.46) in all subsequent results.

8.2.1 Effect of Operating Conditions

Figure 8.6 depicts the effect of operating temperature on the cell potential for air as the cathode gas (Fig. 8.6a), and oxygen as the cathode gas (Fig. 8.6b). Here an un-flooded

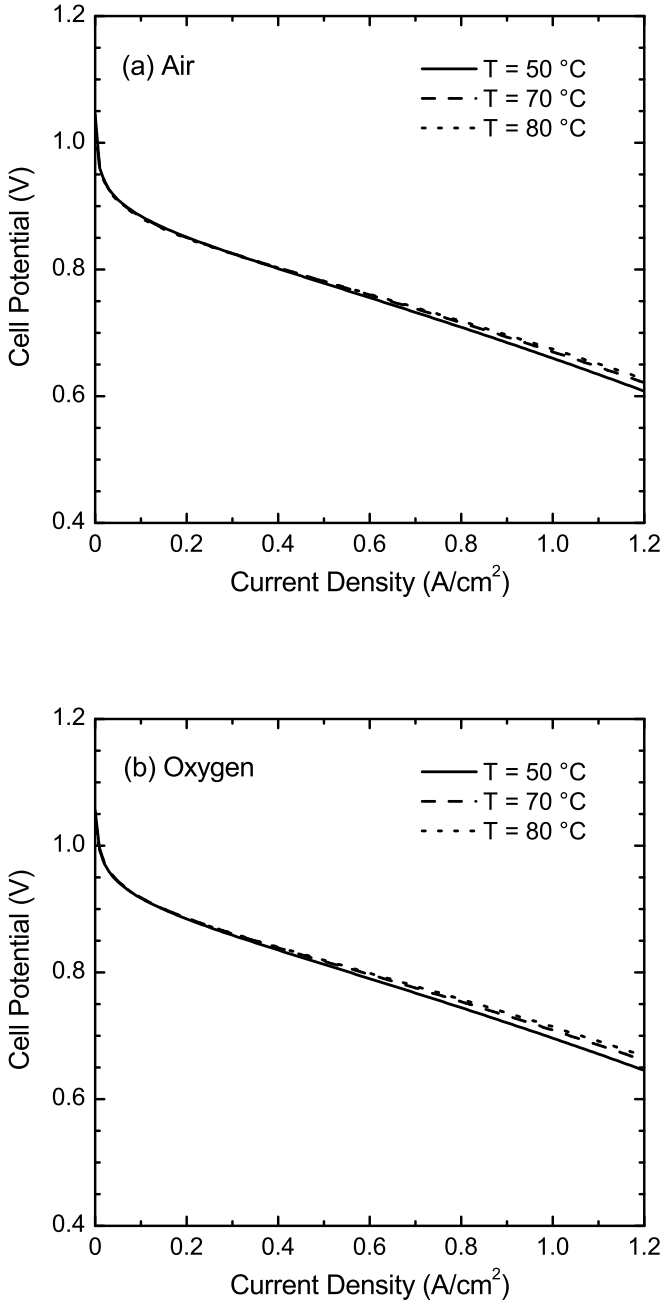

Figure 8.6: Effect of temperature on the performance of PEM fuel cell with a flooded CCL operating at 3 atm with (a) air as the cathode gas, and (b) oxygen as the cathode gas for the base case.

electrode and fully-flooded catalyst layer has been considered to model these results. Detailed description of the base case operating and physical parameters used in the present model calculations are given in Table 8.4. The present model predictions show almost negligible temperature effect on the cell polarization curve for both air and oxygen based fuel cells. However at large current densities, a slight increase in cell potential is observed as temperature is increased. For instance, at $J = 0.8$ A/cm^2 cell potential is about 10 mV higher for 80 ℃ compared to the cell potential at 50 ℃. Ideally, the cell polarization decreases with an increase in the cell operating temperature due to better electrochemical reaction at higher temperatures. Here only small difference has been observed since the reversible cell potential decreases with the temperature as well. However, the Ballard Power Systems suggest that there is approximately a 30% increase in cell potential when the temperature is increased from 30 ℃ to 80 ℃, no such improvement has been observed here like Marr and Li [80]. This is largely due to the fully-flooded catalyst layer, where temperature has less effect on the cell potential than the partially flooded catalyst layer.

A better explanation of such temperature effect might be possible by investigating the response of the activation polarization with temperature. Figure 8.7 shows the variation of the activation overpotential with current density for air as the cathode gas (Fig. 8.7a), and oxygen as the cathode gas (Fig. 8.7b) for three different temperatures as indicated in the legend. For both cases, similar trend has been observed in the activation overpotential as it increases with the temperature. Further, Fig. 8.8 illustrates how the ohmic overpotential varies with the current density when temperature changes. Similar to the activation overpotential, ohmic overpotential also decreases with increasing temperature. Hence, temperature always reduces the total losses for PEM fuel cell, though cell performance did not improve accordingly due to the reduction of reversible cell potential. As seen from the present result, reversible cell potential decreases about 27 mV; and the activation and the ohmic overpotential decrease about 16 mV and 21 mV, respectively, at $J = 0.8$ A/cm^2 for an increase of temperature from 50 ℃ to 80 ℃.

The effect of operating pressure on the cell potential for an un-flooded electrode and fully-flooded catalyst layer of PEM fuel cell is shown in Fig. 8.9. These results are modeled using the identical parameters as used in Fig. 8.6. It is seen that the cell potential increases with the cell operating pressure, and are consistent with the results reported in literature [80]. As the empirical correlation of the ohmic overpotential is independent of cell operating pressure, these changes are purely due to the reduction in activation overpotential with pressure. However, in reality, pressure will affect the water flooding, and hence, the ohmic overpotential. The corresponding variations of activation overpotential with pressure are shown for air in Fig. 8.10a, and for oxygen in Fig. 8.10b. These results suggest that by increasing pressure from 1 atm to 5 atm, it is possible to attain almost 20%

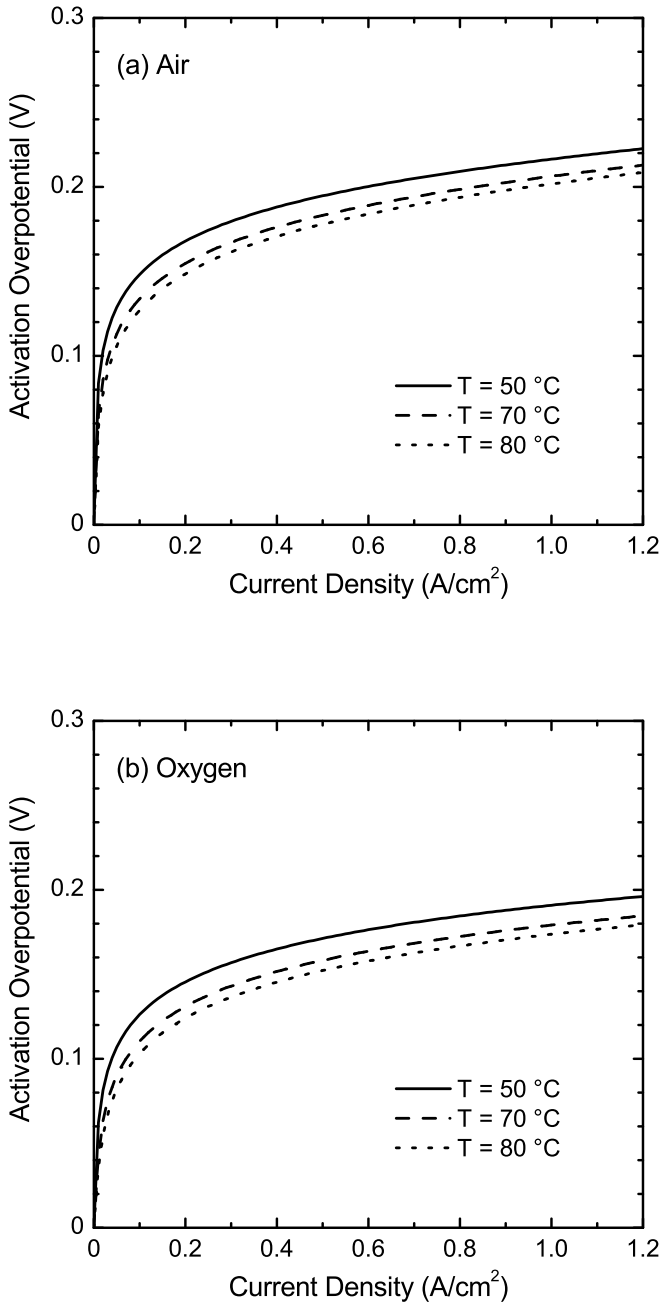

Figure 8.7: Variation of the activation overpotential with current density for the base case with (a) air as the cathode gas, and (b) oxygen as the cathode gas for three different temperatures.

Table 8.4: Base case operating and physical parameters used in the present model calculations.

Parameter	Value
Operating temperature, T (°C)	80
Operating pressure, P (atm)	3
Length of the cell, L (cm)	5
Width of the cell, W (cm)	5
Electrode thickness, δ_{GDL} (μm)	250
Catalyst layer thickness, δ_{CL} (μm)	10
Void fraction of the cathode electrode, ϵ_{GDL}	0.4
Fraction of membrane in the cathode catalyst layer, f_m	0.4
Catalyst layer flooding (%)	100
Catalyst loading per unit area, m_{Pt} (mg/cm^2)	0.3
Platinum percentage on the carbon support, %Pt (%)	20
Membrane conductivity, σ_m (S/cm)	0.17
Density of platinum, ρ_{Pt} (g/cm^3)	21.5
Density of carbon black, ρ_{C} (g/cm^3)	2.0
Reference oxygen concentration, $c_{\mathrm{O_2,ref}}$ (mol/m^3)	1.2
Transfer coefficient, α_c	0.5
Mixed electrode potential, E_{mixed} (V)	0.175

reduction in activation overpotential at $J = 0.8$ A/cm^2. The analytical expression derived for the activation overpotential does not have any pressure term; hence, these reductions are mainly due to the change in oxygen concentration with pressure. Also higher pressures represent higher diffusion coefficients of oxygen through the electrode and enhance cell performance. It is also evident from these results for the effect of the operating conditions that both pressure and temperature have significant effect on the activation overpotential, whereas the ohmic overpotential is only affected by temperature. Therefore, to improve the cell performance or to reduce the cell polarization, it is always important to optimize the activation losses than the ohmic losses. In the following subsections, the optimization of cathode catalyst layer, particularly Nafion content, Pt-loading and CCL thickness, and their optimization for optimum cell performance are presented.

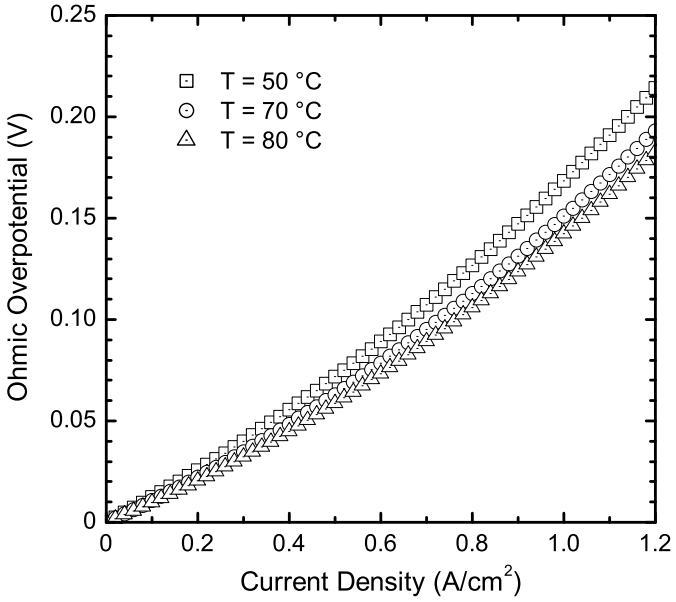

Figure 8.8: Variation of the ohmic overpotential with current density for the base case for three different temperatures.

8.2.2 Optimization of Platinum Loading

As mentioned earlier, one of the barriers to the commercialization of PEM fuel cell is its cost. This is largely due to the high Pt-loading, which is used as the catalyst in the cathode catalyst layer to promote the slow oxygen reduction reaction. Therefore, it is essential to reduce the amount of platinum in the catalyst layer while ensuring sufficient catalyst to enhance oxygen reduction reaction. In this section, the effect of Pt-loading on the cell potential as well as its optimization will be considered. Figure 8.11 shows the variation of cell potential with current density with air as the oxidant in part (a), and oxygen as the oxidant in part (b), for five different Pt-loadings as indicated in the legend. The parameters used in this figure are listed in Table 8.4.

The effect of Pt-loadings on the cell potential shows that an increase in the Pt-loading increases the cell potential for $m_{\mathrm{Pt}} \leq 0.2$ mg/cm^2, while the cell potential drops with an increase in the Pt-loading for $m_{\mathrm{Pt}} > 0.2$ mg/cm^2 for both air and oxygen. For instance, in Fig. 8.11a, the cell voltages are 0.7852 V, 0.7842 V, and 0.7817 V at 0.5 A/cm^2 for Pt-loadings of 0.2 mg/cm^2, 0.25 mg/cm^2, and 0.3 mg/cm^2, respectively. It is evident that increased amount of Pt-loading in the catalyst layer did not improve the oxygen reduction reaction or the cell performance for $m_{\mathrm{Pt}} > 0.2$ mg/cm^2. This is largely due to the reduction in oxygen diffusion, due to the high Pt-content in the catalyst layer that blocks the passage for diffusion. In addition, excessive platinum does not always imply

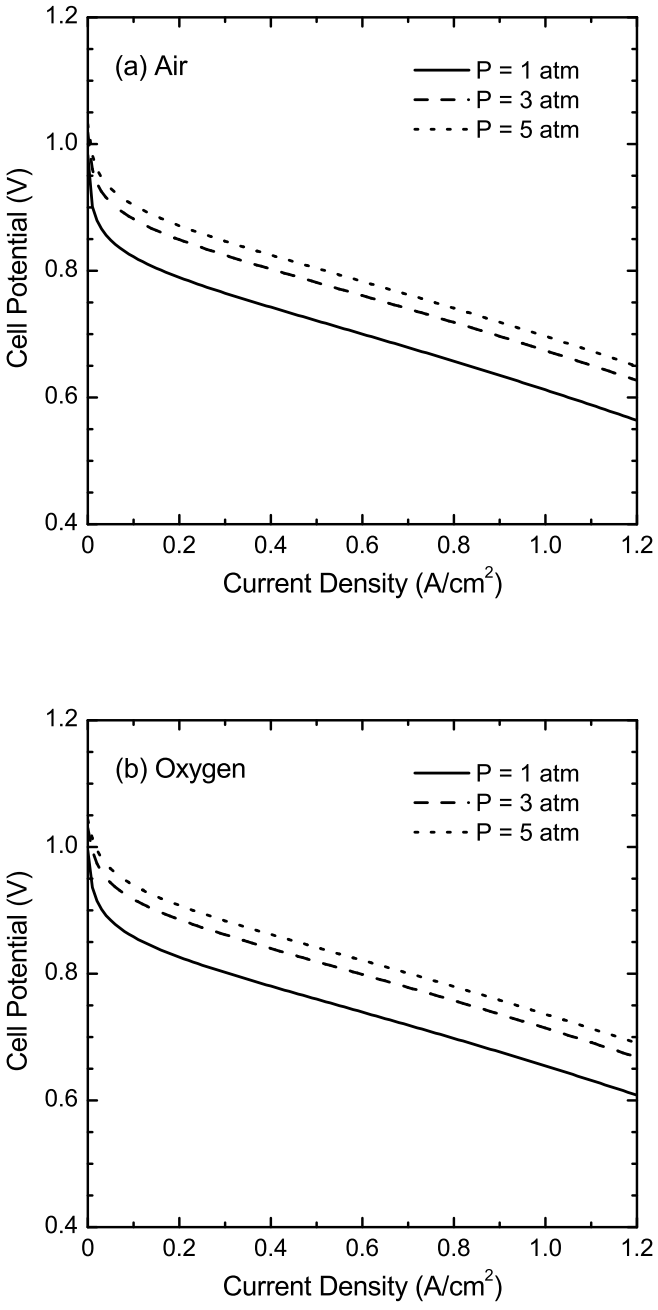

Figure 8.9: Effect of pressure on cell performance for a fully-flooded cathode catalyst layer for the base case with (a) air as the cathode gas, and (b) oxygen as the cathode gas.

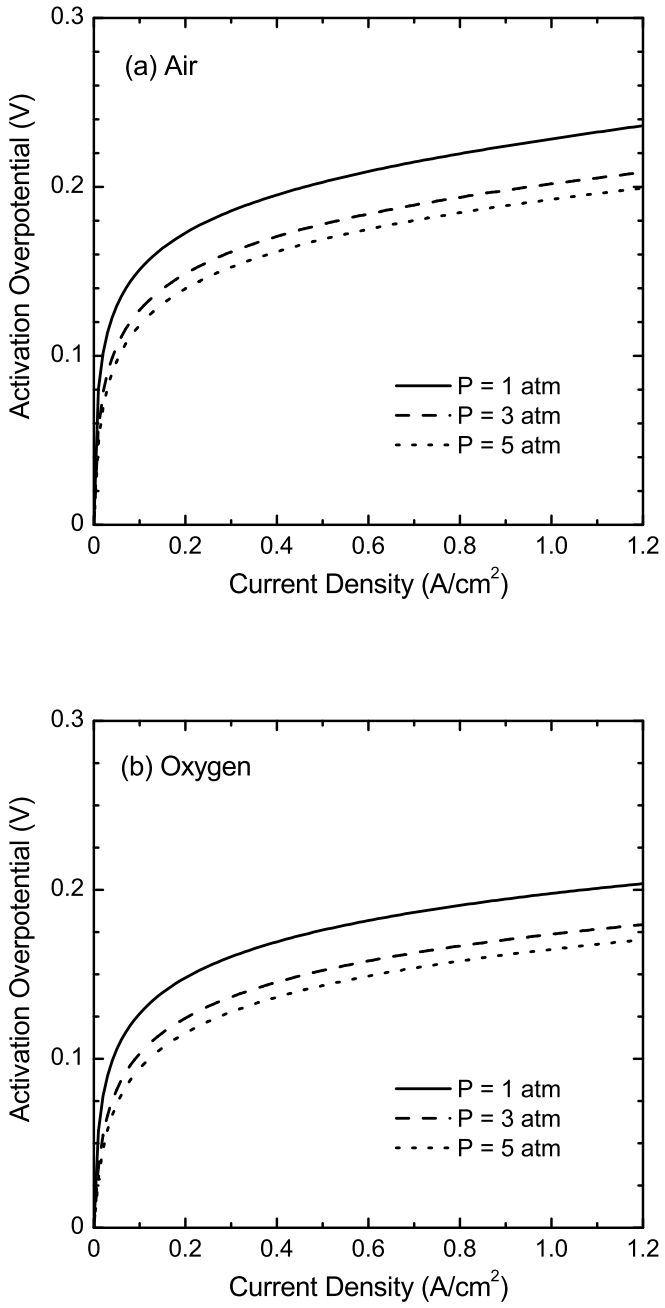

Figure 8.10: Variation of the activation overpotential with current density for the base case with (a) air as the cathode gas, and (b) oxygen as the cathode gas for three different pressures.

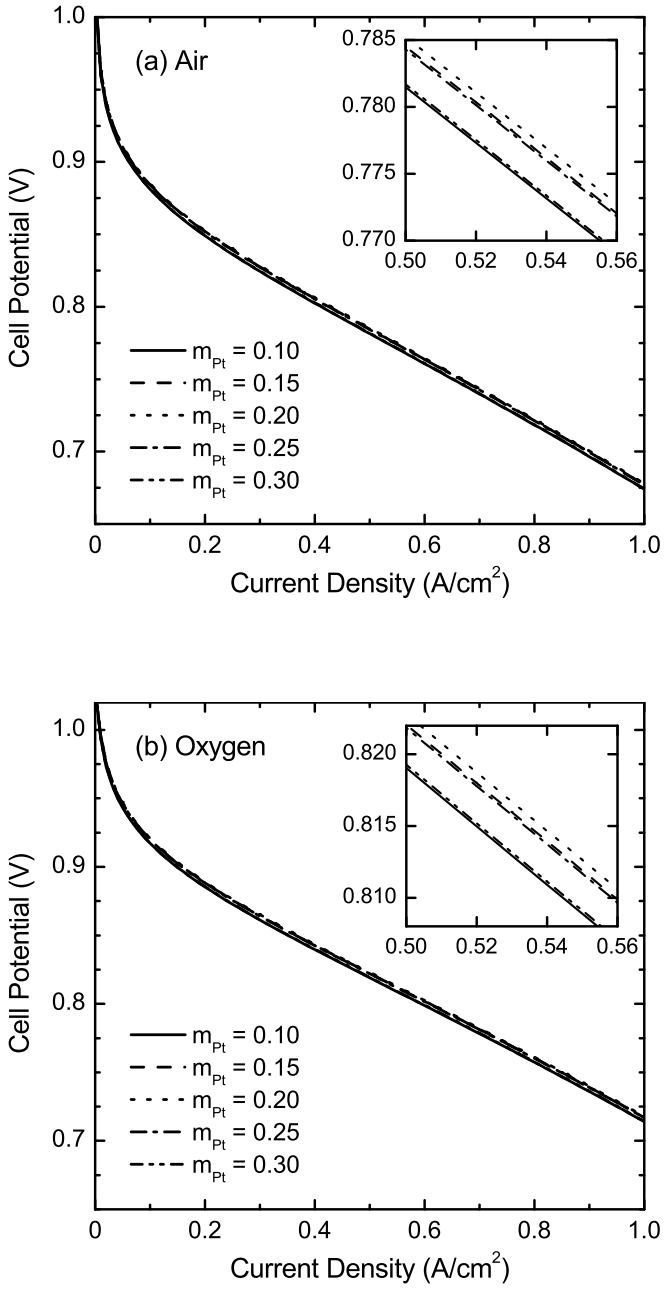

Figure 8.11: Variation of the cell potential with current density for the base case with (a) air as the cathode gas, and (b) oxygen as the cathode gas for different platinum loadings.

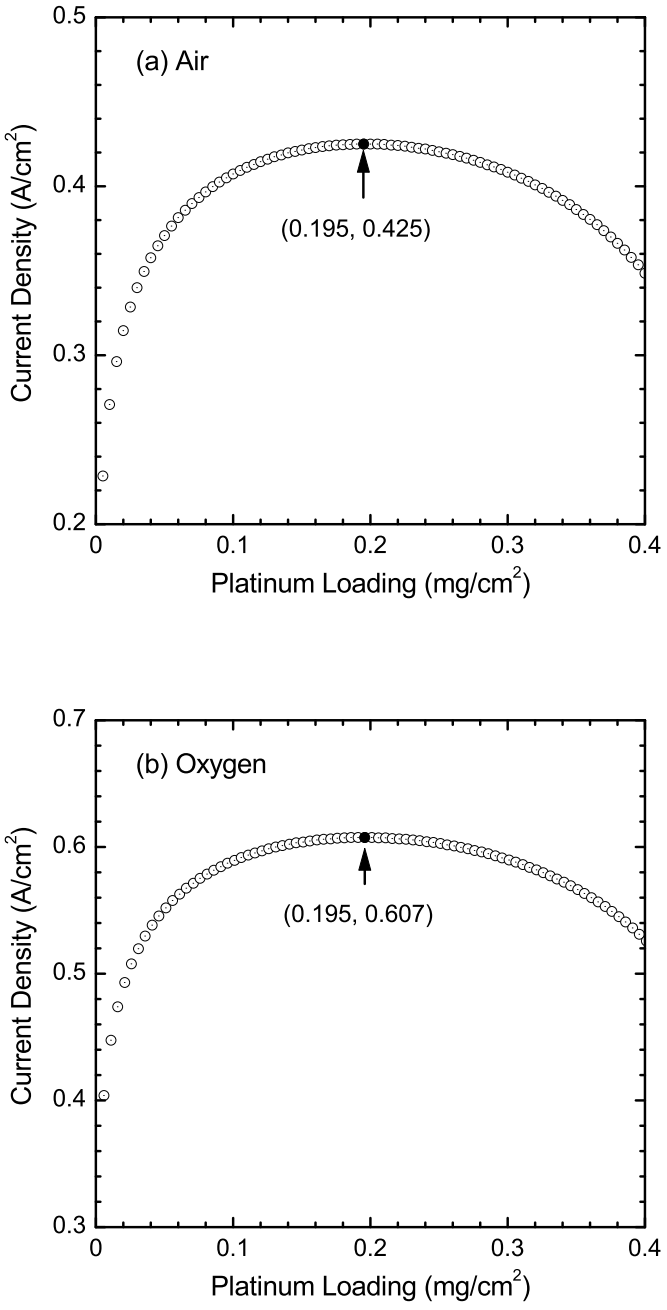

Figure 8.12: Optimum platinum loading as a function of current density at a cell potential of 0.8 V for (a) air as the cathode gas, and (b) oxygen as the cathode gas.

effective use of Pt-catalyst. It also reduces the reactive surface areas for oxygen reduction reaction that eventually reduces the cell performance at higher catalyst loadings.

Figure 8.12 depicts the optimum Pt-loading as a function of the current density at a given cell potential of 0.8 V. Two parts of this figure represent the results of air as the cathode gas and oxygen as the cathode gas as mentioned in the figure. It is found that at the highest current density, the amount of Pt-loading is about 0.195 mg/cm^2 for both air and oxygen. It is close to the conclusion of Song *at el.* [182], though they found 0.21 mg/cm^2 of optimum Pt-loading for the given electrode potential of 0.6 V with completely different parameter values. It also reveals that for 0.4 mg/cm^2 of Pt-loading, the cell power output decreases by about 20% for air and about 13% for oxygen compared to the optimum Pt-loading case. Clearly, optimization not only reduces the cost of the fuel cell but also improves the performance. Once again, Song *at el.* [182] obtained their results using complicated agglomerate model, which also requires numerical solution to a set of governing equations; whereas the present analytical model is easier for practical applications.

8.2.3 Effect of Nafion Fraction

The effect of the various amounts of Nafion fractions in the cathode catalyst layer is shown in Fig. 8.13 for air and oxygen as the cathode gas as indicated in the figure. In these figures, the amount of Pt-loading is used as 0.2 mg/cm^2 and all other parameters are the same as listed in Table 8.4. The results shown in these figures indicate that an increase in the membrane content in the catalyst layer increases the cell potential for both air and oxygen. This is due to the reduction in the resistance to proton transport to the reaction sites, consequently reducing the activation overpotential with higher membrane contents in the catalyst layer. Here an empirical formulation is used for the ohmic overpotential that is a function of current and cell temperature only. Hence, changing the amount of membrane did not change the corresponding ohmic overpotential. Generally, higher Nafion fraction reduces resistance to proton transport but would increase resistance to oxygen transport - a balance gives the "best" or "optimal" Nafion fraction in the CCL.

8.2.4 Optimization of Catalyst Layer Thickness

Conflicting observations have been reported in literature for the effect of CCL thickness on the cell potential. It has been claimed that a thicker catalyst layer can generate a higher current [87] as well as the polarization of PEM fuel cell increases with the increase of the catalyst layer thickness because of the limited rate of mass diffusion [6]. It seems

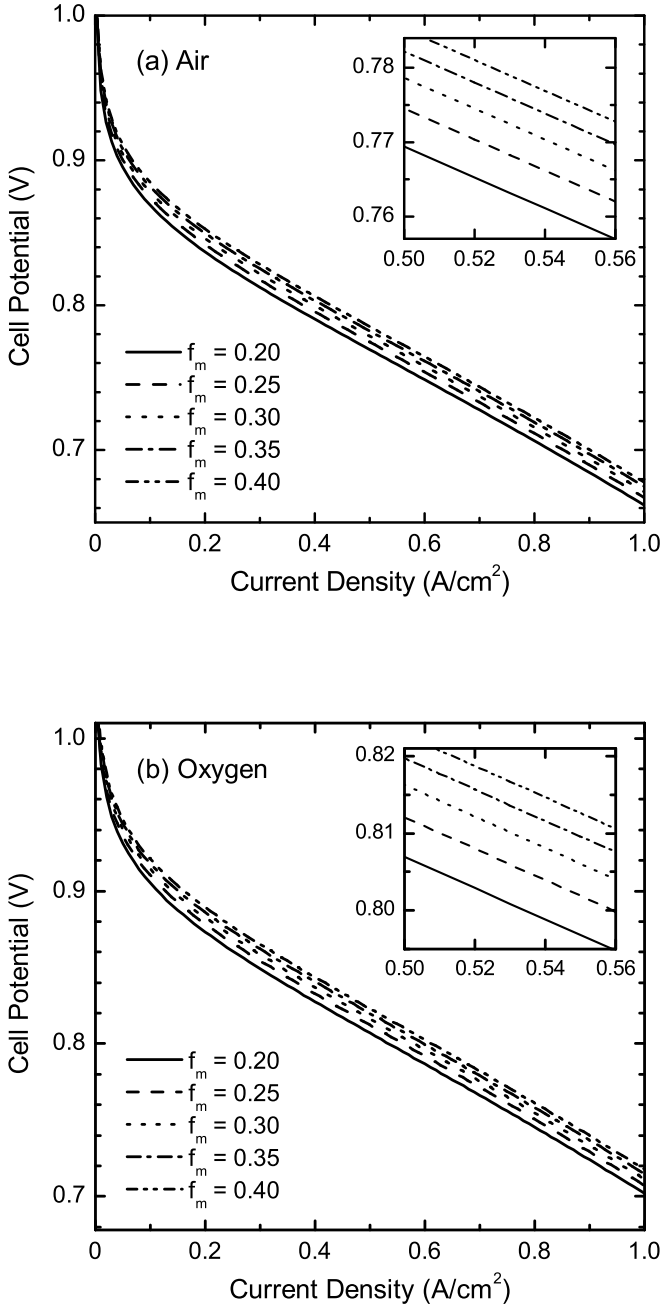

Figure 8.13: Effect of ionomer fraction in the catalyst layer on the cell potential with (a) air as the cathode gas, and (b) oxygen as the cathode gas for a Pt-loading of 0.2 mg/cm^2.

the second statement will be more appropriate as the mass diffusion rate is reduced with the catalyst layer thickness. In this section, the effect of catalyst layer thickness on the cell performance using the present analytical formulation will be investigated. Figure 8.14 shows the effect of catalyst layer thickness on the cell output for air and oxygen as the cathode gas with a Pt-loading of 0.2 mg/cm^2. Five different catalyst layer thicknesses are considered as indicated in the legend. All other parameters are the same as listed in Table 8.4.

For a given Pt-loading, it has been observed that the cell potential increases rapidly with the increase of CCL thickness for $\delta_{\mathrm{CL}} \leq 10$ μm. For $\delta_{\mathrm{CL}} > 10$ μm, the results are completely opposite as the cell potential decreases slowly with the increase of the catalyst layer thickness due to the limited rate of mass diffusion in the catalyst layer as well as lower active surface area per unit volume. One might also question that the increase of CCL thickness will also increase the ohmic overpotential, and hence it is almost impossible to obtain better cell performance with thicker catalyst layer like Wang *et al.* [87] found. It is also noted that the ohmic overpotential formulation used in this study is independent of catalyst layer thickness. Therefore, the changes observed in the cell potential are purely due to the change of activation overpotentials. When the catalyst layer thickness increases, it decreases the catalyst reactive surface area per unit volume since the Pt-loading per unit area is constant; and hence increases the activation overpotential.

To provide clearer evidence how the catalyst layer thickness affect the cell potential, the cell current density is plotted as a function of catalyst layer thickness. Figure 8.15 shows the variation of current density with catalyst layer thickness for a given electrode potential of 0.8 V for air (Fig. 8.15a) and oxygen (Fig. 8.15b) as the cathode gas. Here three lines represent different Pt-loadings as indicated in the legend and all other parameters are identical to the conditions for Fig. 8.14. It is seen again that with the increase of the catalyst layer thickness, initially the cell current density increases rapidly and then decreases slowly after reaching a certain catalyst thickness for both the air and the oxygen cases. The thickness corresponding to highest current density is the optimum thickness of the catalyst layer for that Pt-loading. It is found that the optimum thicknesses are 10.5$\pm$1 μm, 13$\pm$1.5 μm, and 15.75$\pm$1.75 μm for m_{Pt}= 0.2 mg/cm^2, 0.25 mg/cm^2, and 0.3 mg/cm^2, respectively. It also implies that the higher the Pt-loading the wider the optimum zone of the catalyst layer thickness and the higher the optimum catalyst layer thickness. Therefore, it is always desirable to design PEM fuel cells in the vicinity of optimum zone that will eventually decrease the cost with better cell performance.

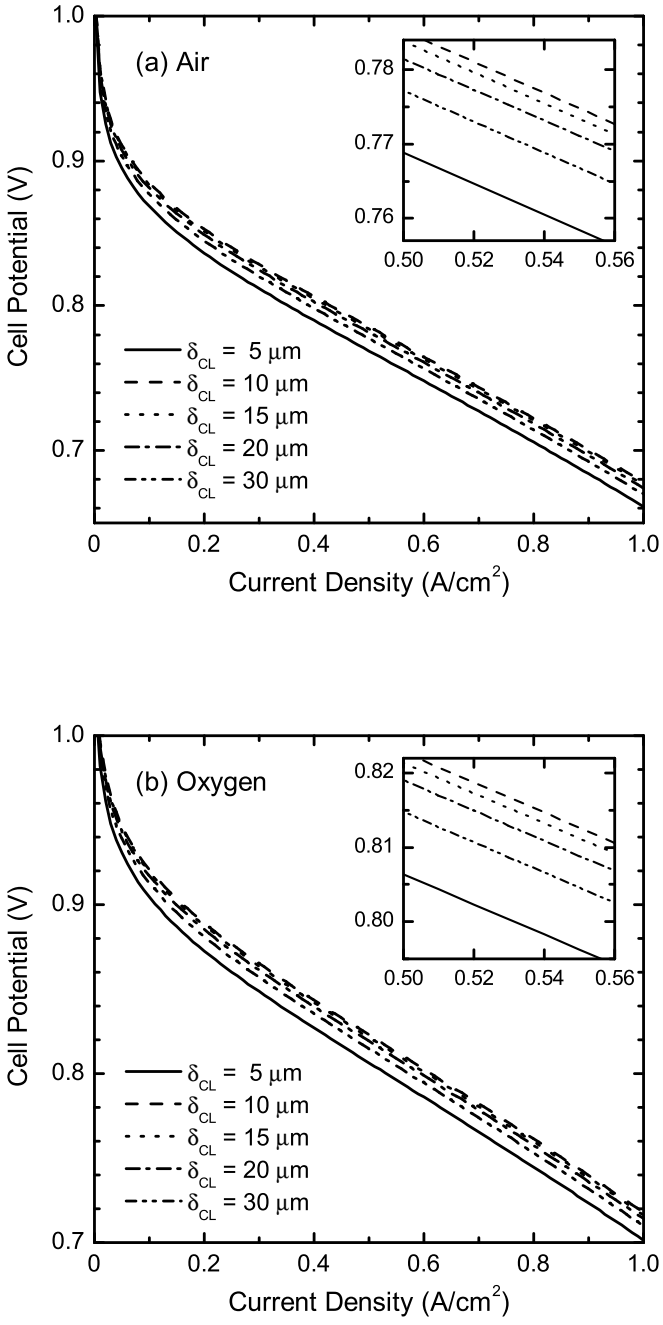

Figure 8.14: Variation of the cell potential with current density for (a) air as the cathode gas, and (b) oxygen as the cathode gas with a Pt-loading of 0.2 mg/cm^2 for different CCL thicknesses.

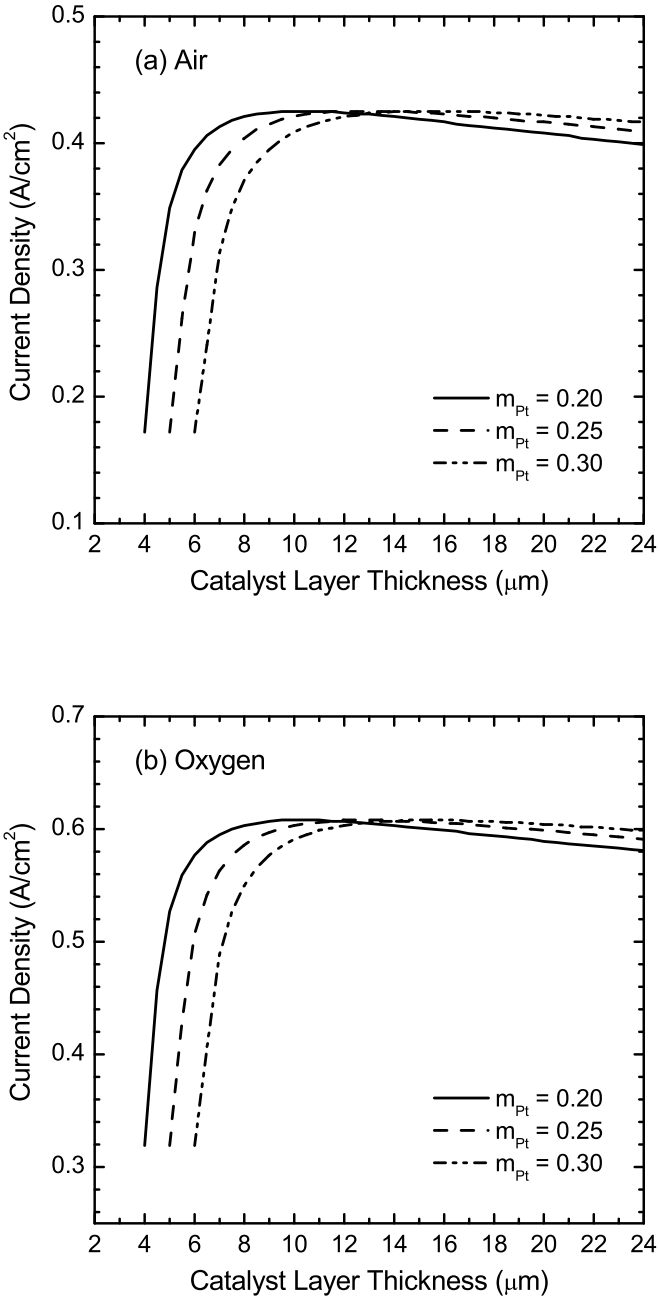

Figure 8.15: Current density as a function of CCL thickness at a cell potential of 0.8 V with (a) air as the cathode gas, and (b) oxygen as the cathode gas for different Pt-loadings in mg/cm^2.

8.3 Analytical Model of Liquid Water Transport

In the following subsections, the results are presented for both hydrophilic and hydrophobic CCLs that are estimated using the analytical solutions of liquid water transport given in Eqs. (6.64) and (6.65) in Chapter 6. The analytical expressions for the liquid water distribution, however, require several physical and electrochemical parameters as well as liquid water saturation at the CCL/GDL interface, oxygen concentration at the reaction site, and cathode activation overpotential. The required physical electrochemical parameters are listed in Table 8.5, while the analytical expressions are already provided in Chapter 6 for liquid water saturation at the CCL/GDL interface, oxygen concentration at the reaction site, and cathode activation overpotential, respectively. It is worthwhile to note that the proposed analytical expressions for liquid water distribution in the CCL do not involve any complicated numerical modeling or solutions to several simultaneous transport equations except the expressions provided in Chapter 6.

8.3.1 Liquid Saturation Profile in Cathode Catalyst Layer

The liquid saturation profiles obtained from the 1D analytical solution of liquid water transport in the CCL are shown in Fig. 8.16 for two different current densities as indicated in the figure. Both hydrophobic and hydrophilic cases are considered, where the solid lines

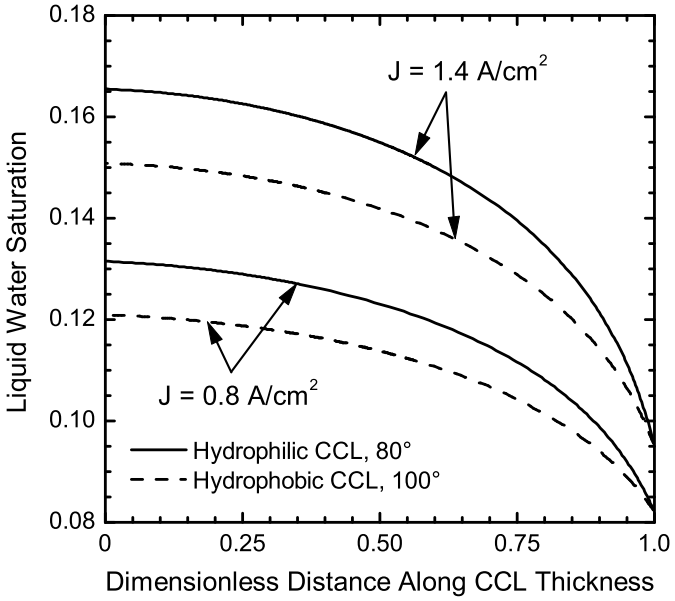

Figure 8.16: Liquid saturation profile across the CCL of a PEM fuel cell predicted by 1D analytical model for two different current densities as indicated in the legend.

represent the profile in a CCL having contact angle of 80° and the dashed lines depict the profile for contact angle of 100° for the case when the electro-osmotic drag is significant than the back-diffusion at the membrane/CCL interface. As observed from Fig. 8.16, the hydrophilic CCL shows higher liquid saturations than the hydrophobic CCL. It should be pointed out that for both cases, the GDL is considered as hydrophobic with a contact angle of 100°. The GDL properties are identical of Ref. [63] that are listed in Table 8.5. In Fig. 8.16, the higher liquid saturation level near the membrane/CCL interface for a hydrophilic CCL than a hydrophobic CCL suggests slower liquid water transport from the CCL to the GDL if the catalyst layer is hydrophilic. This situation might be favorable for the proton transport in the CCL. At the same time, the higher liquid saturation at the membrane/CCL interface also implies that the higher level of water transport from the membrane to the CCL that might eventually dry out membrane. Further, the higher level of liquid accumulation in the CCL, particularly in a hydrophilic CCL, will require a better water management in the GDL.

Table 8.5: Electrochemical and transport properties used by Pasaogullari and Wang [63]

Description	Value
Cell temperature (K)	353
Liquid water density (kg/m^3)	971.8
Liquid water viscosity (Pa·s)	3.56×10^{-4}
Surface tension (N/m)	0.0625
GDL porosity	0.5
GDL permeability (m^2)	6.875×10^{-13}
GDL thickness (m)	300×10^{-6}

8.3.2 Effect of Surface Wettability

Figure 8.17 depicts the effect of contact angle on the liquid water distribution in the CCL for a current density of 0.8 A/cm^2. All the parameters are identical to those for Fig. 8.16, except the CCL contact angles that are indicated in the legend. It is observed that the contact angles have significant influence on the liquid water distribution inside a fuel cell catalyst layer. In a hydrophilic catalyst layer ($\theta_c < 90°$) as shown in Fig. 8.17a, the CCL having a contact angle of 89° shows significantly higher liquid saturation than the CCL having lower contact angle or higher surface wettability. It is mainly due to the capillary

pressure. Since the capillary pressure drives the flow of liquid water in the CCL and the capillary pressure reduces significantly with contact angle, the hydrophilic CCL with high contact angle shows higher liquid saturation. Conversely, in a hydrophobic catalyst layer ($\theta_c > 90°$) as shown in Fig. 8.17b, lower contact angle shows a higher liquid saturation. As the hydrophobicity increases, the liquid saturation in the catalyst layer decreases rapidly. This result also implies that a hydrophobic catalyst layer would enhance water transport from the catalyst layer, whereas a catalyst layer has to be hydrophilic in nature for better proton transport. Hence, a balance between the hydrophlicity and hydrophobicity might be desirable for a PEM fuel cell catalyst layer for better water transport as well as a higher cell performance.

The reason why a lower contact angle or highly hydrophilic CCL (Fig. 8.17a) shows low liquid saturation can be justified if we notice the experimental measurements of the functional dependence of capillary pressure on the liquid saturation that is provided by Ustohal *et al.* [183] for a porous media with hydrophilic pore wettability for an air-water system. It has been observed that the liquid saturation decreases for an air-water system with the increases of wettability of the medium or the pressure difference between the phases [183]. Hence, the results presented in Fig. 8.17 are consistent with what Ustohal *et al.* [183] observed experimentally. The results in Fig. 8.17 also show that the liquid saturation for hydrophilic CCL could be as high as 22% at the membrane/CCL interface and about 20% for hydrophobic CCL, even for the case of no liquid saturation in the gas channel and with a hydrophobic GDL. In other words, the liquid water transport will be significantly reduced due to the lower hydrophilicity of a hydrophilic CCL. Whereas highly hydrophilic CCL (low contact angle) shows lowest liquid saturation, hence better water transport from the CCL to the GDL. Therefore, this study reveals that the higher wettability increases the water transport from a hydrophilic CCL and will reduce the liquid saturation. Therefore, a highly hydrophilic CCL would be quite capable of keeping the reaction site wet enough for favorable electrochemical reaction and proton transport even with low liquid saturation due to the higher surface wettability. Practically, the liquid water saturation at the GDL/GFC interface is higher than zero, hence, the water saturation at the membrane/CCL interface could be significantly higher than the values observed in Fig. 8.17. The trends observed in Fig. 8.17 seem to remain similar even for a higher saturation at the GDL/GFC interface.

The common perception that a highly hydrophilic surface means higher liquid saturation seems not correct. A highly hydrophilic surface represents high wettability, and due to high wettability, less amount of liquid water is required to wet a surface than the amount of water required to wet the same amount of low-hydrophilic surface. In highly hydrophilic pores, the volume of liquid water will be less compared to the liquid water volume in low

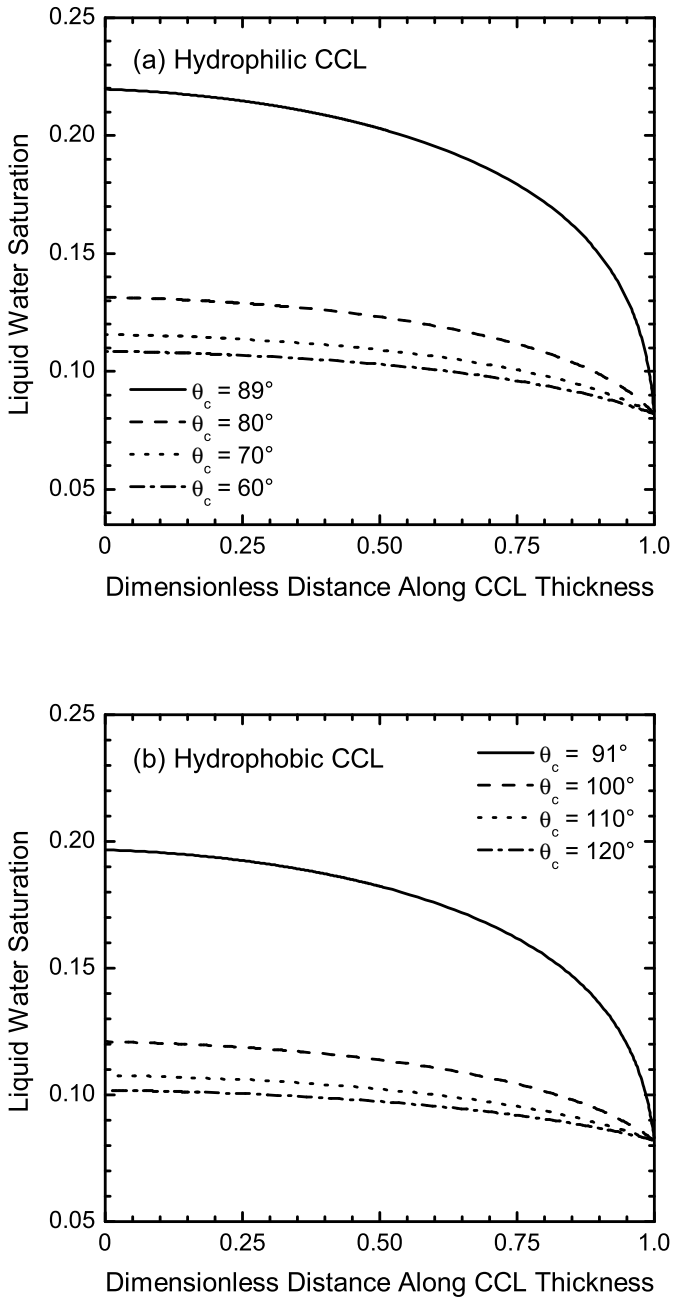

Figure 8.17: Liquid saturation profile across the dimensionless distance along CCL thickness predicted by 1D analytical model of liquid water transport for different CCL contact angles.

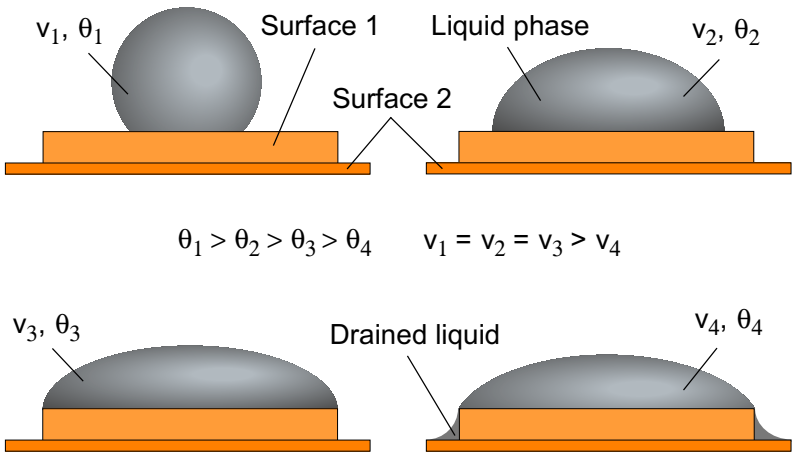

Figure 8.18: Effect of contact angles on the liquid phase volume over a solid surface.

hydrophilic pores that will eventually provide less water saturation for low contact angles and high wettability. This phenomenon can be further explained by considering a liquid droplet over a solid surface and changing its contact angle as shown in Fig. 8.18. Here, the four sub-figures show how the volume of liquid water over a surface changes with contact angles. The top-left figure represents the hydrophobic case and other three figures depict the hydrophilic cases. Although the hydrophobic and hydrophilic cases have the same liquid volume over the solid surface (except the bottom-right figure), the surface wettability becomes higher for the hydrophilic cases. The top-right figure represents a hydrophilic case with higher contact angle when the liquid phase did not wet the surface completely. The bottom-left figure represents the intermediate contact angle case but the liquid phase completely wets the solid surface (surface 1). For both cases, the liquid phase volume over the solid surface is the same. Considering a further lower value of contact angle than the bottom-left figure, as shown in bottom-right part, eventually reveals that the liquid phase is drained out from the solid surface due to the lower contact angle or higher hydrophilicity.

Recalling the definition of capillary pressure in the porous CCL, it can be immediately recognized that the lower contact angles also represent higher capillary pressures. Since the capillary pressure is the gas phase pressure minus the liquid phase pressure for a hydrophilic medium, the liquid phase pressure will decrease with the capillary pressures. Hence, the gas phase will push away the liquid phase from a hydrophilic pore, and eventually reduces the volume of liquid water over the solid phase. Conversely, the reaction site needs to be well hydrated for better electrochemical reaction that can even be achieved with less liquid water if the surface wettability is higher. A balance of liquid saturation and surface wettability is desirable as the high liquid saturation may block pores that will eventually hinder the oxygen transport to the reaction site, while the low liquid saturation may cause

dry out of the reaction site and membrane that will hinder the proton transport to the reaction site.

8.3.3 Effect of Electro-osmotic Drag and Back-diffusion

The significance of water transport from the anode side to the cathode side of a PEM fuel cell due to the electro-osmotic drag and its effect on the catalyst layer liquid saturation are also investigated. Figure 8.19 shows the liquid saturation profile across the CCL thickness predicted by 1D analytical model for several electro-osmotic drag coefficients as indicated in the legend. Here, the liquid saturations are estimated in a CCL having a contact angle of 80° for a current density of 0.8 A/cm^2. All other parameters are identical to those for Figs. 8.16 and 8.17. The level of liquid saturation increases when the electro-osmotic transport is higher than the water transport by back-diffusion ($\alpha > 0$), while the higher back-diffusion ($\alpha < 0$) causes the reduction of liquid saturation in the CCL. To be specific, the liquid saturation would be increased by about 5% at the membrane/CCL interface for the most widely used electro-osmotic drag coefficient ($\alpha = 0.25$) compared to when a balance exists between water transport by the electro-osmotic drag and the back-diffusion process ($\alpha = 0$). Although the variations observed in Fig. 8.19 is much lower than the variations observed in Fig. 8.17 for different contact angles, nonetheless, the significance of water transport from the anode to the cathode side of a PEM fuel cell due to electro-osmotic drag is crucial for proper water balance in the CCL. For instance, the total variation observed at the membrane interface is about 13% while varying the electro-osmotic drag coefficients from -0.25 to 0.5 that seems significant to reduce the performance of a PEM fuel cell.

8.3.4 Effect of Flooding on Performance

It has been widely investigated how the performance of a PEM fuel cell degrades due to the liquid water flooding in the GDL [63, 116, 166]. Flooding in the GDL hinders oxygen transport, whereas flooding in the CCL not only hinders the oxygen transport but also reduces the fuel cell performance by covering electrochemically active site with liquid water. Therefore, flooding seems to be more sensitive to the CCL than the GDL resistance to oxygen transport. Since most of the electrochemical reaction occurs near the membrane/CCL interface, the effect of water flooding in the CCL has been investigated by assuming a uniform liquid saturation that is approximately equal to the liquid saturation observed near the membrane/CCL interface.

Figure 8.20 depicts the activation overpotentials as a function of current density for

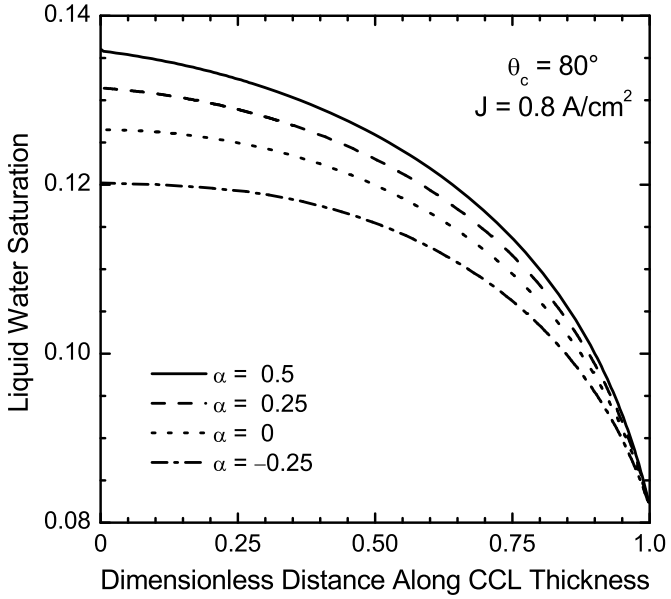

Figure 8.19: Effect of electro-osmotic drag and back-diffusion on the liquid saturation profiles across the CCL thickness predicted by 1D analytical model of liquid water transport.

five different liquid saturations at the CCL as indicated in the legend. Here, four parts of Fig. 8.20 represent four cases of the active area reduction by liquid saturation, namely, $q = 1, 2, 5,$ and 8. In these results, the resistance to oxygen transport to the CCL includes both the GDL and CCL resistances. The CCL and GDL resistances to the oxygen transport is estimated using the formulations given in Sections 6.3.1 and 6.3.2, while the effective oxygen diffusivity in the CCL is estimated using the formulation given in Chapter 5. Surprisingly, the effect of water flooding on the cathode activation overpotential shown in Fig. 8.20a for the case of linear reduction ($q = 1$) of active reaction area by liquid saturation does not show significant variation. Clearly, with 50% liquid saturation, the activation overpotential only increases by about 5% compared to the activation overpotential estimated for 10% liquid saturation at 0.8 A/cm^2. However, it has been observed in literature of high cathode overpotential due to GDL water flooding [63], which includes activation, ohmic, and concentration overpotentials together. Here, we have only shown the activation losses at the CCL. It seems that there might be a threshold limit for the cathode activation overpotential in the CCL, which is less sensitive to the liquid saturation when a linear reduction of active reaction area with liquid saturation is considered. Even for the quadratic reduction of active reaction site with liquid saturation shows only a small variation in the activation potential in catalyst layer as shown in Fig. 8.20b. For the higher order reduction of active reaction area (Figs. 8.20c and 8.20d), the liquid saturation shows significant effect on the cathode activation potential. For instance, activation overpotential at the cathode cathode catalyst layer would be 34% higher at a current density of 1.0

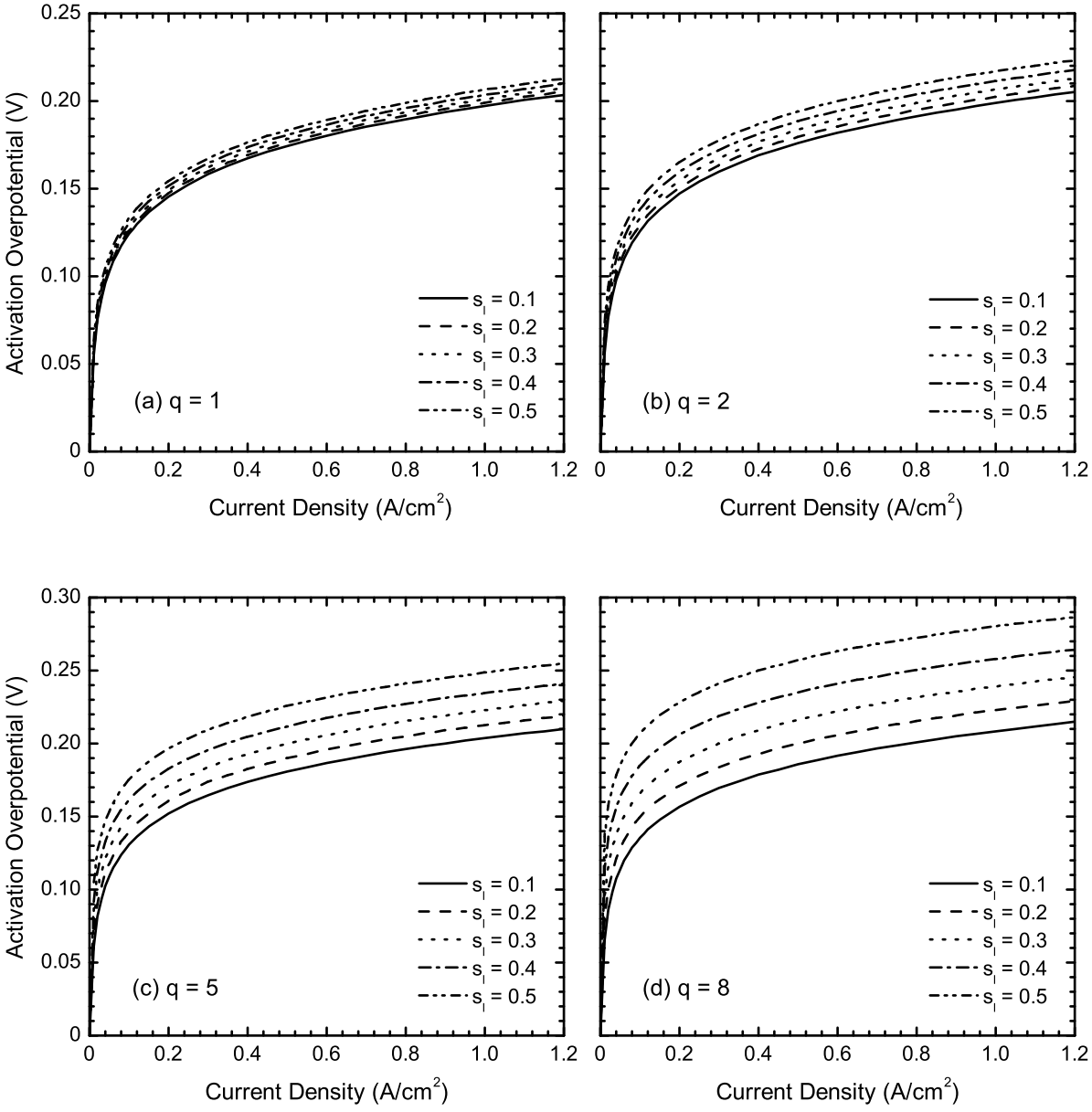

Figure 8.20: Effect of liquid saturation on the cathode activation overpotential for a current density of 0.8 A/cm^2 for different values of saturation exponent, q.

A/cm^2 when the liquid saturation increases from 0.1 to 0.5 as observed in Fig. 8.20d.

Clearly, the approximation of linear reduction of active reaction area due to the liquid saturation might not be a good approximation. Since the catalyst particle has high surface area to volume ratio, the linear reduction of reaction surface area with the liquid water volume in the CCL would always overestimate the active reaction area and underestimate the effect of water flooding on the cell potential. It is worthwhile to note that the resistance to the oxygen transport has been estimated using a linear approximation. If a pore in the GDL is completely blocked by liquid water, then oxygen needs to be dissolved to the liquid water before continuing to diffuse that will encounter a higher resistance to the transport process compared to the resistance estimated considering a diffusion mechanism only. Nonetheless, the results presented in Fig. 8.20 show that the liquid saturation will eventually reduce the fuel cell performance and a higher order approximation for the active area reduction should be considered.

8.3.5 Effect of Time Constants

Figure 8.21 shows the variation of liquid water saturation in the CCL of a PEM fuel cell with different values of "dimensionless time of first kind" as indicated in the legend for a current density of 0.8 A/cm^2. Since the dimensionless time of first kind (Π_1) depends on several geometrical and physical properties of the CCL that will eventually affect the other time constants, the dimensionless time of second kind (Π_2) and third kind (Π_3) were kept constant while investigating the effect of the dimensionless time of first kind. The dimensionless time of second kind (Π_2) and third kind (Π_3) were estimated with the parameter values listed in Tables 8.5 and 8.6. As expected, for the higher values of time constant, the liquid saturation becomes very high in the CCL. Physically, the higher values of Π_1 represent the slower capillary diffusion process or the faster electrochemical production. The maximum liquid saturation in a two-phase situation, which is physically possible to reach in the CCL, is shown by the uppermost curve when $\Pi_1 = 1$. The dimensionless time of first kind of unity means the time requires to produce one unit of liquid water and the time requires to diffuse the same amount of liquid water across the CCL by the capillary diffusion process are the same at that maximum saturation level for a steady-state condition. In other words, the moment the liquid water generated in the CCL, it will be instantly diffused away to the GDL or to the membrane. The liquid water will not be able to occupy further volume in the porous catalyst layer than the saturation shown for $\Pi_1 = 1$ due to the presence of gas phase.

Theoretically, the time constant can be higher than unity. At the values higher than unity, however, the entire CCL will be flooded with liquid water that might eventually

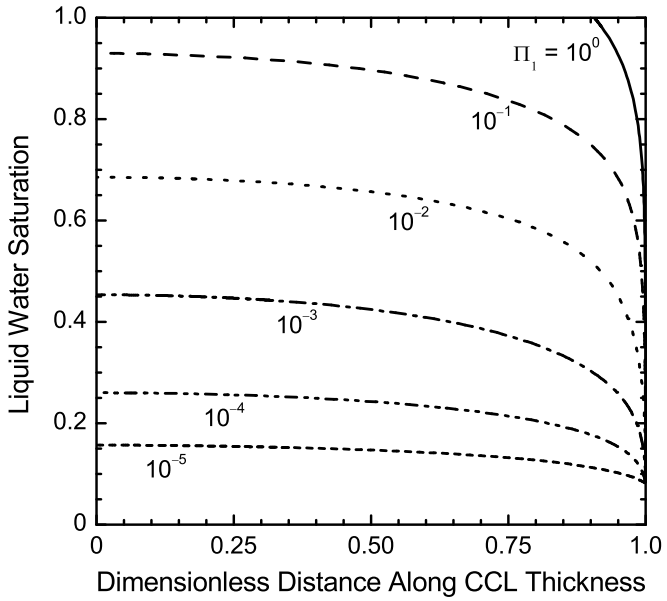

Figure 8.21: Effect of dimensionless time constant, Π_1, on the liquid saturation inside the CCL of a PEM fuel cell for a current density of 0.8 A/cm^2. Each line represents different values of the "dimensionless time of first kind".

stop the electrochemical reaction, hence the fuel cell operation, as there will be no gas phase present in the CCL. In such case, the entire two-phase process will be transformed into a single-phase process, hence the two-phase formulation proposed in this study will not be valid for $\Pi_1 > 1$. Conversely, the liquid saturation will be close to zero when the dimensionless time constant goes to an infinitely small value. However, for a steady fuel cell operation, liquid water has to be present in the CCL. It is always desirable to have a certain liquid saturation that will provide a stable liquid film over the catalyst surface for better proton transport. Even with a high surface wettability, the liquid film can be unstable if the liquid saturation is low due to insufficient liquid water. The discontinuous liquid film or low liquid saturation will then hinder the proton transport, hence reduces the cell performance. Therefore, the lowest possible time constant can be in the order of 10^{-5} as observed from Fig. 8.21 if we assume the CCL has modest wettability.

Figure 8.22 depicts the variation of liquid saturation in the CCL of a PEM fuel cell for the second dimensionless time constant, Π_2 (ratio between capillary diffusion time to phase change time). Here, the dimensionless time of first kind (Π_1) and third kind (Π_3) are estimated with the parameter values listed in Tables 8.5 and 8.6, and kept constant while varying the second dimensionless time constant. Similar to Π_1, the liquid saturation profile for the second time constant also shows similar trend. However, the order of magnitude is found to be very small compared to the first time constant. For instance, it has been

Table 8.6: Parameters used in the model calculations of liquid water transport in CCL

Description	Value	Source
Gas pressure (atm)	3	[-]
Relative humidity (%)	100	[-]
Cell width (cm)	7.07	[7]
Cell height (cm)	7.07	[7]
Flow channel width (mm)	1	[63]
Flow channel height (mm)	1	[63]
Liquid saturation in gas channel	0	[63]
Catalyst layer thickness (μm)	20	[7]
Reference oxygen concentration (mol/m^3)	1.2	[94]
GDL contact angle ($^\circ$)	100	[63]
Drag coefficient, α	0.25	[116]
Condensation rate constant (/s)	100	[116]
Platinum loading (mg/cm^2)	0.3	[7]
%wt of platinum (%)	20	[7]
%wt of Nafion (%)	30	[7]
Membrane conductivity (S/cm)	0.17	[116]
Platinum density (kg/m^3)	21.5×10^3	[116]
Carbon density (kg/m^3)	2.0×10^3	[116]
Nafion density (kg/m^3)	1.9×10^3	[116]

estimated to be in the order of 10^{-14} for the parameter values listed in Tables 8.5 and 8.6, while the order for the first time constant is about 10^{-5}. As observed from Fig. 8.22 at the practical range ($\Pi_2 \approx 10^{-14}$), the effect of dimensionless time of second kind on the liquid saturation in the CCL is negligible compared to the contribution of liquid saturation from the electrochemical process (comparing $\Pi_2 = 10^{-10}$ and 10^{-15}). Physically, the higher values of second time constant represent slower capillary diffusion or faster phase change process. Therefore, the results shown in Fig 8.22 further imply that the capillary diffusion process is much faster than the liquid water production from a condensation process.

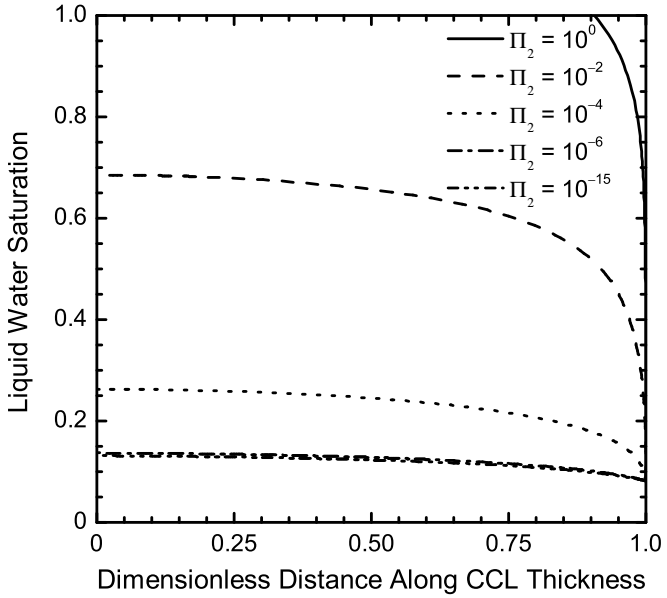

Figure 8.22: Variation of the liquid saturation in the CCL of a PEM fuel cell with the "dimensionless time of second kind" for a current density of 0.8 A/cm^2.

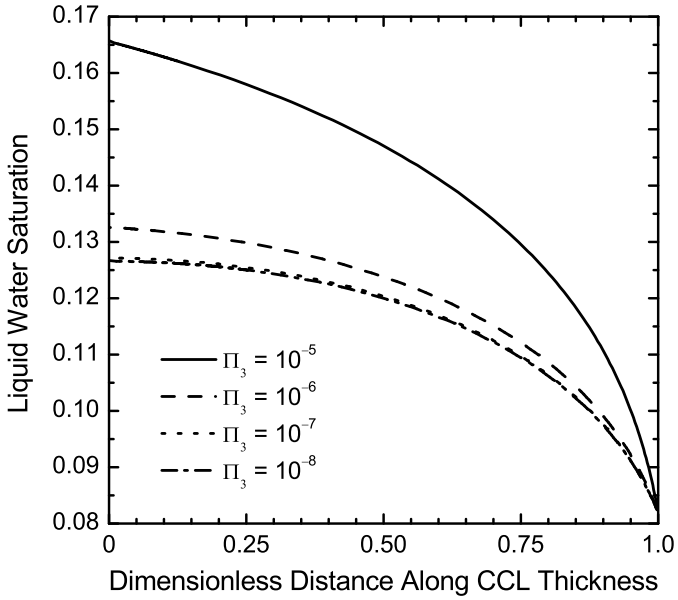

Figure 8.23: Variation of the liquid saturation in the CCL of a PEM fuel cell with the "dimensionless time of third kind" for a current density of 0.8 A/cm^2.

For the "dimensionless time of third kind", the results are shown in Fig. 8.23 for a current density of 0.8 A/cm^2. Here, the variation of liquid saturation across the CCL thickness are shown for several values of third time constant as indicated in the legend, while the dimensionless time of first kind (Π_1) and second kind (Π_2) were kept constant. Since the order of magnitude for the dimensionless time of third kind is found to be 10^{-5} using the parameters listed in Tables 8.5 and 8.6, the result for the dimensionless time of third kind are presented only for the values lower than or equal to 10^{-5}. The liquid saturation profiles across the CCL thickness are found to be almost independent of the time constant for lower values of Π_3. This is mainly due to the fact that the time requires for water transport across the CCL by the capillary diffusion. Physically, the higher values of third time constant represent a slower capillary diffusion or a faster electro-osmotic drag and back-diffusion process. Therefore, the time requires for liquid water transport by the capillary diffusion is small compared to the time requires for the electro-osmotic drag and back-diffusion process at smaller Π_3. It should be pointed out that for the practical range of third time constant, 10^{-5} to 10^{-6}, the effect of the third time constant on the liquid saturation in CCL is significant. Hence, the electro-osmotic drag and back-diffusion process should always be considered during the water management in PEM fuel cell.

8.4 Numerical Model of Agglomerate Catalyst Layer

The structure of a catalyst layer is widely presumed macroscopically as "macro-homogenous" and microscopically as "agglomerate" structures. In reality, the CCL has a complex combination of ionomer membrane, platinum particle, carbon support, and void region that perhaps is not possible to be adequately described by considering either macro-homogenous or agglomerate structures. A combination of macro-homogenous and agglomerate structures would be more realistic. These two cases, however, can provide the lower and upper bounds for the effect of the catalyst layer structures on the cell performance. Therefore, this study focuses on the specific CCL structures and their impact on the PEM fuel cell performance. Here, a 3D agglomerate model of CCL in a PEM fuel cell is developed to study the activation overpotential in the CCL. The effect of agglomerate arrangements on the activation overpotential of PEM fuel cell has been investigated for three different types of agglomerate arrangements, namely, in-line agglomerate arrangement as Case-I, and two staggered agglomerate arrangements as Case-II and Case-III. The catalyst layer geometry is generated assuming that the agglomerates are aligned along the thickness of the catalyst layer in the first case and then by considering staggered arrangements in the subsequent cases. All the three arrangements are simulated for typical operating conditions inside the PEM fuel cell in order to investigate the oxygen transport process through the cathode catalyst layer, and its impact on the activation polarization.

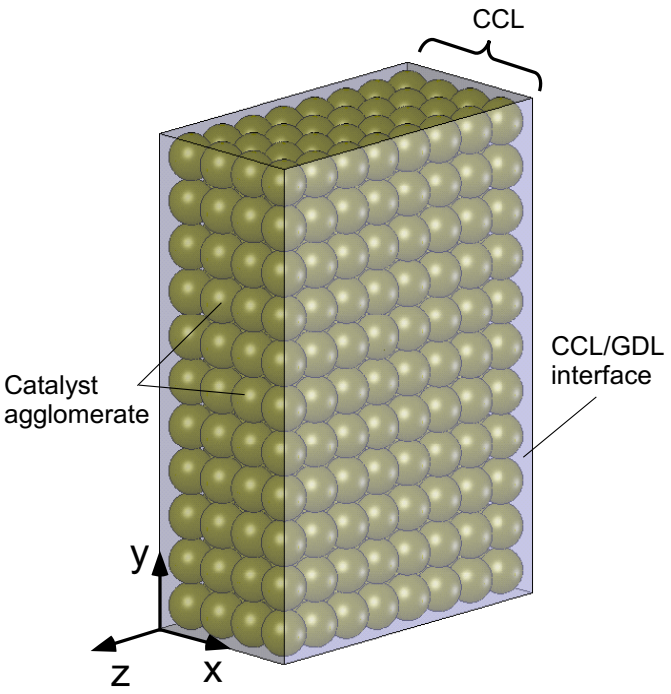

Figure 8.24: A schematic of agglomerate catalyst layer.

In this part of investigation, air is considered as the cathode gas and the concentration of oxygen in the cathode flow channel is considered uniform. The GDL is considered dry; hence, the oxygen diffuses through the un-flooded electrode void region to reach the CCL/GDL interface. In addition, the catalyst agglomerates are considered partially hydrated and water in the void region around the agglomerates is considered in gaseous phase to simulate the un-flooded scenarios. The thickness of the catalyst layer in this part of present study is considered as 10 μm and the agglomerate diameter is considered as 5 μm. Typically, the thickness of the catalyst layer and the agglomerate size depend on the amount of catalyst loading and the fabrication methods. It is found in our earlier study that for the typical operating conditions and physical parameters, the optimum catalyst thickness ranges from 10 μm to 15 μm [7]. Further, the scanning electron micrograph (SEM) of membrane electrode assembly shows that the catalyst layer thickness is around 10 μm to 20 μm and the mean agglomerate diameter is about 6 μm [85].

The catalyst agglomerate is assumed as a mixture of Nafion membrane, supported catalyst, and void space, which is also surrounded by void spaces as shown in Fig. 8.24. Generally, the sizes of the agglomerates are not equal and the arrangement of catalyst agglomerates inside the catalyst layer is also random. In the present study, it has been assumed that the sizes of the agglomerates are equal. The schematic of the agglomerate arrangement in the cathode catalyst layer and the computational domain for the three

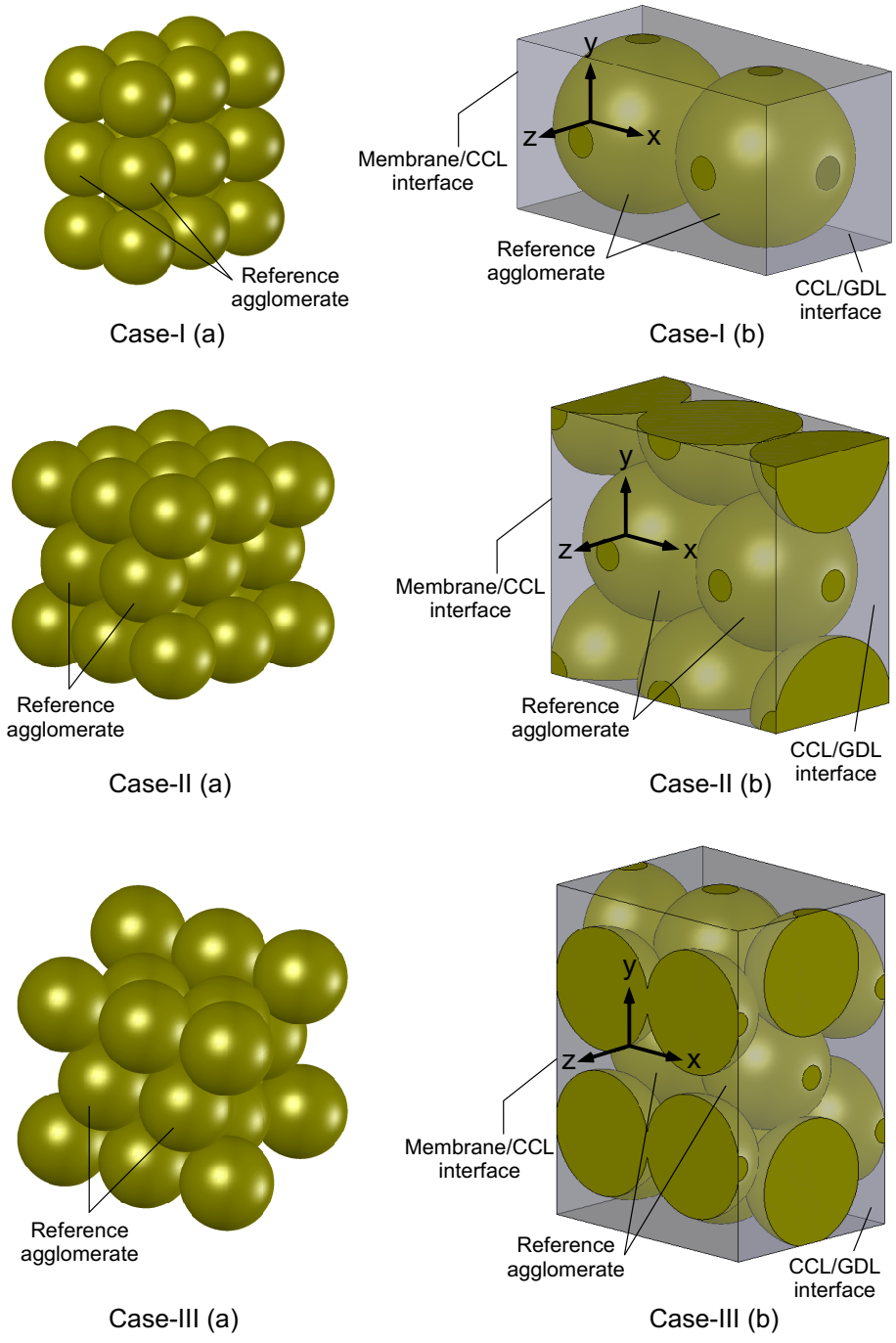

Figure 8.25: Schematic of agglomerate arrangements in the cathode catalyst layer in part (a) and the computational domain in part (b). Case-I represents in-line agglomerate arrangement, Case-II represents staggered arrangement in y-direction, and Case-III depicts staggered arrangement in both y- and z-directions.

cases used in the present investigation is shown in Fig. 8.25. Here, Case-I represents in-line agglomerate arrangement, whereas Case-II and Case-III depict two staggered arrangements (uni-directional and bi-directional staggered arrangements). The orientation of the catalyst agglomerates in the catalyst layer for different agglomerate arrangements are listed in Table 8.7. Here, staggered arrangement is considered in y-direction for Case-II, and for Case-III, both y- and z-directions have staggered arrangements of the catalyst agglomerates. For all the cases, x-direction is considered as in-line arrangement to keep symmetry between these cases. Due to the symmetry in x-direction, all the results are presented along the centerline between the two agglomerates lied on the x-axis. In the following sections, the numerical model results are presented for the three agglomerate arrangements, while the operating parameters and the physical properties used in this numerical computation are listed in Table 8.8.

Table 8.7: Agglomerates orientation in different directions for the cases considered in the present investigation

	x-direction	y-direction	z-direction
Case-I	in-line	in-line	in-line
Case-II	in-line	staggered	in-line
Case-III	in-line	staggered	staggered

8.4.1 Model Validation

The agglomerate model described in the previous section is the first of its kind and none of the previous studies has considered such 3D agglomerate arrangements; hence, direct comparison of the numerical results is not possible. Rather a limiting case of agglomerate model has been invoked for the validation of the accuracy of 3D numerical calculation, where agglomerates are considered in a cylindrical computational domain. The advantage of using such 3D domain is that it can be solved as 2D axi-symmetric problem; hence, the accuracy of the 3D calculation can easily be verified with 2D calculation. The thickness of the catalyst layer is chosen as 10 μm and the agglomerate diameter as 5 μm, i.e. two agglomerates can exist along the thickness of the catalyst layer. A schematic diagram of the 3D computational domain and corresponding axi-symmetric computational domain used for the validation is shown in Fig. 8.26 along with the coordinate systems. Here, the number of agglomerates was kept as two; however, to maintain sufficient contact between the agglomerates, between the agglomerates and GDL, and between the agglomerates and

Table 8.8: The operating and physical parameters in the present model calculations [6, 7]

Parameter	Value
Operating temperature, T (°C)	50 and 80
Operating pressure, P (atm)	1 and 3
Electrode thickness, δ_{GDL} (μm)	250
Catalyst layer thickness, δ_{CL} (μm)	10
Agglomerate diameter (μm)	5
Void fraction of the cathode electrode, ϵ_{GDL}	0.4
Membrane fraction in agglomerate, f_m	0.4
Liquid water fraction in agglomerate, f_l	0.5
Catalyst loading per unit area, m_{Pt} (mg/cm^2)	0.2
%wt of platinum (%)	20
Catalyst surface area per unit mass of catalyst, A_s (m^2/g)	112
Membrane conductivity, σ_m (S/cm)	0.17
Solid catalyst conductivity, σ_s (S/cm)	727
Density of platinum, ρ_{Pt} (g/cm^3)	21.5
Density of carbon black, ρ_{C} (g/cm^3)	2.0
Anodic transfer coefficient, α_a	0.5
Cathodic transfer coefficient, α_c	0.5

membrane, the size of the each agglomerate has been increased by 2% keeping the centers of the agglomerates fixed. Boundary conditions for both the 2D axi-symmetric model and the 3D model are identical as described in Chapter 7.

The oxygen concentration profiles across the catalyst layer thickness along the centerline of the agglomerates (line OO′ in Fig. 8.26) for two current densities are shown in Figure 8.27a. The operating pressure and temperature of the fuel cell is considered as 3 atm and 80 °C, respectively. The numerical procedure for the 3D models is similar as described earlier. However, for axi-symmetric model, the advantage of adaptive mesh refinement technique has been employed for better accuracy. Conversely, Fig. 8.27b depicts the activation polarization for the 3D model and the axi-symmetric model. As observed in Fig. 8.27 for both current densities, numerical solution of the 3D model shows good agreement with the axi-symmetric model results. Further, the activation polarization results also show excellent agreement.

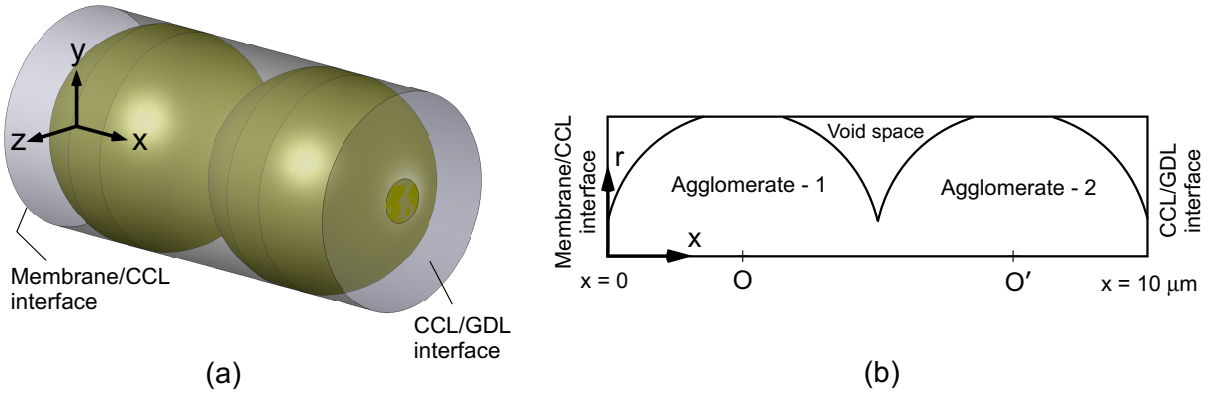

Figure 8.26: Schematic of the computational domains: (a) three-dimensional domain, (b) two-dimensional axi-symmetric domain.

The accuracy of the 2D finite element model using adaptive mesh refinement with commercial software, like COMSOL Multiphysics®, is well established [184, 185]. Furthermore, the 2D numerical model requires less number of grids to represent the curve surfaces. Whereas, the 3D model requires significantly large number of gird for proper representation of spherical surfaces that is limited by computer memory. This limitation of computer memory eventually lowers the accuracy of the 3D numerical calculation. Since the comparisons shown here provide a good agreement with each other, it can easily be concluded that the 3D model results computed in this study are sufficiently accurate for studying the effect of catalyst layer structures on the performance of PEM fuel cell. Once again, these results show the accuracy level of 3D numerical computation, whereas the accuracy of the mathematical formulation has already been established in Ref. [7].

8.4.2 Model Results: In-line Arrangement

Figure 8.28 shows the profiles of oxygen concentration with different current density values for the in-line arrangement, which is referred as Case-I in Fig. 8.25. Each of these profiles is plotted inside the reference agglomerates along the x-axis that is identical of line OO′ as shown in Fig. 8.26. Five different current density values are considered as indicated in the legend. In both figures, the symbols represent the oxygen concentration profile along a line parallel to the x-axis at $y = 0$ and $z = 2.5$ μm (equal to agglomerate radius) for $J_\delta = 0.1$ A/cm^2, i.e. along the interface between two agglomerates on xz-plane. The simulation parameters used to estimate the oxygen concentration are listed in Table 8.8. Two parts of this figure depict two different combinations of operating parameters, namely, $T = 50$ ℃ and $P = 1$ atm, and $T = 80$ ℃ and $P = 3$ atm. Here $x = 0$ represents the membrane/CCL interface and $x = 10$ μm represents the CCL/GDL interface. It is

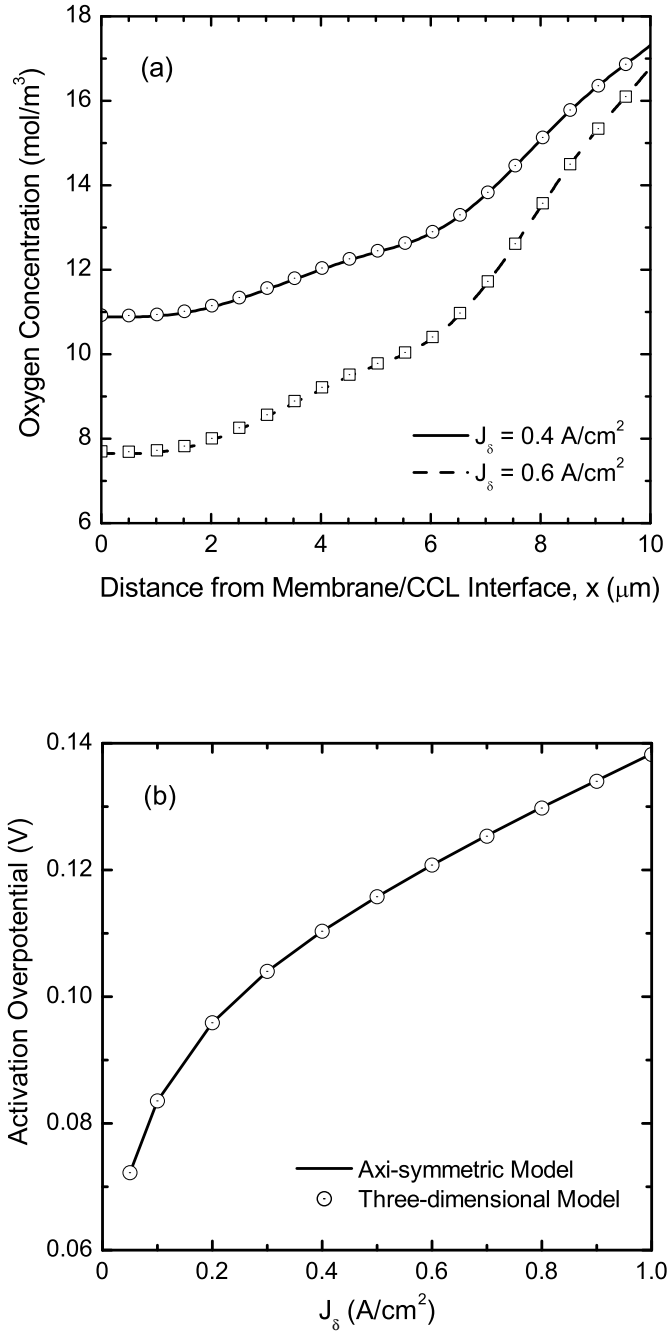

Figure 8.27: Oxygen concentration profile in the cathode catalyst layer across the thickness and activation polarization of a PEM fuel cell operating at 80 ℃ and 3 atm. The lines represent the 2D axi-symmetric model results, whereas the symbols depict the 3D model results.

observed that the oxygen concentration decreases along the centerline from the CCL/GDL interface to the membrane/CCL interface.

For low current densities, the variation in the concentration is less whereas for high current densities an oscillatory behavior is observed in the profile. As expected, the minimum oxygen concentration is observed at the center point of the agglomerate and the two undulations in the profiles represent the two agglomerates. Although the concentration profile shows a decreasing behavior, significant amount of oxygen concentration still exists in the membrane/CCL interface due to the fast oxygen diffusion through the void region around the catalyst agglomerates. Further, an ideal case scenario is considered when there is no flooding outside the catalyst agglomerates, whereas the catalyst agglomerates are considered partially flooded. Hence, oxygen diffusion across the dry void region dominates over the diffusion through the partially flooded catalyst agglomerates as shown by symbols in both figure for $J_\delta = 0.1$ A/cm^2. Here, the oxygen concentration is almost constant in the void region along x-axis due to the favorable oxygen transport. Only variation is observed at the contact surfaces between the reference and surrounding agglomerates. Since no variation is observed in the oxygen concentration profile, in subsequent figures, results in the void region have not been reported. It is also evident from Fig. 8.28 that in the agglomerate, oxygen is transported in two ways; first oxygen diffuses along the axial direction or the thickness of the catalyst layer in the void region, then from the void region, oxygen diffuses in the radial direction towards the center of each agglomerate. The contour plot of oxygen concentration shows the diffusion of oxygen in both the radial and axial directions in Fig. 8.29.

In Fig. 8.30, the cathode activation overpotential is plotted as a function of spatial coordinate x in the catalyst layer for different current density values as indicated in the legend. Similar to Fig. 8.28, two parts show two different combinations of the operating parameters as indicated in the figure. Each line corresponds to the activation overpotential for the oxygen concentration shown in Fig. 8.28. Identical to the concentration profile, the variation of the activation overpotential in the CCL is small at low current densities, whereas the activation overpotential decreases rapidly from the membrane/CCL interface to the CCL/GDL interface for the higher current densities. For all the current densities, the activation overpotential is higher for lower pressure and temperature than the activation overpotential for higher pressure and temperature. This is mainly due to the fast oxygen transport in the catalyst layer at 80 ℃ and 3 atm.

Figure 8.31 illustrates the variations of reaction rate in the CCL corresponding to the oxygen concentration and the activation overpotential shown in Figs. 8.28 and 8.30, respectively, for five different current densities. Here, the lines represent the results for T

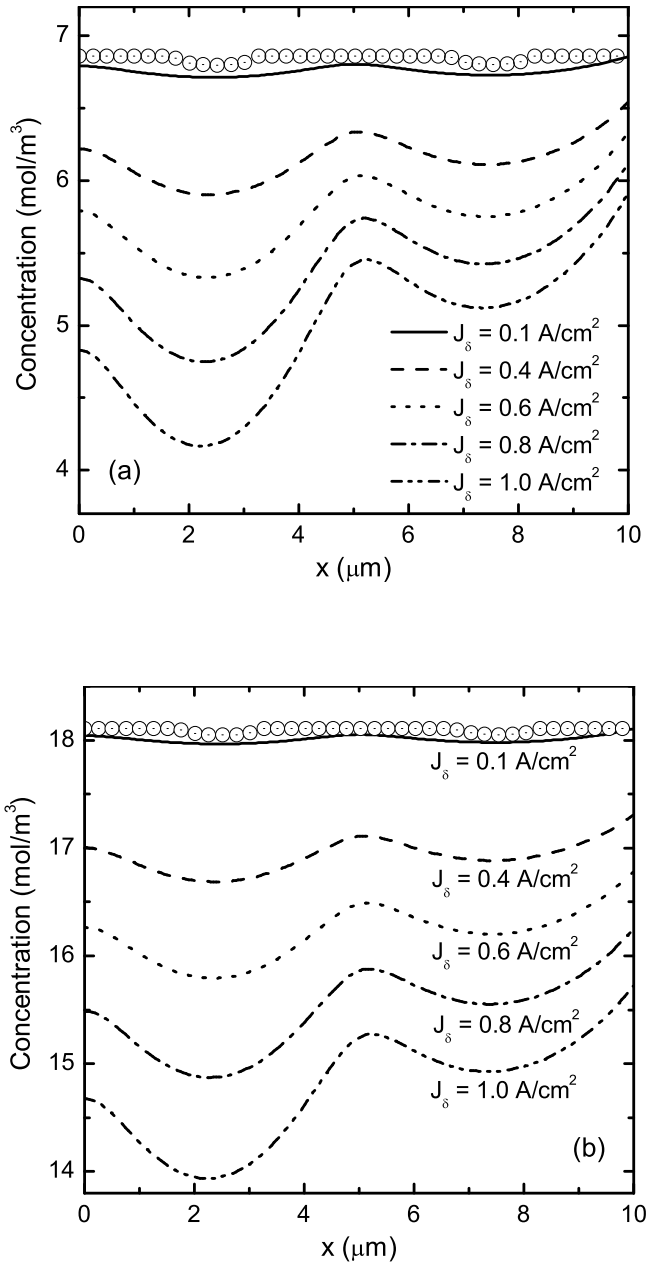

Figure 8.28: Oxygen concentration profile inside the CCL along the center line (x-axis in Fig. 8.25) of the agglomerates for Case-I in a PEM fuel cell operating at (a) T = 50 ℃ and P = 1 atm, and (b) T = 80 ℃ and P = 3 atm. Each line represents result of different current density values as indicated in the legend, while the symbols show the oxygen profile along a line parallel to x-axis at $y = 0$ and $z = 2.5$ μm for $J_\delta = 0.1$ A/cm^2.

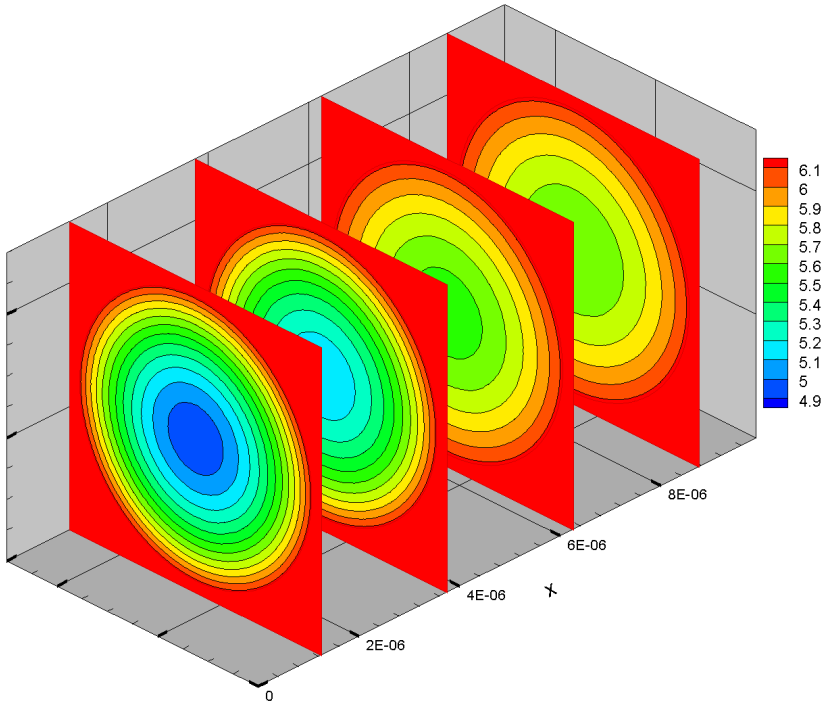

Figure 8.29: Contour plot of oxygen concentration showing the variation of oxygen concentration from the membrane/CCL interface ($x = 0$) to the CCL/GDL interface ($x = 10$ μm).

= 50 ℃ and $P = 1$ atm, and the symbols are for $T = 80$ ℃ and $P = 3$ atm. Surprisingly, changing the operating condition does not show any significant effect on the reaction rate. However, slightly higher reaction rate is observed for $T = 80$ ℃ and $P = 3$ atm at the center of the agglomerates for high current densities. These similarities show that the rate of the electrochemical reaction is not responsible for the difference observed in the activation overpotential in Fig. 8.30 for different operating conditions, which is solely due to the variation of oxygen concentration in the catalyst layer. Although the reactions are faster at higher temperatures and pressures, here it has not been significantly observed since a higher operating temperature and pressure is known to reduce the activation overpotential which is the driving force for the electrochemical reactions occurring in the fuel cells.

8.4.3 Model Results: Uni-directional Staggered Arrangement

For the staggered arrangements of catalyst agglomerates, two cases are considered. In the first staggered arrangement, agglomerates are considered as staggered in y-direction, i.e. uni-directional staggered arrangement, as shown in Fig. 8.25 as Case-II. To maintain a similarity with Case-I, the thickness of the catalyst layer is kept 10 μm. Here, the reference agglomerates (lied on the x-axis) are considered as spherical, whereas the surrounding agglomerates can be either spherical or hemispherical to maintain the thickness of the

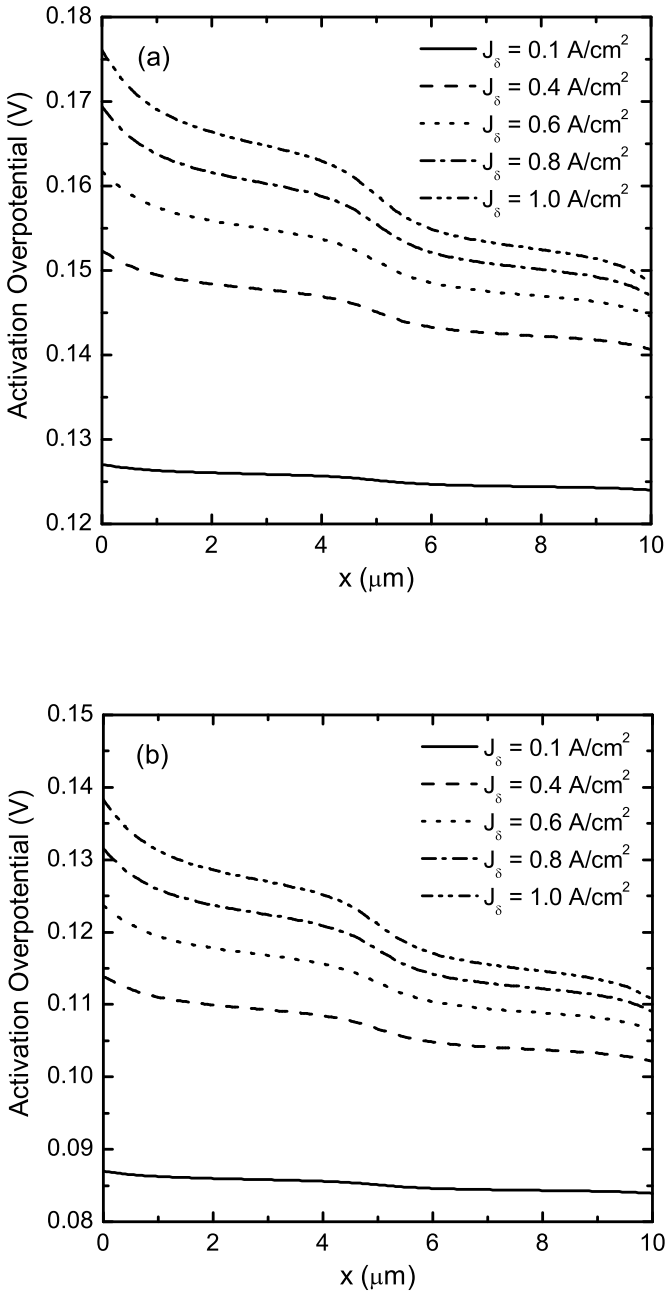

Figure 8.30: Distribution of the activation overpotential in the cathode catalyst layer for Case-I corresponding to the oxygen concentration shown in Fig. 8.28. Each line represents different current density values as indicated in the legend while part (a) for $T = 50$ ℃ and $P = 1$ atm, and part (b) for $T = 80$ ℃ and $P = 3$ atm.

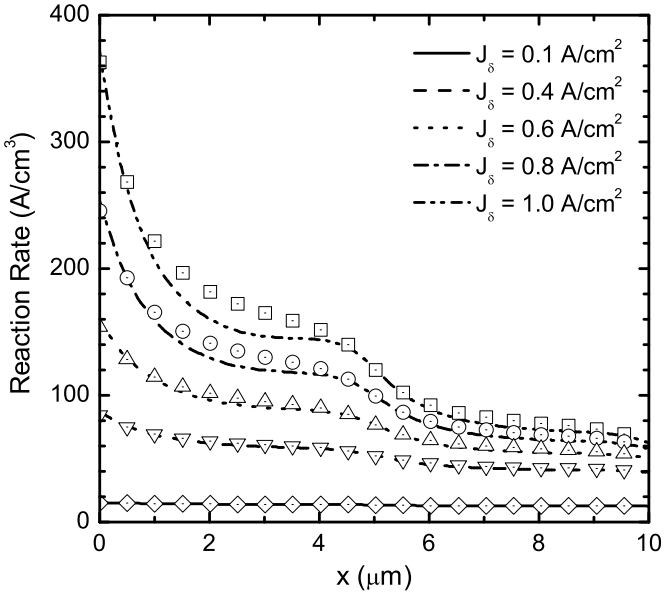

Figure 8.31: Variation of the reaction rate in the cathode catalyst layer along x-axis for Case-I. The lines represent the results for operating conditions of $T = 50$ ℃ and $P = 1$ atm, and the symbols depict the corresponding results for $T = 80$ ℃ and $P = 3$ atm.

catalyst layer same for all cases. All the model results for this case (Case-II) are also presented along the centerline of the two middle agglomerates, i.e. along the $x-$axis. The oxygen concentration profile in the catalyst layer for Case-II is shown with different current density values in Fig. 8.32. All the simulation parameters are identical of Case-I. Results of two different combination of operating parameters, namely, $T = 50$ ℃ and $P = 1$ atm, and $T = 80$ ℃ and $P = 3$ atm are shown in Figs. 8.32a and 8.32b, respectively.

The oxygen concentration at the CCL/GDL interface for similar temperature and pressure are equal for both Case-I and Case-II. A smaller oxygen concentration value is observed at the membrane/CCL interface for Case-II. This is reasonable, since in Case-II, agglomerates are staggered in y-direction. Hence, Case-II has less void space around the agglomerates compared to Case-I, which eventually prevents faster oxygen diffusion through the constricted void spaces. The undulatory profile in the oxygen concentration profile is more prominent in this case. Qualitatively, oxygen concentration profile for both pressure and temperature combinations show similar behavior except their magnitudes. Further inspection on the values of oxygen concentration at the CCL/GDL interface shows that at higher temperature and pressure, concentration is higher than the smaller temperature and pressure combination. This is mainly due to the faster transport processes through the un-flooded GDL at higher pressure and temperature, though oxygen concentration in the gas channel is less for $T = 80$ ℃ and $P = 3$ atm due to the higher fraction of water

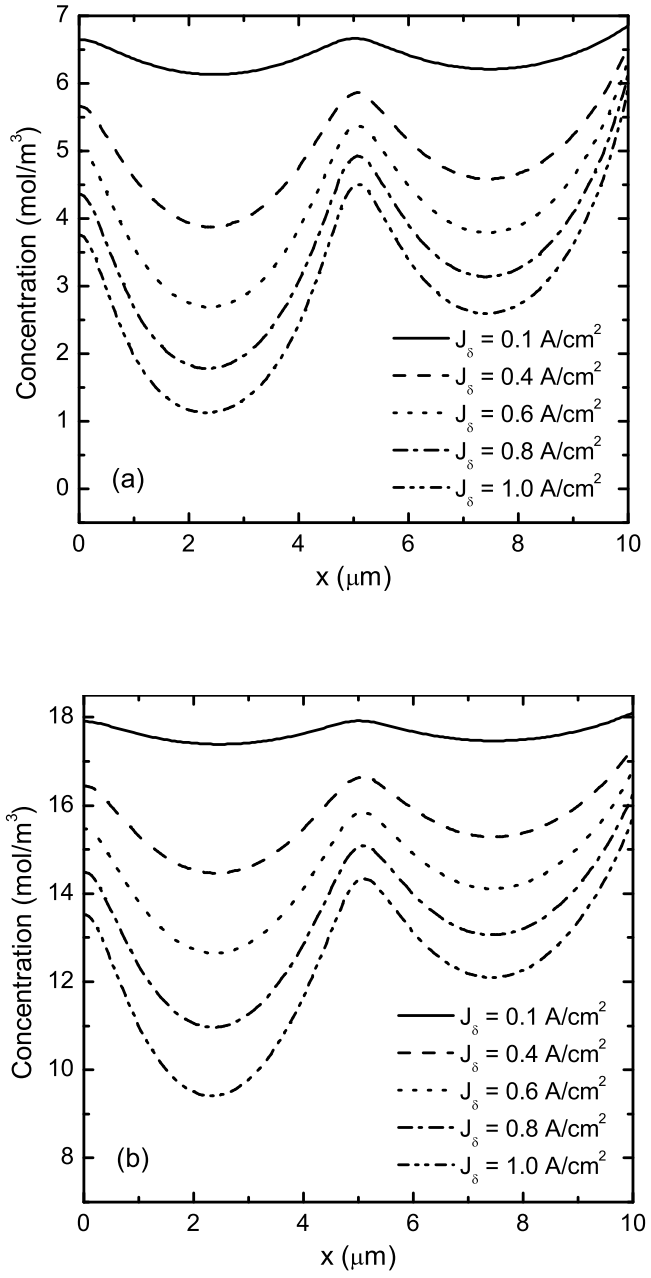

Figure 8.32: Oxygen concentration profile in the CCL along x-axis for Case-II in a PEM fuel cell operating at: (a) T = 50 ℃ and P = 1 atm, and (b) T = 80 ℃ and P = 3 atm. Each line represents result of different current density values as indicated in the legend.

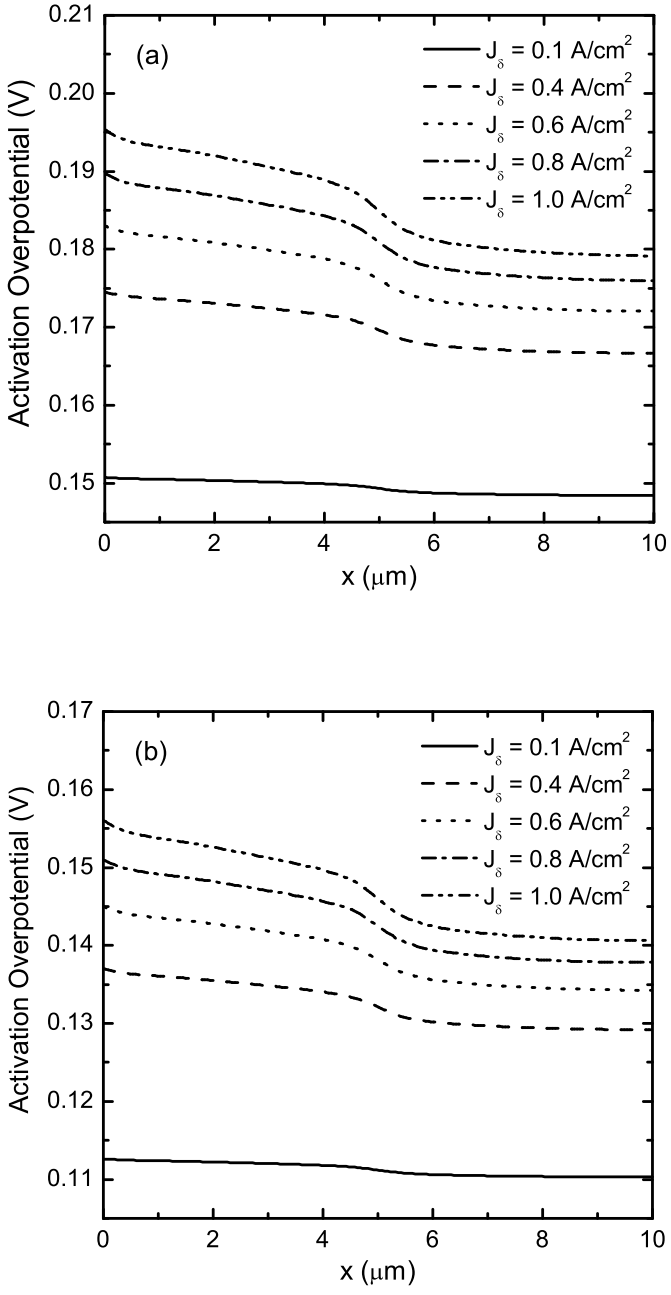

Figure 8.33: Activation overpotential distribution in the CCL for Case-II corresponding to the oxygen concentration shown in Fig. 8.32. Each line represents different current density values as indicated in the legend while part (a) for $T = 50$ ℃ and $P = 1$ atm, and part (b) for $T = 80$ ℃ and $P = 3$ atm.

vapor. Irrespective to the magnitude of the oxygen concentration in the catalyst layer, temperature and pressure do not show any significant effect on the profile of oxygen concentration in the catalyst layer. The variations observed here is mainly due to the catalyst layer structures, or in the other words, operating conditions dictate the quantity in the transport process whereas agglomerate structures dictate the quality of the diffusion in the transport processes.

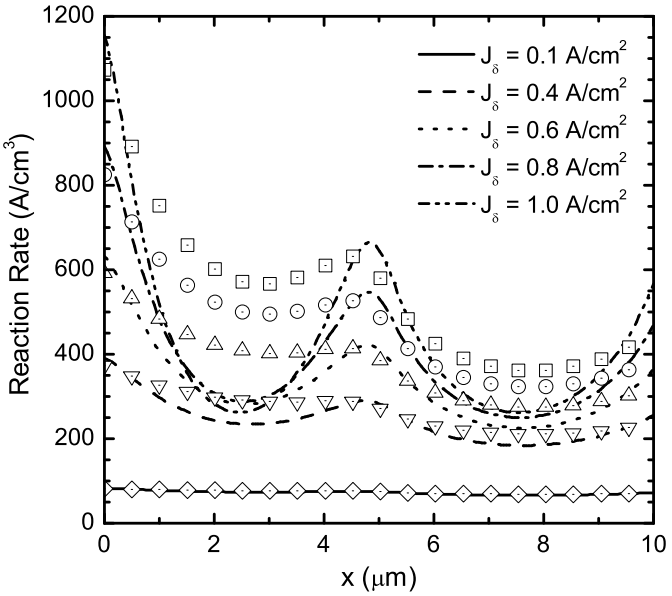

Figure 8.34: Variation of the reaction rate in the CCL along x-axis for Case-II. The lines represent the results for operating conditions of $T = 50$ ℃ and $P = 1$ atm, and the symbols represent the corresponding results for $T = 80$ ℃ and $P = 3$ atm.

Similar to the Case-I, the results of Case-II for $T = 50$ ℃ and $P = 1$ atm show higher activation overpotential than the corresponding overpotential for $T = 80$ ℃ and $P = 3$ atm as shown in Fig. 8.33. Comparing Fig. 8.33 with Fig. 8.30 reveals higher activation loss for staggered agglomerate arrangements, since lesser path available for the oxygen transport due to the staggered agglomerate orientation in the catalyst layer. The variation of the reaction rate in the CCL for the Case-II is shown in Fig. 8.34. Here, the lines represent the results for $T = 50$ ℃ and $P = 1$ atm, and the symbols depict the results corresponding to $T = 80$ ℃ and $P = 3$ atm for five current densities as indicated in the legend.

In Fig. 8.33, a distinct difference is observed in the reaction rate profile for two operating conditions. For higher temperature and pressure, the rate of reaction is higher nearby the center of the agglomerates at high current density values. An undulatory nature has been observed in the reaction rate profile, while a crest exists at the interface between the two

reference agglomerates. This undulatory behavior is more prominent in higher operating parameters values and higher current densities. Further, in some instance, higher current density shows lower reaction rate at the centers of the agglomerates for $T = 50$ ℃ and $P = 1$ atm, which might be due to insufficient oxygen available on the surface of the agglomerates or slow diffusion towards the center of the agglomerates at higher current densities.

8.4.4 Model Results: Bi-directional Staggered Arrangement

In the second type of staggered arrangement, the arrangements of catalyst agglomerates are considered as staggered in y- and z-directions, i.e. bi-directional staggered arrangement, as shown in Fig. 8.25 as Case-III. Like the other two cases, all the results are presented along the centerline of the two reference agglomerates that is along x-axis (see Case-III in Fig. 8.25). Figure 8.35 shows the variations of the oxygen concentration with different current density values as indicated in the legend for $T = 50$ ℃ and $P = 1$ atm (Fig. 8.35a), and $T = 80$ ℃ and $P = 3$ atm (Fig. 8.35b).

In Fig. 8.35, the oxygen concentration profiles show almost identical behavior like Case-II. However, at the center of the agglomerates, oxygen concentration is slightly higher than the Case-II. Since the Case-III has staggered structures of agglomerate arrangements in two directions, the diffusion around the agglomerates is non-uniform. This non-uniformity eventually provides favorable environment for the oxygen diffusion in the radial direction of the agglomerates for Case-III. Further, better oxygen diffusion also reduces the activation overpotential for the Case-III as shown in Fig. 8.36 for both operating conditions compared to the Case-II. This can be better explained by visualizing the agglomerate arrangements. For Case-II, staggered arrangement exists in one direction, therefore, oxygen diffusion outside the agglomerates is faster in the direction where in-line arrangements exist, and slower in the staggered direction. When it comes to the agglomerates surface, then more oxygen is available in certain areas, whereas not all oxygen can diffuse inside the agglomerate through the radial direction.

The aforementioned phenomenon can be visualized by plotting oxygen concentration in the void region for Case-II and Case-III. Figure 8.37 shows oxygen concentration profile outside the agglomerates along a line parallel to the x-axis at $y = 0$ and $z = 2.5$ μm for $T = 80$ ℃ and $P = 3$ atm. Here, the lines depict results for Case-II and the symbols for Case-III for different current density values as indicated in the legend. As observed in Fig. 8.37, the oxygen concentration on the catalyst surface for Case-III is higher than Case-II at the interfaces between two agglomerates (2 μm $< x <$ 3 μm and 7 μm $< x <$ 8 μm) for all the current density values. Therefore, more oxygen available for Case-III to diffuse in the y-direction that is due to the staggered arrangements in the z-direction.

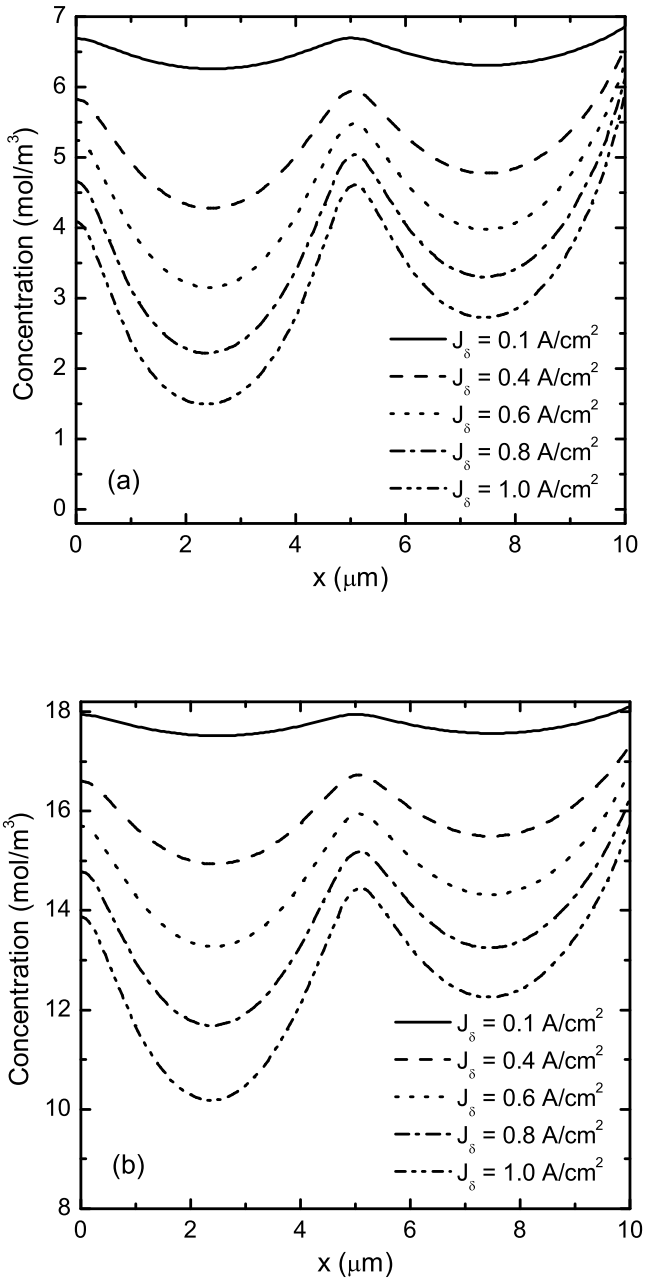

Figure 8.35: Oxygen concentration profile in the cathode catalyst layer along the x-axis for Case-III in a PEM fuel cell operating at: (a) $T = 50$ ℃ and $P = 1$ atm, and (b) $T = 80$ ℃ and $P = 3$ atm. Each line represents the result of different current density values as indicated in the legend.

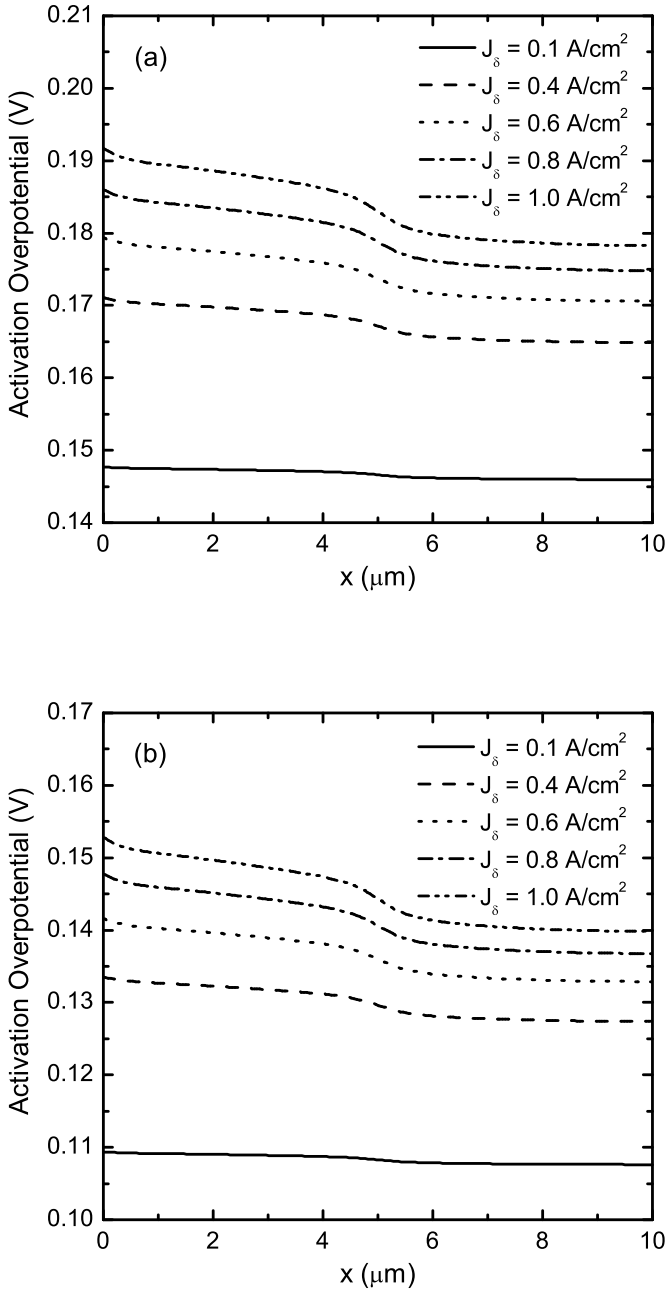

Figure 8.36: Distribution of the activation overpotential in the cathode catalyst layer for Case-III corresponding to the oxygen concentration shown in Fig. 8.35. Each line represents different current density values as indicated in the legend while part (a) for T = 50 ℃ and P = 1 atm, and part (b) for T = 80 ℃ and P = 3 atm.

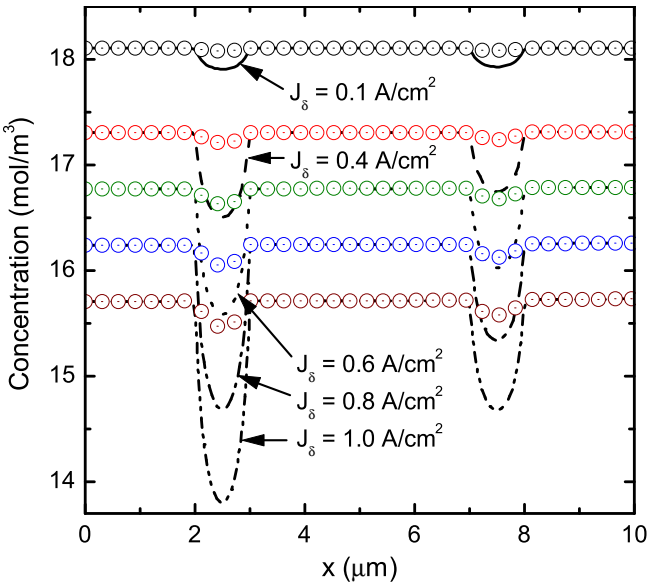

Figure 8.37: Oxygen concentration profile inside the CCL along a line parallel to x-axis at $y = 0$ and $z = 2.5$ μm for $T = 80$ ℃ and $P = 3$ atm. The lines represent the result for Case-II, while the symbols represent Case-III for five different current density values.

Further, due to the higher oxygen concentration in certain areas, diffusion will be faster for Case-III in y-direction.

It has been observed that the less oxygen available in certain areas on the agglomerate surface for Case-II due to the in-line arrangements in two directions, whereas the capacity of diffusion through the radial direction is more. When it comes to the diffusion through the individual agglomerate, all the geometries have same composition inside the agglomerate; hence, the entire diffusion processes is control by the amount of oxygen available at the surface of the agglomerates and how the concentration is distributed over the agglomerate surfaces. In other words, capacity of the diffusion is higher than the amount of oxygen available on the agglomerate surfaces for Case-II. Combining these effects eventually lower the oxygen concentration at the agglomerate center in Case-II (see Fig. 8.32). For Case-III, since staggered structures exist in two directions, available oxygen on the surface of the agglomerates is higher in the y-direction than Case-II. This eventually enhances the diffusion process in the radial direction due to the higher oxygen availability and lowers the activation overpotential as shown in Fig. 8.36. It might be questionable, though Case-III has higher non-uniformity in the catalyst arrangements then why Case-III show better diffusion results. The simple answer will be it provides better passage in the void region in z-direction due to the staggered arrangements.

In the reaction rate of Case-III, similar behavior is observed like Case-II. The plot of

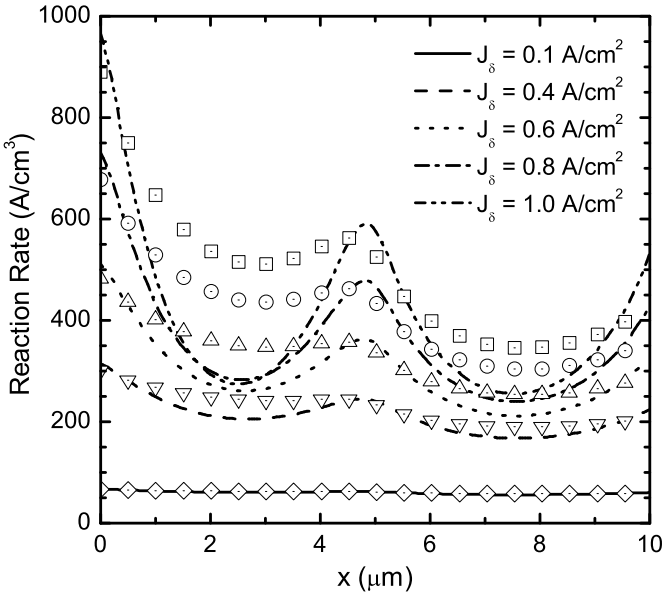

Figure 8.38: Variation of the reaction rate in the cathode catalyst layer along $x-$axis for Case-III. The lines represent the results for operating conditions of $T = 50$ ℃ and $P = 1$ atm, and the symbols represent the results for $T = 80$ ℃ and $P = 3$ atm.

the reaction rate for Case-III is shown in Fig. 8.38 for $T = 50$ ℃ and $P = 1$ atm as lines, and for $T = 80$ ℃ and $P = 3$ atm as symbols. For all the current densities, the reaction rates are higher for higher operating parameters and lower for lower operating parameters. The local variation in the reaction rate observed here mainly due to the local change of oxygen concentration observed in Fig. 8.35 for different operating conditions. Like the activation overpotential, the rate of reaction is also lower for Case-III compared to Case-II as shown in Fig. 8.39.

In Fig. 8.39, the reaction rates are plotted for all the three cases along the x-axis for J_δ = 0.6 A/cm^2 for the fuel cell operating at $T = 80$ ℃ and $P = 3$ atm. For the entire CCL thickness, the reaction rate is highest for the Case-II and lowest for the Case-I. This might be another possible cause for the lower oxygen concentration observed at the center of the agglomerates for Case-II (*cf.* Fig. 8.32) compared to Case-III. In addition, concentration, reaction rate, and activation overpotential are coupled; therefore, it is required to optimize those variables in order to find better cell performance and design. Nonetheless, the results obtained from this investigation reveal a considerable insight on how the governing parameters for a PEM fuel cell change with the structures of the catalyst layer as well as with the operating conditions. Like the Case-II shows highest reaction rate that means the speed of the chemical reaction is faster, hence less catalyst will be required to promote the electrochemical reaction. Conversely, Case-II also shows higher activation losses.

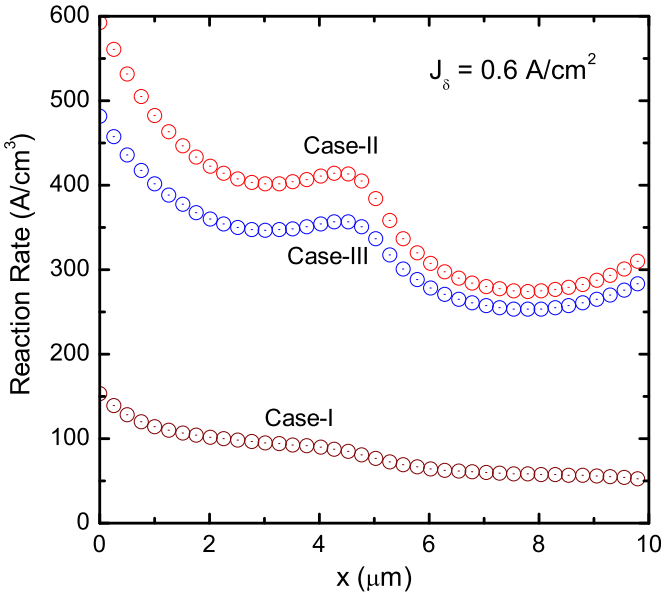

Figure 8.39: Comparison between the reaction rates at $J_\delta = 0.6$ A/cm^2 for the fuel cell operating at $T = 80$ ℃ and $P = 3$ atm.

Therefore, the results presented in these sections providing information, and the direction when and where the optimization is possible or at what extent it is possible.

8.5 Two-dimensional Numerical Model

In this section, the results of a two-dimensional (2D) numerical model of transport phenomena in PEM fuel cell catalyst layer are presented. The computational domain used in the 2D numerical simulation is shown in the previous chapter (Fig. 7.1) along with grid independency test results (Fig. 7.3). Although the grid independency test of a numerical simulation ensures that the results are independent of grid sizes, it does not ensure an accurate estimation if the governing equations are not implemented properly. Therefore, a numerical validation is an essential part of a numerical simulation. In the following sections, the numerical simulation results are first validated and then the results of a parametric study are presented.

8.5.1 Numerical Validation

The most popular approach to validate the numerical results for a PEM fuel cell is to compare the polarization curve with experimental data. The 2D numerical model results presented in this thesis for a half cell of a PEM fuel cell, hence it is required to estimate

the ohmic and concentration overpotentials as well as the mixed potential to generate an accurate polarization curve. As mentioned in Section 8.1 that the experimental results reported in various PEM fuel cell literature lack information on several physical and electrochemical parameters. In some cases, it has been found that replicating published results is very difficult because of the missing information or parameter values. Hence, the comparison with an experimental polarization curve does not always ensure numerical validity unless all the physical and electrochemical parameters involved in the experiment are known.

In this thesis, a different approach has been employed to validate the numerical model results than the typical polarization curve approach. Here, the numerical results are compared with the analytical model of liquid water transport in the CCL of a PEM fuel cell that has also been developed during this thesis research. It is worthwhile to note that the analytical model is based on a 1D approximation that does not include the concentration variation of the reactants along the flow channel or along the GDL/GFC interface. Further, the analytical model needs an accurate estimation of reactant concentration at the CCL/GDL interface. Therefore, the 2D numerical simulation is first performed to obtain the oxygen concentration and liquid saturation at the CCL/GDL interface. Then the numerical data of oxygen concentrations and liquid saturations at the CCL/GDL interface are used in the analytical model to obtain the water saturation profile inside the catalyst layer. Although a theoretical approach is provided in this thesis to estimate the oxygen concentration in various layers of a PEM fuel cell, the use of numerical data will provide better estimation.

Figure 8.40 depicts the comparison of the numerical results with the analytical model results for two different current densities as indicated in the legend. Here the liquid water saturations are plotted across the CCL thickness at two different locations along the CCL/GDL interface, namely $y = w/2$ and $y = w$ from the line of symmetry as shown in Fig. 7.1. The lines represent the analytical model results of liquid saturation across the CCL thickness and the symbols represent the numerical simulation results for a catalyst layer having a contact angle of 80°. All the parameters used in the numerical simulations are the same as the base case except the GDL properties. The values of GDL thickness, porosity, and contact angle are considered as 300 μm, 0.5, and 100°, respectively, while the base case parameters are listed in Table 8.9.

As seen in Fig. 8.40 for high current density (top figure), the analytical model estimates higher liquid saturation than the numerical model. This discrepancy is mainly due to the assumption made in the analytical model and one of the assumptions was constant oxygen concentration across the CCL thickness. In reality, the oxygen concentration varies

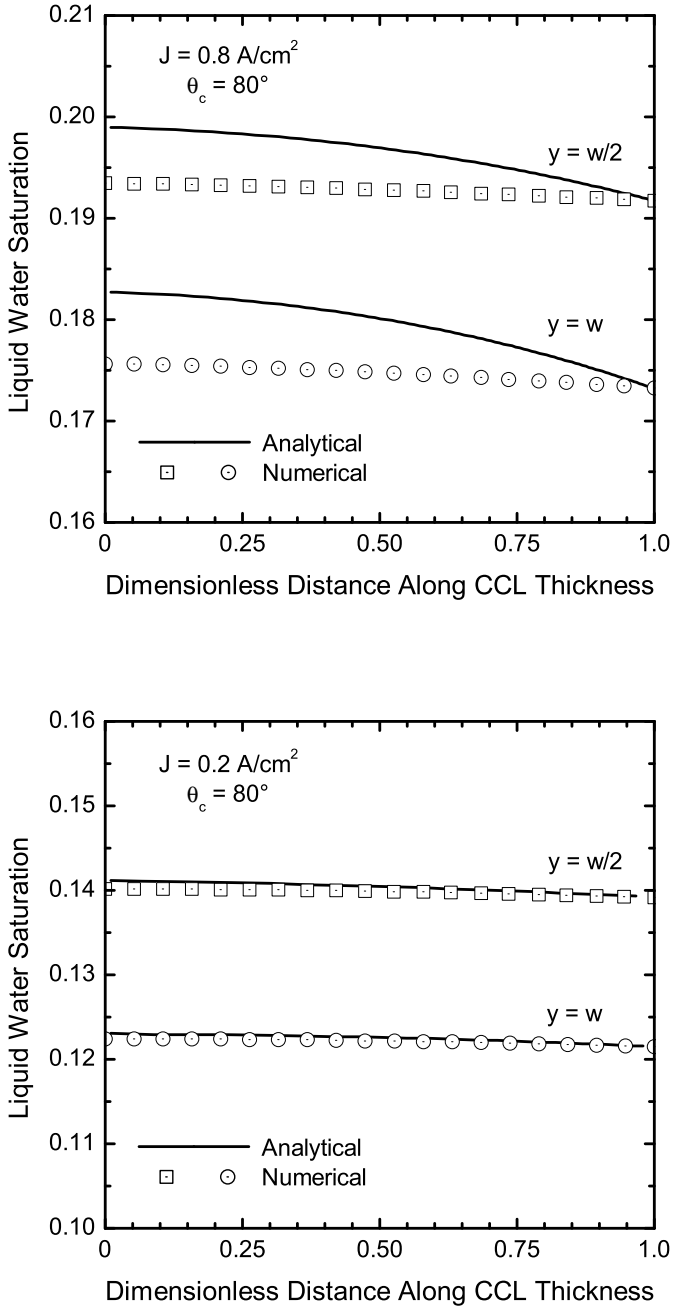

Figure 8.40: Validation of the numerical model results with the analytical model results. The lines represent the analytical results of liquid saturation across the CCL thickness at two different locations under the flow channel as indicated in the legend and the symbols represent the numerical simulation results. The GDL properties, thickness, porosity, and contact angle, are considered as 300 μm, 0.5, and 100°, respectively.

significantly across the CCL thickness at higher current densities and it will be lower at the membrane/CCL interface than the oxygen concentration at the CCL/GDL interface. Since the reaction rate is also a function of oxygen concentration, an assumption of higher oxygen concentration at the membrane/CCL interface implies higher reaction rate; hence the liquid water production from the electrochemical reaction is also higher. Therefore, the analytical expression of liquid water saturation at the CCL of a PEM fuel cell will always overestimate liquid saturation at higher current densities.

At low current density ($J = 0.2$ A/cm^2), the variation of oxygen concentration in the CCL is relatively low. Hence, the assumption made during the analytical formulation of liquid water profile in the CCL makes the analytical expression valid for the low current densities. The bottom part of Fig. 8.40 shows almost identical liquid saturation profile for both the numerical simulation and analytical estimation. Although a small variation between the numerical and analytical results is still visible near the membrane/CCL interface, it can be again attributed to the assumption of uniform oxygen concentration in the analytical formulation. Nonetheless, it is reasonable to claim that the numerical results are accurate and the comparison shown in Fig. 8.40b will serve as the validation of the numerical results presented in this thesis.

8.5.2 Effect of Water Density

The mathematical model of liquid water transport developed in thesis is derived from the fundamental conservation equations using a volume-average technique as described in Chapters 3 and 4. It has been observed that the PEM fuel cell literatures confuse the superficial and intrinsic water densities and eventually present a wrong result of the liquid water saturation in the PEM fuel cell [186, 187]. Most of these numerical models are implemented on commercial software Fluent® using a wrong interpretation of water density. Here a comparison between the result obtained using the mathematical formulation of liquid water transport given in Fluent® user guide [186] and the mathematical formulation developed in this thesis has been provided. For both cases, the parameter values are identical of that are listed in Table 8.9. For convenience, the results of Fluent® formulation is referred as "Case 1" and the results of present formulation is referred as "Case 2". To be specific, the Case 1 represents the results of Fluent® formulation when the water density in the liquid water equation is interpreted as intrinsic density [187]. Conversely, the Case 2 represent the results based on Eq. (4.51), which is a volume-averaged equation.

Figure 8.41 shows the liquid water profile along the CCL and GDL thicknesses from the membrane/CCL interface ($x = 0$) to the CCL/GDL interface ($x = 220$ μm) at $y = 3w/4$ from the bottom line of symmetry in Fig. 7.1, which is under the flow channel along a line

Table 8.9: Parameters used in the numerical simulation for the base case

Parameter	Value
Channel width, w (mm)	1
Channel height, h (mm)	1
Operating temperature, T (°C)	80
Operating pressure, P (atm)	3
Operating current density, J (A/cm^2)	0.8
Relative humidity (%)	100
Liquid saturation in gas channel	0
Drag coefficient, α	0
GDL thickness, δ_{GDL} (μm)	200
GDL contact angle (°)	110
GDL porosity, ϵ_{GDL}	0.6
CCL contact angle (°)	80
CCL thickness, δ_{CL} (μm)	20
Catalyst loading per unit area, m_{Pt} (mg/cm^2)	0.3
CCL platinum content, %Pt (%)	20
CCL Nafion content, %N (%)	30
Permeability, K (m^2)	8×10^{-12}
Membrane phase conductivity, σ_m (S/cm)	0.17
Solid phase conductivity in CCL, $\sigma_{s,\text{CL}}$ (S/cm)	0.9
Solid phase conductivity in GDL, $\sigma_{s,\text{GDL}}$ (S/cm)	12.5
Carbon density, ρ_{C} (g/cm^3)	2
Nafion density, ρ_m (g/cm^3)	1.9
Platinum density, ρ_{Pt} (g/cm^3)	21.5
Reference oxygen concentration, $c_{\text{O}_2,\text{ref}}$ (mol/m^3)	1.2
Anodic transfer coefficient, α_a	0.5
Cathodic transfer coefficient, α_c	0.5

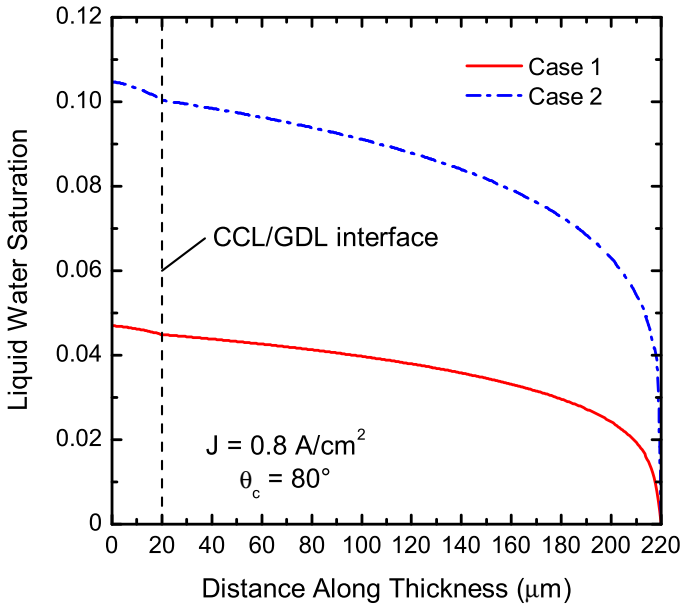

Figure 8.41: Liquid water saturation profile along the thickness from the membrane/CCL interface ($x = 0$) to the GDL/GFC interface ($x = 220$ μm) under the flow channel at $y = 3w/4$. The solid line represents the numerical results obtained using the liquid water equation given in Fluent® user guide with intrinsic liquid water density as Case 1, while the dashed-dot line depicts the results obtained using the volume-averaged formulation developed in this thesis as Case 2.

parallel to the line of symmetry and channel wall. The solid line represents the numerical results obtained using the formulation given in Fluent® user guide as Case 1 that can be interpreted by Eq. (4.52) if we remove the liquid phase volume fraction (i.e. using constant superficial density) [187]. For example, the superficial water density is considered as 970 kg/m^3 in Ref. [187] that seems inappropriate. Conversely, the present formulation utilized the appropriate transformation as described in the volume-averaged formulation in Chapter 4, while replacing the superficial quantity with a intrinsic or phase-averaged quantity. As mentioned earlier, the intrinsic quantity is the measurable quantity; hence the intrinsic liquid water density is considered constant not the superficial water density. The results of the present formulation is depicted by the dashed-dot line in Fig. 8.41 as Case 2. Clearly, the results are completely different and the estimation based on the Fluent® formulation with intrinsic water density (Case 1) significantly under-estimate the liquid water saturation. At the membrane/CCL interface, the liquid water saturation is about 55% lower than the estimation of based on the volume-averaged formulation that is developed in this thesis.

A comparison between the liquid water distribution inside the CCL and GDL for

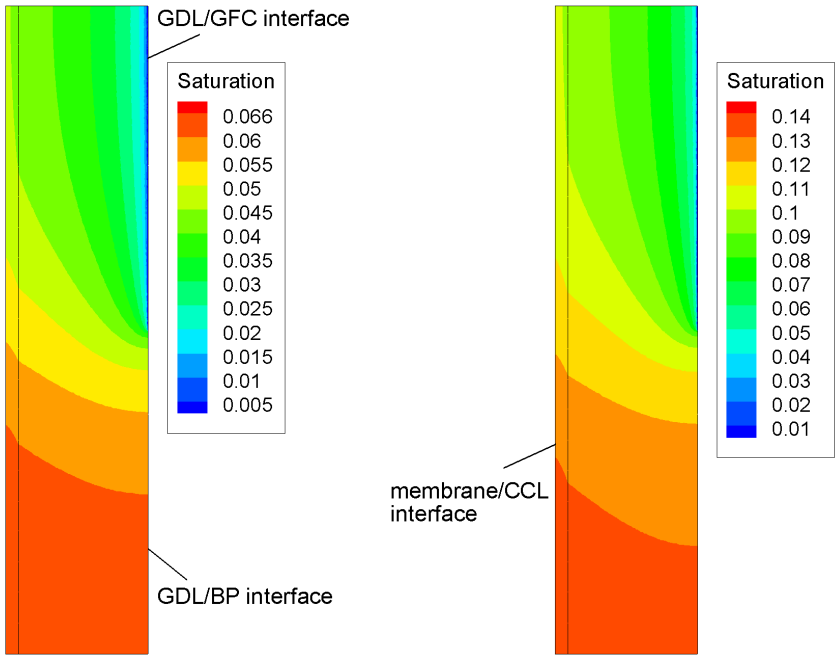

Figure 8.42: Distribution of the liquid water inside the CCL and GDL of a PEM fuel cell estimated for (a) Case 1 (using intrinsic liquid density) and (b) Case 2 (using superficial liquid density or present volume-averaged formulation). The minimum liquid saturation is at the GDL/GFC interface, while the maximum liquid saturation presents near the membrane/CCL interface under the bipolar plate.

Case 1 and Case 2 are shown in Fig. 8.42. These figures show the entire map of liquid water saturation for both cases, where the leftmost interface of each figure represents the membrane/CCL interface and the rightmost interface has two parts: the top-half is under the flow channel (GDL/GFC interface) and the bottom-half is under the land area (GDL/BP interface) as indicated in Fig. 8.42. Comparing the maximum liquid saturation that occurs near the membrane/CCL interface under the land (the bottom-left corner in each figure), we see exactly similar estimation, which is about 55% lower for Case 1 compared to Case 2 (present volume-averaged formulation). Hence, it can be easily claimed that the liquid water saturation is significantly under-estimated that is about 50% to 55% for the catalyst layer. These results also reveal that why the PEM fuel cell experiments show high liquid saturation and the numerical models predict only a small liquid saturation, which is in the order of 0.05 to 0.1 [187].

Similarly, the reactant concentration estimates based on the above-mentioned two cases are also compared. In this case, the oxygen mass fraction distributions are compared as shown in Fig. 8.43. Although a significant difference observed in the liquid saturation

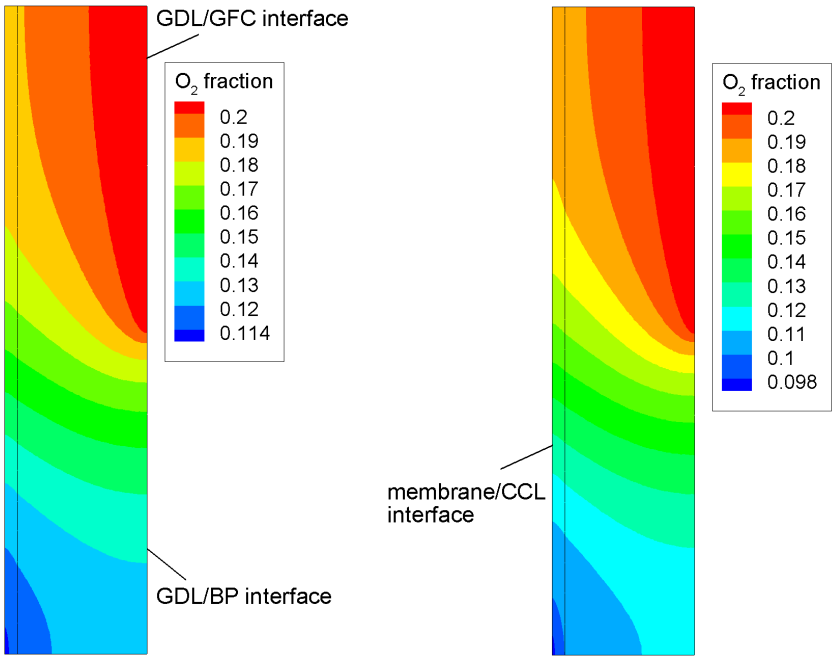

(a) Case 1 (b) Case 2

Figure 8.43: Distribution of the oxygen mass fraction inside the CCL and GDL of a PEM fuel cell estimated for (a) Case 1 (using intrinsic liquid density) and (b) Case 2 (using superficial liquid density or present volume-averaged formulation). The highest oxygen mass fraction is at the GDL/GFC interface, while the lowest oxygen mass fraction presents near the membrane/CCL interface under the bipolar plate.

distributions, the oxygen mass fraction distributions show about 13% lower estimate for the present under-estimate formulation compared to the Case 1 (Fluent® formulation with intrinsic water density) when we compare the lowest values of oxygen mass fraction. It seems a small liquid saturation that is observed in Case 1 is sufficient to hinder the oxygen transport. A significant increase of liquid saturation, in this case from 0.07 to 0.14, only has a negligible effect on the oxygen transport. This is probably due to the fact that the additional liquid water accumulates in the pores those are already hindering the oxygen transport. Therefore, the additional liquid water only increase the amount of saturation inside the pores and it does not further hinder the oxygen transport unless it occupies a dry pore.

The variation observed in the oxygen mass fraction can also be attributed to the effective diffusivity formulation. The effective diffusivity expression provided in Chapter 5 considers a random liquid water film that only reduces or partially covers the reaction surface area inside the catalyst layer. Therefore, a 50% increase of liquid saturation, shown in Fig. 8.42, does not block the reaction surface completely. It can be further concluded

that a mobile liquid saturation of 0.14 is insufficient to significantly hinder the oxygen transport for a current density of 0.8 A/cm^2 that is already hindered by a small liquid saturation. If the immobile saturation is included to the mobile saturation, we might see a significant reduction in the oxygen transport due to the liquid water. Nonetheless, the results presented in this section provide enough evidence that the model based on the Fluent® formulation will significantly under-estimate the liquid water saturation and will eventually over-estimate the oxygen transport if the water density is interpreted incorrectly. Conversely, the volume-averaged approach does not confuse the intrinsic and superficial densities as they are well-defined.

8.5.3 Effect of Gas Density

The results shown in the previous section encourage investigating how the gas phase density will affect the oxygen transport if the intrinsic term is confused by the superficial term or vice versa. Therefore, the effect of intrinsic and superficial gas densities on the oxygen transport has been investigated in this section. There different cases are considered. The first case (Case 1) represents a case when the gas density is considered as an intrinsic density in the Stefan-Maxwell (SM) module in COMSOL Multiphysics®. The second case (Case 2) represents the gas density as a superficial density; hence the intrinsic density is multiplied by the gas phase volume fraction before providing the input for the Stefan-Maxwell equation. As mentioned in Chapter 7, the diffusivity of reactant is also a function of liquid water saturation in the CCL and GDL of PEM fuel cell. The effective diffusivity of the reactants in the SM module should be defined such a way so that it is also a function of liquid water saturation. Therefore, a correction should be made to the effective diffusivity that is represented by Case 3.

Figure 8.44 depicts the oxygen mass fraction profile along the entire CCL and GDL thickness at $y = 3w/4$ for the above-mentioned three cases for a current density of 0.8 A/cm^2. All the parameters used in these calculations are identical of Fig. 8.41. For the case of intrinsic density (Case 1), the result shows an over-estimation compared to the case of superficial density. If the intrinsic density is used in the governing equation, the gas phase density inside the CCL and GDL is assumed higher compared to its real value because of the two-phase flow and the fact that part of the pores are filled with liquid water. Once we consider the gas phase density as a superficial density and corrected with the gas phase volume fraction before plugging into the SM module in the COMSOL Multiphysics®, the mass fraction of the oxygen decreases significantly inside the porous layer as shown by the dashed line (Case 2). These two cases are presented without correcting the effective diffusivity with the mobile liquid water saturation. Once the liquid water saturation is incorporated to the effective diffusivity term, further reduction in the oxygen mass fraction

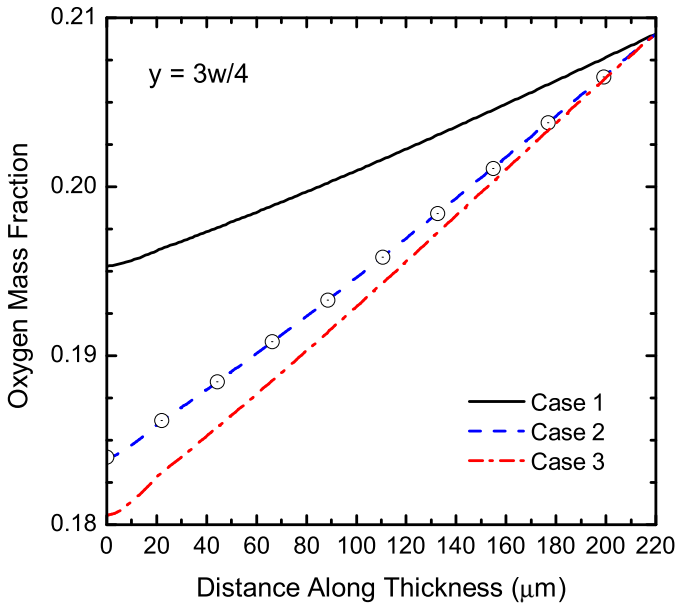

Figure 8.44: Variation of the oxygen mass fraction along the thickness from the membrane/CCL interface ($x = 0$) to the GDL/GFC interface ($x = 220$ μm) under the flow channel at $y = 3w/4$ for various cases.

has been observed that is shown as Case 3 in Fig. 8.44. The variations observed between Case 1 and Case 2 are purely due to the gas phase densities, while the differences observed between the Case 2 and Case 3 are due to the lower diffusion coefficients for the Case 3. The variations of the oxygen mass fraction are clearer if we compare the contour plots of oxygen mass fraction for these cases. The contour plots of oxygen mass fraction are shown in Fig. 8.45. As observed, the difference between the highest and lowest oxygen mass fraction is almost double for the Case 3 (Fig. 8.45c) compared to the Case 1 (Fig. 8.45a).

The symbols in Fig. 8.44 depict a case when the gas phase density in the MS module is corrected with the gas phase volume fraction but the gas density in the Darcy module is not corrected. Surprisingly, we did not see any differences between the results of when the gas phase densities are corrected in all the gas phase governing equations (Case 2) and when the densities are corrected only in the Stefan-Maxwell transport equation. Hence, it is clearly indicating that the Darcy equation has almost negligible effect on the gas transports. In other words, this result shows that the diffusion is the dominant transport mechanism inside the porous CCL and GDL of PEM fuel cell. This comparison (the dashed line and the symbols in Fig. 8.44) also raises the concern whether the assumption of a uniform gas pressure in the catalyst layer (as considered in the analytical formulation of liquid water transport in Chapter 6) is accurate and how it will affect the estimation of liquid water saturation based on the analytical expressions provided in this thesis.

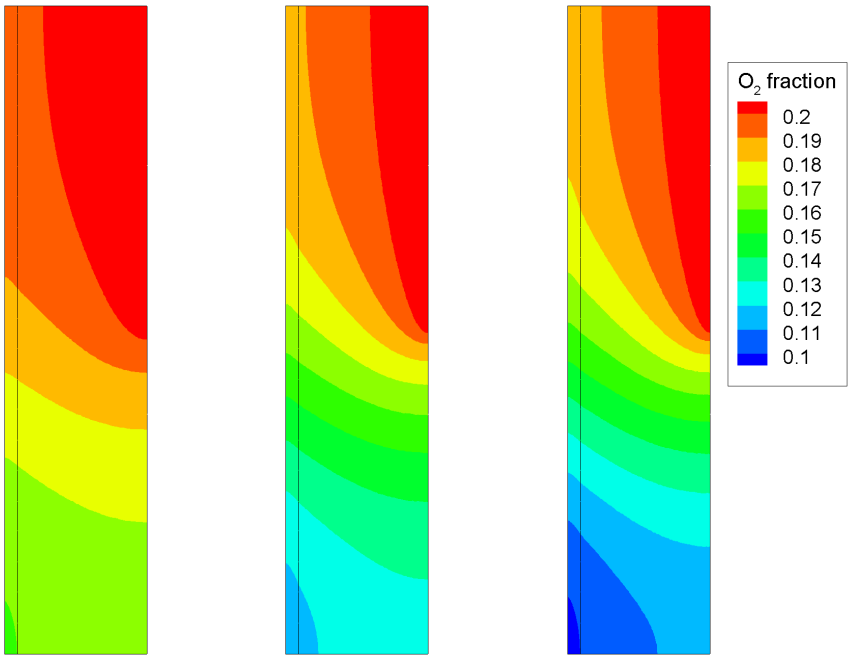

Figure 8.45: Distribution of the oxygen mass fraction in the cathode catalyst and gas diffusion layers of a PEM fuel cell for (a) intrinsic gas density, (b) superficial gas density, and (c) superficial gas density with diffusivity correction used in the Stefan-Maxwell transport equation. The highest oxygen mass fraction is about 0.209, which is at the GDL/GFC interface (top-right part in each figure).

Figure 8.46 depicts the comparison of the liquid water saturation for the cases discussed in previous paragraphs. Similar to the oxygen mass fraction profile in Fig. 8.44, the results are plotted along the CCL and GDL thicknesses from the membrane/CCL interface to the GDL/GFC interface at $y = 3w/4$ and all the parameters are identical. Surprisingly, the liquid water profiles for these cases are identical throughout the thickness. Even in the catalyst layer, the differences between the Case 1 result and the Case 3 result are less than 0.2%. Hence, it is reasonable to claim that the assumption of uniform gas phase pressure made in the analytical formulation of liquid water transport in Chapter 6 is appropriate to predict the liquid water saturation inside the CCL of PEM fuel cell using the analytical expressions developed in this thesis.

8.5.4 Effect of CCL Porosity

As mentioned earlier while investigating the liquid water transport in the CCL using the analytical solution of liquid water transport equation that the catalyst layer surface wettability has significant effect on the overall liquid water transport from the CCL of

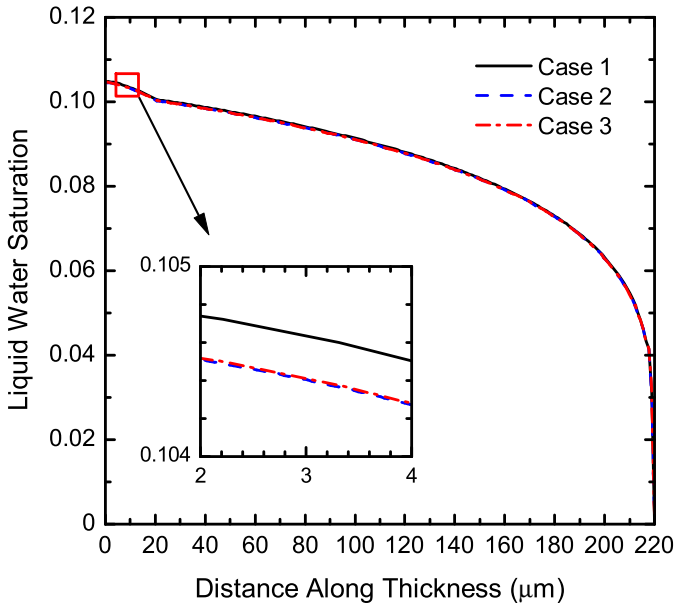

Figure 8.46: Liquid saturation profile along the thickness from the membrane/CCL interface to the GDL/GFC interface at $y = 3w/4$ for various cases.

a PEM fuel cell. In addition, it has been shown in Section 8.4 that the catalyst layer structure has significant effect on the reactant transport. Here a parametric study has been conducted to investigate how the catalyst layer structure and its wettability influence the liquid water transport. Since the catalyst layer is considered as a macro-homogenous layer, the physical structure of the CCL is quantified by its porosity. Obviously, the pores inside a CCL are random and it is not possible to physically quantify a random structure. Hence, it is assumed that the CCL porosity is sufficient to describe the physical nature of a catalyst layer. Since the catalyst layer porosity depends on the platinum and Nafion contents in the CCL, the results are presented as the functions of Nafion content and platinum loading.

Figure 8.47 shows the variation of liquid water saturation with different Nafion contents (%wt of Nafion) in the catalyst layer along the through-plane direction of CCL and GDL at $y = w/4$ for a current density of 0.8 A/cm^2. The parameter values used in these calculations are identical of that are listed in Table 8.9. For low Nafion contents ($\%N \leq 30\%$), the variations of liquid water saturation with the Nafion contents are negligible for the entire thickness of the CCL and GDL. For high Nafion contents ($\%N > 30\%$), the Nafion content increases the liquid saturation inside the catalyst layer. For the entire range of Nafion contents shown in Fig. 8.47, the liquid saturation remains almost identical throughout the GDL thickness. Since the Nafion content is inversely proportional to the CCL porosity, it seems that the CCL porosity does not have any significant effect on the

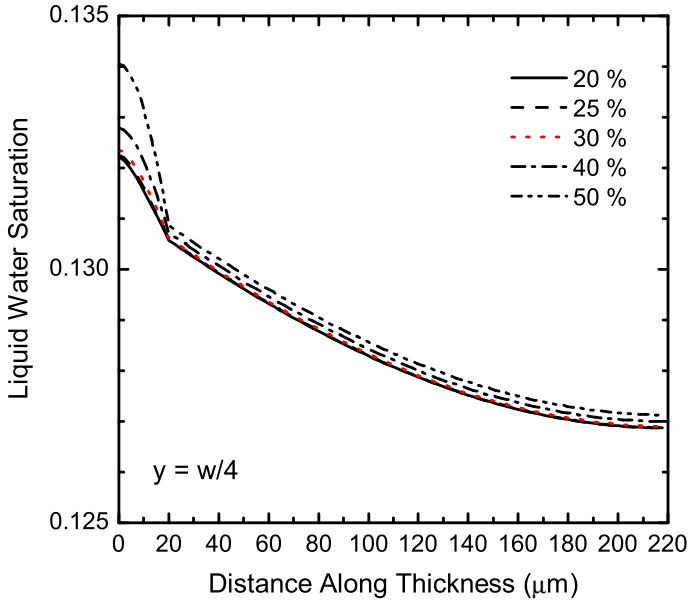

Figure 8.47: Variation of the liquid water saturation with Nafion contents along the through-plane direction of CCL and GDL under the land of bipolar plate at $y = w/4$.

liquid water saturation inside the GDL. If the oxygen concentrations for the various Nafion contents are compared, we see a variation in the oxygen mass fraction.

The variations of the oxygen mass fractions are shown in Fig. 8.48 for different Nafion contents as indicated in the legend. At the membrane/CCL interface, the variation is about 10% between the highest and lowest Nafion contents. Since the effective oxygen diffusivity decreases with the catalyst layer porosity, at higher Nafion contents, the effective oxygen diffusivity is lower. Hence, the oxygen transport is hindered by the higher Nafion contents. Conversely, the production of liquid water inside the catalyst layer is significantly dictated by the electrochemical reaction, hence by the activation overpotential.

The local activation overpotential profiles along the catalyst layer thickness for different Nafion contents are shown in Fig. 8.49. Clearly, the local activation overpotential decreases with the Nafion contents near the membrane/CCL interface. Since local activation overpotential is highest at the membrane/CCL interface, the value at the membrane/CCL interface will be the fuel cell's activation loss. Hence, the value at the membrane/CCL interface is simply referred as "*activation overpotential*" and the value along the CCL thickness is referred as "*local activation overpotential*". For the higher Nafion contents, the effective protonic conductivity increases significantly that provides lower membrane phase potential inside the catalyst layer and hence, reduces the activation overpotential (maximum value in the activation overpotential profile). As the activation overpotential

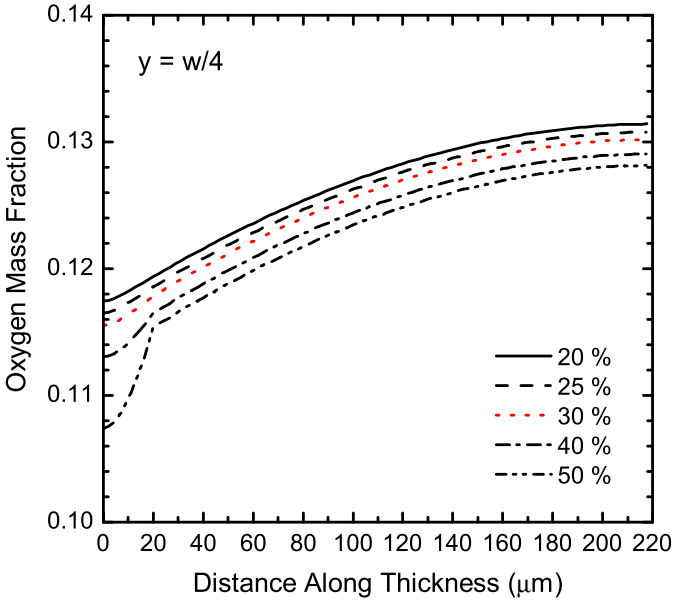

Figure 8.48: Oxygen mass fraction profile with Nafion contents along the through-plane direction of CCL and GDL under the land of bipolar plate at $y = w/4$.

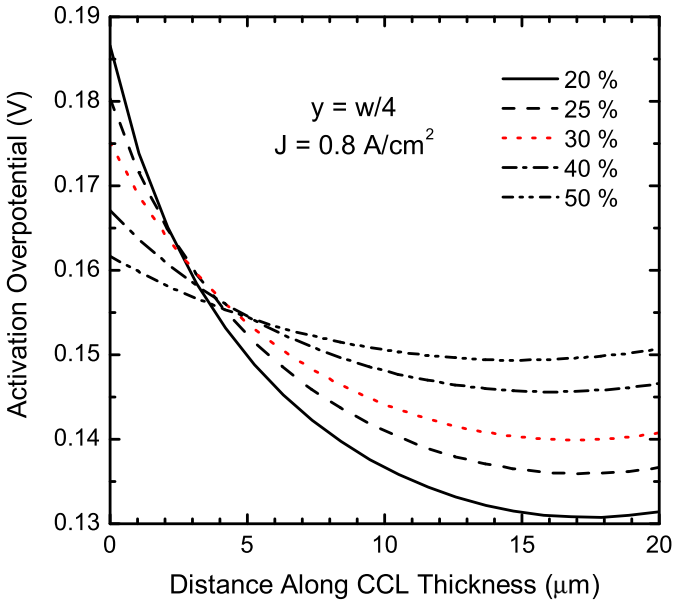

Figure 8.49: Local activation overpotential profile along the CCL thickness at $y = w/4$ for different Nafion loadings.

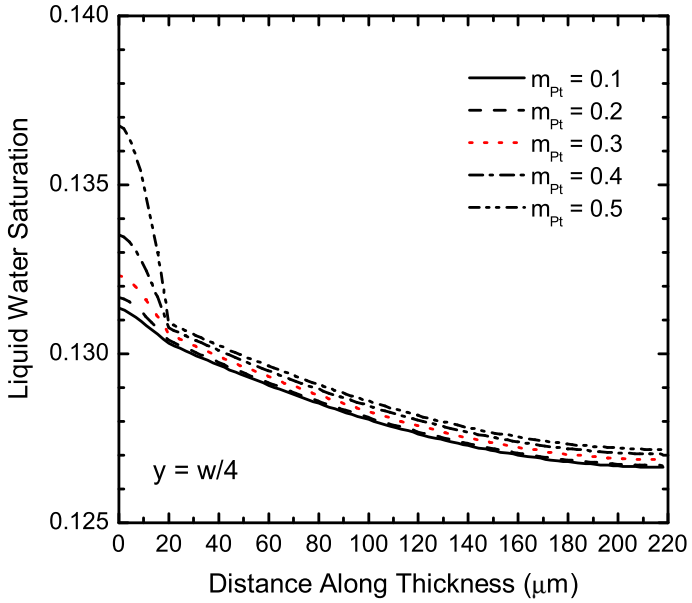

Figure 8.50: Variation of the liquid water saturation with Pt-loadings (mg/cm^2) along the through-plane direction of CCL and GDL at $y = w/4$.

goes down, the electrochemical reaction rate reduces. Therefore, the production of liquid water is low for the higher Nafion content. Hence, the variation of the liquid water saturation profile observed (Fig. 8.47) is the net increase of liquid water saturation due to the porosity reduction and the activation overpotential reduction. At the same time, the results shown in Figs. 8.47 and 8.48 indicate that the optimum performance of a PEM fuel cell should be obtained when a Nafion content of about 30% is considered for the catalyst layer.

Figure 8.50 shows the variation of liquid water saturation along the through-plane direction of CCL and GDL for five different Pt-loadings in mg/cm^2 as indicated in the legend. The parameter values used in these calculations are identical of that are listed in Table 8.9. For low Pt-loadings ($m_{\rm Pt} \leq 0.3$ mg/cm^2), the variations of liquid water saturation with Pt-loadings are almost negligible for the entire GDL thickness that is almost identical behavior what has been observed for the various Nafion contents in Fig. 8.47. For high Pt-loadings ($m_{\rm Pt} > 0.3$ mg/cm^2), Pt-loading increases liquid saturation significantly inside the CCL but the variation of liquid saturation is relatively small inside the GDL. This is due to the fact that the Pt-loading changes the CCL porosity, while the CCL porosity does not have any significant effect on the liquid water saturation inside the GDL.

Similarly Fig. 8.51 depicts the variation of oxygen mass fraction along the through-plane

direction of CCL and GDL under the bipolar plate's land for five different Pt-loadings as indicated in the legend. Unlike Fig. 8.48, the oxygen mass fractions with various Pt-loadings show a significant variation throughout the CCL and GDL thicknesses. The variation is even more prominent inside the catalyst layer. Comparing Fig. 8.51 with Fig. 8.48, we observe about 30% reduction of the oxygen mass fraction when the Pt-loading changes from a value of 0.1 mg/cm^2 to 0.5 mg/cm^2. It is worthwhile to mention that Fig. 8.48 is plotted as a function of %wt of Nafion, while Fig. 8.51 shows the results as a function Pt-loading in mg/cm^2. Therefore, the highest value of the Pt-loading corresponds to a different porosity than the porosity corresponds to the highest value of Nafion content. Nonetheless, Figs. 8.50 and 8.51 depict that the optimum Pt-loading should be in the range of 0.3 mg/cm^2 or lower. In fact, the analytical model results provided in Section 8.2.2 indicate that the optimum Pt-loading is about 0.2 mg/cm^2 for the parameter values listed in Table 8.4. Hence, the numerical results shown in this section provide similar insight that is predicted by the analytical model developed in this thesis.

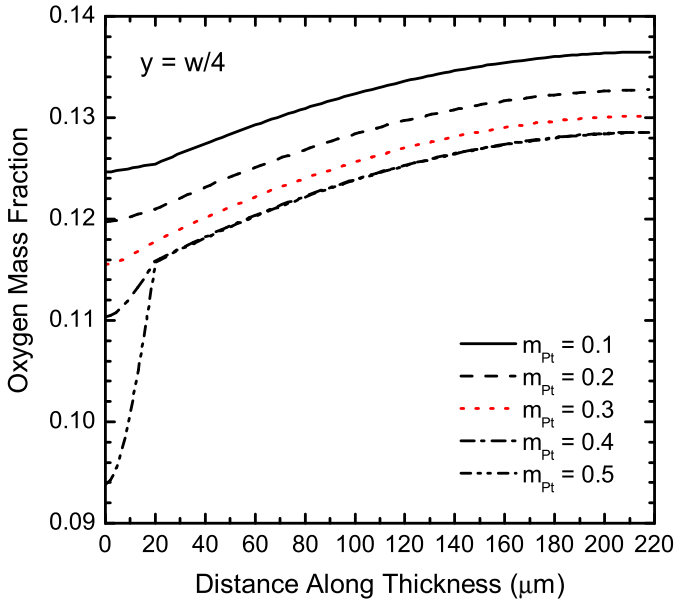

Figure 8.51: Oxygen mass fraction profile with Pt-loadings (mg/cm^2) along the through-plane direction of CCL and GDL under the land of bipolar plate at $y = w/4$.

The local activation overpotential profiles along the CCL thickness with the five different Pt-loadings are shown in Fig. 8.52. The activation overpotentials decrease significantly with Pt-loadings that are mainly due to the better electrochemical reaction. Although the higher Pt-loading reduces porosity and hinders the oxygen transport, it provides better transport of electrons and protons. It should be mentioned here that these results are calculated by changing Pt-loadings only. Both the %wt of platinum and %wt of Nafion

were kept constant. Therefore, the higher Pt-loading also represents the higher volume fraction of Nafion membrane, which provides a higher effective protonic conductivity for the membrane phase in the catalyst layer. Although a 26% reduction in the activation overpotential is possible to achieve by increasing Pt-loading from a value of 0.1 mg/cm^2 to 0.5 mg/cm^2, it might not be favorable for the PEM fuel cell due to the cost associated with platinum catalyst. Therefore, an optimum Pt-loading is always desirable.

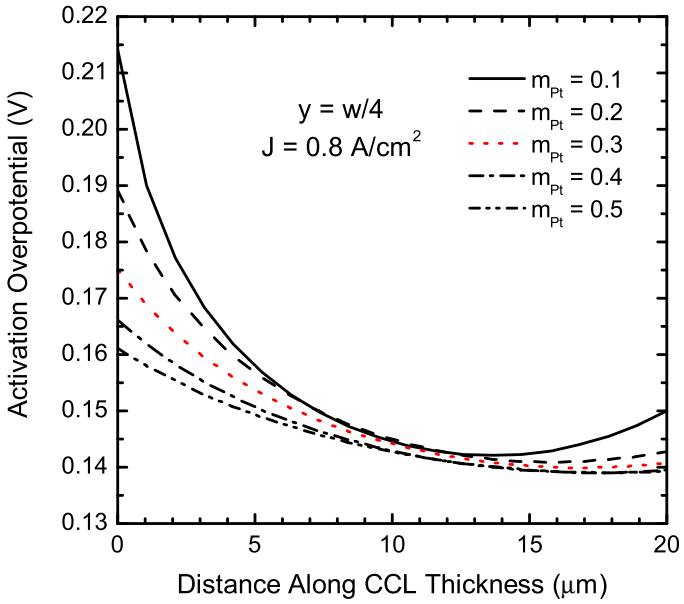

Figure 8.52: Local activation overpotential profile along the CCL thickness under the land of bipolar plate at $y = w/4$ for different Pt-loadings in mg/cm^2.

8.5.5 Effect of CCL Contact Angle

Figure 8.53 shows the variation of liquid water saturation with different CCL contact angles at various locations of CCL and GDL along the through-plane and in-plane directions for a current density of 0.8 A/cm^2. Here Fig. 8.53a represents the liquid water saturation profile under the flow channel ($y = 3w/4$) and Fig. 8.53b represents the liquid water saturation profile under the land area ($y = w/4$), respectively. Conversely, Fig. 8.53c shows the result along the in-plane direction inside the CCL at two different locations. The lines represent the results near the membrane/CCL interface at $x = 1$ μm and the symbols represent the results near the CCL/GDL interface at $x = 19$ μm. The last part of Fig 8.53 shows the variation of liquid water saturation along the in-plane direction at the middle of the GDL ($x = 120$ μm). The parameter values used to estimate the results shown Fig. 8.53 are listed in Table 8.9, except the CCL contact angles that are indicted in the legend.

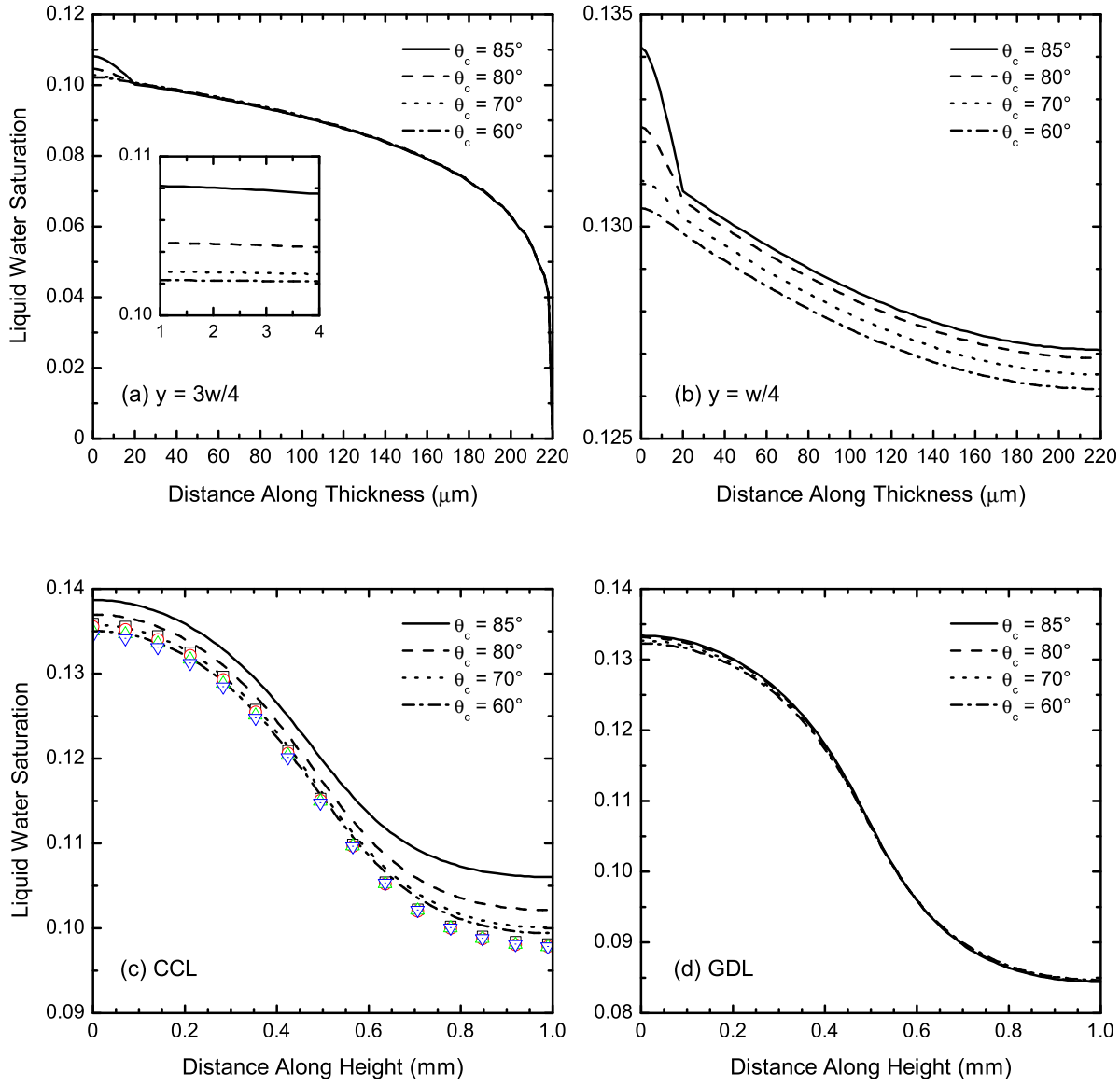

Figure 8.53: Variation of the liquid water saturation with CCL contact angles along the through-plane direction (part a and b), in-plane direction of CCL (part c), and in-plane direction of GDL (part d) for a current density of 0.8 A/cm^2.

The contact angles for a hydrophilic CCL do not have any effect on the liquid water saturation in the GDL under the flow channel ($y = 3w/4$). For the CCL, the contact angles show a change in the liquid saturation values. The higher the contact angles, the higher the liquid saturations. The variation in the liquid saturation profile is small compared to the variation observed during the study based on the 1D analytical expressions of liquid water saturation for the CCL (shown in Fig. 8.17). However, the trend in the saturation profiles remains identical in both Figs. 8.53 and 8.17 for the CCL. As mentioned in Section 8.5.1, the analytical expressions of liquid water saturation at the CCL always overestimate the liquid saturation at the higher current density. The variations observed between the numerical (Figs. 8.53) and the analytical results (Fig. 8.17) inside the catalyst layer can be attributed to the assumptions used in the analytical formulation and the current density value used in the numerical simulation ($J = 0.8$ A/cm^2). Conversely, the liquid saturation profile under the bipolar plate's land ($y = w/4$) shows almost identical trend in both CCL and GDL for low contact angles. For the higher contact angles, the variations are more prominent inside the CCL. Since the catalyst layer needs to be well hydrated for better electrochemical reaction and the oxygen transport can be hindered by the higher liquid water, it seems a hydrophilic catalyst layer with lower contact angles ($\theta_c \leq 70°$) would perform better as it provides a smoother transition for the liquid transport at the CCL/GDL interface ($x = 20$ μm).

In the in-plane direction inside the CCL, the liquid water saturation profiles are shown in Fig. 8.53c. Here the lines are showing the results near the membrane/CCL interface and the symbols are showing the results near the CCL/GDL interface. For both cases, the contact angles do not show any significant effect on the liquid saturation for $\theta_c \leq 70°$. For a higher contact angle ($\theta_c > 80°$), a higher liquid saturation near the membrane/CCL interface than the CCL/GDL interface has been observed. In fact, the capillary pressure is less for the higher contact angle; hence, the driving force for the liquid water is also less that eventually reduces the liquid water transport. Since the liquid saturation profile inside the CCL remain almost unchanged for $\theta_c \leq 70°$, it can be concluded again that a CCL with lower contact would perform better for both the electrochemical reaction and oxygen transport. Like the through-plane direction under the flow channel, the liquid saturation profile remain independent of the CCL contact angles in the in-plane direction inside the GDL as illustrated in Fig. 8.53d.

Although the catalyst layer contact angles show a distinct effect on the liquid water saturation inside the CCL, the oxygen mass fractions remain unchanged for all these contact angles. The contour plots of oxygen mass fraction inside the CCL and GDL are shown in Fig. 8.54 for the two extreme contact angles as indicted in the figure. As seen in Fig 8.54 for two extreme contact angles, the contour of oxygen mass fraction are exactly

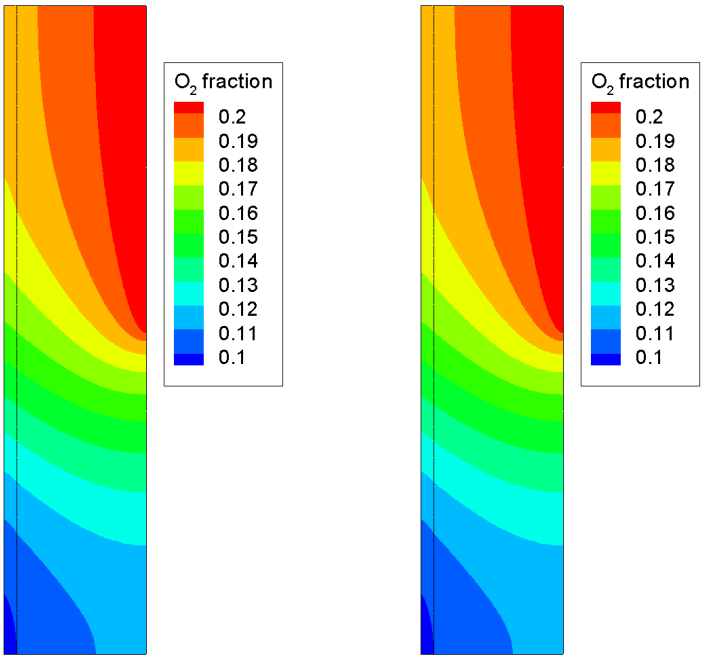

(a) $\theta_c = 85°$ (b) $\theta_c = 60°$

Figure 8.54: Distribution of the oxygen mass fraction inside the CCL and GDL of a PEM fuel cell for two CCL contact angles.

the same even inside the catalyst layer. The main reason why we do not see any significant variation in the oxygen mass fraction is the effective oxygen diffusivity. The amount of variation observed in liquid saturation in the CCL (Fig. 8.53a) is unable to further hinder the oxygen transport or the effective transport properties. It is believed that the reactant transport will only be affected if the pores are completely blocked by the liquid water. The effective property formulations are developed based on the assumption that if the pores are partially filled by liquid water, it will only reduce the effective oxygen diffusivity but the order of magnitude will remain the same. Hence, a significant change will be observed between the dry-case and flooded-case. Once the cell is flooded, the oxygen concentration will only be further hindered if the liquid water saturation is extremely high.

Figure 8.55 depicts the local activation overpotential profile along the CCL thickness for different contact angles as indicated in the legend. Although the liquid water saturation changes about 6% under the flow channel and about 3% under the land when the CCL contact angle changes from 60° to 85°, the activation overpotentials remain exactly the same for different contact angles. Recalling the result shown in Fig. 8.20, we can immediately recognize that the linear reduction of active reaction area with the liquid saturation used in the numerical simulation is the main reason for the identical activation overpotential profiles observed in Fig 8.55. This result also raises the concern that whether the

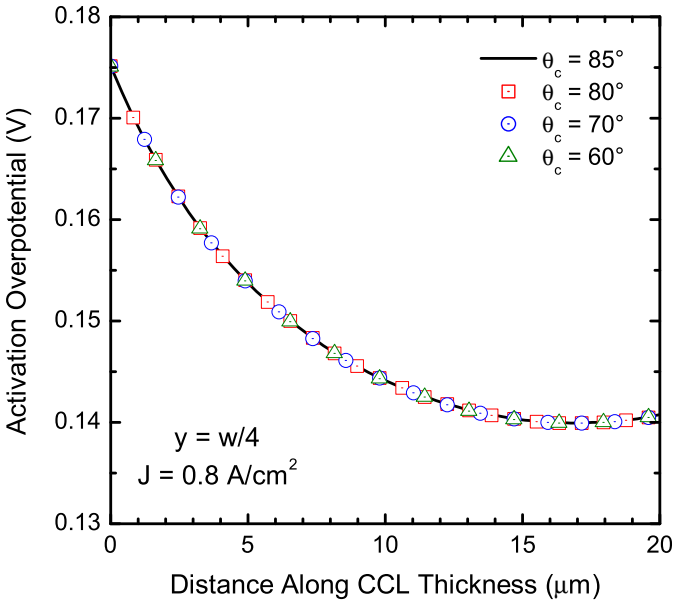

Figure 8.55: Local activation overpotential profile along the catalyst layer thickness at $y = w/4$ for different CCL contact angles.

linear reduction of active reaction area with the liquid saturation should be sufficient for the PEM fuel cell modeling, although it has been widely used over the last decade. At the same time, the numerical results prove that the analytical model developed in this thesis has the same capability as the numerical model to predict the cell performance.

8.5.6 Effect of GDL Porosity

Figure 8.56 shows the variation of liquid water saturation along the through-plane direction of CCL and GDL at $y = 3w/4$ (under the flow channel) and $y = w/4$ (under the bipolar plate's land) for three different values of GDL porosity as indicated in the legend. The parameter values used in these calculations are identical of those are listed in Table 8.9. At $y = w/4$, the liquid saturation profiles are almost uniform throughout the entire thickness but the liquid saturation decreases with GDL porosities. Hence, the water transport is hindered by the lower GDL porosity. Similar saturation profiles are observed under the flow channel ($y = 3w/4$). Here the liquid saturation is sharply decreased at the GDL/GFC interface indicates the removal of liquid water through the flow channel. These results also indicate that the higher GDL porosity will keep the liquid water saturation low inside the CCL.

Figure 8.57 depicts the variation of oxygen mass fraction along the through-plane direc-

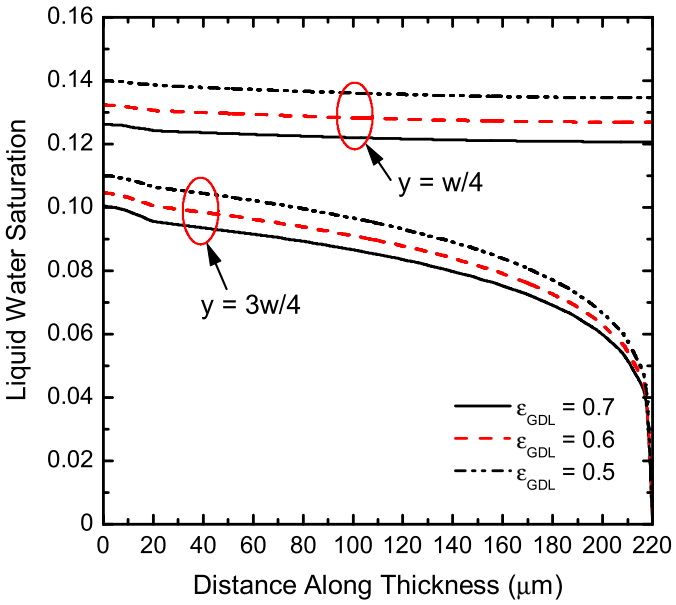

Figure 8.56: Variation of the liquid water saturation with GDL porosity along the through-plane direction of CCL and GDL at $y = 3w/4$ (under the channel) and $y = w/4$ (under the land) as indicated in the legend.

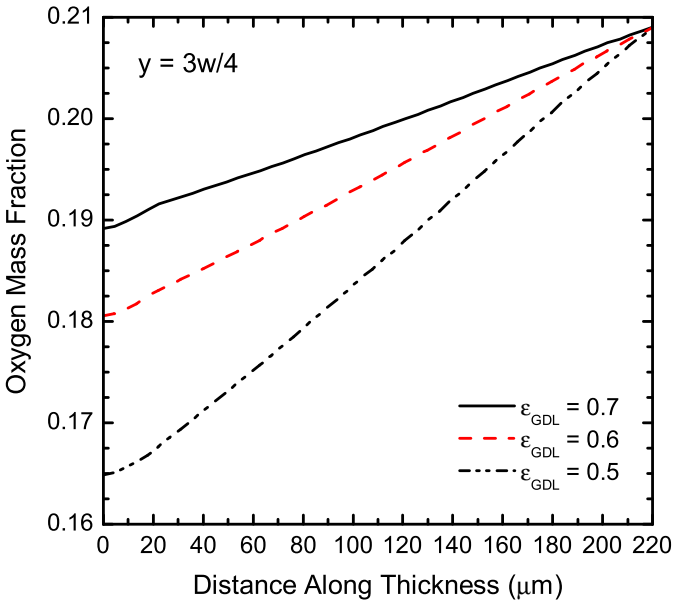

Figure 8.57: Oxygen mass fraction profile with GDL porosity along the through-plane direction of CCL and GDL at $y = 3w/4$.

tion of CCL and GDL at $y = 3w/4$ for three different GDL porosities. Similar to Fig. 8.56, the oxygen transport is also hindered by the lower GDL porosity. Although the oxygen mass fraction profiles under the flow channel show that the oxygen concentration decreases significantly with the increase of GDL porosity near the membrane/CCL interface, there is sufficient oxygen concentration still available for the electrochemical reaction to take place. Therefore, it would be worthwhile to investigate whether the oxygen available over the entire catalyst layer is sufficient to run the fuel cell below its concentration polarization limit. The contour plots of oxygen mass fraction for the GDL porosity values of 0.5 and 0.7 are shown in the two part of Fig. 8.58 for a current density of 0.8 A/cm^2. These contour plots clearly indicate that the oxygen concentration is significantly low under the land area near the membrane/CCL interface for the porosity value of 0.5 (part a) compared to the value of 0.7 (part b). Hence, the fuel cell operated at 0.8 A/cm^2 with a GDL porosity of 0.7 can even operate at a higher current density, while the cell with GDL porosity of 0.5 is susceptible to the concentration polarization at 0.8 A/cm^2. The results shown in Figs. 8.56–8.58 also suggest that the higher GDL porosity is always favorable for the reactant and water transports as well as it would be possible to run the fuel cell at a higher current density without the concentration polarization losses.

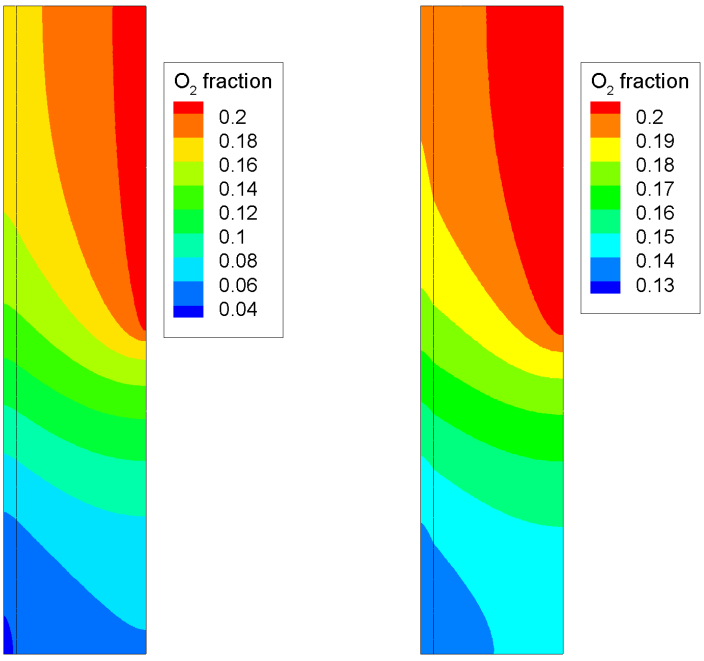

(a) $\epsilon_{GDL} = 0.5$ (b) $\epsilon_{GDL} = 0.7$

Figure 8.58: Distribution of the oxygen mass fraction inside the CCL and GDL for two different GDL porosities at a current density of 0.8 A/cm^2.

The local activation overpotential profiles along the catalyst layer thickness for three different GDL porosities are shown in Fig. 8.59. Since the activation overpotential is seen to be a maximum value under the land of the bipolar plate, the profiles shown in Fig. 8.59 are plotted along the line of symmetry under the land (at $y = 0$ in Fig. 7.1). It has been observed that the changing GDL porosity from 0.7 to 0.6 causes about 7.4% reduction of activation loss, while the reduction of activation loss is about 2.7% when the GDL porosity changes from 0.6 to 0.5. Since the higher GDL porosity shows better cell performance in terms of the reactant and water transports, it seems that the GDL porosity near a value of 0.6 would provide the optimum performance without sacrificing significant amount of cell output. At the same time, the higher GDL porosity would reduce the GDL's mechanical strength.

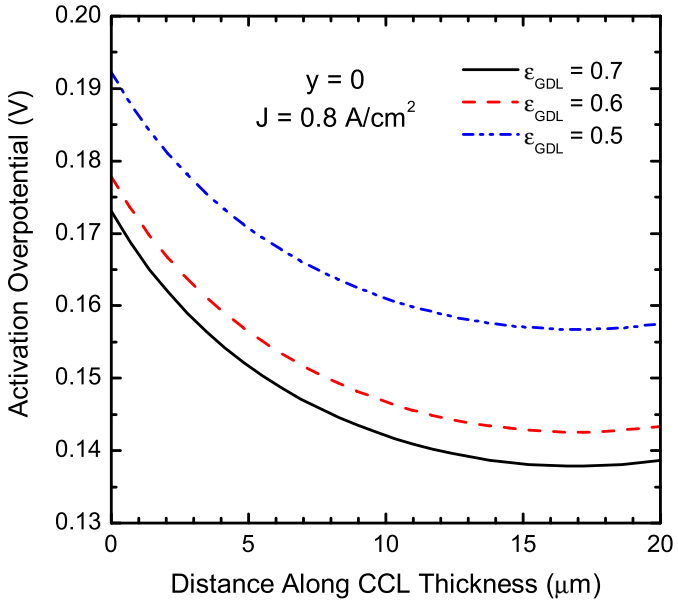

Figure 8.59: Local activation overpotential profile along the catalyst layer thickness under the land of bipolar plate at $y = 0$ for different GDL porosities.

8.5.7 Effect of GDL Contact Angle

Figure 8.60 shows the variation of liquid water saturation with GDL contact angles at two different locations along the through-plane direction of CCL and GDL for a current density of 0.8 A/cm^2. The parameter values used in these calculations are identical of that are listed in Table 8.9 except the GDL contact angles that are indicated in the figure legend. Unlike the effect of CCL contact angles on the liquid saturation (Fig. 8.53), the GDL contact angles show a large variation on the liquid saturation throughout the

entire CCL and GDL thicknesses for both locations. It also indicates the highest liquid saturation will always be under the land area due to the longer transport path for water to be removed through the GDL to the GFC. It is also clear that the higher the GDL contact angle (hydrophobicity), the lower the liquid saturation. Hence, the GDL hydrophobicity enhances the liquid water removal from the CCL to the GFC.

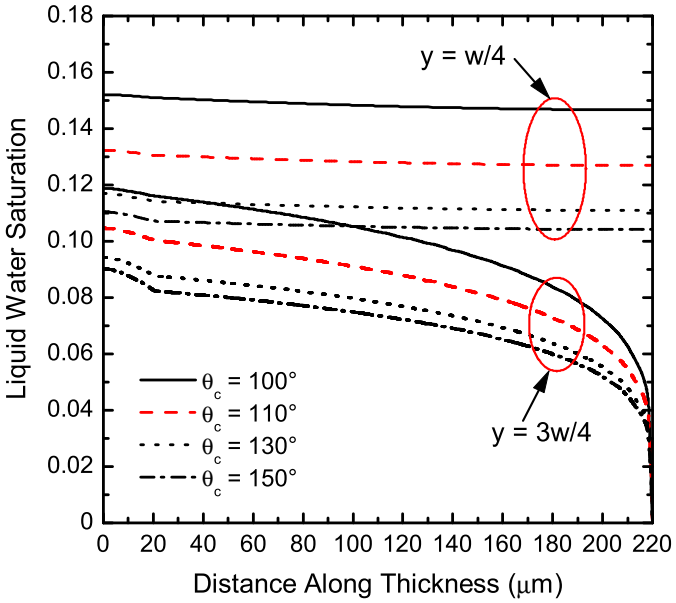

Figure 8.60: Variation of the liquid water saturation along the through-plane direction of CCL and GDL at $y = 3w/4$ (under the channel) and $y = w/4$ (under the land) with GDL contact angles.

The variations of oxygen mass fraction with GDL contact angles inside the CCL and GDL are illustrated in Fig. 8.61 along the through-plane direction at $y = 3w/4$ and $y = w/4$ as indicated in the legend. Although a significant change in liquid saturation has been observed with the GDL contact angles, it seems that the amount of liquid saturation observed in Fig. 8.60 does not hinder the oxygen transport, particularly under the flow channel. However, it does show that the oxygen transport is hindered by the liquid water under the land area. Since the liquid saturation decreases with GDL contact angles, the oxygen mass fraction also decreases with GDL contact angles under the bipolar plate's land ($y = w/4$).

Figure 8.62 depicts the local activation overpotential profile in the catalyst layer along the CCL thickness for different GDL contact angles as indicated in the legend. Similar to the effect of CCL contact angles on the activation overpotential, the GDL contact angles also do not show any significant effect on the activation overpotential. In fact, the activation losses (highest value at the membrane/CCL interface) for all of the contact angles

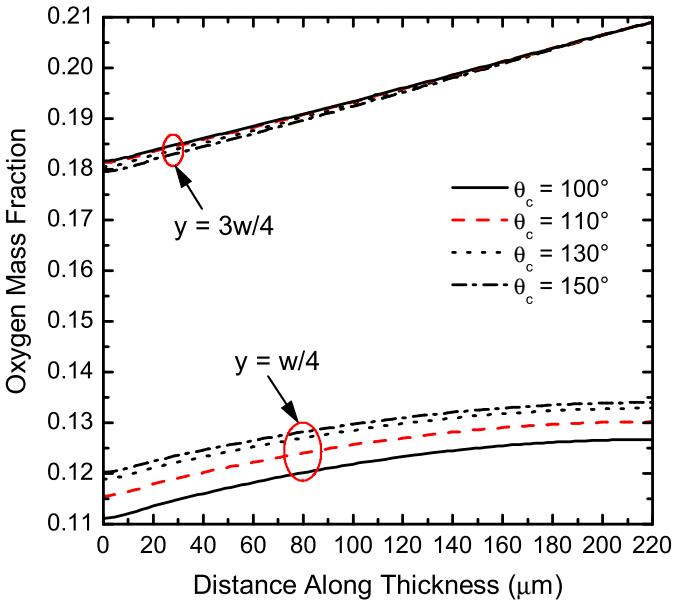

Figure 8.61: Variation of the oxygen mass fraction with GDL contact angles along the through-plane direction at $y = 3w/4$ (under the channel) and $y = w/4$ (under the land) for the entire CCL and GDL thicknesses.

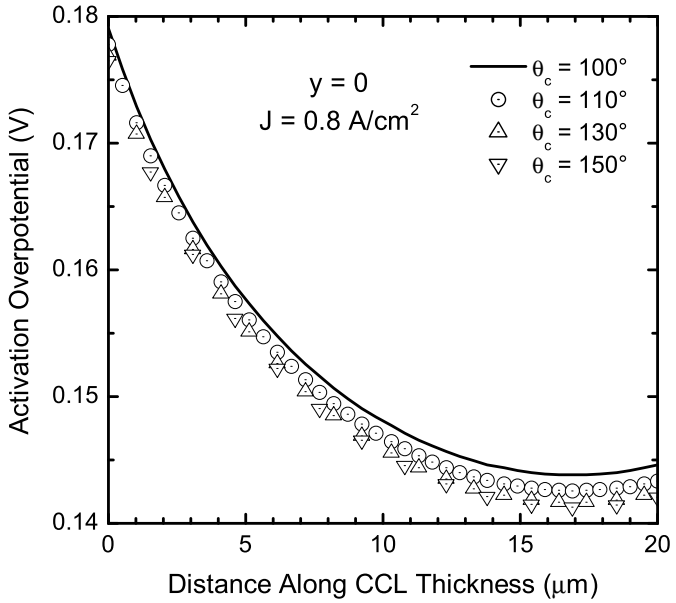

Figure 8.62: Local activation overpotential profile along the catalyst layer thickness under the land of bipolar plate at $y = 0$ for different GDL contact angles.

remain almost constant. The GDL contact angles, however, show local variations that can be attributed to the local variations of oxygen concentration. Although the liquid water saturation reduces about 30% under the land ($y = w/4$) when the GDL contact angle changes from 100° to 150°, the activation overpotentials remain identical at the membrane/CCL interface. As mentioned earlier that the widely used linear reduction of active reaction area by the liquid saturation is insufficient to capture the effect of liquid saturation on the activation overpotential, Fig. 8.62 is again providing the evidence. Figures 8.60–8.62 indicate that the higher GDL contact angles enhance the liquid water removal without hindering the oxygen transport and without increasing the activation losses, hence a higher GDL contact angle will always improve the fuel cell performance. However, a higher hydrophobicity requires higher PTFE loading for the GDL that may reduces the GDL's electronic and thermal conductivity. Hence, a proper measure is required to find the optimum PTFE loading for the GDL. Since the model developed in this thesis did not consider PTFE loading for the GDL, it is not possible to optimize the GDL hydrophobicity. Nonetheless, the results shown in Figs. 8.60–8.62 provide enough insight how the GDL hydrophobicity will impact the cell performance and transport processes.

8.6 Three-dimensional Numerical Model

In this section, the results of a three-dimensional (3D) numerical model of transport phenomena in PEM fuel cell catalyst layer are presented. The computational domain used in the 3D numerical simulation is shown in Fig. 7.1. The parameters used in the 3D simulations are identical of that are listed in Table 8.9 for the 2D case except the channel dimension and boundary conditions for the liquid water equation. Instead of using a 1 mm × 1 mm channel, a smaller channel is considered for the 3D case to reduce the computational load. In addition, a non-zero boundary condition is adopted for the liquid water equation at the GDL/GFC interface. At the membrane/CCL interface, the water drag coefficient is considered to be 0.5 and the liquid water saturation at the GDL/GFC interface is considered to be 10^{-3} to avoid singularity in the liquid water equation. These parameters are listed in Table 8.10. It is worthwhile to note that the main objective for the 3D simulation is to implement the volume-averaged mathematical formulations for 3D geometry so that it can be used for future studies.

8.6.1 Numerical Accuracy of Three-dimensional Model

To ensure the numerical accuracy, a 2D model with parameters listed in Table 8.10 is also simulated. A comparison of the liquid water saturation along the through-plane direction

of CCL and GDL is shown in Fig. 8.63 for a current density of 0.8 A/cm^2. Here the 3D results are plotted in a plane at the flow channel inlet and in the 2D model, the boundary conditions are considered similar to the inlet conditions of 3D model. It has been seen that the 3D numerical results are almost identical of the 2D numerical results when the liquid water saturation is plotted under the flow channel at a location of $y = 3w/4$. The differences between the results are about or less than 2% throughout the entire thickness. The liquid saturation profile under the bipolar land ($y = w/4$) shows slightly higher discrepancy with the 2D numerical model results. The deference between the 3D and 2D results for $y = w/4$ is about or less than 4%.

Table 8.10: Parameters used in the 3D numerical simulation

Parameter	Value
Channel width, w (mm)	0.5
Channel height, h (mm)	0.5
Channel length, L (mm)	15
Liquid saturation in gas channel	10^{-3}
Drag coefficient, α	0.5

The differences between the 2D and 3D cases observed in Fig. 8.63 can be attributed to the boundary conditions and the gas phase velocities in the flow channel. In the 2D model, the boundary conditions at the GDL/GFC interface are considered to be identical of inlet conditions that are artificial conditions. In addition, the pressure for the Darcy equation is considered constant and to be the same as the operating pressure. Conversely, the inlet concentrations and velocities are assigned at least 5mm away from the channel entrance to avoid entrance effect in the 3D model. Hence, the boundary conditions at the GDL/GFC interface in the 3D model are true boundary conditions. Further, the convection effect due to high gas velocity in the GFC is not involved in the 2D model, while the convection due to the velocity along the flow channel is significant for the 3D case. Furthermore, the reactants are diffusing in x- and y-directions only for the 2D case while the diffusion process is a true three-dimensional process for the 3D case. Due to the z-velocity in the flow channel, the diffusion of oxygen towards the CCL will be lower for the 3D case than the 2D case as the gradient of oxygen concentration along the thickness is less. This phenomenon can be shown by plotting oxygen mass fraction along the CCL and GDL thicknesses for these two cases. Figure 8.64 shows the variation of oxygen mass fraction along the CCL and GDL thicknesses under the flow channel for 2D and 3D cases. Clearly, the oxygen mass fraction inside the CCL is lower for the 3D case due to the

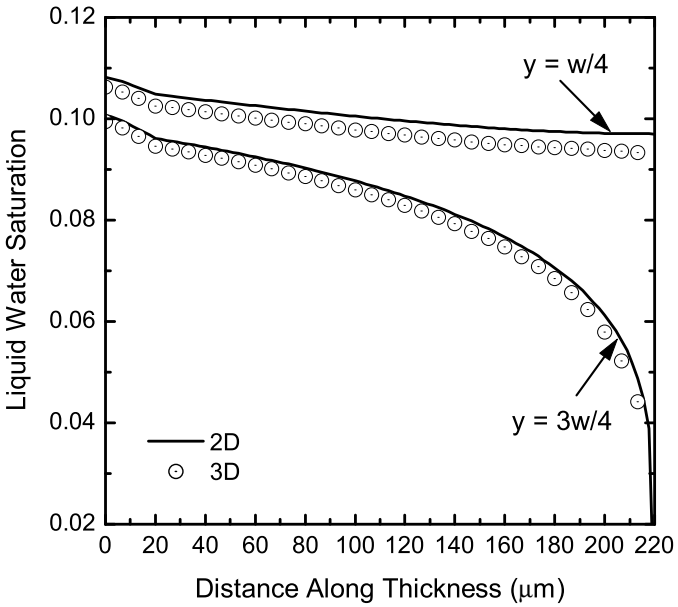

Figure 8.63: Liquid water saturation profiles along the thicknesses of CCL and GDL under the flow channel ($y = 3w/4$) and under the land of bipolar plate ($y = w/4$) for a current density of 0.8 A/cm^2. The lines depict the results of a 2D numerical model and the symbols represent the 3D numerical results at the plane of channel inlet ($z = 0$).

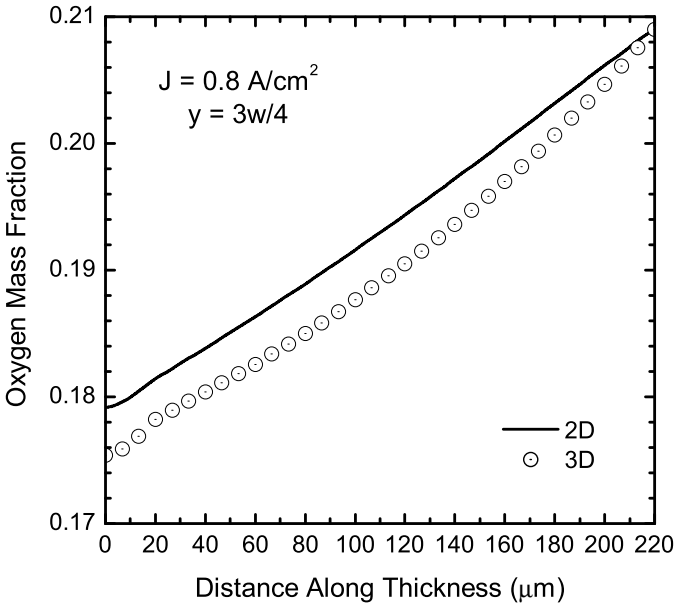

Figure 8.64: Variation of the oxygen concentration along the thicknesses of CCL and GDL under the flow channel ($y = 3w/4$) for a current density of 0.8 A/cm^2. The line depicts the 2D numerical model result and the symbols represent the 3D numerical results at the plane of channel inlet.

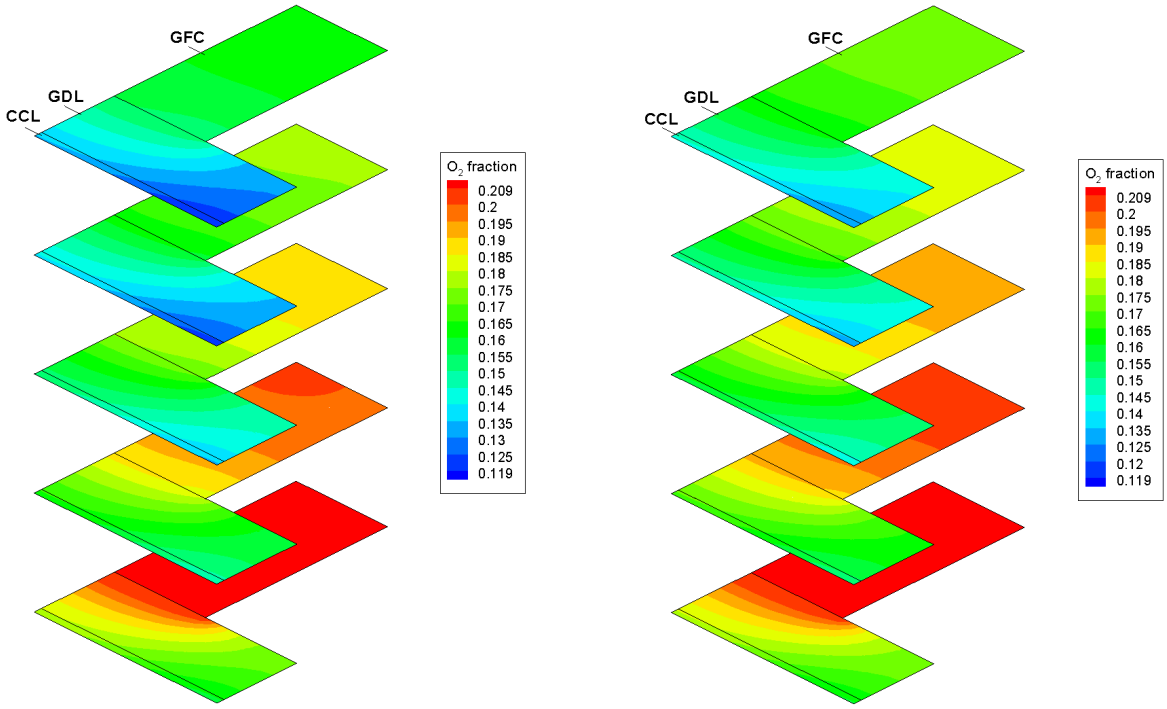

(a) No-slip GDL/GFC Interface

(b) Slip GDL/GFC Interface

Figure 8.65: Distribution of the oxygen mass fraction for (a) no-slip GDL/GFC interface and (b) slip GDL/GFC interface for a current density of 0.8 A/cm^2. The bottom slice represents the plane at the channel inlet and the oxygen mass fraction at the GFC inlet is about 0.209, while the top slice represents the plane at the channel outlet.

diffusion towards the z-direction that is absent in the 2D case. Hence, the comparison in Fig. 8.63 shows the numerical accuracy for the 3D simulation and the comparison in Fig. 8.64 depicts why the liquid water saturation shows 4% discrepancy under the bipolar plate's land.

8.6.2 Boundary Conditions at GDL/GFC Interface

The results shown in the previous section indicate that an artificial boundary condition at the GDL/GFC interface can introduce errors in the numerical estimation. In addition, the PEM fuel cell module presented in COMSOL Multiphysics® uses a no-slip boundary condition at the GDL/GFC interface [180], which is an artificial condition. Although the gas phase velocity inside the porous CCL and GDL is significantly lower than the gas phase velocity in the GFC, we cannot ignore the convection effect inside the porous CCL and GDL, particularly in the two-phase model. Hence, a comparison between no-slip and slip boundary conditions at the GDL/GFC interface is provided in this section.

Figure 8.65 shows the oxygen mass fraction distribution inside the CCL, GDL, and GFC for a current density of 0.8 A/cm^2 for a no-slip boundary condition at the GDL/GFC interface in part (a) and for a slip boundary condition in part (b). As observed, the oxygen concentration decreases for both cases along the flow channel (from bottom to top slice) due to the consumption of oxygen in the electrochemical reaction at the CCL. At the channel inlet (bottom slice), the oxygen mass fraction distributions are identical for both the no-slip and slip boundary conditions. At the channel outlet (top slice), a significant variation has been observed between these cases, particularly under the land of bipolar plate inside the CCL. For no-slip condition, which is an artificial condition, the convection effect at the GDL/GFC interface has been neglected. Therefore, the oxygen is only allowed to diffuse from the GFC to the GDL. Conversely, the convection effect is counted in the slip boundary condition. A higher oxygen mass fraction in the CCL, shown in the top slice of Fig. 8.65b, indicates that the oxygen simultaneously diffuses and convects through the GDL/GFC interface. If we compare the lowest values of the oxygen mass fractions, it has been observed that the oxygen concentration is about 10% lower in the CCL for the no-slip case. Hence, an artificial no-slip boundary condition at the GDL/GFC interface would under-estimate the oxygen concentration and eventually the fuel cell performance.

8.6.3 Tetrahedral vs. Hexahedral Mesh

The use of hexahedral mesh will allow to solve a PEM fuel cell model faster as it require less computational memory due to the less number of degrees of freedom. However, the use of hexahedral mesh requires fairly regular-shaped geometries, while the tetrahedral mesh can be used for irregular-shaped geometries. The catalyst layer structure in PEM fuel cell is a combination of both agglomerate and macro-homogeneous. It should be kept in mind that a tetrahedral mesh might need more time to solve a PEM fuel cell model but it would allow modeling a real CCL. Since the objective of the 3D simulation is to open avenues for future studies, a comparison between tetrahedral and hexahedral meshes for PEM fuel cell modeling is also provided. Here the macro-homogeneous structure for the CCL has been used to implement the mathematical model developed in this thesis; hence, it is expected to generate identical result for both meshes.

Figure 8.66 shows the oxygen mass fraction distribution inside the CCL, GDL, and GFC for a current density of 0.8 A/cm^2 for a tetrahedral mesh in part (a) and for a hexahedral mesh in part (b). Here the GDL is considered as hydrophobic and the CCL is considered as hydrophilic. The contact angles for CCL and GDL are 80° and 110°, respectively. Clearly, both meshes show almost identical distribution of oxygen mass fraction. However, the values for oxygen mass fraction are slightly different. The oxygen mass fraction under

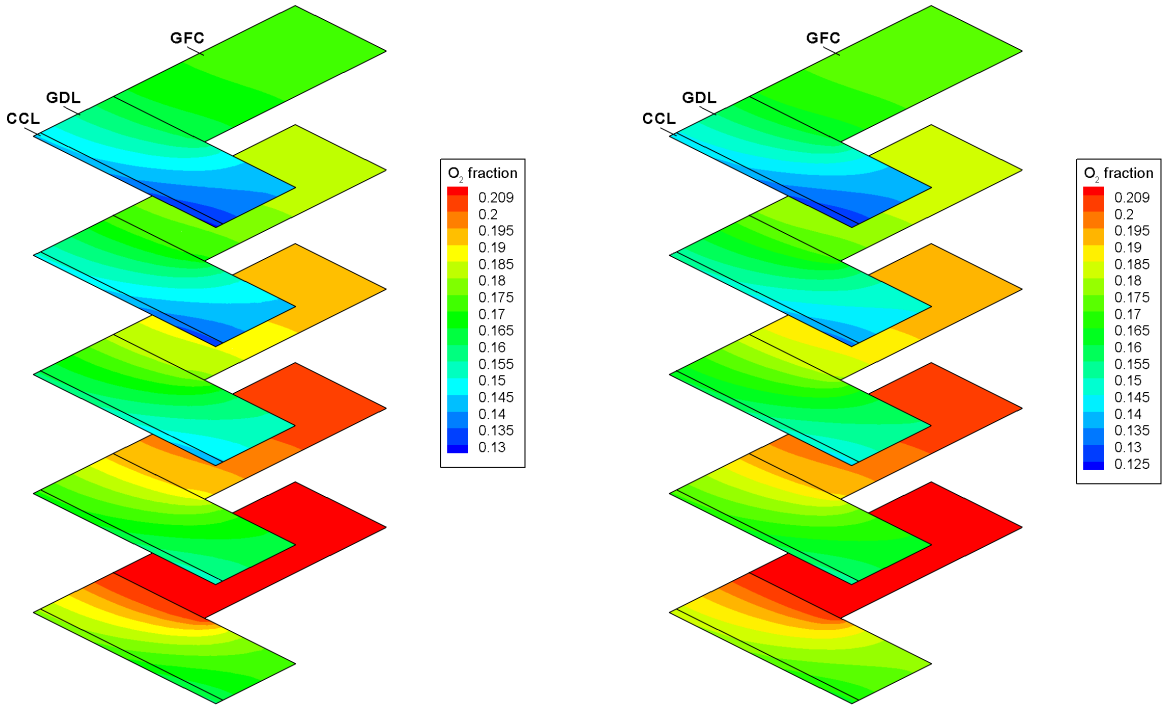

(a) Tetrahedral Mesh (b) Hexahedral Mesh

Figure 8.66: Distribution of the oxygen mass fraction using (a) a tetrahedral mesh and (b) a hexahedral mesh for a current density of 0.8 A/cm^2. The bottom slice represents the plane at the channel inlet and the oxygen mass fraction at the GFC inlet is about 0.209, while the top slice represents the plane at the channel outlet.

the bipolar plate's land at the channel outlet is about 3% lower for the hexahedral mesh than the tetrahedral mesh. Similarly, the liquid water saturation for tetrahedral mesh and hexahedral mesh show exactly identical distribution inside the CCL and GDL of a PEM fuel cell, except near the channel outlet. The distribution of liquid water saturation for tetrahedral and hexahedral meshes are shown in two parts of Fig. 8.67, where the bottom slice represents the plane at the channel inlet and the top slice represents at the channel outlet. Unlike the distribution of oxygen mass fraction, both the minimum and maximum values of liquid saturation are the same for both types of meshes.

A close inspection to the top slice under the bipolar plate's land shows that the amount of liquid water is higher for the hexahedral mesh as more area is occupied by the maximum liquid water saturation. Since the oxygen concentration is slightly lower for the hexahedral mesh at the channel outlet, the consumption of oxygen is higher and the production of liquid water is also higher. Therefore, the amount of liquid water is higher for the hexahedral mesh though the maximum values of the liquid water saturation are the same for both meshes. Nonetheless, the comparisons shown here indicate that the types of

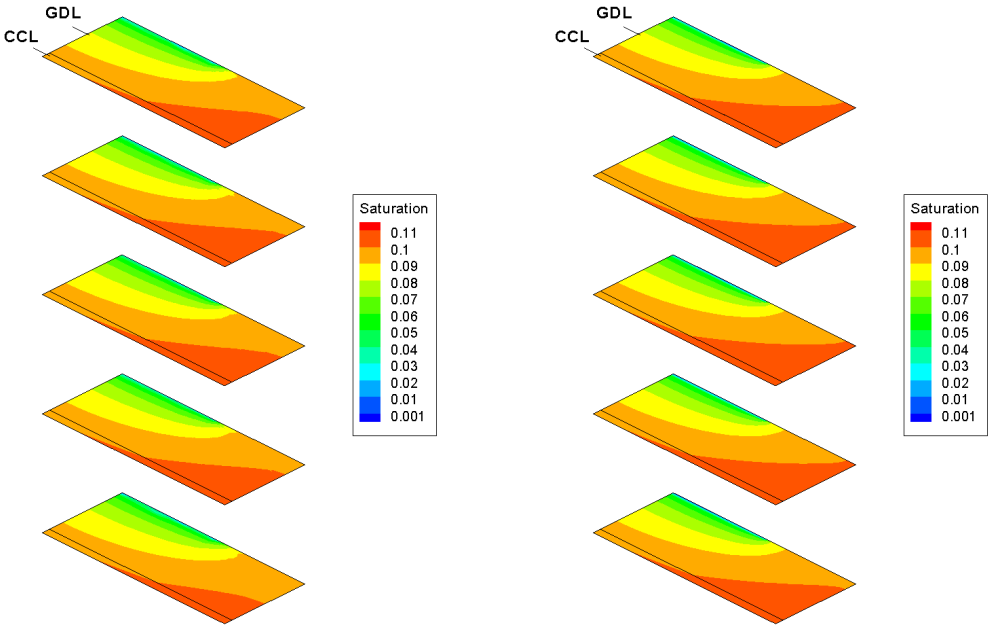

(a) Tetrahedral Mesh (b) Hexahedral Mesh

Figure 8.67: Distribution of the liquid water for (a) tetrahedral mesh and (b) hexahedral mesh for a current density of 0.8 A/cm^2. The bottom slice represents the plane at the channel inlet, while the top slice represents the plane at the channel outlet. The minimum liquid saturation (10^{-3}) is assigned at the GDL/GFC interface.

meshes are less important in terms of numerical accuracy. However, the type of mesh would be important if the computational time is considered as a determining factor. A typical simulation with hexahedral mesh takes about few days to a week, while the tetrahedral mesh takes about a week to two weeks to run the PEM fuel cell model that is developed in this thesis.

8.6.4 Effect of CCL Contact Angle

The oxygen mass fraction and liquid water distributions for a CCL contact angle of 80° are already shown in part (a) of Figs. 8.66 and 8.67. To investigate the effect of CCL contact angles on the oxygen concentration and liquid water saturation, both the oxygen mass fraction and liquid water distributions for CCL contact angle of 60° are shown in Fig. 8.68. All the parameters are identical of that are used in Figs. 8.66 and 8.67 except the CCL contact angle. Comparing Fig. 8.66a with Fig. 8.68a, it has been observed that the consumption of oxygen is slightly better for the contact angle of 60°. Therefore, the electrochemical reaction is also improved with higher surface wettability of CCL or lower contact angle. At the same time, the maximum value of liquid water saturation decreases

for the contact angle of 60°. Although the higher consumption of oxygen should produce a higher amount of liquid water, the maximum value of liquid water saturation decreases because of a better distribution of liquid water throughout the CCL and GDL volume as shown in Fig. 8.68b. Therefore, the CCL surface wettability can be utilized to re-distribute the liquid water within the volume of CCL and GDL without increasing the liquid water saturation that would improve the fuel cell performance.

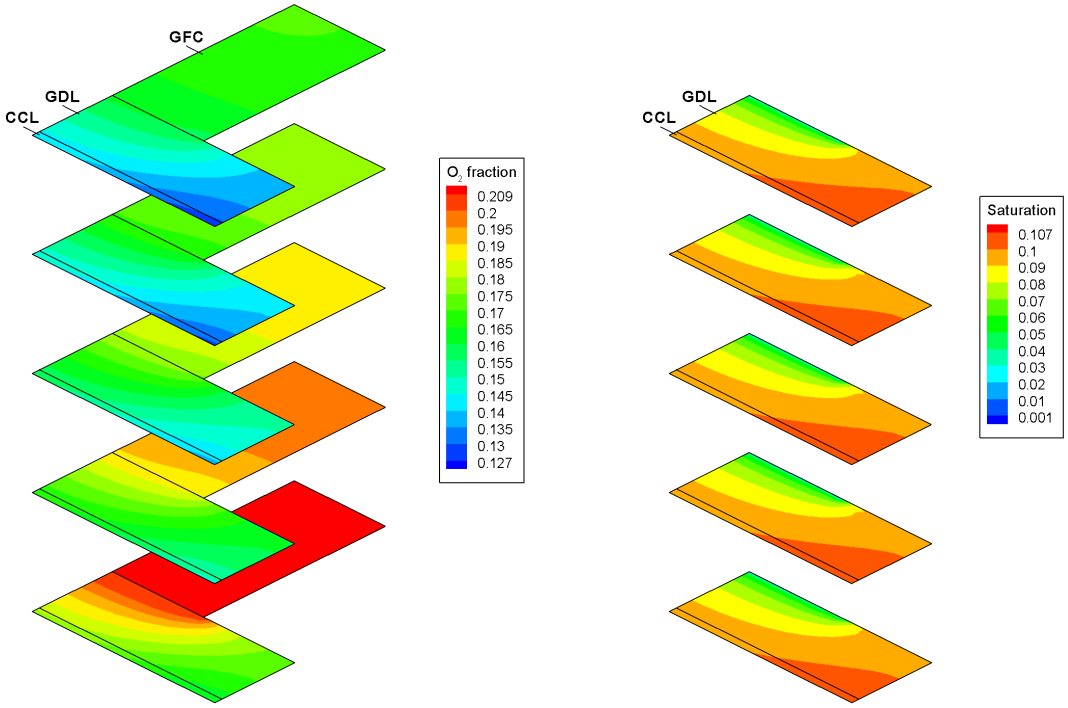

(a) Oxygen Mass Fraction (b) Water Saturation

Figure 8.68: Distribution of the oxygen mass fraction and liquid water saturation in a catalyst layer having a contact angle of 60° for a current density of 0.8 A/cm^2. The highest oxygen mass fraction is at the GFC inlet (bottom slice in part a), while the minimum liquid saturation (10^{-3}) is assigned at the GDL/GFC interface.

8.6.5 Condensation/Evaporation of Liquid Water

It has been widely presumed that the PEM fuel cell performance is significantly affected by the condensation/evaporation of water inside the CCL and GDL and this phase change process can also affect the water management in the PEM fuel cell. Therefore, we compare the production of liquid water from the electrochemical reaction with the production of water from the condensation/evaporation process. Since a fully-humidified reactant stream is considered in this study, it was anticipated that the condensation process will dominate

over the evaporation process. In fact, the water saturation pressure is always lower than the water vapor partial pressure inside the gas flow channel. Therefore, there will be no evaporation process inside the flow channel for the fully-humidified gas stream. Inside the porous CCL and GDL, the partial pressure of water vapor depends on the consumption of oxygen. Hence, the phase change process is completely depending on the partial pressure of water vapor not on the relative humidity of the reactant stream. It has been observed that the water vapor partial pressure is lower than the saturation pressure inside the CCL and GDL near the channel inlet. Along the flow channel inside the CCL and GDL, the partial pressure of water vapor increases slowly and eventually becomes higher than the saturation pressure. Hence, both the evaporation and condensation are happening inside the porous CCL and GDL.

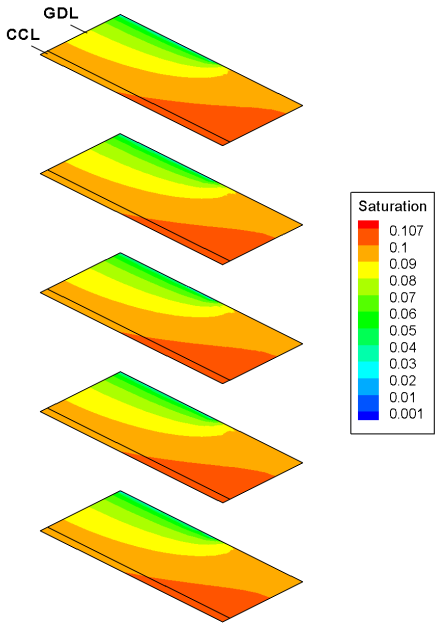

Figure 8.69: Distribution of the liquid water production (in kg/m^3·s) from the phase change process for a catalyst layer having a contact angle of 60° for a current density of 0.8 A/cm^2. The bottom slice represents the plane at the GFC inlet, while the top slice represents the plane at the GFC outlet.

Figure 8.69 depicts the distribution of liquid water production inside the CCL and GDL from the phase change process for a catalyst layer having a contact angle of 60° for a current density of 0.8 A/cm^2. Here the negative numbers represent the evaporation and the positive numbers represent the condensation of water in kg/m^3·s. As observed in the bottom slice of Fig. 8.69 that is on the same plane of channel inlet, the entire plane is under evaporation process. Conversely, the three middle slices are showing that the entire plane is under condensation process. At the last slice that is along the channel

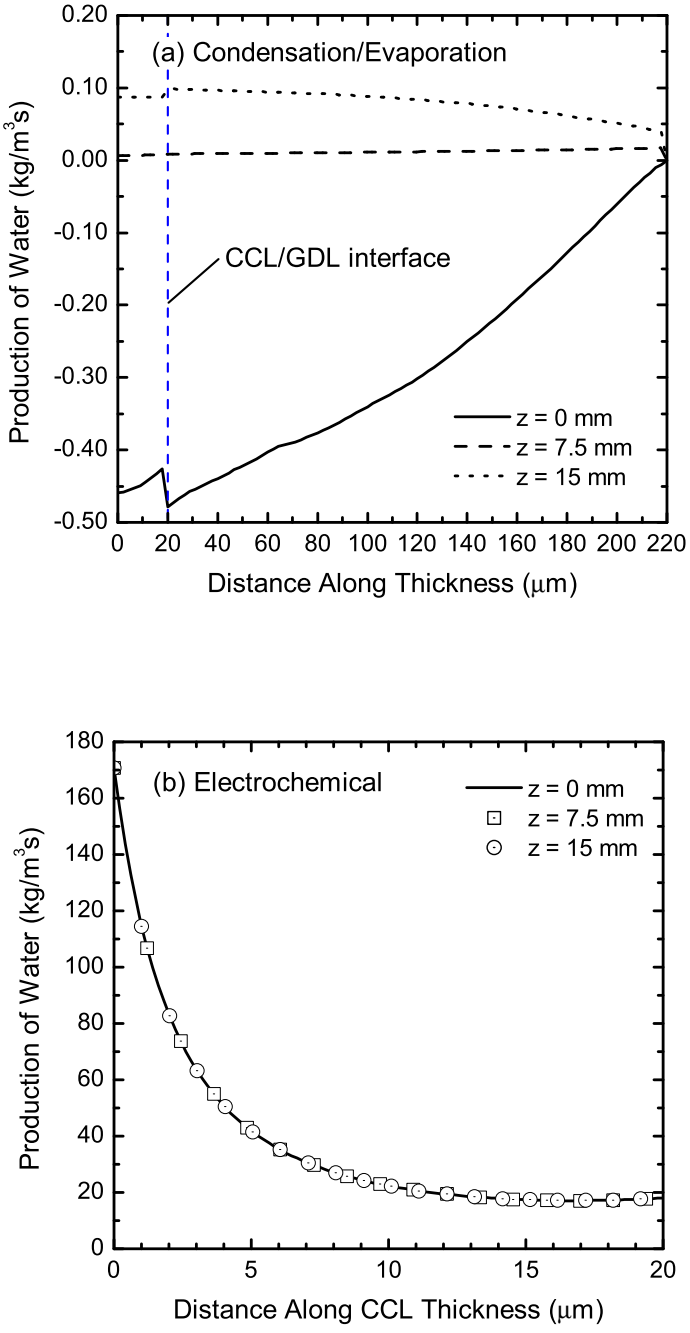

Figure 8.70: Water production from the phase change and electrochemical processes for a catalyst layer having a contact angle of 60° for a current density of 0.8 A/cm^2 at three different locations as indicated in the legend.

outlet plane, the condensation processes is more prominent. Hence, the evaporation can takes place even with a fully-humidified reactant stream near the channel inlet inside the porous layer though the condensation process is dominated over a large volume. It has been shown in Section 8.3.5 using a time constant analysis that the production of liquid water from the electrochemical reaction is very large compared to the water production for the condensation/evaporation process. Figure 8.70 shows the production of water from condensation/evaporation process along the thicknesses of CCL and GDL and the production of water from the electrochemical reaction at three different locations along the flow channel as indicated in the figure legend, where $z = 0$ mm represents the plane at channel inlet and $z = 15$ mm represents the plane at channel outlet. These profiles are plotted under the flow channel at location of $y = 0.4w$. Clearly, the amount of water production from the phase change process is significantly smaller than the water production from the electrochemical reaction. Part (b) of Fig. 8.70 reveals that the water production from the electrochemical reaction is independent of the location along the flow channel. It also reveals that almost the entire amount of liquid water is produced near the membrane/CCL interface. Therefore, the assumption of thin CCL or consider the CCL as an interface might not be a good approximation while modeling a PEM fuel cell. Conversely, part (a) of Fig. 8.70 reveals that the interface effect is significant when the CCL and GDL contact angels are too far from 90°. Hence, the interface effect should also be considered in the numerical modeling of PEM fuel cell. At the same time, it is believed that the use of micro-porous layer between the CCL and GDL would diminish the interface effect and provide a smoother transition for the liquid transport from the CCL to the GDL. Therefore, a future study with micro-porous layer can be done with this 3D model.

8.7 Summary

In this chapter, the results using the mathematical model of PEM fuel cell that is developed using a volume-average technique are presented. Here, both the analytical and numerical approaches have been adopted. The analytical approach is simple, fast, and easy to implement. Conversely, the numerical model requires significant amount of computational time depending on the type of meshes. It should also be mentioned here that the analytical model can only provide an overview about the transport processes in the PEM fuel cell. If the detailed of the transport processes are needed then the numerical model would provide better results of the transport processes inside the PEM fuel cell. Nonetheless, the results provided in this chapter show that both the analytical and numerical models that are developed in this thesis would be useful in predicting the fuel cell performance and its optimization, and for water management.

Chapter 9

Summary and Future Work

This thesis presents a comprehensive general formulation for transport phenomena in PEM fuel cell. The general formulation was derived by considering the fuel cell to be composed of several co-existing phases. The transport of mass, momentum, and species within each phase are governed by the fundamental microscopic conservation equations. The direct solution of these microscopic conservation equations is impractical, and such a solution may contain more information than is needed. Therefore, a multi-phase volume-averaging method is applied to derive the macroscopic conservation equations. The interaction between various phases in a PEM fuel cell was also captured that is connected through the source terms of the volume-averaged conservation equations.

The primary goal of this thesis research was to understand the two-phase transport processes inside the CCL of a PEM fuel cell. Therefore, the volume-averaged conservation equations were simplified for the CCL assuming the fuel cell was isothermal and operating in steady-state. Also, the polymer electrolyte was assumed impervious to the gas phase and liquid water was considered in a mist state that can be instantaneously removed by the gas flow. It was also assumed that the production of water in the CCL is liquid form only, and the GDL and CCL are isotropic and homogeneous. The inertia effect is negligible in the porous GDL and CCL for the gas phase, i.e. the conservation mass and momentum equations for the gas phase were simplified using the Darcy's law. The liquid phase mass and momentum equations were combined together by considering both the capillary and convection effects. Since the liquid water flows opposite to the gas flow, the gas flow velocities inside the porous layer will hinder the flow of liquid water. Hence, the convection term in the liquid water equation cannot be neglected. The production of liquid water from the condensation/evaporation process, and the transport of water due to the electro-osmotic drag and back-diffusion were also considered. The charge transport equations were simplified using the Butler-Volmer equation.

The simplified model developed in this thesis research requires several effective transport properties for the numerical implementation including relative permeability and capillary pressure. Several correlations are available in literature for the relative permeability. Each of these correlations has limitation. In this thesis research, the cubical relation was adopted as it has been widely used for the PEM fuel cell GDL and CCL. Similarly for the capillary pressure, several correlations are available in literature. A comprehensive discussion on these correlations is provided in Chapter 5. It has been observed that none of these correlations is a perfect fit for the numerical modeling of PEM fuel cell. Since the Leverett function has been widely used for the PEM fuel cell, this thesis adopted the Leverett function to be consistent with the majority of the PEM fuel cell literatures.

An accurate estimation of the effective properties in PEM fuel cell, e.g. effective conductivities and diffusivities in the CCL and GDL, is crucial for accurately predicting the fuel cell performance and optimizing design parameters in the numerical modeling/simulation. For the PEM fuel cell, the Bruggeman approximation has widely been used for estimating the effective conductivity and diffusivity, which is based on the Bruggeman's Effective Medium Theory. It provides empirical correlation for the effective properties of a composite system; therefore, a unique correlation based on the Bruggeman approximation does not always hold for the PEM fuel cell effective properties. Rather, the Bruggeman correlation is a cell specific and experiment dependent correlation that depends on structure, phase composition, water saturation, experimental parameters, etc. Further, this correlation needs to be combined with other correlations to estimate the effective diffusivities. Therefore, a set of mathematical expression has been developed for the effective transport properties in PEM fuel cell.

The mathematical expressions of effective transport properties were derived from the Hashin coated sphere model and have an exact mathematical foundation for effective conductivities and diffusivities. The effective conductivity and diffusivity expressions were also compared with the results available in literature for a limiting case. It has been found that the proposed mathematical expressions for the effective transport properties are quite capable of predicting reasonably accurate and comparable results. Further, the complexities involved in using the Bruggeman approximation and Weiner models together can be avoided by employing the effective diffusivity formulation developed in this thesis research. Hence, these expressions are recommended for the numerical modeling of PEM fuel cell. Although these expressions are derived focusing on the PEM fuel cell, the present formulations for the effective transport properties are equally applicable for other hydrogen fuel cells, porous media flow, and multi-phase composite systems.

For the PEM fuel cell performance optimization, it is required to estimate the re-

versible cell voltage and various losses. Among the various losses,the ohmic and activation overpotentials are the most significant in typical operating ranges of a PEM fuel cell. The formulation of ohmic overpotential is well established and does not require complicated mathematical formulation or numerical computation for fully-hydrated membranes, while the activation overpotential formulation is rare in literature. Therefore, an analytical expression for the activation overpotential has been developed using the simplified volume-averaged conservation equations.

The analytical expression of activation overpotential has shown an accurate predictive capability when a proper estimates of ohmic overpotential was incorporated to the analytical formulation. It also provides an excellent agreement with available experimental, numerical, and empirical results. Further, the analytical expression of activation overpotential can be used for optimization studies. Using an optimization study, it is found that catalyst layer performance is much more sensitive to the thickness of the catalyst layer than the other parameters, particularly below the optimum thickness. It has also been found that changing the catalyst layer thickness and Pt-loading can provide an optimum value compared to the other operating and physical parameters. The optimum catalyst loading is found to be 0.195 mg/cm^2 for either air or oxygen as the cathode gas with a Nafion fraction of 0.4 and 20% wt of Pt/C. The optimum catalyst layer thicknesses were found to be 10.5 ± 1, 13 ± 1.5, and 15.75 ± 1.75 μm for 0.2, 0.25, and 0.3 mg/cm^2 of Pt-loadings, respectively, with a Nafion fraction of 0.4 and 20% wt of Pt/C in the catalyst layer. Overall, the analytical expression developed in this thesis is easy to implement and it can accurately predict the fuel cell performance.

The simplified volume-averaged conservation equations were also used to develop a one-dimensional (1D) analytical model of liquid water transport across the CCL. The 1D analytical solutions of liquid water profile have been derived for both hydrophilic and hydrophobic CCLs. In-situ measurement of water flooding in the CCL is quite difficult and the numerical simulation requires significant amount of computational time. Therefore, the analytical expressions of liquid water saturation will provide a quick estimate of liquid water transport in the CCL of a PEM fuel cell. These analytical solutions also include the electro-osmotic transport, back-diffusion, condensation/evaporation of water, and removal of liquid water through the GDL. Based on these analytical expressions, it has been shown that the wetting properties of a CCL control the flooding behavior and hydrophilic characteristics of the CCL can play a significant role on the cell performance. Further, a novel dimensionless time-constant analysis has been provided to investigate the liquid water accumulation and transport in the CCL due to the electro-osmotic drag and back-diffusion, condensation/evaporation of water, and electrochemical production of liquid water. Furthermore, the effect of water flooding on the activation overpotential has

been found to be less sensitive if a linear reduction of active reaction area is assumed, whereas the higher order reduction of active reaction area shows significant increase of activation overpotential due to the liquid saturation. Hence, it has been concluded that the widely used linear approximation of active reaction area reduction due to the liquid water saturation seems to be under-estimation.

Finally, the volume-averaged two-phase model has been implemented numerically for both the 2D and 3D geometries for a macro-homogeneous catalyst layer. Although an investigation has been carried out to quantify the effect of catalyst layer structure on the reactant transport and cell performance, it has been found that the computational load is tremendous for an agglomerate catalyst layer. With the available computational resources, an agglomerate catalyst layer structure can only be considered if the catalyst layer is the only computational domain. In such situation, the boundary condition at the CCL/GDL interface needs to be approximated and determined separately, which is cumbersome. Nonetheless using an approximated boundary condition for the CCL/GDL interface, the effect of an agglomerate catalyst layer structure has been shown and it has been found that the catalyst layer performance can be improved by optimizing the agglomerate arrangements.

The numerical simulation of the volume-averaged two-phase transport model were performed using COMSOL Multiphysics®, utilizing a finite element method to solve the system of coupled partial differential equations. In order to ensure the numerical solutions are grid independent, the governing variables are estimated in different grid sizes. To validate the numerical models, the numerical results are compared with the analytical model of liquid water transport in the CCL of a PEM fuel cell. It has been observed that the numerical results have a good agreement with the analytical model results at low current density and differ at high current density, which is mainly due to the fact that the analytical expression of liquid water saturation at the CCL of a PEM fuel cell will always over-estimate liquid saturation at higher current densities.

While implementing the volume-averaged two-phase transport equations in COMSOL Multiphysics®, it has been observed that some models available in literature represent the liquid water equation erroneously, particularly those were modeled using the commercial software Fluent®. A comparison between the mathematical model developed in this thesis and the liquid water model available in Fluent® has also been provided. It has been shown that the mobile liquid water saturation calculated using Fluent® model will always under-estimate. This error is due to the conflict between the intrinsic (phase-averaged) and superficial (volume-averaged) properties, particularly for the liquid and gas phase densities. Hence, the model based on the Fluent® formulation will significantly under-estimate the

liquid water saturation and will eventually over-estimate the oxygen transport if the water density is interpreted incorrectly. Conversely, the present volume-averaged approach does not confuse the intrinsic and superficial densities as they are well-defined and derived directly from the volume-averaged conservation equations. Therefore, the mathematical model developed in this thesis for the liquid water transport is recommended for future studies.

Based on the 2D numerical simulation, it has been shown that the structure and surface wettability of a macro-homogeneous CCL have significant effect on the liquid water and reactant transports inside the CCL. The structure of a macro-homogeneous CCL was considered to be quantified by its porosity, i.e. by the platinum (Pt) loading and Nafion content. The liquid water saturation increases with the Nafion content, which also hinders the oxygen transport to the CCL. However, a higher Nafion content can significantly lower the activation overpotential for the PEM fuel cell. Similarly, a higher Pt-loading increases the liquid water saturation and reduces the oxygen transport to the CCL but improve the cell performance by reducing the activation overpotential. Since both the Pt-loading and Nafion content reduce the CCL porosity, the increase in liquid water saturation is mainly due to the low volume available to the liquid water.

The catalyst layer surface wettability (i.e. contact angle) shows no effect on the liquid water saturation inside the GDL under the flow channel. Conversely, the liquid water saturation in the GDL can be reduced under the bipolar plate's land using a highly hydrophilic catalyst layer (low contact angle). The liquid water saturation inside the CCL is always less for catalyst layer having a low contact angle. Although the CCL contact angles show a distinct effect on the liquid water saturation inside the CCL and GDL, the oxygen mass fractions remain unchanged for various contact angles. As concluded earlier that the widely used linear approximation of active reaction area reduction due to the liquid water saturation is an under-estimation, the variation of liquid water saturation due to the contact angles are insufficient to further hinder the oxygen transport. It is worthwhile to note that these liquid water saturations are mobile liquid water saturations. Once the irreducible liquid saturation is added to the mobile liquid saturation, it might capture the change in the reactant transport due to the liquid water saturation. Conversely, the GDL porosity and wetting properties show significant effect on both the liquid water and oxygen transports. A highly porous GDL not only reduces the liquid saturation but also provides better transport of reactant gases. It also reduces the activation overpotential.

In the 3D numerical simulation, the major objective was to implement the mathematical model developed in this thesis and investigate how the concentration variation along the gas flow channel affects the water and oxygen transport inside the CCL. The

3D numerical model were performed using COMSOL Multiphysics®. Here the similar set of conservation equations was used that was used in the 2D simulation, except the mass and momentum equations for the gas phase inside the flow channel. Further, a true slip boundary condition was applied at the GDL/GFC interface and compared with the no-slip boundary condition that is most common in PEM fuel cell literatures.

The numerical accuracy of the 3D model was compared with the numerical accuracy of the 2D model. Since the 2D model was validated with literature, the comparison of 3D model with 2D model serves the numerical validation for the 3D model. Although the gas velocity inside the porous GDL is negligible compared to the gas velocity inside the flow channel, a no-slip boundary condition at the GDL/GFC interface would under-estimate the oxygen concentration inside the CCL. Further, the 3D model was implemented using both the tetrahedral and hexahedral meshes. The use of hexahedral mesh will allow to solve a PEM fuel cell model faster as it require less computational memory due to the less number of degrees of freedom. However, the use of hexahedral mesh requires fairly regular-shaped geometries, while the tetrahedral mesh can be used for irregular-shaped geometries. Both meshes show almost identical results. Therefore, the tetrahedral mesh is recommended for the CCL model as it will allow considering the agglomerate or any other complex structure for the catalyst layer. Since the oxygen concentration varies along the flow channel, the actual oxygen concentration and liquid water saturation inside the CCL are completely different than the 2D model. Clearly, a 2D model can capture the inlet condition only. Since the flow channel in a PEM fuel cell can be straight, serpentine, or interdigitated, the 3D numerical model will provide the true nature of the various transport process in a PEM fuel cell. The effect of condensation/evaporation process on the liquid water production was found to be negligible compared to the water production from the electrochemical reaction. Furthermore, the 3D numerical model will also be able to capture the condensation/evaporation process inside the porous CCL and GDL that cannot be captured using a 2D model. It has also been noticed that almost the entire amount of liquid water is produced near the membrane/CCL interface for a typical current density from the electrochemical reaction. Therefore, the widely used assumption of thin CCL or consider the CCL as an interface is not a valid approximation. A finite thickness of CCL is always required to understand the true transport processes in the cathode of a PEM fuel cell.

The 3D numerical model is only being implemented and validated but it opens the opportunities to carry this thesis research forward. Further, the PEM fuel cell is considered as isothermal. In reality, the PEM fuel cell is not isothermal. The temperature gradient inside the CCL is significant that would change the condensation/evaporation process inside the porous CCL and GDL. Therefore, there are several areas that are opened up

for future studies. A brief summary for possible future studies are listed below:

- An agglomerate catalyst layer structure should be incorporated in the 3D model.
- Since the real flow channel can be straight, serpentine, or interdigitated, these geometries can be considered.
- The energy equation should be incorporated as the PEM fuels are not isothermal.
- The liquid water saturation at the GDL/GFC interface was considered negligible, while almost the entire amount of liquid water that is produced from the electrochemical reaction is transported via GDL to the flow channel. Hence, a sophisticated model is required that can estimate the liquid water saturation at the GDL/GFC interface.
- Although a mathematical model has been developed for the effective transport properties, the empirical correlations for the relative permeability and capillary pressure were taken from literature. Therefore, a fundamental mathematical formulation is required for the relative permeability and capillary pressure.
- The present mathematical model can be used for a fuel cell stack.

References

[1] Environment Canada. http://www.msc.ec.gc.ca.

[2] U.S. Department of Energy. http://www.energy.gov.

[3] The Pembina Institute. http://www.pembina.org.

[4] X. Li. *Principles of Fuel Cells*. Taylor & Francis, New York, 2006.

[5] J. Larminie and A. Dicks. *Fuel Cell Systems Explained*. John Wiley & Sons Ltd., New York, 2003.

[6] C. Marr and X. Li. Composition and performance modelling of catalyst layer in a proton exchange membrane fuel cell. *Journal of Power Sources*, 77(1):17–27, 1999.

[7] P. K. Das, X. Li, and Z. S. Liu. Analytical approach to polymer electrolyte membrane fuel cell performance and optimization. *Journal of Electroanalytical Chemistry*, 604(2):72–90, 2007.

[8] K. Feindel, L. LaRocque, D. Starke, S. Bergens, and R. Wasylishen. In situ observations of water production and distribution in an operating H_2/O_2 PEM fuel cell assembly using ^{1}H NMR microscopy. *Journal of the American Chemical Society*, 126(37):11436–11437, 2004.

[9] T. Trabold, J. Owejan, D. Jacobson, M. Arif, and P. Huffman. In-situ investigation of water transport in an operating PEM fuel cell using neutron radiography: Part 1 Experimental method and serpentine flow field results. *International Journal of Heat and Mass Transfer*, 49(25–26):4712–4720, 2006.

[10] J. Park, X. Li, D. Tran, T. Abdel-Baset, D. Hussey, D. Jacobson, and M. Arif. Neutron imaging investigation of liquid water distribution in and the performance of a PEM fuel cell. *International Journal of Hydrogen Energy*, 33(13):3373–3384, 2008.

[11] P. Costamagna and S. Srinivasan. Quantum jumps in the PEMFC science and technology from the 1960s to the year 2000 Part I. Fundamental scientific aspects. *Journal of Power Sources*, 102(1–2):242–252, 2001.

[12] P. Costamagna and S. Srinivasan. Quantum jumps in the PEMFC science and technology from the 1960s to the year 2000 Part II. Engineering, technology development and application aspects. *Journal of Power Sources*, 102(1–2):253–269, 2001.

[13] A. Parthasarathy, S. Srinivasan, A. Appleby, and C. Martin. Temperature-dependence of the electrode-kinetics of oxygen reduction at the platinum nafion interface - A microelectrode investigation. *Journal of the Electrochemical Society*, 139(9):2530–2537, 1992.

[14] J. Amphlett, R. Baumert, R. Mann, B. Peppley, P. Roberge, and T. Harris. Performance modeling of the Ballard-Mark-IV solid polymer electrolyte fuel cell. 1. Mechanistic model development. *Journal of the Electrochemical Society*, 142(1):1–8, 1995.

[15] J. Amphlett, R. Baumert, R. Mann, B. Peppley, P. Roberge, and T. Harris. Performance modeling of the Ballard-Mark-IV solid polymer electrolyte fuel cell. 2. Empirical model development. *Journal of the Electrochemical Society*, 142(1):9–15, 1995.

[16] J. Kim, S. Lee, S. Srinivasan, and C. Chamberlin. Modeling of proton exchange membrane fuel cell performance with an empirical equation. *Journal of the Electrochemical Society*, 142(8):2670–2674, 1995.

[17] G. Squadrito, G. Maggio, E. Passalacqua, F. Lufrano, and A. Patti. An empirical equation for polymer electrolyte fuel cell (PEFC) behaviour. *Journal of Applied Electrochemistry*, 29(12):1449–1455, 1999.

[18] F. Standaert, K. Hemmes, and N. Woudstra. Analytical fuel cell modeling. *Journal of Power Sources*, 63(2):221–234, 1996.

[19] F. Standaert, K. Hemmes, and N. Woudstra. Analytical fuel cell modeling; non-isothermal fuel cells. *Journal of Power Sources*, 70(2):181–199, 1998.

[20] M. Eikerling and A. Kornyshev. Modelling the performance of the cathode catalyst layer of polymer electrolyte fuel cells. *Journal of Electroanalytical Chemistry*, 453(1–2):89–106, 1998.

[21] Z. Farhat. Modeling of catalyst layer microstructural refinement and catalyst utilization in a PEM fuel cell. *Journal of Power Sources*, 138(1–2):68–78, 2004.

[22] A. Kulikovsky. The voltage-current curve of a polymer electrolyte fuel cell: Exact and fitting equations. *Electrochemistry Communications*, 4(11):845–852, 2002.

[23] D. Bernardi and M. Verbrugge. Mathematical model of a gas-diffusion electrode bonded to a polymer electrolyte. *AIChE Journal*, 37(8):1151–1163, 1991.

[24] D. Bernardi and M. Verbrugge. A mathematical model of the solid polymer electrolyte fuel cell. *Journal of the Electrochemical Society*, 139(9):2477–2491, 1992.

[25] M. Verbrugge and R. Hill. Ion and solvent transport in ion-exchange membranes. 1. A macrohomogeneous mathematical model. *Journal of the Electrochemical Society*, 137(3):886–893, 1990.

[26] T. Springer, T. Zawodzinski, and S. Gottesfeld. Polymer electrolyte fuel cell model. *Journal of the Electrochemical Society*, 138(8):2334–2342, 1991.

[27] T. Springer, M. Wilson, and S. Gottesfeld. Modeling and experimental diagnostics in polymer electrolyte fuel cells. *Journal of the Electrochemical Society*, 140(12):3513–3526, 1993.

[28] T. Fuller and J. Newman. Water and thermal management in solid-polymer-electrolyte fuel cells. *Journal of the Electrochemical Society*, 140(5):1218–1225, 1993.

[29] T. V. Nguyen and R. White. A water and heat management model for proton-exchange-membrane fuel-cells. *Journal of the Electrochemical Society*, 140(8):2178–2186, 1993.

[30] D. Thirumalai and R. White. Mathematical modeling of proton-exchange-membrane fuel-cell stacks. *Journal of the Electrochemical Society*, 144(5):1717–1723, 1997.

[31] J. Yi and T. V. Nguyen. An along-the-channel model for proton exchange membrane fuel cells. *Journal of the Electrochemical Society*, 145(4):1149–1159, 1998.

[32] M. Wohr, K. Bolwin, W. Schnurnberger, M. Fischer, W. Neubrand, and G. Eigenberger. Dynamic modelling and simulation of a polymer membrane fuel cell including mass transport limitation. *International Journal of Hydrogen Energy*, 23(3):213–218, 1998.

[33] A. Rowe and X. Li. Mathematical modeling of proton exchange membrane fuel cells. *Journal of Power Sources*, 102:82–96, 2001.

[34] G. Maggio, V. Recupero, and C. Mantegazza. Modelling of temperature distribution in a solid polymer electrolyte fuel cell stack. *Journal of Power Sources*, 62(2):167–174, 1996.

[35] S. Shimpalee and S. Dutta. Numerical prediction of temperature distribution in PEM fuel cells. *Numerical Heat Transfer Part A - Applications*, 38(2):111–128, 2000.

[36] P. Costamagna. Transport phenomena in polymeric membrane fuel cells. *Chemical Engineering Science*, 56(2):323–332, 2001.

[37] H. Ju, H. Meng, and C. Y. Wang. A single-phase, non-isothermal model for PEM fuel cells. *International Journal of Heat and Mass Transfer*, 48(7):1303–1315, 2005.

[38] Y. Shan and S. Choe. A high dynamic PEM fuel cell model with temperature effects. *Journal of Power Sources*, 145:30–39, 2005.

[39] V. Gurau, H. Liu, and S. Kakac. Two-dimensional model for proton exchange membrane fuel cells. *AIChE Journal*, 44(11):2410–2422, 1998.

[40] S. Um, C. Y. Wang, and K. Chen. Computational fluid dynamics modeling of proton exchange membrane fuel cells. *Journal of the Electrochemical Society*, 147(12):4485–4493, 2000.

[41] S. Um and C. Y. Wang. Three-dimensional analysis of transport and electrochemical reactions in polymer electrolyte fuel cells. *Journal of Power Sources*, 125(1):40–51, 2004.

[42] S. Um and C. Y. Wang. Computational study of water transport in proton exchange membrane fuel cells. *Journal of Power Sources*, 156(2):211–223, 2006.

[43] T. Okada, G. Xie, and M. Meeg. Simulation for water management in membranes for polymer electrolyte fuel cells. *Electrochimica Acta*, 43(14–15):2141–2155, 1998.

[44] M. Eikerling, Y. Kharkats, A. Kornyshev, and Y. Volfkovich. Phenomenological theory of electro-osmotic effect and water management in polymer electrolyte proton-conducting membranes. *Journal of the Electrochemical Society*, 145(8):2684–2699, 1998.

[45] T. Thampan, S. Malhotra, H. Tang, and R. Datta. Modeling of conductive transport in proton exchange membranes for fuel cells. *Journal of the Electrochemical Society*, 147(9):3242–3250, 2000.

[46] N. Siegel, M. Ellis, D. Nelson, and M. von Spakovsky. A two-dimensional computational model of a PEMFC with liquid water transport. *Journal of Power Sources*, 128(2):173–184, 2004.

[47] H. Wu, P. Berg, and X. Li. On the modeling of water transport in PEM fuel cells. *Electrochimica Acta*, 54:6913–6927, 2009.

[48] H. van Bussel, F. Koene, and R. Mallant. Dynamic model of solid polymer fuel cell water management. *Journal of Power Sources*, 71(1–2):218–222, 1998.

[49] F. Chen, Y. Su, C. Soong, W. Yan, and H. Chu. Transient behavior of water transport in the membrane of a PEM fuel cell. *Journal of Electroanalytical Chemistry*, 566(1):85–93, 2004.

[50] H. Wu, P. Berg, and X. Li. Non-isothermal transient modeling of water transport in PEM fuel cells. *Journal of Power Sources*, 165(1):232–243, 2007.

[51] C. Y. Wang and P. Cheng. A multiphase mixture model for multiphase, multicomponent transport in capillary porous media. 1. Model development. *International Journal of Heat and Mass Transfer*, 39(17):3607–3618, 1996.

[52] W. He, J. Yi, and T. V. Nguyen. Two-phase flow model of the cathode of PEM fuel cells using interdigitated flow fields. *AIChE Journal*, 46(10):2053–2064, 2000.

[53] G. Janssen. A phenomenological model of water transport in a proton exchange membrane fuel cell. *Journal of the Electrochemical Society*, 148(12):A1313–A1323, 2001.

[54] Z. Wang, C. Y. Wang, and K. Chen. Two-phase flow and transport in the air cathode of proton exchange membrane fuel cells. *Journal of Power Sources*, 94(1):40–50, 2001.

[55] L. You and H. Liu. A two-phase flow and transport model for the cathode of PEM fuel cells. *International Journal of Heat and Mass Transfer*, 45(11):2277–2287, 2002.

[56] T. Berning and N. Djilali. A 3D, multiphase, multicomponent model of the cathode and anode of a PEM fuel cell. *Journal of the Electrochemical Society*, 150(12):A1589–A1598, 2003.

[57] A. Kulikovsky. Quasi-3D modeling of water transport in polymer electrolyte fuel cells. *Journal of the Electrochemical Society*, 150(11):A1432–A1439, 2003.

[58] S. Mazumder and J. Cole. Rigorous 3D mathematical modeling of PEM fuel cells - II. Model predictions with liquid water transport. *Journal of the Electrochemical Society*, 150(11):A1510–A1517, 2003.

[59] D. Natarajan and T. V. Nguyen. A two-dimensional, two-phase, multicomponent, transient model for the cathode of a proton exchange membrane fuel cell using conventional gas distributors. *Journal of the Electrochemical Society*, 148(12):A1324–A1335, 2001.

[60] D. Natarajan and T. V. Nguyen. A two-dimensional, two-phase, multicomponent, transient model for the cathode of a proton exchange membrane fuel cell using conventional gas distributors (vol 148, pg a1324, 2001). *Journal of the Electrochemical Society*, 150(3):L5–L5, 2003.

[61] M. Hu, X. Zhu, M. Wang, A. Gu, and L. Yu. Three dimensional, two phase flow mathematical model for PEM fuel cell: Part II. Analysis and discussion of the internal transport mechanisms. *Energy Conversion and Management*, 45(11–12):1883–1916, 2004.

[62] G. Lin, W. He, and T. V. Nguyen. Modeling liquid water effects in the gas diffusion and catalyst layers of the cathode of a PEM fuel cell. *Journal of the Electrochemical Society*, 151(12):A1999–A2006, 2004.

[63] U. Pasaogullari and C. Y. Wang. Liquid water transport in gas diffusion layer of polymer electrolyte fuel cells. *Journal of the Electrochemical Society*, 151(3):A399–A406, 2004.

[64] U. Pasaogullari and C. Y. Wang. Two-phase transport and the role of micro-porous layer in polymer electrolyte fuel cells. *Electrochimica Acta*, 49(25):4359–4369, 2004.

[65] U. Pasaogullari and C. Y. Wang. Two-phase modeling and flooding prediction of polymer electrolyte fuel cells. *Journal of the Electrochemical Society*, 152(2):A380–A390, 2005.

[66] U. Pasaogullari, C. Y. Wang, and K. Chen. Two-phase transport in polymer electrolyte fuel cells with bilayer cathode gas diffusion media. *Journal of the Electrochemical Society*, 152(8):A1574–A1582, 2005.

[67] M. Chang, F. Chen, and H. Teng. Effects of two-phase transport in the cathode gas diffusion layer on the performance of a PEMFC. *Journal of Power Sources*, 160(1):268–276, 2006.

[68] G. Lin and T. V. Nguyen. A two-dimensional two-phase model of a PEM fuel cell. *Journal of the Electrochemical Society*, 153(2):A372–A382, 2006.

[69] G. Hu and J. Fan. A three-dimensional, multicomponent, two-phase model for a proton exchange membrane fuel cell with straight channels. *Energy & Fuels*, 20(2):738–747, 2006.

[70] Y. Wang and C. Y. Wang. A nonisothermal, two-phase model for polymer electrolyte fuel cells. *Journal of the Electrochemical Society*, 153(6):A1193–A1200, 2006.

[71] L. You and H. Liu. A two-phase flow and transport model for PEM fuel cells. *Journal of Power Sources*, 155(2):219–230, 2006.

[72] H. Meng. Numerical investigation of transient responses of a PEM fuel cell using a two-phase non-isothermal mixed-domain model. *Journal of Power Sources*, 171:738–746, 2007.

[73] T. Koido, T. Furusawa, and K. Moriyama. An approach to modeling two-phase transport in the gas diffusion layer of a proton exchange membrane fuel cell. *Journal of Power Sources*, 175:127–136, 2008.

[74] V. Gurau, T. Zawodzinski, and J. Mann. Two-phase transport in PEM fuel cell cathodes. *Journal of Fuel Cell Science and Technology*, 5:021009–1–12, 2008.

[75] Y. Wang, S. Basu, and C. Wang. Modeling two-phase flow in PEM fuel cell channels. *Journal of Power Sources*, 179:603–617, 2008.

[76] D. Gerteisen, T. Heilmann, and C. Ziegler. Modeling the phenomena of dehydration and flooding of a polymer electrolyte membrane fuel cell. *Journal of Power Sources*, 187:165–181, 2009.

[77] P. Li, L. Schaefer, Q. Wang, T. Zhang, and M. Chyu. Multi-gas transportation and electrochemical performance of a polymer electrolyte fuel cell with complex flow channels. *Journal of Power Sources*, 115:90–100, 2003.

[78] B. Sivertsen and N. Djilali. CFD-based modelling of proton exchange membrane fuel cells. *Journal of Power Sources*, 141:65–78, 2005.

[79] D. Harvey, J. Pharoah, and K. Karan. A comparison of different approaches to modelling the PEMFC catalyst layer. *Journal of Power Sources*, 179:209–219, 2008.

[80] C. Marr and X. Li. An engineering model of proton exchange membrane fuel cell performance. *ARI - An International Journal for Physical and Engineering Sciences*, 50(4):190–2000, 1998.

[81] N. Siegel, M. Ellis, D. Nelson, and M. von Spakovsky. Single domain PEMFC model based on agglomerate catalyst geometry. *Journal of Power Sources*, 115(1):81–89, 2003.

[82] J. Baschuk and X. Li. Modelling of polymer electrolyte membrane fuel cells with variable degrees of water flooding. *Journal of Power Sources*, 86(1–2):181–196, 2000.

[83] M. Wilson and S. Gottesfeld. Thin-film catalyst layers for polymer electrolyte fuel cell electrodes. *Journal of Applied Electrochemistry*, 22(1):1–7, 1992.

[84] Y. Rho, S. Srinivasan, and Y. Kho. Mass transport phenomena in proton exchange membrane fuel cells using O_2/He, O_2/Ar, and O_2/N_2 mixtures II. Theoretical analysis. *Journal of the Electrochemical Society*, 141(8):2089–2096, 1994.

[85] K. Broka and P. Ekdunge. Modelling the PEM fuel cell cathode. *Journal of Applied Electrochemistry*, 27(3):281–289, 1997.

[86] M. Perry, J. Newman, and E. Cairns. Mass transport in gas-diffusion electrodes: A diagnostic tool for fuel-cell cathodes. *Journal of the Electrochemical Society*, 145(1):5–15, 1998.

[87] Q. Wang, D. Song, T. Navessin, S. Holdcroft, and Z. S. Liu. A mathematical model and optimization of the cathode catalyst layer structure in PEM fuel cells. *Electrochimica Acta*, 50(2–3):725–730, 2004.

[88] K. Yin. Parametric study of proton exchange membrane fuel cell cathode using an agglomerate model. *Journal of the Electrochemical Society*, 152(3):A583–A593, 2005.

[89] Q. Wang, M. Eikerling, D. Song, and Z. S. Liu. Structure and performance of different types of agglomerates in cathode catalyst layers of PEM fuel cells. *Journal of Electroanalytical Chemistry*, 573(1):61–69, 2004.

[90] W. Sun, B. Peppley, and K. Karan. An improved two-dimensional agglomerate cathode model to study the influence of catalyst layer structural parameters. *Electrochimica Acta*, 50(16–17):3359–3374, 2005.

[91] A. Fischer, J. Jindra, and H. Wendt. Porosity and catalyst utilization of thin layer cathodes in air operated PEM fuel cells. *Journal of Applied Electrochemistry*, 28(3):277–282, 1998.

[92] C. Du, X. Cheng, T. Yang, G. Yin, and P. Shi. Numerical simulation of the ordered catalyst layer in cathode of proton exchange membrane fuel cells. *Electrochemistry Communications*, 7(12):1411–1416, 2005.

[93] D. Song, Q. Wang, Z. S. Liu, T. Navessin, and S. Holdcroft. Numerical study of PEM fuel cell cathode with non-uniform catalyst layer. *Electrochimica Acta*, 50(2–3):731–737, 2004.

[94] P. K. Das, X. Li, and Z. S. Liu. A three-dimensional agglomerate model for the cathode catalyst layer in PEM fuel cells. *Journal of Power Sources*, 179(1):186–199, 2008.

[95] M. Ishii. *Thermo-Fluid Dynamic Theory of Two-Phase Flow*. Eyrolles, 1975.

[96] J. Steinbrenner, C. Hidrovo, F. Wang, S. Vigneron, E. Lee, T. Kramer, C. Cheng, J. Eaton, and K. Goodson. Measurement and modeling of liquid film thickness evolution in stratified two-phase microchannel flows. *Applied Thermal Engineering*, 27(10):1722–1727, 2007.

[97] Z. Ogumi, T. Kuroe, and Z. Takehara. Gas permeation in SPE method II. Oxygen and hydrogen permeation through Nafion. *Journal of the Electrochemical Society*, 132(11):2601–2605, 1985.

[98] T. Gierke and W. Hsu. The cluster-network model of ion clustering in perfluorosulfonated membranes. In A. Eisenberg and H. Yeager (eds.), *Perfluorinated Ionomer Membranes*, ACS Symposium Series 180, pages 283–307. American Chemical Society, Washington, U.S.A, 1982.

[99] G. Birkhoff. Averaged conservation laws in pipes. *Journal of Mathematical Analysis and Applications*, 8(1):66–77, 1964.

[100] J. C. Slattery. Flow of viscoelastic fluids through porous media. *AIChE Journal*, 13(6):1066–1071, 1967.

[101] Y. Bultel, P. Ozil, and R. Durand. Modelling the mode of operation of PEMFC electrodes at the particle level: influence of ohmic drop within the active layer on electrode performance. *Journal of Applied Electrochemistry*, 28(3):269–276, 1998.

[102] P. Cheng. Heat trasfer in geothermal sustems. *Advances in Heat Transfer*, 14:1–105, 1979.

[103] D. A. Neild and A. Bejan. *Convection in Porous Media*. Springer, New York, 1999.

[104] S. Whitaker. Diffusion and dispersion in porous media. *AIChE Journal*, 13(3):420–427, 1967.

[105] W. G. Gray. A derivation of the equations for multiphase transport. *Chemical Engineering Science*, 30(2):229–233, 1975.

[106] S. Whitaker. The transport equations for multi-phase systems. *Chemical Engineering Science*, 28(1):139–147, 1971.

[107] R. Bird, W. Stewart, and E. Lightfoot. *Transport Phenomena*. John Wiley & Sons Inc., New York, 1960.

[108] M. Kimble and N. Vanderborgh. Reactant gas flow fields in advanced PEM fuel cell designs. *Proceedings of the Intersociety Energy Conversion Engineering Conference*, pages 3.413–3.417, 1992.

[109] F. Boyer. A theoretical and numerical model for the study of incompressible mixture flows. *Computers and Fluids*, 31(1):41–68, 2002.

[110] K. Vafai and C. Tien. Boundary and inertia effects on flow and heat transfer in porous media. *International Journal of Heat and Mass Transfer*, 24(2):195–203, 1981.

[111] K. Vafai and R. Thiyagaraja. Analysis of flow and heat transfer at the interface region of a porous medium. *International Journal of Heat and Mass Transfer*, 30(7):1391–1405, 1987.

[112] K. Vafai and S. Kim. Fluid mechanics of the interface region between a porous medium and a fluid layer - an exact solution. *International Journal of Heat and Fluid Flow*, 11(3):254–256, 1990.

[113] C. Y. Wang and P. Cheng. Multiphase flow and heat transfer in porous media. *Advances in Heat Transfer*, 30:93–196, 1997.

[114] C. Y. Wang. A fixed-grid numerical algorithm for two-phase flow and heat transfer in porous media. *Numerical Heat Transfer, Part B*, 32(1):85–105, 1997.

[115] C. Y. Wang. Two-phase flow and transport. *Handbook of Fuel Cells - Fundamentals, Technology and Applications*, 3:337–347, 2003.

[116] D. Song, Q. Wang, Z. S. Liu, and C. Huang. Transient analysis for the cathode gas diffusion layer of PEM fuel cells. *Journal of Power Sources*, 159(2):928–942, 2006.

[117] Y. Wang and C. Y. Wang. A nonisothermal, two-phase model for polymer electrolyte fuel cells. *Journal of the Electrochemical Society*, 153(6):A1193–A1200, 2006.

[118] W. A. Cole and W. A. Wakeham. The viscosity of nitrogen, oxygen, and their binary mixtures in the limit of zero density. *Journal of Physical and Chemical Reference Data*, 14(1):209–226, 1985.

[119] J. Sengers and J. Watson. Improved international formulations for the viscosity and thermal conductivity of water substance. *Journal of Physical and Chemical Reference Data*, 15(4):1291–1314, 1986.

[120] H. Ju, G. Luo, and C. Y. Wang. Probing liquid water saturation in diffusion media of polymer electrolyte fuel cells. *Journal of the Electrochemical Society*, 154(2):B218–B228, 2007.

[121] D. R. Lide, ed. *CRC Handbook of Chemistry and Physics*. CRC Press/Taylor and Francis, Boca Raton, FL, 88$^{\text{th}}$ (internet version) edition, 2008.

[122] D. Song, Q. Wang, Z. S. Liu, M. Eikerling, Z. Xie, T. Navessin, and S. Holdcroft. A method for optimizing distributions of Nafion and Pt in cathode catalyst layers of PEM fuel cells. *Electrochimica Acta*, 50(16–17):3347–3358, 2005.

[123] G. Castellan. *Physical Chemistry*. Addison-Wesley, Boston, 1983.

[124] K. Sutton and P. Gnoffo. Multi-component diffusion with application to computational aerothermodynamics. *7th AIAA/ASME Joint Thermophysics and Heat Transfer Conference*, (AIAA 98–2575), 1998.

[125] R. Taylor and R. Krishna. *Multicomponent Mass Transfer*. John Wiley & Sons Inc., New York, 1993.

[126] C. Curtiss and R. Bird. Multicomponent diffusion. *Industrial & Engineering Chemistry Research*, 38:2515–2522, 1999.

[127] R. H. Perry and D. W. Green. *Perry's Chemical Engineers' Handbook*. McGraw-Hill, New York, 1997.

[128] A. Kulikovsky, T. Wuester, A. Egmen, and D. Stolten. Analytical and numerical analysis of PEM fuel cell performance curve. *Journal of the Electrochemical Society*, 152(6):A1290–A1300, 2005.

[129] J. Newman. *Electrochemical Systems*. Prentice-Hall, New Jersey, 2$^{\text{nd}}$ edition, 1991.

[130] K. Vetter. *Electrochemical Kinetics*. Academic Press, New York, 1967.

[131] J. Baschuk and X. Li. A comprehensive, consistent and systematic mathematical model of PEM fuel cells. *Applied Energy*, 86:181–193, 2009.

[132] D. Poirier and E. McBride. Thermal conductivities of hypoeutectic al-cu alloys during solidification and cooling. *Materials Science and Engineering A*, 224:48–52, 1997.

[133] G. H. Neale and W. K. Nader. Prediction of transport processes within porous media - diffusive flow processes within an homogeneous swarm of spherical-particles. *AIChE Journal*, 19:112–119, 1973.

[134] M. M. Tomadakis and S. V. Sotirchos. Ordinary and transition regime diffusion in random fiber structures. *AIChE Journal*, 39:397–412, 1993.

[135] M. Mezedur, M. Kaviany, and W. Moore. Effect of pore structure, randomness sand size on effective mass diffusivity. *AIChE Journal*, 48:15–24, 2002.

[136] P. Jackson, D. Taylorsmith, and P. Stanford. Resistivity-porosity-particle shape relationships for marine sands. *Geophysics*, 43:1250–1268, 1978.

[137] K. Mendelson and M. Cohen. The effect of grain anisotropy on the electrical-properties of sedimentary-rocks. *Geophysics*, 47:257–263, 1982.

[138] O. Delima and M. Sharma. A grain conductivity approach to shaly sandstones. *Geophysics*, 55(10):1347–1356, 1990.

[139] D. Mu, Z. S. Liu, C. Huang, and N. Djilali. Prediction of the effective diffusion coefficient in random porous media using the finite element method. *Journal of Porous Materials*, 14:49–54, 2007.

[140] X. Shan and G. Doolen. Diffusion in a multicomponent lattice Boltzmann equation model. *Physical Review E*, 54:3614–3620, 1996.

[141] Z. Hashin. The elastic moduli of heterogeneous materials. *Journal of Applied Mechanics*, 29:143–150, 1962.

[142] Z. Hashin and S. Shtrikman. A variational approach to theory of effective magnetic permeability of multiphase materials. *Journal of Applied Physics*, 33:3125–3131, 1962.

[143] G. W. Milton. *The Theory of Composites*. Cambridge University Press, New York, 2002.

[144] M. Uchida, Y. Aoyama, N. Eda, and A. Ohta. New preparation method for polymer-electrolyte fuel-cells. *Journal of the Electrochemical Society*, 142:463–468, 1995.

[145] O. Wiener. Die theorie des mischkorpers fur das feld der stationaren stromung. *Abh. Math. Phys. Kl. Sachs. Akad. Wiss. (Leipzig)*, 32:507–604, 1912.

[146] D. E. Aspnes. Local-field effects and effective-medium theory - a microscopic perspective. *American Journal of Physics*, 50:704–709, 1982.

[147] M. Silva, P. Kerkhof, and W. Coumans. Estimation of effective diffusivity in drying of heterogeneous porous media. *Industrial & Engineering Chemistry Research*, 39:1443–1452, 2000.

[148] B. Poling, J. Prausnitz, and J. O'Connell. *The Properties of Gases and Liquids*. McGraw-Hill, 5th edition, 2001.

[149] A. Corey. *Mechanics of Heterogenous Fluids in Porous Media*. Water Resources Publications, 1st edition, 1977.

[150] M. van Genuchten. A closed-form equation for predicting the hydraulic conductivity of unsaturated soils. *Soil Science Society of America Journal*, 44:892–898, 1980.

[151] J. Gostick, M. Fowler, M. Ioannidis, M. Pritzker, Y. Volfkovich, and S. Sakars. Capillary pressure and hydrophilic porosity in gas diffusion layers for polymer electrolyte fuel cells. *Journal of Power Sources*, 156(2):375–387, 2006.

[152] E. Kumbur, K. Sharp, and M. Mench. On the effectiveness of Leverett approach for describing the water transport in fuel cell diffusion media. *Journal of Power Sources*, 168:356–368, 2007.

[153] J. Hwang. A complete two-phase model of a porous cathode of a PEM fuel cell. *Journal of Power Sources*, 164:174181, 2007.

[154] H. Meng. Multi-dimensional liquid water transport in the cathode of a PEM fuel cell with consideration of the micro-porous layer. *International Journal of Hydrogen Energy*, 34:5488–5497, 2009.

[155] A. Adamson. *Physical Chemistry of Surfaces*. Wiley, New York, 5th edition, 1990.

[156] M. C. Leverett. Capillary behavior in porous solids. *Transactions of AIME*, 142(1):152–169, 1941.

[157] K. S. Udell. Heat transfer in porous media considering phase change and capillarity - The heat pipe effect. *International Journal of Heat and Mass Transfer*, 28(2):485–495, 1985.

[158] T. Berning, M. Odgaard, and S. Kaer. A computational analysis of multiphase flow through pemfc cathode porous media using the multifluid approach. *Journal of the Electrochemical Society*, 156(11):B1301–B1311, 2009.

[159] L. Pisani, G. Murgia, M. Valentini, and B. D'Aguanno. A working model of polymer electrolyte fuel cells - Comparisons between theory and experiments. *Journal of the Electrochemical Society*, 149(7):A898–A904, 2002.

[160] A. Weber, R. Darling, and J. Newman. Modeling two-phase behavior in PEFCs. *Journal of the Electrochemical Society*, 151(10):A1715–A1727, 2004.

[161] P. K. Das, X. Li, and Z. S. Liu. Effective transport coefficients in PEM fuel cell catalyst and gas diffusion layers: Beyond Bruggeman approximation. *Applied Energy*, 87(9):2785–2796, 2010.

[162] E-TEK. *Gas Diffusion Electrodes and Catalyst Materials Catalogue*. 1995.

[163] P. K. Das, X. Li, and Z. S. Liu. Effect of catalyst layer structure on PEM fuel cell performance. In *Proc. of 11th Ulm ElectroChemical Talks*. Ulm, Germany, 2008.

[164] M. Eikerling, A. Kornyshev, A. Kuznetsov, J. Ulstrup, and S. Walbran. Mechanisms of proton conductance in polymer electrolyte membranes. *Journal of Physical Chemistry B*, 105(17):3646–3662, 2001.

[165] L. You and H. Liu. A parametric study of the cathode catalyst layer of PEM fuel cells using a pseudo-homogeneous model. *International Journal of Hydrogen Energy*, 26(9):991–999, 2001.

[166] D. Natarajan and T. V. Nguyen. Three-dimensional effects of liquid water flooding in the cathode of a PEM fuel cell. *Journal of Power Sources*, 115(1):66–80, 2003.

[167] M. Sahraoui, C. Kharrat, and K. Halouani. Two-dimensional modeling of electrochemical and transport phenomena in the porous structures of a PEMFC. *International Journal of Hydrogen Energy*, 34(7):3091–3103, 2009.

[168] J. Benziger, J. Nehlsen, D. Blackwell, T. Brennan, and J. Itescu. Water flow in the gas diffusion layer of PEM fuel cells. *Journal of Membrane Science*, 261(1-2):98–106, 2005.

[169] H. Yamada, T. Hatanaka, H. Murata, and Y. Morimoto. Measurement of flooding in gas diffusion layers of polymer electrolyte fuel cells with conventional flow field. *Journal of the Electrochemical Society*, 153(9):A1748–A1754, 2006.

[170] U. Jung, S. Jeong, K. Park, H. Lee, K. Chun, D. Choi, and S. Kim. Improvement of water management in air-breathing and air-blowing PEMFC at low temperature using hydrophilic silica nano-particles. *International Journal of Hydrogen Energy*, 32(17):4459–4465, 2007.

[171] J. Owejan, T. Trabold, D. Jacobson, M. Arif, and S. Kandlikar. Effects of flow field and diffusion layer properties on water accumulation in a PEM fuel cell. *International Journal of Hydrogen Energy*, 32(17):4489–4502, 2007.

[172] X. Liu, H. Guo, F. Ye, and C. Ma. Flow dynamic characteristics in flow field of proton exchange membrane fuel cells. *International Journal of Hydrogen Energy*, 33(3):1040–1051, 2008.

[173] J. Owejan, J. Gagliardo, J. Sergi, S. Kandlikar, and T. Trabold. Water management studies in PEM fuel cells, Part I: Fuel cell design and in-situ water distributions. *International Journal of Hydrogen Energy*, 34(8):3436–3444, 2009.

[174] Z. Lu, S. Kandlikar, C. Rath, M. Grimm, W. Domigan, A. White, M. Hardbarger, J. Owejan, and T. Trabold. Water management studies in PEM fuel cells, Part II: Ex-situ investigation of flow maldistribution, pressure drop and two-phase flow pattern in gas channels. *International Journal of Hydrogen Energy*, 34(8):3445–3456, 2009.

[175] T. Ous and C. Arcoumanis. The formation of water droplets in an air-breathing PEMFC. *International Journal of Hydrogen Energy*, 34(8):3476–3487, 2009.

[176] E. Birgersson, M. Noponen, and M. Vynnyckya. Analysis of a two-phase non-isothermal model for a PEFC. *Journal of the Electrochemical Society*, 152(5):A1021–A1034, 2005.

[177] Y. H. Park and J. A. Caton. An experimental investigation of electro-osmotic drag coefficients in a polymer electrolyte membrane fuel cell. *International Journal of Hydrogen Energy*, 33(24):7513–7520, 2008.

[178] P. K. Das, X. Li, and Z. S. Liu. Modeling of liquid water transport in cathode catalyst layer of PEM fuel cells. In *Proc. of ASME 2009 Seventh International Fuel Cell Science, Engineering and Technology Conference*, pages 1–10. Newport Beach, California, 2009. Paper ID 85189.

[179] P. K. Das, X. Li, and Z. S. Liu. Analysis of liquid water transport in cathode catalyst layer of PEM fuel cells. *International Journal of Hydrogen Energy*, 35(6):2403–2416, 2010.

[180] COMSOL Inc. *User's Guide*. version 3.2a, 2006.

[181] C. Stone. Technology leadership: A roadmap to commercially viable PEMFC stack technology. In *Proc. of the International Green Energy Conference*. Waterloo, Ontario, Canada, 2005.

[182] D. Song, Q. Wang, Z. S. Liu, T. Navessin, M. Eikerling, and S. Holdcroft. Numerical optimization study of the catalyst layer of PEM fuel cell cathode. *Journal of Power Sources*, 126(1–2):104–111, 2004.

[183] P. Ustohal, F. Stauffer, and T. Dracos. Measurement and modeling of hydraulic characteristics of unsaturated porous media with mixed wettability. *Journal of Contaminant Hydrology*, 33(1–2):5–37, 1998.

[184] P. K. Das, S. Bhattacharjee, and W. Moussa. Electrostatic double layer force between two spherical particles in a straight cylindrical capillary: Finite element analysis. *Langmuir*, 19(10):4162–4172, 2003.

[185] P. K. Das and S. Bhattacharjee. Finite element estimation of electrostatic double layer interaction between colloidal particles inside a rough cylindrical capillary: effect of charging behavior. *Colloids and Surfaces A: Physicochemical and Engineering Aspects*, 256(2–3):91–103, 2005.

[186] Fluent, Inc. *User Manual*. version 6.3, 2006.

[187] H. Wu. *Mathematical modeling of transient transport phenomena in PEM fuel cells*. Ph.D. thesis, University of Waterloo, Canada, 2009.